

UNIVERSIDADE DE SÃO PAULO

Instituto de Ciências Matemáticas e de Computação

New models and Numerical Methods in Hydrodynamic Lubrication

Alfredo Del Carmen Jaramillo Palma

Tese de Doutorado do Programa de Pós-Graduação em Ciências de Computação e Matemática Computacional (PPG-CCMC)

SERVIÇO DE PÓS-GRADUAÇÃO DO ICMC-USP

Data de Depósito:

Assinatura: _____

Alfredo Del Carmen Jaramillo Palma

New models and Numerical Methods in Hydrodynamic Lubrication

Thesis submitted to the Institute of Mathematics and Computer Sciences – ICMC-USP – in accordance with the requirements of the Computer and Mathematical Sciences Graduate Program, for the degree of Doctor in Science. *FINAL VERSION*

Concentration Area: Computer Science and Computational Mathematics

Advisor: Prof. Dr. Gustavo Carlos Buscaglia

USP – São Carlos
March 2019

Ficha catalográfica elaborada pela Biblioteca Prof. Achille Bassi
e Seção Técnica de Informática, ICMC/USP,
com os dados inseridos pelo(a) autor(a)

J37n Jaramillo Palma, Alfredo Del Carmen
New models and Numerical Methods in Hydrodynamic Lubrication / Alfredo Del Carmen Jaramillo Palma;
orientador Gustavo Carlos Buscaglia. -- São Carlos, 2019.
166 p.

Tese (Doutorado - Programa de Pós-Graduação em Ciências de Computação e Matemática Computacional) -- Instituto de Ciências Matemáticas e de Computação, Universidade de São Paulo, 2019.

1. Hydrodynamic Lubrication. 2. cavitation modeling. 3. Reynolds equation. 4. Reynolds-Rayleigh-Plesset coupling. 5. numerical simulation.
I. Buscaglia, Gustavo Carlos, orient. II. Título.

Alfredo Del Carmen Jaramillo Palma

**Novos modelos e métodos numéricos em Lubrificação
Hidrodinâmica**

Tese apresentada ao Instituto de Ciências
Matemáticas e de Computação – ICMC-USP,
como parte dos requisitos para obtenção do título
de Doutor em Ciências – Ciências de Computação e
Matemática Computacional. *VERSÃO REVISADA*

Área de Concentração: Ciências de Computação e
Matemática Computacional

Orientador: Prof. Dr. Gustavo Carlos Buscaglia

USP – São Carlos
Março de 2019

*A mis padres, Ida y Victor,
y a mi amigo y colega, Hugo Checo.*

ACKNOWLEDGEMENTS

Firstly, I want to thank Gustavo Buscaglia, my mentor, for its patience and excellent ideas. I also want to thank my colleagues of the Applied Mathematics and Scientific Computing Laboratory: Stevens, Hugo and Roberto.

To my colleagues from INSA de Lyon, Guy Bayada, Mohammed Jai and Ionel Ciuperca. And my friends abroad: Virginie, Miguel, Geneviève & Jean Marc, Pietro, Jaap and Stéphanie.

To my parents, Ida and Victor. To my friends in São Carlos, specially to: Paola, Daniel Smania, Helen, Guilherme, Juan Luis, Adriano, Sabrina, Emanoel, Daniel Gutierrez, Luiz Sato, Leonardo, Nereida, Jorge, Aurea, Oscar and Thais.

An special thanks to Coordenação de Aperfeiçoamento de Pessoal de Nível Superior (CAPES) (grant PROEX-8434433/D) for funding my research during my PhD and internship abroad (grant 88881.133497/2016-01).

I also want to thank to all professors and faculty members from ICMS-USP who, directly or indirectly contributed to this work. I am sure there are many names missing here, to all of them, thanks!

“*O fortuna...*”
Carmina Burana

ABSTRACT

JARAMILLO, J. P. **New models and Numerical Methods in Hydrodynamic Lubrication.** 2019. 166 p. Tese (Doutorado em Ciências – Ciências de Computação e Matemática Computacional) – Instituto de Ciências Matemáticas e de Computação, Universidade de São Paulo, São Carlos – SP, 2019.

The simulation of lubricated mechanisms has an economic and academic interest reflected in dozens of theoretical and experimental works published in the last decades. Industry has given constant attention to the research for robust numerical codes that allow predicting the efficiency of different designs (e.g., load carrying capacity, energy loss, wear). The Reynolds equation along a cavitation model is one of the main tools to perform those studies, allowing to estimate the lubricant flow between the surfaces in proximity.

The state-of-the-art in cavitation modeling is represented by the mass-conserving Elrod-Adams model. Aiming to augment the physical accuracy of this model, in this dissertation an extension of it is proposed in order to accommodate non-homogeneous boundary conditions for pressure, which is proven to be mandatory for some mechanical devices like the Piston-Ring. This is done while assuring that mass conservation is maintained in the extended model.

A new trend in hydrodynamics is to incorporate the physics of cavitation by modeling the behavior of a distribution of gas/vapor bubbles immersed in a Newtonian liquid. This is done by means of a coupled model, called the Reynolds-Rayleigh-Plesset (RRP) coupling, where the Reynolds equation is used for the mixture flow and the Rayleigh-Plesset equation is used for the bubbles dynamics. In this work some results on the well-posedness of the RRP model are obtained and numerical methods are developed for both the cases where the inertial terms in the Rayleigh-Plesset equation are disregarded or not.

Keywords: Hydrodynamic Lubrication, cavitation modeling, Reynolds equation, Reynolds-Rayleigh-Plesset coupling, numerical simulation.

RESUMO

JARAMILLO, J. P. **Novos modelos e métodos numéricos em Lubrificação Hidrodinâmica.** 2019. 166 p. Tese (Doutorado em Ciências – Ciências de Computação e Matemática Computacional) – Instituto de Ciências Matemáticas e de Computação, Universidade de São Paulo, São Carlos – SP, 2019.

A simulação de mecanismos lubrificados tem um interesse econômico e acadêmico refletido em dezenas de trabalhos teóricos e experimentais publicados nas últimas décadas. A indústria tem dado atenção constante à pesquisa de códigos numéricos robustos que permitem prever a eficiência de diferentes configurações dos parâmetros de desenho (por exemplo, capacidade de carga, perda de energia, desgaste). A equação de Reynolds junto com um modelo de cavitação é uma das principais ferramentas para realizar esses estudos, permitindo estimar o fluxo de lubrificante entre as superfícies em proximidade.

O estado da arte na modelagem da cavitação é representado pelo modelo conservativo de Elrod-Adams. Com o objetivo de aumentar a acurácia física deste modelo, nesta dissertação propõe-se uma extensão dele para acomodar condições de contorno não homogêneas para a pressão, o que é comprovado como sendo mandatório para alguns dispositivos mecânicos como o Pistão-Anel. Isso é feito garantindo que a conservação de massa seja mantida no novo modelo.

Uma nova tendência em Hidrodinâmica é incorporar a física da cavitação modelando o comportamento de uma distribuição de bolhas de gás/vapor imersas em um líquido newtoniano. Isto é feito usando o modelo chamado de *Acoplamento de Reynolds-Rayleigh-Plesset* (RRP), onde a equação de Reynolds é usada para computar o fluxo da mistura de líquido-gás/vapor e a equação de Rayleigh-Plesset é usada para computar a dinâmica das bolhas. Neste trabalho são obtidos alguns resultados sobre a boa colocação do modelo RRP e são desenvolvidos métodos numéricos para ambos os casos em que os termos iniciais na equação de Rayleigh-Plesset são considerados ou não.

Palavras-chave: Lubrificação Hidrodinâmica, equação de Reynolds, Cavitação, modelo de cavitação de Reynolds-Rayleigh-Plesset.

LIST OF SYMBOLS

\mathbb{R}_*^+ — Strictly positive real numbers

$\frac{\partial}{\partial x}$ — Partial derivative with respect to x

∂_x — Same as $\frac{\partial}{\partial x}$

∇f — Gradient of f

∇^2 — The Laplacian operator

$\mathbf{v} \cdot \nabla$ — The operator $\sum_i v_i \partial_{x_i}$

$\frac{D}{Dt}$ — The operator $\partial_t + \mathbf{v} \cdot \nabla$

$H_0^1(\Omega)$ — Sobolev space of one-time weakly differentiable functions with compact support on Ω

$\llbracket f \rrbracket_{\mathbf{n}}$ — $\llbracket f \rrbracket_{\mathbf{n}}(\mathbf{x}) = \lim_{\epsilon \rightarrow 0} (f(\mathbf{x} + \epsilon \mathbf{n}) - f(\mathbf{x} - \epsilon \mathbf{n}))$: jump of the function f on \mathbf{x} in the direction \mathbf{n}

$\partial\Omega$ — Boundary of the domain Ω

$L^\infty(\Omega)$ — The space of measurable functions from Ω to \mathbb{R} such that $\mu(\{x : f(x) > M\}) = 0$ for some $M \in \mathbb{R}$

$\bar{\Omega}$ — Topological closure of Ω

$C^p(X; Y)$ — Space of p -times Fréchet differentiable functions $X \mapsto Y$, both Banach spaces

$L^p(\Omega)$ — The space $\{f : \Omega \mapsto \mathbb{R} \text{ measurable s.t. } \int_{\Omega} |f|^p d\mu < \infty\}$

E^{-1} — Dual space of the Banach E

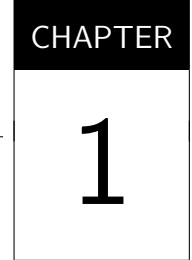
D_k — Fréchet derivative with respect to the k -th variable

CONTENTS

| | | |
|---------|---|----|
| 1 | INTRODUCTION | 21 |
| 1.1 | Motivation | 21 |
| 1.2 | Outline | 23 |
| 1.3 | Contributions | 24 |
| 2 | MATHEMATICAL MODELS IN LUBRICATION | 25 |
| 2.1 | Dynamical variables and their coupling | 25 |
| 2.2 | The compressible Reynolds equation | 26 |
| 2.2.1 | <i>Mass fluxes approximation in thin films</i> | 26 |
| 2.2.2 | <i>The compressible Reynolds equation</i> | 28 |
| 2.3 | Cavitation modeling | 28 |
| 2.3.1 | <i>Reynolds cavitation model</i> | 29 |
| 2.3.2 | <i>Elrod-Adams cavitation model</i> | 30 |
| 2.3.3 | <i>Boundary conditions in the interface $\partial\Omega_+$</i> | 31 |
| 2.4 | Model problems in lubrication | 32 |
| 2.4.1 | <i>The Journal Bearing</i> | 32 |
| 2.4.2 | <i>The Piston-Ring-Liner</i> | 33 |
| 2.4.3 | <i>The Fracture</i> | 35 |
| 2.5 | Nonhomogeneous boundary conditions for pressure | 35 |
| 3 | NONHOMOGENEOUS BOUNDARY CONDITIONS AND CAVITATION MODELING | 39 |
| 3.1 | The mass-flux continuity condition | 40 |
| 3.2 | The continuous problem | 42 |
| 3.3 | Extending the Elrod-Adams algorithm | 45 |
| 3.3.1 | <i>A second approach for transient 1D problems</i> | 48 |
| 3.4 | Numerical examples | 54 |
| 3.4.1 | <i>Stationary cases along Algorithm 1</i> | 54 |
| 3.4.1.1 | <i>1D cases with $\epsilon = 0, 1$</i> | 54 |
| 3.4.1.2 | <i>A maximum value for p_{cc}</i> | 56 |
| 3.4.2 | <i>Transient cases along Algorithm 1</i> | 57 |
| 3.4.2.1 | <i>One-dimensional cases</i> | 57 |
| 3.4.2.2 | <i>Two-dimensional cases</i> | 60 |

| | | |
|--------------|---|------------|
| 3.4.3 | <i>Transient cases along Algorithm 2</i> | 70 |
| 3.4.3.1 | <i>Semi-analytical solutions</i> | 71 |
| 3.4.3.2 | <i>Traveling pockets</i> | 72 |
| 3.5 | Chapter Summary | 74 |
| 4 | THE REYNOLDS-RAYLEIGH-PLESSET COUPLING | 77 |
| 4.1 | The Rayleigh-Plesset equation | 77 |
| 4.1.1 | <i>Cavitation pressure for a gas/vapor bubble</i> | 79 |
| 4.1.2 | <i>The linearized equation</i> | 79 |
| 4.1.3 | <i>Bubbles resonance and inertial terms</i> | 82 |
| 4.2 | Coupling the Reynolds and the Rayleigh-Plesset equations | 83 |
| 4.2.1 | <i>The mass and momentum conservation equations</i> | 84 |
| 4.2.2 | <i>The multigroup approach</i> | 86 |
| 4.2.3 | <i>The Reynolds-Rayleigh-Plesset coupling</i> | 88 |
| 4.2.3.1 | <i>Modeling the bubble number density</i> | 88 |
| 4.2.3.2 | <i>The bubbles radii field $R(\mathbf{x}, t)$</i> | 88 |
| 4.2.3.3 | <i>The full RRP model</i> | 89 |
| 5 | MATHEMATICAL ANALYSIS OF THE RRP COUPLING | 91 |
| 5.1 | Mathematical framework | 92 |
| 5.2 | Well-posedness with inertial terms | 94 |
| 5.2.1 | <i>Existence of a local solution</i> | 95 |
| 5.2.2 | <i>Existence of stationary solutions</i> | 95 |
| 5.2.3 | <i>Stability Analysis</i> | 97 |
| 5.3 | Well-posedness without inertial terms | 101 |
| 5.3.1 | <i>Existence of a local solution</i> | 101 |
| 5.3.2 | <i>Stability analysis</i> | 103 |
| 6 | NUMERICAL METHODS FOR THE RRP COUPLING | 107 |
| 6.1 | Disregarding the inertial terms | 107 |
| 6.1.1 | <i>The Staggered scheme</i> | 108 |
| 6.1.2 | <i>The Single-step scheme</i> | 110 |
| 6.1.3 | <i>Numerical results and stability analysis</i> | 111 |
| 6.1.3.1 | <i>The Planar Fracture</i> | 111 |
| 6.1.3.2 | <i>Parameters setup</i> | 113 |
| 6.1.3.3 | <i>Results for the Staggered scheme</i> | 113 |
| 6.1.3.4 | <i>Stability analysis</i> | 114 |
| 6.1.3.5 | <i>Results for the Single-step scheme</i> | 117 |
| 6.1.3.6 | <i>A 2D example of the Fracture Problem</i> | 122 |
| 6.1.4 | <i>The Journal Bearing</i> | 126 |

| | | |
|---------------------|--|-----|
| 6.1.4.1 | <i>Stability and convergence</i> | 126 |
| 6.1.4.2 | <i>Comparison with Elrod-Adams and Reynolds models</i> | 129 |
| 6.2 | Including the inertial terms | 133 |
| 6.2.1 | <i>Discretization</i> | 134 |
| 6.2.1.1 | <i>A one-dimensional dynamically loaded Journal</i> | 135 |
| 6.2.2 | <i>Numerical results</i> | 136 |
| 6.2.2.1 | <i>Comparison with inertial terms / without inertial terms</i> | 136 |
| 7 | CONCLUSIONS | 141 |
| 7.1 | Conclusions | 141 |
| 7.2 | Future Work | 143 |
| BIBLIOGRAPHY | | 145 |
| APPENDIX A | FINITE VOLUME METHODS NOTATION | 155 |
| APPENDIX B | SOME MATHEMATICAL BACKGROUND | 157 |
| APPENDIX C | PUBLISHED WORKS LIST | 161 |



INTRODUCTION

1.1 Motivation

Numerical simulation allows to predict mechanical devices efficiency dependence on parameters design by means of available physics-based models. Different scientific tasks related to this activity can be identified, among them: the development of new models, the development of robust computational codes and qualitative analysis (like the well-posedness assessment of the related mathematical problems).

Hydrodynamical Lubrication concerns the dynamics of two surfaces in proximity where solid-solid contact is prevented. Roughly speaking, the load forces that tend to diminish the distance between the surfaces are balanced by the hydrodynamical force generated by a fluid, or *lubricant*, placed between them. Considering that lubricant as a Newtonian fluid, the hydrodynamical pressure is generally computed by means of the Reynolds equation (CAMERON, 1971; BAYADA; CHAMBAT, 1986). Divergent geometries and squeeze motion may produce tensile stresses (negative pressures) that can lead to a local rupture of the fluid film, which constitutes a non-linear physical phenomenon known as cavitation (see Fig. 1.1.1) (DOWSON; TAYLOR, 1979). The Elrod-Adams cavitation model represents the state-of-the-art when including these effects by means of a Reynolds-like equation. This is a mass-conserving model, a property that has been proved to be essential in order to obtain accurate results when the surfaces are not smooth. This was numerically shown by Ausas *et al.* (2007) and confirmed in (ZHANG; MENG, 2012) and (SHEN; KHONSARI, 2013) performing a comparison with experimental results. Like other cavitation models, the Elrod-Adams cavitation model imposes $p \geq p_{\text{cav}}$, where the threshold p_{cav} is called *cavitation pressure*.

Regarding the simulation of fluid-dynamic bearings, several numerical and theoretical works have been published during the last decades. An example of this is the

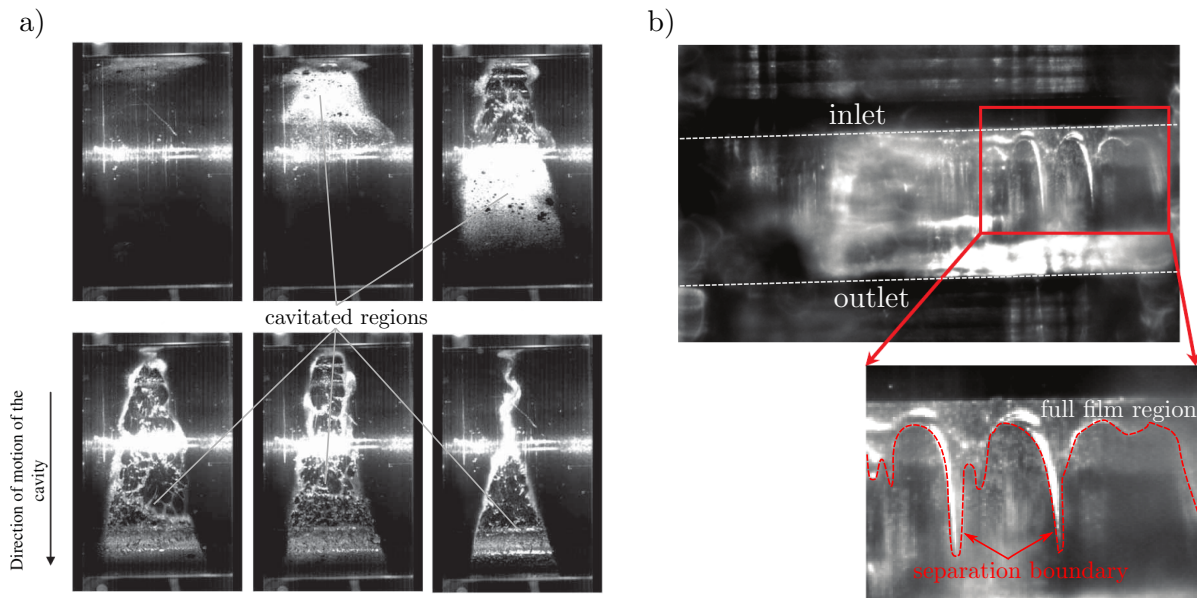


Figure 1.1.1 – Cavitation in a) a Journal Bearing, adapted from ([BRAUN; HANNON, 2010](#)); b) single ring test rig, adapted from ([POLYCHRONIS, 2018](#)). In both cases the cameras are Eulerian in nature.

Piston-Ring-Liner mechanism, which is responsible for about 5% of the fuel consumption in a passengers car ([HOLMBERG; ANDERSSON; ERDEMIR, 2012](#)). Several factors must be considered in the modeling of that system: developed forces, surface features (e.g, manufactured textures, surface roughness), and pressure boundary conditions are among these factors. Several works have been focused in friction reduction in lubricated devices by means of manufactured surfaces ([BRIZMER; KLIGERMAN; ETSION, 2003](#); [KO-VALCHENKO *et al.*, 2004](#); [ETSION, 2005](#); [TOMANIK, 2008](#); [ETSION, 2013](#); [TOMANIK, 2013](#); [PENG; HUANG, 2017](#); [SÖDERFJALL *et al.*, 2017](#); [ANDERBERG *et al.*, 2018](#)). Using the Elrod-Adams model, [Checo *et al.* \(2014\)](#) found numerically that traveling textures (manufactured on the moving surface) may have beneficial effects only for moderate to high conformity between the cylinder and the rings, reducing up to 73% the friction coefficient. This is in line with previous numerical findings of [Dobrica *et al.* \(2010\)](#) within a stationary regime, and with the results obtained by [Gadeschi, Backhaus and Knoll \(2012\)](#), among other numerical works. However, the most part of the published studies regarding the Piston-Ring-Liner do not take into account the highly variable mechanical pressure of the combustion chamber, and the few ones considering that variation use a non mass-conserving model ([MORRIS *et al.*, 2014](#); [MORRIS *et al.*, 2015](#); [USMAN; PARK, 2016](#)). There appears one of the problems studied in this dissertation: to develop a mass-conserving cavitation model that accommodates non-homogeneous boundary conditions. This could be made starting from the Elrod-Adams cavitation model, than only accepts $p = p_{\text{cav}}$ as a Dirichlet condition for pressure.

The Elrod-Adams model is a *phenomenological* model where the time scales are

governed by the macroscopic dynamics of the modeled mechanisms. This type of model assumes some compressibility law relating the pressure p and the fluid density ρ . Another example of such type of model is the one given by [Vijayaraghavan and Keith \(1989\)](#), in fact, their model is obtained as an outgrowth of the one due to Elrod and Adams. A different trend in Hydrodynamic Lubrication is to incorporate the physics of cavitation by assuming the lubricant as a two-phase mixture of pure liquid and gas and postulating equations for the averaged variables describing the gas phase and an equation mixture flow. The gas phase is regarded as a distribution of bubbles immersed in the liquid phase, which is assumed to be continuous. The Reynolds-Rayleigh-Plesset (RRP) cavitation model is an example of that. It consists in a coupled system of equations where the Reynolds equation is used to compute the mixture flow and the Rayleigh-Plesset equation is used to compute the bubbles dynamics. This kind of modeling has also been used along other flow equations, like the Navier-Stokes equations, and it is present in commercial softwares like Fluent ([KUBOTA; KATO; YAMAGUCHI, 1992](#); [SCHNERR; SAUER, 2001](#); [SINGHAL *et al.*, 2001](#); [ZWART; GERBER; BELAMR, 2004](#); [LIUZZI, 2012](#); [SCHMIDT *et al.*, 2014](#); [LIU; WANG; ZHU, 2015](#); [WALTERS, 2015](#); [ZHAO *et al.*, 2016](#); [DHANDE; PANDE, 2016](#)). Many questions can be posed around the RRP coupling, some of them are answered in the present document, some of them are subject of current research. For instance, although there exist mathematical studies on other cavitation models ([CIMATTI, 1976](#); [CIMATTI, 1980](#); [KINDERLEHRER; STAMPACCHIA, 1980](#); [BAYADA; CHAMBAT, 1983](#); [BERMÚDEZ; DURANY, 1989](#); [BUSCAGLIA; CIUPERCA; JAI, 2005](#); [BUSCAGLIA; CIUPERCA; JAI, 2007](#); [BUSCAGLIA; El Alaoui Talibi; JAI, 2015](#)), and for the Rayleigh-Plesset equation itself ([HAKL; TORRES; ZAMORA, 2012](#); [OHNAWA; SUZUKI, 2016](#)), to our knowledge there are no works where a mathematical analysis is performed on the RRP system. Furthermore, during this research the robustness of the numerical codes available in the literature was unclear. For these reasons, the well-posedness of the RRP model and its numerical treatment embodies other two problems that are tackled in this thesis.

1.2 Outline

This document's structure is as follows: in Chapter [2](#) the Reynolds equation is introduced as an asymptotic approximation for the Navier-Stokes equations. Some classical cavitation models are given and a series of mechanical devices able to be simulated along the presented modeling are described. The details on the RRP cavitation model are left for Chapter [4](#).

To model cavitation with non-homogeneous boundary conditions for pressure an extension of the Elrod-Adams model is developed in Chapter [3](#). Firstly, for cases where the moving surface is flat and smooth (null surface roughness), based on the imposition of a null pressure gradient condition on the rupture boundary. And secondly, for cases were

textures are allowed to be placed on the moving surface, and the pressure gradient is not prescribed to be null.

The Rayleigh-Plesset equation and the RRP cavitation model are presented in Chapter 4, there a Multicomponent Fluid framework is proposed and some heuristic arguments are given to justify the modeling.

Some mathematical results on the well-posedness of the RRP model are established in Chapter 5. For the same model, robust numerical codes are developed in Chapter 6 for both the cases where the inertial terms in the Rayleigh-Plesset equation are included or not.

1.3 Contributions

During this work original contributions were made on the modeling, mathematical analysis and numerical methods for the simulation of hydrodynamical mechanisms:

- An extension of the Elrod-Adams model that accommodates non-homogeneous boundary conditions for pressure was developed for special cases (presented in Chapter 3). The general case where the moving surface is allowed to be textured is treated in a different one-dimensional approach. This was made by means of an analysis similar to the one performed by [Ausas et al. \(2013\)](#) and [Checo \(2015\)](#) for a different extension of the Elrod-Adams model (where the transport velocity coefficient a in (2.24) is able to be in the interval $[\frac{1}{2}, 1]$, while for the Elrod-Adams model it is restricted to $a = \frac{1}{2}$).
- A framework for the Reynolds-Rayleigh-Plesset cavitation model is given in Chapter 4, being proposed as a three-equations coupled system: the Reynolds equation, the Rayleigh-Plesset equation, and a Boltzmann transport equation for the bubbles number density.
- A mathematical analysis of the RRP coupling well-posedness was performed: theorems for local existence in time, stationary solutions existence and stability are obtained in Chapter 5.
- The development of robust numerical codes for the RRP coupling is presented in Chapter 6. Two cases are identified and suitable codes were developed for both: 1) regarding the inertial terms in the Rayleigh-Plesset equation or 2) disregarding them.



MATHEMATICAL MODELS IN LUBRICATION

This chapter aims to provide a general description for the modeling of lubricated devices; secondly, it aims to detail the particular characteristics of model lubrication problems, like geometrical parameters, boundary conditions, etc.

In Section 2.1 the dynamical variables are presented and their coupling is described. Section 2.2 is devoted to an asymptotic derivation of the compressible Reynolds equation from the Navier-Stokes equations by means of the thin-film hypothesis. Section 2.3 provides the cavitation models generally used to determine a relation between density and pressure for the compressible Reynolds equation. Finally, in Section 2.4 lubrication problems commonly studied in the literature are described.

2.1 Dynamical variables and their coupling

There are three components common to any lubricated mechanism: two surfaces in close proximity and a fluid (liquid or gas) placed between them. The fluid allows a smooth contact, diminishing energy losses and augmenting the lifetime of the device. A typical simulation in tribology will solve for the dynamical variables described in Table 1.

| Variable | Model |
|------------------------------|--------------------------------|
| Hydrodynamical pressure: p | Compressible Reynolds equation |
| Fluid's density: ρ | A cavitation model |
| Surfaces gap: h | Newton's equation |

Table 1 – Dynamical variables and corresponding mathematical models.

The hydrodynamical pressure (p) is computed by means of the Reynolds equation (or

some of its modified forms). Generally, its integral (the hydrodynamical force) enters in the Newton's equation for the surfaces gap (h) as a load-supporting force, preventing the surfaces to became *too close each other*. Thus, there is a natural coupling between h and p . Having provided boundary conditions, different models for the fluid density (ρ) can be used to close the problem. The simpler cavitation model corresponds to “ ρ constant and equal to the liquid density” and it provides *the full-Sommerfeld pressure curve* (DOWSON; TAYLOR, 1979).

2.2 The compressible Reynolds equation

2.2.1 Mass fluxes approximation in thin films

Let us assume there exist two maps $h_U : \Omega' \rightarrow \mathbb{R}$ and $h_L : \Omega' \rightarrow \mathbb{R}$, with $\Omega' = \Omega \times [0, T]$, Ω a regular domain in \mathbb{R}^2 , $T \in \mathbb{R}_*^+$ and $h_U > h_L$ on Ω' , that describe the topography of two parallel surfaces in proximity. Lubrication Theory studies the dynamics of the surfaces when some fluid (lubricant) is placed in the gap between them. This gap can be described by the function $h = h_U - h_L$ (see Fig. 2.2.1). Assuming a Newtonian

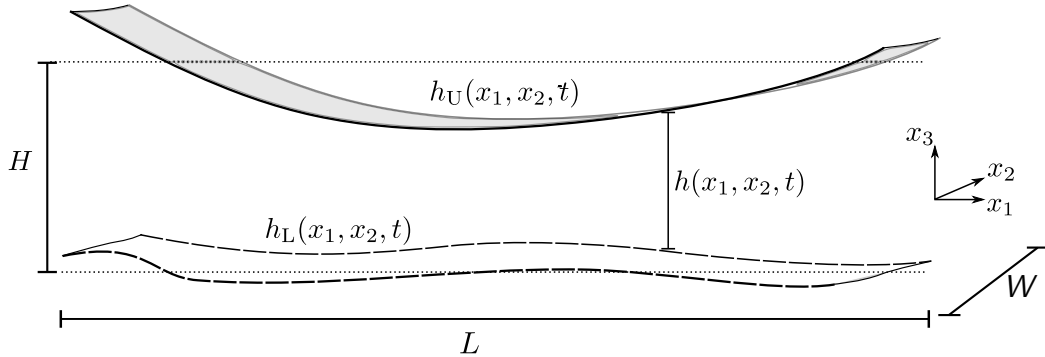


Figure 2.2.1 – Three-dimensional scheme of the physical framework.

fluid and disregarding body forces, the Navier-Stokes equations read (KUNDU; COHEN, 2004):

$$\rho \left(\frac{\partial \mathbf{u}}{\partial t} + (\mathbf{u} \cdot \nabla) \mathbf{u} \right) = -\nabla p + \mu \nabla^2 \mathbf{u}, \quad \text{in } \Omega, \quad (2.1)$$

where ρ is the fluid density, μ the fluid dynamic viscosity, $\mathbf{u} = (u, v, w)$ its velocity vector and p the hydrodynamical pressure. The next boundary conditions are set: $u(x_3 = h_U) = U_H$, $u(x_3 = h_L) = U_L$, $v(x_3 = h_U) = V_H$, $v(x_3 = h_L) = V_L$, and

$$w(x_3 = h_U) = W_H = \frac{Dh_U}{Dt} = \frac{\partial h_U}{\partial t} + U_H \frac{\partial h_U}{\partial x_1} + V_H \frac{\partial h_U}{\partial x_2},$$

$$w(x_3 = h_L) = W_L = \frac{Dh_L}{Dt} = \frac{\partial h_L}{\partial t} + U_L \frac{\partial h_L}{\partial x_1} + V_L \frac{\partial h_L}{\partial x_2}.$$

Denoting by L a reference length for the x_1 and x_2 axis, H a reference length for the x_3 axis and by U a reference speed, the hypothesis of surfaces proximity is introduced by means of the non-dimensional variables:

$$\hat{x}_1 = \frac{x_1}{L}, \quad \hat{x}_2 = \frac{x_2}{L}, \quad \hat{x}_3 = \frac{x_3}{H}, \quad (2.2)$$

$$\hat{u} = \frac{u}{U}, \quad \hat{v} = \frac{v}{U}, \quad \hat{w} = \frac{w}{U \frac{H}{L}}, \quad \hat{t} = \frac{t U}{L}, \quad \hat{p} = p \frac{H^2}{\mu L U}. \quad (2.3)$$

Denoting the Reynolds Number $\text{Re} = \rho U H / \mu$ and $\epsilon = H/L$ the system (2.1) can be written as

$$\begin{aligned} \frac{\partial \hat{p}}{\partial \hat{x}_1} &= \frac{\partial^2 \hat{u}}{\partial \hat{x}_3^2} - \epsilon \text{Re} \left(\frac{\partial \hat{u}}{\partial \hat{t}} + \hat{u} \frac{\partial \hat{u}}{\partial \hat{x}_1} + \hat{v} \frac{\partial \hat{u}}{\partial \hat{x}_2} + \hat{w} \frac{\partial \hat{u}}{\partial \hat{x}_3} \right) + \mathcal{O}(\epsilon^2), \\ \frac{\partial \hat{p}}{\partial \hat{x}_2} &= \frac{\partial^2 \hat{v}}{\partial \hat{x}_3^2} - \epsilon \text{Re} \left(\frac{\partial \hat{v}}{\partial \hat{t}} + \hat{u} \frac{\partial \hat{v}}{\partial \hat{x}_1} + \hat{v} \frac{\partial \hat{v}}{\partial \hat{x}_2} + \hat{w} \frac{\partial \hat{v}}{\partial \hat{x}_3} \right) + \mathcal{O}(\epsilon^2), \\ \frac{\partial \hat{p}}{\partial \hat{x}_3} &= -\epsilon^3 \text{Re} \left(\frac{\partial \hat{w}}{\partial \hat{t}} + \hat{u} \frac{\partial \hat{w}}{\partial \hat{x}_1} + \hat{v} \frac{\partial \hat{w}}{\partial \hat{x}_2} + \hat{w} \frac{\partial \hat{w}}{\partial \hat{x}_3} \right) + \epsilon^4 \left(\frac{\partial^2 \hat{w}}{\partial \hat{x}_1^2} + \frac{\partial^2 \hat{w}}{\partial \hat{x}_2^2} \right) + \epsilon^2 \frac{\partial^2 \hat{w}}{\partial \hat{x}_3^2} = \mathcal{O}(\epsilon^2). \end{aligned}$$

Thus, neglecting terms of order ϵRe and higher, and returning to the original variables we obtain

$$\frac{\partial p}{\partial x_1} = \mu \frac{\partial^2 u}{\partial x_3^2}, \quad (2.4)$$

$$\frac{\partial p}{\partial x_2} = \mu \frac{\partial^2 v}{\partial x_3^2}, \quad (2.5)$$

$$\frac{\partial p}{\partial x_3} = 0. \quad (2.6)$$

Integrating two times on x_3 between $x_3 = h_L$ and $x_3 = h_U$, we have:

$$u(x_3) = -\frac{1}{2\mu} \frac{\partial p}{\partial x_1} (h_U - x_3)(x_3 - h_L) + \frac{x_3 - h_L}{h_U - h_L} U_H + \frac{h_U - x_3}{h_U - h_L} U_L, \quad (2.7)$$

$$v(x_3) = -\frac{1}{2\mu} \frac{\partial p}{\partial x_2} (h_U - x_3)(x_3 - h_L) + \frac{x_3 - h_L}{h_U - h_L} V_H + \frac{h_U - x_3}{h_U - h_L} V_L. \quad (2.8)$$

Integrating the last equations for $x_3 \in [h_L, h_U]$ the mass-flux functions are obtained:

$$J_{x_1} = \int_{h_L}^{h_U} \rho u \, dx_3 = -\frac{\rho h^3}{12\mu} \frac{\partial p}{\partial x_1} + \frac{U_L + U_H}{2} \rho h, \quad (2.9)$$

$$J_{x_2} = \int_{h_L}^{h_U} \rho v \, dx_3 = -\frac{\rho h^3}{12\mu} \frac{\partial p}{\partial x_2} + \frac{V_L + V_H}{2} \rho h, \quad (2.10)$$

where $h = h_U - h_L$ and it is assumed that $\frac{\partial p}{\partial x_3} = 0$. The first term in these fluxes corresponds to the Poiseuille flow due to the pressure gradient and the second term corresponds to the Couette flow due to the relative motion between the surfaces.

2.2.2 The compressible Reynolds equation

The mass transport equation reads

$$\frac{\partial \rho}{\partial t} + \nabla \cdot (\rho \mathbf{u}) = 0. \quad (2.11)$$

Integrating in x_3 we have

$$h \frac{\partial \rho}{\partial t} + \int_{h_L}^{h_U} \frac{\partial}{\partial x_1} (\rho u) dx_3 + \int_{h_L}^{h_U} \frac{\partial}{\partial x_2} (\rho v) dx_3 + \int_{h_L}^{h_U} \frac{\partial}{\partial x_3} (\rho w) dx_3 = 0.$$

Using the Leibniz integration rule and Eqs. (2.9) and (2.10) we obtain

$$h \frac{\partial \rho}{\partial t} + \frac{\partial J_{x_1}}{\partial x_1} + \frac{\partial J_{x_2}}{\partial x_2} + \rho \frac{\partial h}{\partial t} = 0,$$

substituting the definitions of the mass-fluxes it is obtained the compressible Reynolds equation, reading:

$$\nabla \cdot \left(\frac{\rho h^3}{12\mu} \nabla p \right) - \nabla \cdot \left(\frac{\mathbf{U}}{2} \rho h \right) = \rho \frac{\partial h}{\partial t} + h \frac{\partial \rho}{\partial t}, \quad (2.12)$$

where $\mathbf{U} = (\bar{U}, \bar{V})$ is the surfaces relative velocity, with $\bar{U} = U_H + U_L$ and $\bar{V} = V_H + V_L$.

2.3 Cavitation modeling

In the lubricated mechanisms considered in this work the non-linear physical phenomenon of cavitation can take place. Experimentally it is observed the occurrence of regions composed by a mixture of gas and vapor (DOWSON; TAYLOR, 1979; KU; TICHY, 1990; QIU; KHONSARI, 2011; ZHANG; MENG, 2012; BAI; MENG; ZHANG, 2016), in these regions the pressure is approximately constant and equal to a certain value called *cavitation pressure*, hereafter denoted p_{cav} ; and on the full-film regions it is observed that $p > p_{cav}$. Two main types of cavitation can be distinguished depending on its physical origin. *Vaporous cavitation* takes place when the pressure reaches the saturation vapor pressure of the fluid components. Thus, vaporous cavitation consists in a phase change from liquid to vapor due to this fall in pressure. *Gaseous cavitation* happens when the pressure reaches the saturation pressure of the gases dissolved in the fluid (DOWSON; TAYLOR, 1979).

In sections 2.3.1 and 2.3.2 two standard cavitation models are presented, the Reynolds and the Elrod-Adams cavitation models. They are based on the observed consequences of cavitation mentioned before, this is, the pressure field is restricted by $p \geq p_{cav}$ on the whole domain and $p = p_{cav}$ in the cavitated regions. A third model is presented in Chapter 4, the Reynolds-Rayleigh-Plesset cavitation model. It is focused in gaseous cavitation and, differently to the two first models, it aims to capture the physics of cavitation rather than reproduce its consequences.

2.3.1 Reynolds cavitation model

To simplify the discussion, here we assume that $p_{\text{cav}} = 0$ and $\bar{V} = 0$ (there is no relative motion of the surfaces along the x_2 -axis). The Reynolds cavitation model assumes the fluid's density to be constant and imposes the constrain $p \geq 0$ by means of a variational formulation (KINDERLEHRER; STAMPACCHIA, 1980). Its implementation is simple and its numerical results are satisfactory when compared to experimental results for non-textured surfaces (AUSAS *et al.*, 2007).

Variational formulation without cavitation

As the fluid's density is constant, the variational formulation of the Reynolds equation (2.12) consists in looking for $p \in H_0^1(\Omega)$ such that:

$$\int_{\Omega} \frac{h^3}{12\mu} \nabla p \nabla \phi \, d\Omega = \frac{\bar{U}}{2} \int_{\Omega} h \frac{\partial \phi}{\partial x_1} \, d\Omega - \int_{\Omega} \phi \frac{\partial h}{\partial t} \, d\Omega, \quad \forall \phi \in H_0^1(\Omega). \quad (2.13)$$

Variational formulation of the Reynolds cavitation model

The Reynolds cavitation model incorporates the restriction $p \geq 0$ into the Reynolds equation by looking for

$$p \in K = \{v \in H_0^1(\Omega) : v \geq 0 \text{ a.e. in } \Omega\}$$

(the cone of non-negative functions) such that

$$\int_{\Omega} \frac{h^3}{12\mu} \nabla p \nabla (\phi - p) \, d\Omega \geq \frac{\bar{U}}{2} \int_{\Omega} h \frac{\partial (\phi - p)}{\partial x_1} \, d\Omega - \int_{\Omega} (\phi - p) \frac{\partial h}{\partial t} \, d\Omega, \quad \forall \phi \in K. \quad (2.14)$$

Let us denote the mass-flux vector $\mathbf{J} = (J_{x_1}, J_{x_2})$ with components defined by Eqs. (2.9) and (2.10). In the sense of distributions, this last inequality can be written as

$$\frac{\partial h}{\partial t} + \nabla \cdot \mathbf{J} \geq 0 \quad \text{in } \Omega. \quad (2.15)$$

Let us define the partition $\Omega = \Omega^+ \cup \Omega_0$ by

$$\Omega_+ = \{p > 0 \text{ in } \Omega\}, \quad \Omega_0 = \Omega \setminus \Omega_+. \quad (2.16)$$

It can be proved (KINDERLEHRER; STAMPACCHIA, 1980) that

$$\frac{\partial h}{\partial t} + \nabla \cdot \mathbf{J} \geq 0 \quad \text{in } \Omega_0 \quad \text{and} \quad \frac{\partial h}{\partial t} + \nabla \cdot \mathbf{J} = 0 \quad \text{in } \Omega_+, \quad (2.17)$$

which means that the Reynolds equations is accomplished in each pressurized region Ω_+ . Although simple 1D cases where the lack of mass-conservation of this model can be

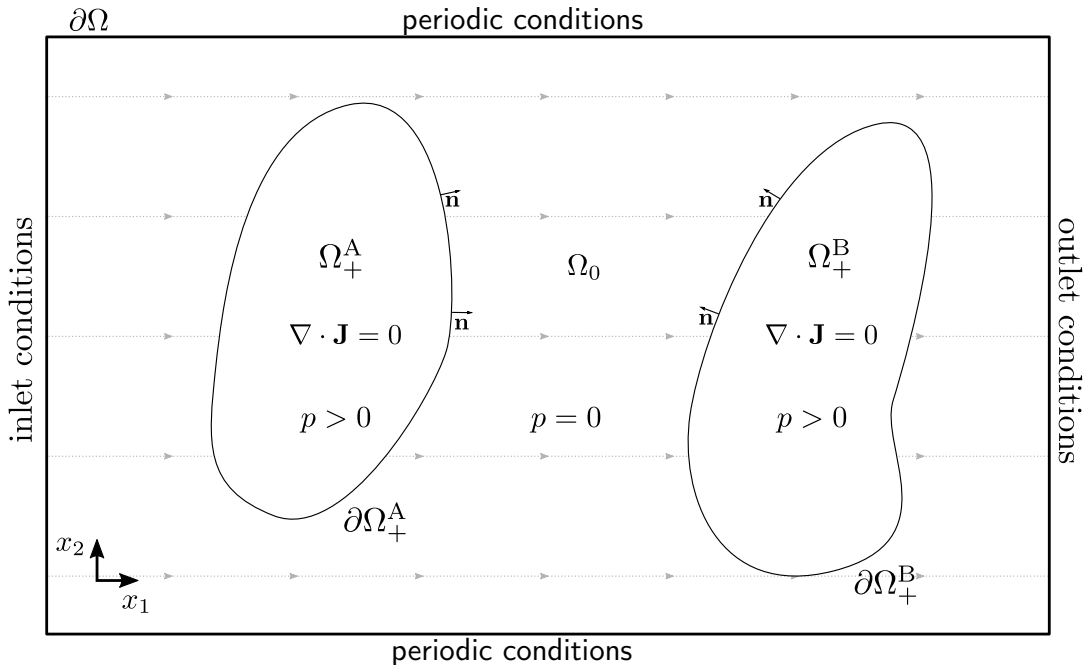


Figure 2.3.1 – Scheme of pressurized regions along a cavitation model and a flux function \mathbf{J} .

given ([JARAMILLO, 2015](#)), let us illustrate here a 2D argument that will be useful when presenting the Elrod-Adams model in the next section.

Assuming a stationary regime, Fig. 2.3.1 shows a typical situation for a square domain with suitable boundary conditions and $\bar{U} > 0$. Notice that two pressurized regions are shown, Ω_A^+ and Ω_B^+ . The dotted flux-lines show the direction of the flux function on Ω_0 , which can be written as $\mathbf{J} = \left(\frac{\bar{U}}{2} \rho h, 0 \right)$, thus $\frac{\partial h}{\partial x_1} \geq 0$ in Ω_0 (the geometry is divergent or flat there). It can be observed that in the center of the domain there are paths that exit the rupture boundary of Ω_A^+ ($\mathbf{J} \cdot \mathbf{n} > 0$) and enter the reformation boundary of Ω_B^+ ($\mathbf{J} \cdot \mathbf{n} < 0$). As p depends continuously on h (e.g., Theorem 4.4 ([RODRIGUEZ, 1987](#))) a small perturbation of h in Ω_A^+ will produce a small perturbation of $\partial\Omega_A^+$. Therefore, the set Ω_B^+ and the restriction $p|_{\Omega_B^+}$ will remain unchanged. This is a non-conservative situation as the perturbation of h in Ω_A^+ will affect the flux in that subdomain but not the flux in Ω_B^+ , in spite of being *connected* by the flux-lines.

The reason behind this issue is that the Reynolds model does not impose mass conservation in the cavitated region Ω_0 . In the next section a mass-conserving model that considers a fluid-fraction variable in Ω_0 is presented.

2.3.2 Elrod-Adams cavitation model

Mass-conservation had been proved to be essential in order to obtain accurate results when modeling textured lubricated devices ([AUSAS *et al.*, 2007](#); [QIU](#); [KHONSARI, 2009](#)). [Elrod and Adams \(1974\)](#) looked for a conservative cavitation model introducing a

relation between ρ and p that reads

$$p = \begin{cases} p_{\text{cav}} + \beta \ln \rho / \rho_\ell & \text{if } \rho > \rho_\ell, \\ p_{\text{cav}} & \text{otherwise,} \end{cases} \quad (2.18)$$

where ρ_ℓ is the liquid density and β is the compressibility factor. Introducing the fluid's fraction variable $\theta = \rho / \rho_\ell$ and the function g such that $g(\theta) = 1$ for $\theta > 1$, $g(\theta) = 0$ for $\theta \leq 1$, Equation (2.12) may be rewritten as

$$\nabla \cdot \left(g(\theta) \theta \frac{h^3}{12\mu} \nabla p \right) - \nabla \cdot \left(\frac{\mathbf{U}}{2} h \theta \right) = \frac{\partial}{\partial t} (h \theta),$$

where it has been used the fact that $\nabla p = 0$ for $\theta \leq 1$. Rewrite Eq. (2.18) as

$$(p - p_{\text{cav}}) / \beta = g(\theta) \ln \theta,$$

formally, taking the limit for $\beta \rightarrow +\infty$ we obtain the Elrod-Adams cavitation model

$$\nabla \cdot \left(\frac{h^3}{12\mu} \nabla p \right) - \nabla \cdot \left(\frac{\mathbf{U}}{2} h \theta \right) = \frac{\partial}{\partial t} (h \theta) \quad \text{on } \Omega, \quad (2.19)$$

with the complementary relations:

$$\begin{cases} p \geq p_{\text{cav}} & \text{for } \theta = 1 \\ p = p_{\text{cav}} & \text{for } \theta < 1 \end{cases} \quad \text{on } \Omega. \quad (2.20)$$

Recalling the partition of Ω given in (2.16) one notices that in the pressurized region Ω_+ this is the elliptic PDE corresponding to the incompressible Reynolds equation (ρ constant in Eq. (2.12)), while in the cavitated region Ω_0 this is a hyperbolic transport equation for the volume fraction $h\theta$, i.e.,

$$\frac{\partial}{\partial t} (h\theta) + \nabla \cdot \left(\frac{\mathbf{U}}{2} h\theta \right) = 0 \quad \text{on } \Omega_0. \quad (2.21)$$

Notice that this time the mass flux-function in Fig. 2.3.1 corresponds to $\mathbf{J} = \left(\frac{\bar{U}}{2} \rho_\ell h\theta, 0 \right)$ and for the stationary cases it must be accomplished $\nabla \cdot \mathbf{J} = 0$ also on Ω_0 and thus mass-conservation is imposed on the whole domain.

2.3.3 Boundary conditions in the interface $\partial\Omega_+$

The Elrod-Adams model implicitly imposes boundary conditions for the rupture/reformation interface between Ω_+ and Ω_0 that are known as the Jacobson-Flober-Olsson conditions (JAKOBSON; FLOBERG, 1957; OLSSON, 1965). For this, the Rankine-Hugoniot condition (e.g., (LEVEQUE, 2002)) for continuity of the flux reads:

$$[\![\mathbf{J}]\!] \cdot \mathbf{n} = [\![h\theta]\!] \mathbf{V}^i \cdot \mathbf{n}, \quad (2.22)$$

where the brackets denote the jump of the function at the interface, \mathbf{V}^i denotes the interface velocity, and \mathbf{n} is the vector normal to $\partial\Omega_+$. Let us assume h to be continuous in space, $\mathbf{e}_c = \mathbf{U}/\|\mathbf{U}\|$ to be the unitary vector along the Couette flow direction, $\bar{U} > 0$ and $\bar{V} = 0$ to simplify the exposition, then Eq. (2.22) implies

$$a\bar{U}h\theta_0\mathbf{e}_c\cdot\mathbf{n} + \frac{h^3}{12\mu}\frac{\partial p}{\partial\mathbf{n}} - \frac{\bar{U}}{2}h\mathbf{e}_c\cdot\mathbf{n} = h(\theta_0 - 1)\mathbf{V}^i\cdot\mathbf{n}, \quad (2.23)$$

where $a\bar{U}$ is the transport speed of the Couette flow at the cavitated region ($a = \frac{1}{2}$ in the Elrod-Adams model). For the steady state this gives

$$\frac{h^3}{12\mu}\frac{\partial p}{\partial\mathbf{n}} = \bar{U}h\left(\frac{1}{2} - a\theta_0\right)\mathbf{e}_c\cdot\mathbf{n}, \quad (2.24)$$

where θ_0 is the value of θ at the cavitated side of the interface. The left hand side in the last equation is the Poiseuille flux at the interface from the pressurized side. If the point \mathbf{x} being considered is a rupture point, then $\mathbf{e}_c\cdot\mathbf{n} > 0$, and for a reformation point $\mathbf{e}_c\cdot\mathbf{n} < 0$. Taking $a = \frac{1}{2}$ Eq. (2.24) implies

$$\frac{\partial p}{\partial\mathbf{n}} = \begin{cases} 0 & \text{if } \mathbf{x} \text{ is a rupture point,} \\ \frac{6\mu\bar{U}}{h^2}(1 - \theta_0)\mathbf{e}_c\cdot\mathbf{n} & \text{if } \mathbf{x} \text{ is a reformation point,} \end{cases} \quad (2.25)$$

where we have used the fact that $\frac{\partial p}{\partial\mathbf{n}} \leq 0$ since p in Ω_+ is always greater or equal to p in Ω_0 . Notice that the conditions (2.25) lead to a well-posed problem for the steady state (in the sense that there exists a unique solution for the free boundary problem). However, in cases like the Piston-Ring setting $a \approx 1$ would be more realistic, but this leads to a loss of well-posedness (AUSAS *et al.*, 2013).

To compute the condition (2.25) on the pressure gradient at the rupture points it has been used the fact that the Elrod-Adams model assumes the restriction $p \geq p_{\text{cav}}$ to not depend on \mathbf{x} . This will be an important point when looking for a generalization of this cavitation model in Chapter 3, as the independence of p_{cav} on the position will no longer be assumed.

2.4 Model problems in lubrication

2.4.1 The Journal Bearing

This is the most common hydrodynamic bearing, used for instance in thermal engines, combustion engines, compressors, turbomachines and alternators (BOU-SAÏD, 2013). This mechanical device supports hydrodynamically the load of a rotating solid cylinder (Journal) encased within a circular Bush. Figure 2.4.1 shows a simplified scheme of this mechanism where the gap between the surfaces depends only on the longitudinal coordinate x_1 (along the sliding direction). Typical boundary conditions for pressure are

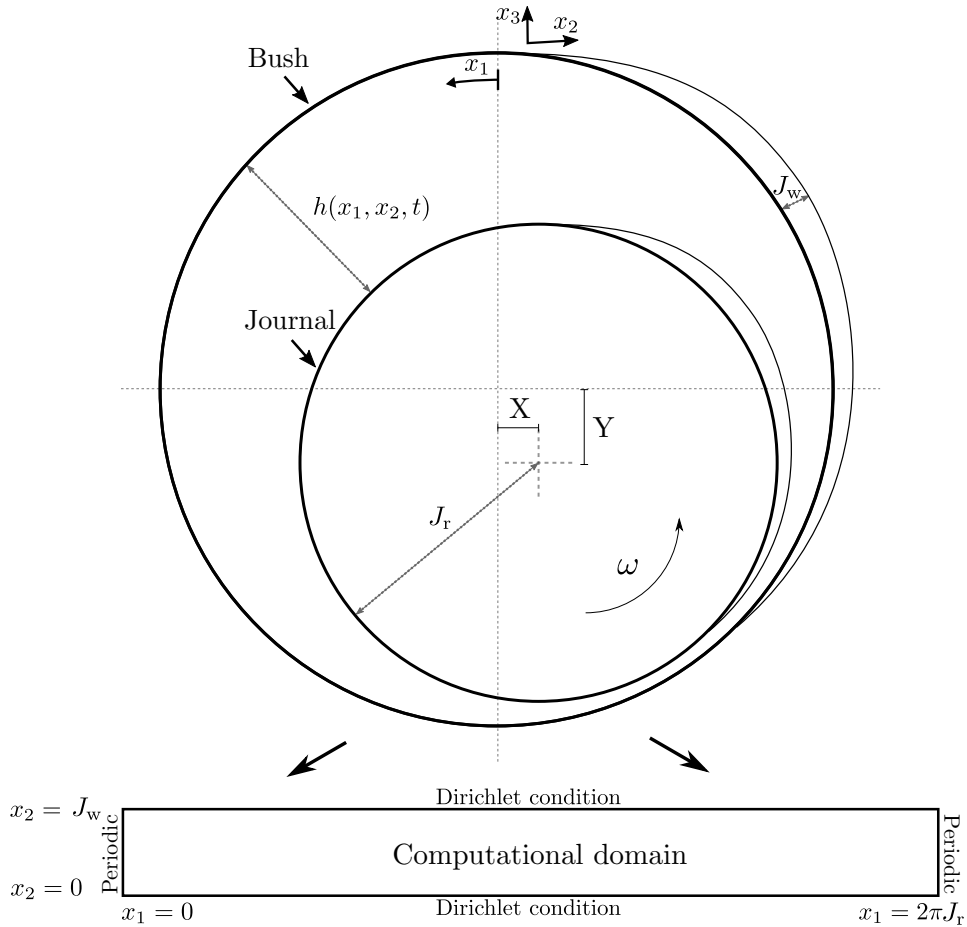


Figure 2.4.1 – Scheme of the Journal Bearing.

also indicated for the computational domain $\Omega = [0, 2\pi J_r] \times [-J_w, J_w] \subset \mathbb{R}^2$, where J_r is the journal radius and J_w its width.

The surfaces gap reads

$$h(x_1, x_2, t) = c + X(t) \cos(x_1/J_r) + Y(t) \sin(x_1/J_r) + h_T(x_1, x_2), \quad (2.26)$$

where c is the journal clearance and h_T is a texture function.

The Newton's equation for the Journal center $\mathbf{X}(t) = [X(t), Y(t)]$ may be written:

$$M_J \frac{d^2 \mathbf{X}}{dt^2} = \mathbf{W}(t) + \mathbf{W}^a(t), \quad (2.27)$$

where M_J is the mass of the journal, $\mathbf{W}^a(t)$ is the applied load (datum) and

$$\mathbf{W}(t) = \left[\int_{\Omega} p(x_1, x_2, t) \cos(x_1/J_r) d\Omega, \int_{\Omega} p(x_1, x_2, t) \sin(x_1/J_r) d\Omega \right], \quad (2.28)$$

is the hydrodynamical support.

2.4.2 The Piston-Ring-Liner

This mechanical system is the central part of the combustion engines, an illustration of it is shown in Fig. 2.4.2. A pack of rings is attached to the piston, these rings are placed

there in order to seal the combustion chamber and control the lubricating oil. Periodical explosions in the combustion chamber generate a difference in pressure at both sides of the piston producing a reciprocal motion of the piston between the Bottom Dead Center (BCD) and the Top Dead Center (TDC).

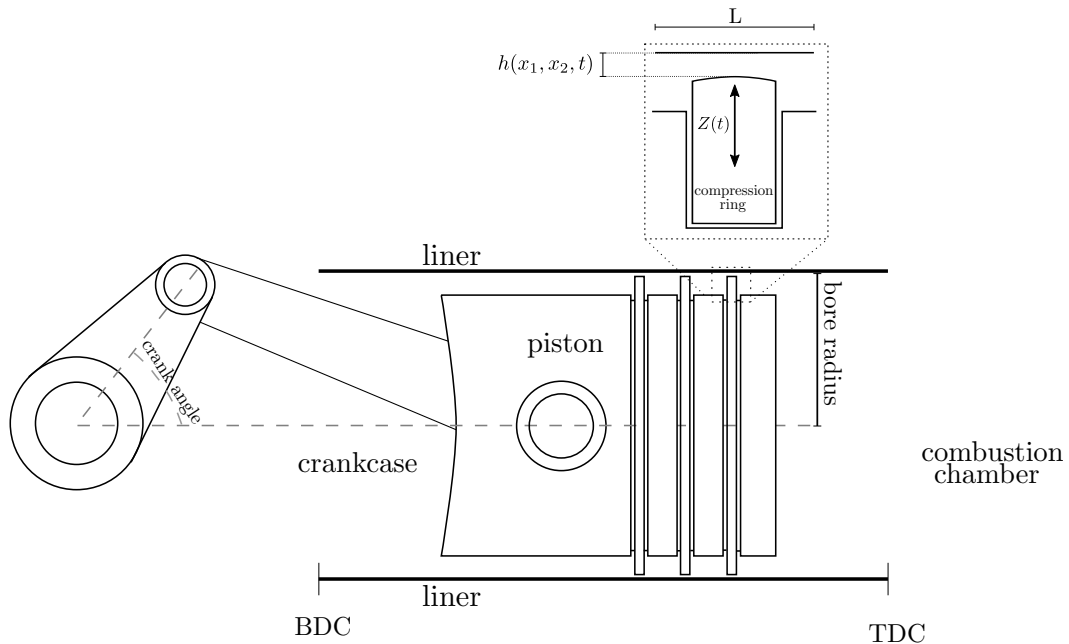


Figure 2.4.2 – Scheme of the Piston-Ring-Liner mechanism.

The computational domain may be written $\Omega =]0, L[\times]0, B[\subset \mathbb{R}^2$ where L is in the scale of the ring thickness ($\simeq 1$ mm) and B is the domain width, typically $B \simeq 0.1$ mm. For this case the surfaces' gap may be written

$$h(x_1, x_2, t) = \begin{cases} h_T(x_1, x_2) + Z(t) + h_R(x_1, x_2) & \text{if } a \leq x_1 \leq b \\ h_T(x_1, x_2) + h_g & \text{otherwise} \end{cases},$$

where $Z(t) > 0$ is the ring position along the x_3 -axis, h_R is the ring profile, $0 < a < b < L$, and h_g is a constant gap between the piston and the liner. A typical ring profile may be written

$$h_R(x_1) = R_c - \sqrt{R_c^2 - (x_1 - R_{x_1})^2}, \quad x_1 \in [a, b],$$

where R_c is the ring curvature and R_{x_1} is the center of the ring along the x_1 -axis.

The Newton's equation reads:

$$M_R \frac{d^2 Z}{dt^2} = \frac{1}{B} \int_0^B \int_a^b p(x_1, x_2, t) dx_1 dx_2 + W^a(t), \quad (2.29)$$

where M_R is the mass per unit width of the ring and W^a is the load applied on the ring per unit width (datum).

Typical values for the Combustion Chamber Pressure (CCP) and the piston speed in function of the crank angle are shown in Fig. 2.4.3.

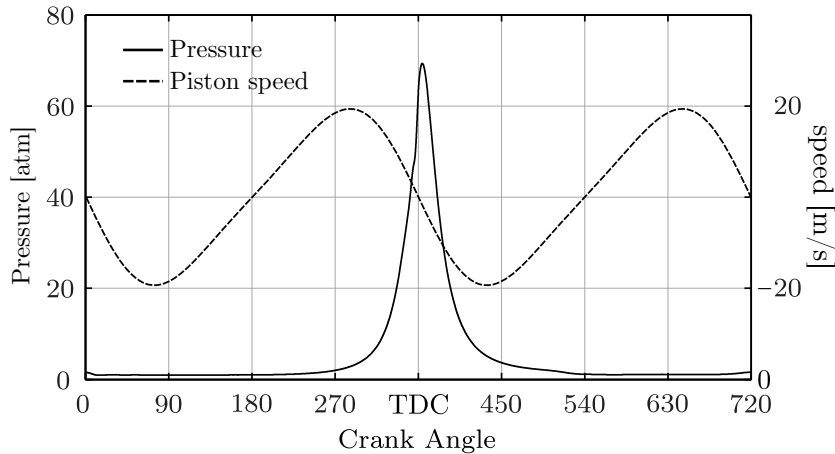


Figure 2.4.3 – Combustion chamber pressure and piston speed at 1500 rpm, adapted from ([LYUBARSKYY; BARTEL, 2016](#)).

2.4.3 The Fracture

This is a special problem used in this work when testing numerical methods in Chapter 6. In that chapter the relation between the pressure and the density is given by means of the Reynolds-Rayleigh-Plesset coupling. The fluid is assumed to be composed by liquid and tiny gas bubbles distributed in the liquid. These gas bubbles respond dynamically to changes in the average hydrodynamical pressure. Due to this, while for other cavitation models (e.g., Reynolds model, Elrod-Adams model) the term $h \frac{\partial p}{\partial t}$ in Eq. (2.12) is null, in the Reynolds-Rayleigh-Plesset cavitation model this is not the case. The correct numerical treatment of this term was studied in one of the published articles related to this thesis ([JARAMILLO; BUSCAGLIA, 2019](#)). In the fracture problem there are no squeeze effects ($\partial_t h = 0$) and the surfaces relative speed is null ($\mathbf{U} = 0$), thus the fluid dynamics in that case is purely related to the compression or expansion of the bubbles.

2.5 Nonhomogeneous boundary conditions for pressure

The pressure boundary condition in lubricated devices does not always correspond to the cavitation pressure. This represents a challenging modeling problem that will be presented in detail in Chapter 3. In the case of the Journal bearing, p is different from p_{cav} at the inlet boundary, a situation that can be properly handled by mass-conserving models. For instance, in the case of the Elrod-Adams model, θ can be set equal to 1 at the inlet (fully-flooded condition). For a majority of the applications the pressure at the boundaries is equal to 1 atm. Since $|p_{cav}|$ is generally lower than 1 atm and due to the fact that the maximum value of $|p|$ normally reaches hundreds of atm, it is customary to set both the boundary condition for pressure and p_{cav} as being null.

The case of the Piston-Ring-Liner mechanism is more involved. The compression

ring faces the combustion chamber through the gap present between the piston and the liner (see Fig. 2.4.2). During the compression stroke, the combustion chamber pressure (CCP) may achieve values in the order of 100 atm, and the piston is moving away from the explosion (crankangle \simeq TDC in Fig. 2.4.3). Thus, the CCP must be imposed as a Dirichlet condition for pressure at the boundary inlet/outlet, which brings difficulties when trying to impose mass-conservation there. In Chapter 3 it is shown that this issue is related to the imposition of the pressure gradient in the separation boundary.

Different conditions for the pressure gradient at the separation boundary can be found in the literature. The research group of Dowson et al. published a series of works (DOWSON, 1993; PRIEST *et al.*, 1996; PRIEST; DOWSON; C., 2000) regarding the boundary conditions for Reynolds equation with focus on the Piston-Ring-Liner. They concluded that the boundary conditions at the separation boundary are related to the nature of the cavitation taking place in that region. They also observed that the hydrodynamics of the lubricant oil is strongly dependent on such boundary conditions. The authors also stressed the fact that few experimental works were available at that time to be contrasted against numerical results for different separation boundary models (to our knowledge, such scarcity remains). Nevertheless, they mentioned that the boundary conditions due to Elrod and Coyne (COYNE; ELROD, 1970; COYNE; ELROD, 1971) gave closer results to the ones found in the literature.

Arcoumanis et al. (ARCOUMANIS *et al.*, 1995) designed a test-rig experiment to simulate the lubrication of the Piston-Ring-Liner. They compared their experimental findings with numerical simulations along with different separation boundary models: the Elrod and Coyne (COYNE; ELROD, 1970; COYNE; ELROD, 1971) model; the Reynolds model (null gradient condition); and a model due to Floberg (FLOBERG, 1965). The numerical results obtained along the Reynolds model were closer to the measurement results.

Few works have studied the effect of including the CCP time variation, performing simulations where the CCP is included as a boundary condition and comparing them with simulations where the CCP is not considered. Kligerman et al. (KLIGERMAN; SHINKARENKO, 2015) compared the predicted friction force and minimum clearance between two type of simulations. The “Real engine simulation” imposed boundary conditions according to the CCP time variation, while the “Approximate solution” was based in a quasi-static simulation and imposing homogeneous boundary condition equal to the ambient pressure. The authors found that the minimum clearance is strongly affected by the CCP time variation. Also, they found that the “Approximate solution” underestimated up to 30% the friction force in the engine cycle phase where the CCP varies rapidly.

Many other works have been published regarding the Piston-Ring-Liner and the imposition of the CCP as a boundary condition (e.g., Morris *et al.* (2014), Morris *et al.*

(2015), Usman and Park (2016)). However, none of these works have considered cavitation in a mass-conserving way. The next chapter is dedicated to an extension of the Elrod-Adams model in order to accommodate this non-homogeneous boundary conditions for pressure.



NONHOMOGENEOUS BOUNDARY CONDITIONS AND CAVITATION MODELING

The available mathematical models for the simulation of lubricated contacts allow to predict friction losses, hydrodynamical support and minimum film clearance for a large variety of mechanisms. Considering devices where cavitation takes place, the current mass-conserving modeling is not suitable to impose a Dirichlet condition different from the cavitation pressure. In this chapter, extensions for Elrod-Adams model are explored. These extensions are one of the main contributions of this work, and they were published in conference papers ([JARAMILLO; CHECO; BUSCAGLIA, 2016a](#); [JARAMILLO; CHECO; BUSCAGLIA, 2016b](#); [JARAMILLO; BUSCAGLIA; M., 2017](#)).

Let us focus on the mechanical setting of the Piston-Ring-Liner (or simply Piston-Ring) introduced in Section 2.4.2. It is a mechanical device that has received a great deal of attention during the last years, where the setting of the boundary conditions for pressure considering the Combustion Chamber Pressure (CCP) time variation may lead to more accurate results. This has been shown in some recent papers ([MORRIS *et al.*, 2014](#); [MORRIS *et al.*, 2015](#)) and in the current work by means of a mass-conserving model. Hereafter the frame of reference is that where the upper surface (ring) does not move horizontally (x_1 -axis) and the lower surface (liner) does not move vertically (x_3 -axis). The configuration of the contact between the lubricant and the ring just after the explosion in the combustion chamber is depicted in Fig. 3.0.1, where the liner is moving with speed $\bar{U} > 0$. The boundary $\partial\Omega$ is partitioned as $\partial\Omega = \Gamma_0 \cup \Gamma_+ \cup \Gamma_*$. On Γ_0 the pressure is set to $p = 0$ and on Γ_+ it is taken equal to the CCP, denoted $p_{cc}(t)$. Periodic conditions are set on Γ_* . The boundary conditions for the fluid fraction on the inlet (*oil-feeding conditions*) are specified in each case. In the next section, we present a mass-flux continuity condition that will play an important role when taking the Elrod-Adams cavitation model as a starting point for this Chapter goal. For sake of simplicity, in this Chapter it is assumed

that there is no relative motion of the surfaces along the x_2 -axis (i.e., $\bar{V} = 0$).

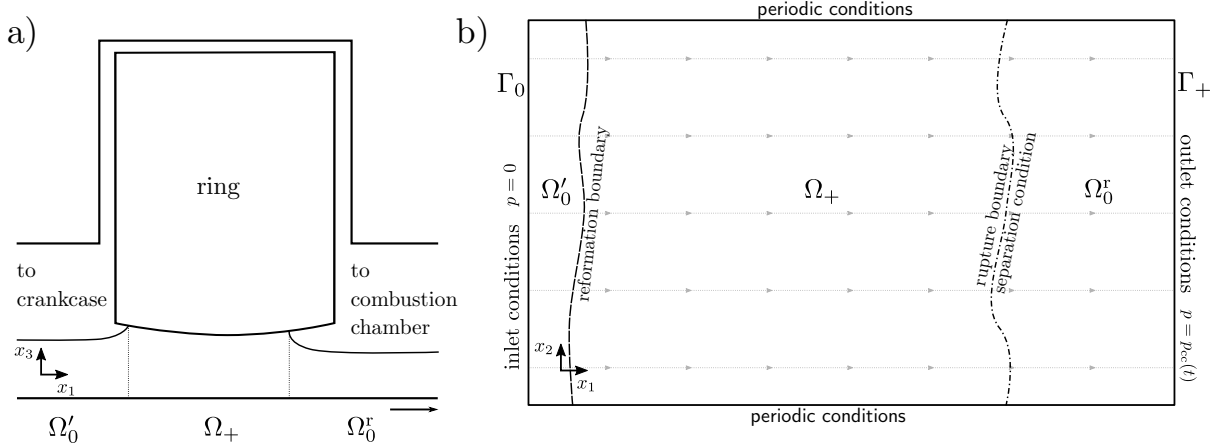


Figure 3.0.1 – Left: scheme of the Piston-Ring system. Right: decomposition of the domain and boundary conditions.

3.1 The mass-flux continuity condition

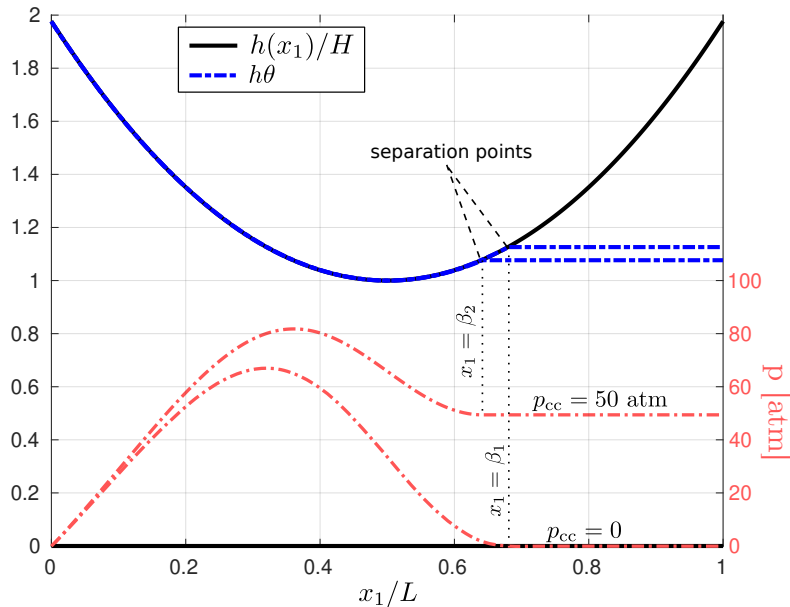


Figure 3.1.1 – Typical stationary solutions for the Piston-Ring for two values of p_{cc} . $H = 1 \mu\text{m}$, $L = 1 \text{ mm}$.

Denoting by $\{\Omega_{0,i}\}_{i=1}^n$ the connected components of $\Omega_0 = \{\theta < 1\}$, it is useful to introduce the notations (see Fig. 3.0.1):

$$\Omega_0^r = \bigcup_{i=1}^n \{x \in \Omega_{0,i} : \partial\Omega_{0,i} \cap \Gamma_r \neq \emptyset\}, \quad \Omega'_0 = \Omega_0 \setminus \Omega_0^r. \quad (3.1)$$

The development presented in Section 2.3.2 holds for $p_{cc}(t) = 0$, and a typical stationary solution of that case is shown in Fig. 3.1.1. For that solution the partition

$\Omega = \Omega_+ \cup \Omega'_0 \cup \Omega^r_0$ corresponds to $\Omega_+ =]0, \beta_1]$, $\Omega'_0 = \emptyset$ and $\Omega^r_0 =]\beta_1, 1[$, with $\beta_1 \approx 0.67$. In that case, the set $\partial\Omega^r_0$ also contains the outlet boundary where $p = p_{cc}$. Thus, if p_{cc} is slightly augmented, it is natural to expect that the whole region Ω^r_0 , where the film is a mixture of liquid and gas/vapor, will pressurize up-to p_{cc} . While the separation boundary will move in order to re-accommodate mass-conservation.

An example of the above mentioned *expected* solution is shown in Figure 3.1.1 for the case $p_{cc} = 50$ atm. There, p is obtained integrating the 1D Reynolds equation (2.12) with ρ constant) in the interval $[0, \beta_2]$ and imposing $p(0) = 0$, $p(\beta_2) = p_{cc}$ and $\frac{\partial p}{\partial x_1}(\beta_2) = 0$. The fluid fraction is set to $\theta = 1$ on $]0, \beta_2]$ and $\theta(x_1) = h(\beta_2)/h(x_1)$ for $x_1 \in]\beta_2, 1[$. In this case $\Omega_+ =]0, \beta_2]$, $\Omega'_0 = \emptyset$ and $\Omega^r_0 =]\beta_2, 1[$, where $\beta_2 < \beta_1$, which can be interpreted as a movement of the separation point to the left due to the higher value of p_{cc} . This proposed solution conserves mass since β_2 is a rupture point and the Rankine-Hugoniot condition (2.25) is accomplished there.

In this last construction a null pressure gradient condition was imposed, nevertheless for $p_{cc} > 0$ this is not the only possibility. In fact, the condition $\frac{\partial p}{\partial n} = 0$ at the rupture points in Section 2.3.2 was a necessary condition since in that case the pressure in Ω_+ is higher than in Ω_0 . But this restriction does not hold between Ω_+ and Ω^r_0 (where $p = p_{cc}$). In fact, a non-null pressure gradient accomplishing the Rankine-Hugoniot condition (2.22), reading

$$(1 - \theta_0) \dot{\beta} = (1 - \theta_0) \frac{\bar{U}}{2} - \frac{h^2}{12\mu} \left. \frac{\partial p}{\partial x_1} \right|_{x_1=\beta_-}, \quad (3.2)$$

is possible in this case (with $\dot{\beta} = \frac{d\beta}{dt}$ being the interface speed). Particularly, in the steady-state, where $\dot{\beta} = 0$, the pressure gradient in β can take any value between 0 (for $\theta_0 = 1$) and $\frac{6\mu\bar{U}}{h^2}$ (for $\theta_0 = 0$). While in the Elrod-Adams model mass-conversation implies $\theta_0 = 1$ and $\left. \frac{\partial p}{\partial x_1} \right|_{x_1} = 0$, this time (with $p_{cc} > 0$) one may choose θ_0 . This represents a loss of uniqueness already stressed by [Buscaglia et al. \(2013\)](#) in a work where the transport speed at the cavitated regions was allowed to be some value in the range $[\bar{U}/2, \bar{U}]$. In this thesis the transport speed at the cavitated regions is fixed to $\bar{U}/2$, which corresponds to the transport speed for the Elrod-Adams model.

Remark 3.1. Two typical values for θ_0 in Eq. (3.2) can be found in the literature ([PRIEST et al., 1996](#)) for the steady state, $\theta_0 = 1$ and $\theta_0 = 2/3$. The former corresponds to the Reynolds separation condition (null pressure gradient) and, for h continuous, it is equivalent to the Reynolds cavitation model presented in Chapter 2. The latter corresponds to

$$\left. \frac{\partial p}{\partial x_1} \right|_{x_1=\beta} = \frac{2\mu\bar{U}}{h^2}, \quad (3.3)$$

a rupture condition that was computed by [Dowson and Taylor \(1979\)](#) based in the reversing flux condition $\left. \frac{\partial u}{\partial z} \right|_{z=h_U} = 0$ in the velocity profile (2.7).

3.2 The continuous problem

Here an extension of the Elrod-Adams cavitation model (ELROD; ADAMS, 1974) is presented for certain situations where the Dirichlet boundary condition for p differs from the cavitation pressure. This is done regarding the situation of the Piston-Ring and its time-dependent boundary conditions.

Fix a domain $\Omega \in \mathbb{R}^N$, $N = 1, 2$. Where $\Omega =]0, L[\times]0, B[$, $\Gamma_0 = \{(0, x_2), x_2 \in [0, B]\}$ and $\Gamma_+ = \{(L, x_2), x_2 \in [0, B]\}$ for $N = 2$; and $\Omega =]0, L[$, $\Gamma_0 = \{0\}$ and $\Gamma_+ = \{L\}$ for $N = 1$. And consider the problem of looking for the real fields (in suitable functional spaces) $p(\mathbf{x}, t)$ and $\theta(\mathbf{x}, t)$, $\mathbf{x} \in \Omega$ and $t \in [0, t_f > 0]$, such that

$$\nabla \cdot \left(\frac{h^3}{12\mu} \nabla p \right) - \frac{\bar{U}}{2} \frac{\partial}{\partial x_1} (h\theta) = \frac{\partial h\theta}{\partial t} \quad \text{in } \Omega, \quad (3.4)$$

$$p \geq T(\theta) \quad \text{in } \Omega, \quad (3.5)$$

$$0 \leq \theta \leq 1 \quad \text{in } \Omega, \quad (3.6)$$

$$(p - T(\theta))(1 - \theta) = 0 \quad \text{in } \Omega, \quad (3.7)$$

$$p = 0 \quad \text{on } \Gamma_0, \quad (3.8)$$

$$p = p_{cc} \quad \text{on } \Gamma_+, \quad (3.9)$$

$$\theta = \theta_{in} \quad \text{on } \partial\Omega, \quad (3.10)$$

where $\bar{U} \in \mathbb{R}_*$ and T is an operator that defines the restriction on p as a function of θ . The standard Elrod-Adams model is recovered by taking $T \equiv 0$. Notice that in that case, since p is continuous in space, the boundary condition (3.9) implies the existence of a full-film region ($\theta = 1$) at the outlet whenever $p_{cc} > 0$, as it can be inferred from (3.7). This issue forbids solutions like the one shown in Fig. 3.1.1. Thus, when $p_{cc} > 0$ the modeling of such physical setting by means of the Elrod-Adams model is not satisfactory.

As shown in Fig. 3.0.1, one expects the presence of a region Ω_0^r where the fluid will be separated from one of the surfaces ($\theta < 1$). Since in that region there exists a mixture of gas/vapor and liquid that does not constitutes a full-film, it is reasonable for the gas present there to be at the same pressure imposed at Γ_+ . Thus, a first soundly definition for T is given by

$$(T\theta)(\mathbf{x}) = \begin{cases} p_{cc}(t) & \text{if } \mathbf{x} \in \Omega_0^r \\ 0 & \text{if } \mathbf{x} \in \Omega_0' \cup \Omega_+ \end{cases}. \quad (3.11)$$

The model obtained that way, i.e., Eqs. (3.4)-(3.10) along the conditions (3.8)-(3.10) and definition (3.11) is a *natural* extension of the Elrod-Adams model. Just like in that classical model, the *extended* one does not impose some restriction related to mass conservation and it consists of a sole partial differential equation for the whole domain. Unfortunately, this extended model is ill-posed as proven in the next result.

Proposition 3.1. Set $N = 1$. Assume $p_{cc} > 0$, $\bar{U} > 0$, $h \in C^1(\Omega)$, $h > 0$ and there exists some $x^m \in]0, L[$ such that $h'(x_1) < 0$ for $x_1 < x^m$, $h'(x_1) > 0$ for $x_1 > x^m$. Then, the stationary problem associated to problem (3.4)-(3.11) admits infinite many solutions.

Proof. Let us introduce the function $\Lambda : \Omega \mapsto \mathbb{R}$, defined by

$$\Lambda(\beta) = \tilde{U} \int_0^\beta \frac{h(s) - h(\beta)}{h^3(s)} ds, \quad (3.12)$$

where $\tilde{U} = 6\mu\bar{U}$. The function Λ has the following properties:

$$\text{sign } \Lambda' = -\text{sign } h', \quad \text{and} \quad \Lambda^* := \max_{\Omega} \Lambda \in \mathbb{R}_*^+. \quad (3.13)$$

In fact, computing

$$\Lambda' = \frac{d\Lambda}{d\beta} = \tilde{U} \int_0^\beta \frac{-h'(\beta)}{h^3(s)} ds - \frac{h(\beta) - h(\beta)}{h^3(\beta)} = -\tilde{U} h'(\beta) \int_0^\beta \frac{1}{h^3(s)} ds,$$

the first property comes directly. Because of this and the continuity of h' and the hypotheses on its sign the existence of Λ^* is clear, moreover $\Lambda^* = \Lambda(x^m)$.

Introduce also the family of curves $(p^{(\beta)}, \theta^{(\beta)})$ on Ω , $\beta \in [x^m, L]$, defined as

$$p^{(\beta)}(x_1) = \begin{cases} \tilde{U} \int_0^{x_1} \frac{h(s) - h(\beta)}{h^3(s)} ds & x_1 \in [0, \beta], \\ p^{(\beta)}(\beta) & x_1 \in]\beta, L]. \end{cases}, \quad \theta^{(\beta)}(x_1) = \begin{cases} 1 & x_1 \in [0, \beta], \\ \frac{h(\beta)}{h(x_1)} & x_1 \in]\beta, L]. \end{cases} \quad (3.14)$$

By construction and the definition of Λ , $(p^{(\beta)}, \theta^{(\beta)})$ is solution of the stationary problem

$$\begin{cases} \frac{d}{dx_1} \left(\frac{h^3}{12\mu} \frac{dp}{dx_1} \right) - \frac{\bar{U}}{2} \frac{dh\theta}{dx_1} = 0, & \text{in } \Omega \\ (p - T(\theta))(1 - \theta) = 0, & \text{in } \Omega \\ 0 \leq \theta \leq 1, & \text{in } \Omega \\ p(0) = 0, & \\ p(L) = \Lambda(\beta), & \\ \theta(0) = 1. & \end{cases} \quad (3.15)$$

with T defined by 3.11. These curves also accomplish $p \geq T(\theta)$. In fact, notice that for $s \in]0, \beta[$ the derivative of $p^{(\beta)}$ accomplishes

$$\frac{dp^{(\beta)}}{dx_1} \Big|_{x_1=s} = \tilde{U} \frac{h(s) - h(\beta)}{h^3(s)}, \quad (3.16)$$

therefore $p^{(\beta)}$ has a unique critical point in $[0, \beta[$, which is a maximum placed at $\lambda < x^m$ such that $h(\lambda) = h(\beta)$ and by definition

$$p^{(\beta)}(\lambda) = \tilde{U} \int_0^\lambda \frac{h(s) - h(\beta)}{h^3(s)} ds = \tilde{U} \int_0^\lambda \frac{h(s) - h(\lambda)}{h^3(s)} ds,$$

thus

$$p^{(\beta)}(\lambda) = \Lambda(\lambda). \quad (3.17)$$

Fix now some $p_{cc} \in]0, \Lambda^*]$, we have shown the existence of a solution for the stationary problem associated to problem (3.4)-(3.11). This solution corresponds to the unique pair $(p^{(\beta)}, \theta^{(\beta)})$ for which $p^{(\beta)} = \Lambda(\beta) = p_{cc}$ (this is depicted in Fig. 3.2.1). Next, by a continuity argument around the solution $(p^{(\beta)}, \theta^{(\beta)})$ it is shown that there exist infinite many others. For this, the next family of curves is defined

$$p^{(\beta,\gamma)}(x_1) = \begin{cases} \tilde{U} \left[\int_0^{x_1} \frac{1}{h^2(s)} ds + \frac{\int_0^{x_1} \frac{1}{h^3(s)} ds}{\int_0^{\beta+\gamma} \frac{1}{h^3(s)} ds} \left(- \int_0^{\beta+\gamma} \frac{1}{h^2(s)} ds + \frac{p_{cc}}{\tilde{U}} \right) \right] & x_1 \in [0, \beta + \gamma], \\ p_{cc} & x_1 \in]\beta + \gamma, L]. \end{cases} \quad (3.18)$$

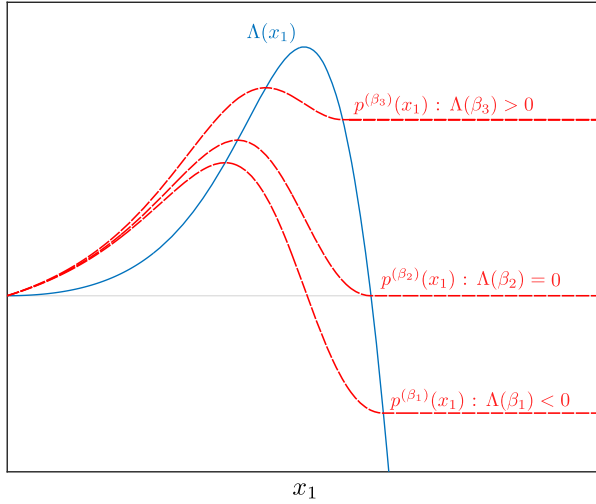


Figure 3.2.1 – Examples of the curves $\Lambda(\beta)$ for different values of β , and the corresponding curves $p^{(\beta)}$.

$$\theta^{(\beta,\gamma)}(x_1) = \begin{cases} 1 & x_1 \in [0, \beta], \\ \frac{h(\beta)}{h(x_1)} - \theta'_0 & x_1 \in]\beta + \gamma, L]. \end{cases} \quad (3.19)$$

To specify θ'_0 , observe that condition (3.2) (with $\dot{\beta} = 0$) implies as a necessary condition

$$\left. \frac{dp^{(\beta,\gamma)}}{dx_1} \right|_{x_1=\beta+\gamma} = (1 - \theta_0) \frac{\tilde{U}}{h(\beta + \gamma)^2}, \quad (3.20)$$

thus, taking $\theta_0 = 1 - \theta'_0$, one obtains

$$\theta'_0 = \frac{1}{\tilde{U}} h(\beta + \gamma)^2 \left. \frac{dp^{(\beta,\gamma)}}{dx_1} \right|_{x_1=\beta+\gamma}. \quad (3.21)$$

We affirm that there exist $\epsilon > 0$ small enough such that all the curves $(p^{(\beta,\gamma)}, \theta^{(\beta,\gamma)})$ with $\gamma \in [0, \epsilon]$ are solutions of the stationary problem associated to problem (3.4)-(3.11), which is the result we are looking for. To prove this, it is enough to show that, for γ small enough,

$p^{(\beta,\gamma)}$ accomplishes the restriction $p > T(\theta)$ and that θ'_0 is well defined, i.e., $0 \leq \theta'_0 < 1$ and thus $0 < \theta_0 \leq 1$. In fact, using the definition of $\Lambda(\beta)$, we have

$$\begin{aligned} \frac{dp^{(\beta,\epsilon)}}{dx_1} \Big|_{x_1=\beta+\epsilon} &= \frac{\tilde{U}}{h(\beta+\epsilon)^2} + \frac{\tilde{U}/h(\beta+\epsilon)}{\int_0^{\beta+\epsilon} \frac{1}{h(s)^3} ds} \left(-\int_\beta^{\beta+\epsilon} \frac{1}{h(s)} ds - \int_0^\beta \frac{h(\beta)}{h(s)^3} ds \right) \\ &= \frac{\tilde{U}}{h(\beta+\epsilon)^2} \left[1 + \frac{1}{\int_0^{\beta+\epsilon} \frac{1}{h(s)^3} ds} \left(\int_\beta^{\beta+\epsilon} \frac{h(s)/h(\beta+\epsilon)}{h(s)^3} ds - \int_0^\beta \frac{h(\beta)/h(\beta+\epsilon)}{h(s)^3} ds \right) \right] > 0 \end{aligned}$$

where we used the properties of h . As $\frac{dp^{(\beta,\epsilon)}}{dx_1} \Big|_{x_1=\beta} = 0$ and since the last equation shows that $\frac{dp^{(\beta,\epsilon)}}{dx_1} \Big|_{x_1=\beta+\epsilon}$ is continuous and positive for $\epsilon > 0$, we have that θ'_0 is well defined for ϵ small enough.

Finally, observe that the definitions of $p^{(\beta,\epsilon)}$ and $p^{(\beta)}$ clearly imply

$$\|p^{(\beta,\epsilon)} - p^{(\beta)}\|_{C^0([\beta,L])} \xrightarrow[\epsilon \rightarrow 0]{} 0.$$

Additionally

$$\begin{aligned} (p^{(\beta,\epsilon)} - p^{(\beta)}) (x_1) &= \tilde{U} \frac{\int_0^{x_1} \frac{1}{h(s)^3} ds}{\int_0^{\beta+\epsilon} \frac{1}{h(s)^3} ds} \left(-\int_0^\beta \frac{h(\beta)}{h(s)^3} ds - \int_\beta^{\beta+\epsilon} \frac{1}{h(s)^2} ds \right) + \tilde{U} \int_0^{x_1} \frac{h(\beta)}{h(s)^3} ds \\ &= \tilde{U} \int_0^{x_1} \frac{h(\beta)}{h(s)^3} ds \left(1 - \frac{\int_0^\beta \frac{h(\beta)}{h(s)^3} ds + \int_\beta^{\beta+\epsilon} \frac{1}{h(s)^2} ds}{\int_0^{\beta+\epsilon} \frac{h(\beta)}{h(s)^3} ds} \right), \end{aligned} \tag{3.22}$$

therefore $\|p^{(\beta,\epsilon)} - p^{(\beta)}\|_{C^0([0,\beta])} \xrightarrow[\epsilon \rightarrow 0]{} 0$ and we conclude that

$$\|p^{(\beta,\epsilon)} - p^{(\beta)}\|_{C^0(\Omega)} \xrightarrow[\epsilon \rightarrow 0]{} 0.$$

□

Remark 3.2. Notice from this last proof that when considering the family of curves $(p^{(\beta)}, \theta^{(\beta)})$ and fixing $\theta_0 = 1$, there exists a maximum value Λ^* such that if $p_{cc} > \Lambda^*$ there is no stationary solution. And when $p_{cc} \leq \Lambda^*$ that solution exists and it is unique.

In Section 3.4 it is shown an example where even for θ_0 fixed there exist multiple solutions for the stationary case. For this, in the next section it is presented an algorithm to handle numerically more complex geometries.

3.3 Extending the Elrod-Adams algorithm

Divide the domain Ω in $N_{x_1} \times N_{x_2}$ cells (using half-cells at the boundaries) and denote by I the set of indexes of the cells corresponding to internal nodes (where the

unknowns are placed). A finite volumes scheme for Eq. (3.4) is used, for this, the x_1 flux component going from node $(i-1, j)$ to node (i, j) can be discretized by

$$-\frac{h^3}{12\mu} \frac{\partial p}{\partial x_1} + \frac{\bar{U}}{2} h\theta \approx -\frac{1}{12\mu} \frac{(h_{i-1,j}^n)^3 + (h_{i,j}^n)^3}{2} \frac{p_{i,j}^n - p_{i-1,j}^n}{\Delta x_1} + \frac{\bar{U}}{2} h_{i-1,j}^n \theta_{i-1,j}^n, \quad (3.23)$$

where an upwind scheme is used for the Couette term. Balancing the fluxes on each cell (for the x_2 components only diffusive terms need to be included) and discretizing time along an implicit scheme for the temporal term $\frac{\partial h\theta}{\partial t}$ one gets a system of equations that reads for each $(i, j) \in I$

$$a_{i,j}^{00} p_{i,j}^n + e_{i,j}^{00} \theta_{i,j}^n = C_{i,j}(\mathbf{p}^n, \boldsymbol{\theta}^n), \quad (3.24)$$

$$p_{i,j}^n \geq T(\boldsymbol{\theta}^n)_{i,j}, \quad (3.25)$$

$$0 \leq \theta_{i,j}^n \leq 1, \quad (3.26)$$

$$(p_{i,j}^n - T(\boldsymbol{\theta}^n)_{i,j}) (1 - \theta_{i,j}^n) = 0, \quad (3.27)$$

where

$$C_{i,j}(\mathbf{p}^n, \boldsymbol{\theta}^n) = -a_{i,j}^{-0} p_{i-1,j}^n - a_{i,j}^{+0} p_{i+1,j}^n - a_{i,j}^{0+} p_{i,j+1}^n - a_{i,j}^{0-} p_{i,j-1}^n - e_{i,j}^{-0} \theta_{i-1,j}^n + f_{i,j}^n, \quad (3.28)$$

with

$$\begin{aligned} a_{i,j}^{00} &= s_{i+1,j}^n + s_{i-1,j}^n + (\Delta x_1 / \Delta x_2)^2 (s_{i,j+1}^n + s_{i,j-1}^n), & e_{i,j}^{00} &= (\bar{U} \Delta x_1 + 2 \Delta x_1^2 / \Delta t) h_{i,j}^n, \\ a_{i,j}^{+0} &= -s_{i+1,j}^n, & a_{i,j}^{-0} &= -s_{i-1,j}^n, \\ a_{i,j}^{0-} &= -(\Delta x_1 / \Delta x_2)^2 s_{i,j-1}^n, & a_{i,j}^{0+} &= -(\Delta x_1 / \Delta x_2)^2 s_{i,j+1}^n, \\ e_{i,j}^{-0} &= -\bar{U} \Delta x_1 h_{i-1,j}^n, & s_{i\pm 1,j\pm 1}^n &= \frac{1}{12\mu} ((h_{i,j}^n)^3 + (h_{i\pm 1,j\pm 1}^n)^3), \\ f_{i,j}^n &= 2 \Delta x_1^2 / \Delta t h_{i,j}^{n-1} \theta_{i,j}^{n-1}. \end{aligned}$$

Notice that $a_{i,j}^{00}, e_{i,j}^{00}, f_{i,j}^n \geq 0$, and each term $a_{i,j}^{+0}, a_{i,j}^{-0}, a_{i,j}^{0+}, a_{i,j}^{0-}, e_{i,j}^{-0}$ is non-positive, thus $C_{i,j}(\mathbf{p}^n, \boldsymbol{\theta}^n) \geq 0$. This type of discrete system was already studied for the case $T \equiv 0$ (standard Elrod-Adams algorithm) in (ALT, 1980) by means of a fixed-point method and in (MARINI; PIETRA, 1986) where the convergence of some Gauss-Seidel-like algorithms was proved. However, for the general case the condition $\theta \geq 0$ is not always satisfied as shown next.

Dropping the superscript n and denoting by N the number of unknowns, the system of equations (3.24)-(3.27) can be written as a fixed-point problem by defining the operator $B_T : \mathbb{R}^N \times \mathbb{R}^N \mapsto \mathbb{R}^N \times \mathbb{R}^N$ as

$$B_T(\mathbf{p}, \boldsymbol{\theta})_{i,j} = \begin{cases} \left(\frac{C_{i,j}(\mathbf{p}, \boldsymbol{\theta}) - e_{i,j}^{00}}{a_{i,j}^{00} (T\boldsymbol{\theta})_{i,j}}, 1 \right) & \text{if } \frac{C_{i,j}(\mathbf{p}, \boldsymbol{\theta}) - e_{i,j}^{00}}{a_{i,j}^{00} (T\boldsymbol{\theta})_{i,j}} \geq 0 \\ \left(T(\boldsymbol{\theta})_{i,j}, \frac{C_{i,j}(\mathbf{p}, \boldsymbol{\theta}) - a_{i,j}^{00} T(\boldsymbol{\theta})_{i,j}}{e_{i,j}^{00}} \right) & \text{if } \frac{C_{i,j}(\mathbf{p}, \boldsymbol{\theta}) - e_{i,j}^{00}}{a_{i,j}^{00} (T\boldsymbol{\theta})_{i,j}} < 0 \end{cases}, \quad (3.29)$$

for each cell $(i, j) \in I$. This way, the Eq. (3.24) can be rewritten as the next fixed point problem

$$B_T(\mathbf{p}, \boldsymbol{\theta}) = (\mathbf{p}, \boldsymbol{\theta}). \quad (3.30)$$

Let us split the set I as $I = I_0 \overset{\circ}{\cup} I_r$, where I_r is the subset of cells in the region Ω_0^r and $I_0 = I \setminus I_r$. A solution of Eq. (3.30) accomplishes automatically the conditions (3.25) and (3.27) for any $(i, j) \in I$. However, the only immediate condition accomplished by $\theta_{i,j}$ is that $\theta_{i,j} \leq 1$. In fact, we have

$$C_{i,j}(\mathbf{p}, \boldsymbol{\theta}) - a_{i,j}^{00} T(\boldsymbol{\theta})_{i,j} = f_{i,j} + S \Delta x_1 h_{i-1,j} \theta_{i-1,j} + \Delta''_{i,j},$$

where $f_{i,j} + S \Delta x_1 h_{i-1,j} \theta_{i-1,j} \geq 0$ and

$$\begin{aligned} \Delta''_{i,j} &= s_{i-1,j} (p_{i-1,j} - T(\boldsymbol{\theta})_{i,j}) + s_{i+1,j} (p_{i+1,j} - T(\boldsymbol{\theta})_{i,j}) + \\ &+ q^2 \{ s_{i,j-1} (p_{i,j-1} - T(\boldsymbol{\theta})_{i,j}) + s_{i,j+1} (p_{i,j+1} - T(\boldsymbol{\theta})_{i,j}) \}, \end{aligned}$$

with q a constant not depending on \mathbf{p} nor $\boldsymbol{\theta}$. Thus, $\theta_{i,j}$ may be negative in the cells of I_r for which some of its neighbors belongs to the set I_0 .

The discrete version of the operator $T = T_\epsilon$ is defined as follows

$$T_\epsilon(\boldsymbol{\theta})_{i,j} = \begin{cases} p_{cc}(t) & \text{if } (i, j) \in I_r \cup V^\epsilon, \\ 0 & \text{if } (i, j) \notin I_r \cup I^\epsilon, \end{cases} \quad (3.31)$$

Where I^ϵ , $\epsilon \in \{0, 1\}$, corresponds to the indexes (i, j) of the cells contained in Ω_+ such that some of its neighbor cells (i.e., $\{(i \pm 1, j), (i, j \pm 1)\}$) belongs to Ω_0^r when $\epsilon = 1$, and $I^\epsilon = \emptyset$ for $\epsilon = 0$. Figure 3.3.1 illustrates the action of the discrete operator T_ϵ . Alt (1980) proposed an algorithm to solve Eq. (3.30) for the case $T_\epsilon \equiv 0$. Algorithm 1 is a natural extension of Alt's algorithm for T_ϵ non-trivial.

Next it is shown that the Eq. (3.30) along definition (3.31) for the discrete operator T_ϵ is not a well-posed problem. It is also shown the relation between this ill-posedness and the mass-conserving condition (3.2).

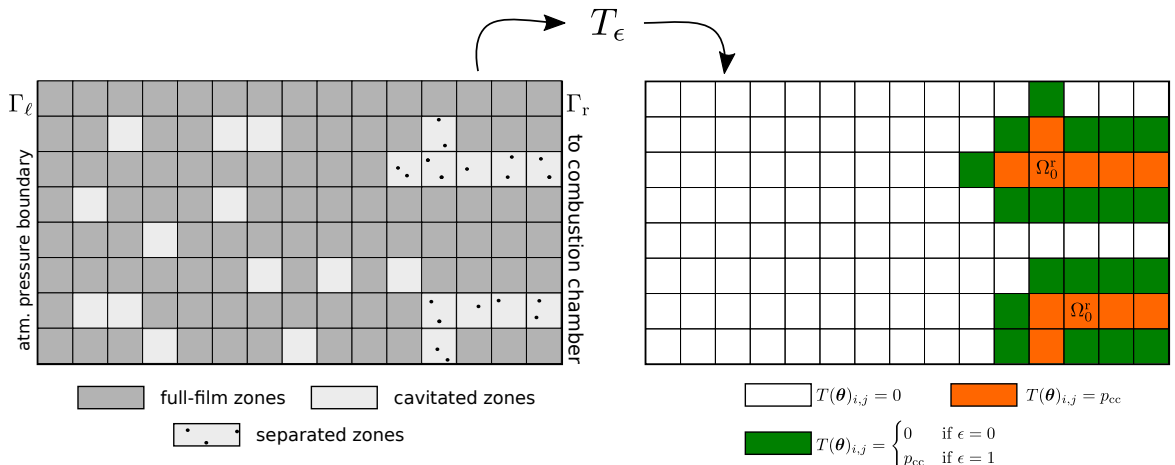


Figure 3.3.1 – Illustration of the action of the discrete operator T_ϵ .

```

Input:  $h$ : gap function;  $\mathbf{p}^{n-1}$ ,  $\boldsymbol{\theta}^{n-1}$ : initial guess;  $\delta_T$ : parameter defining  $T$ 
1 begin
2    $k = 1$ ;
3    $\mathbf{p}^{n,0} = \mathbf{p}^{n-1}$ ;  $\boldsymbol{\theta}^{n,0} = \boldsymbol{\theta}^{n-1}$ ;
4    $\mathbf{p}^{n,k} = \mathbf{p}^{n,0}$ ;  $\boldsymbol{\theta}^{n,k} = \boldsymbol{\theta}^{n,0}$ ;
5   while  $change > tol$  do
6     for  $i = 1 \dots N_{x_1}$ ,  $j = 1 \dots N_{x_2}$  do
7       if  $(C_{i,j} - e_{i,j}^{00}) / a_{i,j}^{00} \geq T(\boldsymbol{\theta}^{n,k-1})_{i,j}$  then
8          $p_{i,j}^{n,k} = (C_{i,j} - e_{i,j}^{00}) / a_{i,j}^{00}$ ;
9          $\theta_{i,j}^{n,k} = 1$ ;
10        else
11           $\theta_{i,j}^{n,k} = (C_{i,j} - a_{i,j}^{00} T(\boldsymbol{\theta}^{n,k-1})_{i,j}) / e_{i,j}^{00}$ ;
12           $p_{i,j}^{n,k} = T(\boldsymbol{\theta}^{n,k-1})_{i,j}$ ;
13        end
14      end
15    end
16     $change = \|\mathbf{p}^{n,k} - \mathbf{p}^{n,k-1}\| + \|\boldsymbol{\theta}^{n,k} - \boldsymbol{\theta}^{n,k-1}\|$ ;
17     $\mathbf{p}^{n,k+1} = \mathbf{p}^{n,k}$ ;  $\boldsymbol{\theta}^{n,k+1} = \boldsymbol{\theta}^{n,k}$ ;
18     $k = k + 1$ ;
19  end
20  return  $\mathbf{p}^{n,k}$ ,  $\boldsymbol{\theta}^{n,k}$ ;
21 end

```

Algorithm 1: Adaptation of the numerical algorithm presented by Alt (1980) to solve system (3.30).

3.3.1 A second approach for transient 1D problems

In this Section a particular 1D model is exposed to tackle the issue of the existence of multiple solutions for the stationary case of the system (3.30). This is based in a work by Ausas *et al.* (2013) for another type of extension of the Elrod-Adams model. The basic idea is to set a model for θ_0 in Eq. (3.20). Here the value $\theta_0 = \hat{\theta}_0 \stackrel{\text{def}}{=} 2/3$ is chosen. This corresponds to the value of θ_0 obtained in (2.7) when the flux reversion condition $\frac{\partial u}{\partial z} \Big|_{h=h_U} = 0$ is imposed. Moreover, in the work of Coyne and Elrod (1971) it is shown that this value of θ_0 agrees with experimental results for a typical surface tension of mineral oil (≈ 0.03 N/m).

Here we propose to impose $\theta_0 = \hat{\theta}_0$ in the mass-conservation equation (3.2), and then to solve that ODE coupled with the 1D version of the continuous problem (3.30). In that case, Eq. (3.2) reads

$$\frac{d\beta}{dt} = \frac{\bar{U}}{2} - \frac{1}{1 - \hat{\theta}_0} \frac{h(\beta)^2}{12\mu} p'(\beta_-). \quad (3.32)$$

A front-tracking strategy is set to solve this equation in time, i.e., given the value of β at the initial time $t = 0$, denoted β_0 , the cells at both sides of β are modified to accommodate the fluxes at the interface $x_1 = \beta$. For this, the next hypotheses are made:

- $\beta(t)$ is a rupture point. Thus,

$$\frac{d\beta}{dt} < \frac{\bar{U}}{2}.$$

- The pressurized region at the left side of beta is at least of length $2\Delta x_1$. Thus, there must exist a curve $x(t)$ such that $0 \leq x(t) < \beta(t)$, $\theta([x(t), \beta(t)]) = 1$ and $|x(t) - \beta(t)| \geq 2\Delta x_1$ for all t .

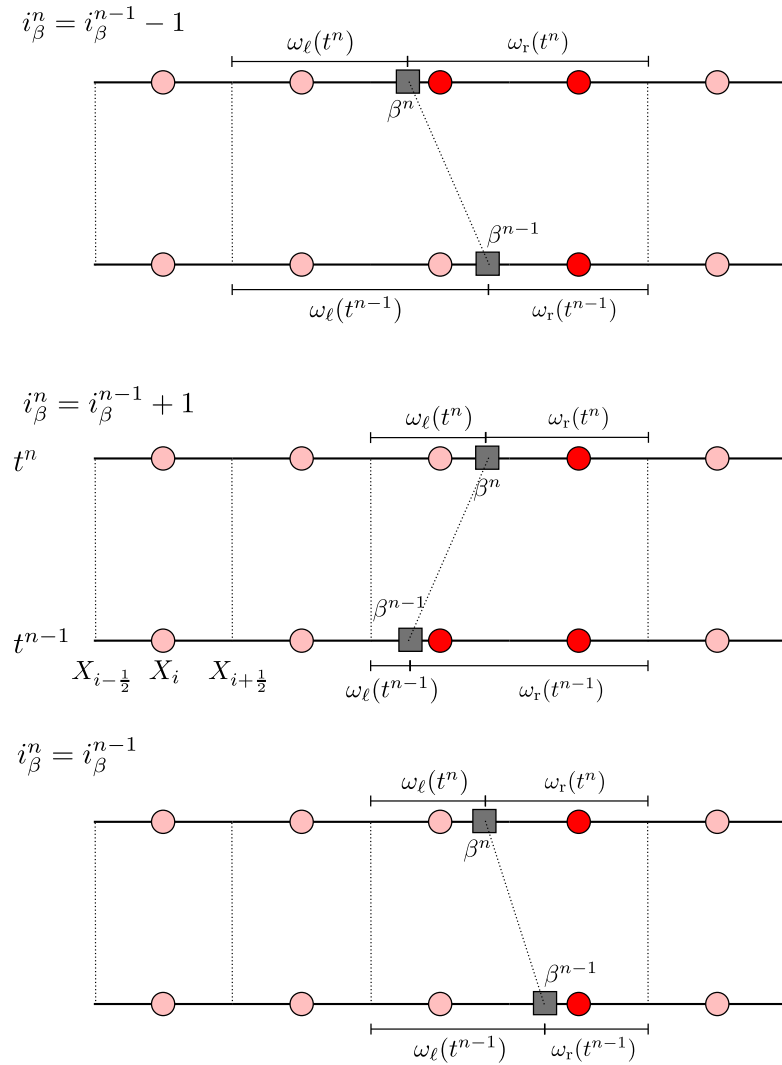


Figure 3.3.2 – Cells scheme around the rupture point β^n for Algorithm 2. Adapted from (AUSAS et al., 2013).

A Finite Volume Method is adopted, in Appendix A it is presented a description of these methods for the cases where the cells are allowed to move. Here it is assumed that the nodes at the right side of β^n are always *separated* ($\theta < 1$) and thus $p_i^n = p_{cc}(t)$ there. The cells partition $\mathcal{T}^{\Delta x_1}$ of the domain $]0, L[$ at time t^n depends on time: the center of the regular cells is placed at $X_i = i \Delta x_1$ and its boundaries are $X_{i-\frac{1}{2}} = X_i - \Delta x_1/2$ and $X_{i+\frac{1}{2}} = X_i + \Delta x_1/2$; the cells at the left side and the right side of the rupture point are

denoted by $\omega_\ell(t)$ and $\omega_r(t)$ resp., their limits depend on the position of β at both times t^n and t^{n-1} , a detailed description of these volumes is given in Fig. 3.3.2.

Before describing the algorithm Eq. (3.32) is discretized according to

$$V_\beta^n = \frac{\bar{U}}{2} - \frac{1}{1 - \hat{\theta}_0} \frac{h(\beta^n)^2}{12\mu} \frac{(p_{cc} - p_{i_\beta^n-1}^n)}{\beta^n - X_{i_\beta^n-1}}. \quad (3.33)$$

The numerical procedure is as follows:

1. Compute the pressure field \mathbf{p}^n and the saturation field $\boldsymbol{\theta}^n$ at the left side of β^n . For this, denoting by i_β^n the cell placed at the right side of β^n (see Fig. 3.3.2), the equation for p_i^n and θ_i^n at the nodes i such that $i < i_\beta^n - 1$ reads

$$\Delta x_1 (h_i^n \theta_i^n - h_i^{n-1} \theta_i^{n-1}) = -\Delta t \left[\frac{\left(h_{i-\frac{1}{2}}^n\right)^3}{12\mu} \frac{(p_i^n - p_{i-1}^n)}{\Delta x_1} - \frac{\bar{U}}{2} h_{i-1}^n \theta_{i-1}^n \right. \\ \left. - \frac{\left(h_{i+\frac{1}{2}}^n\right)^3}{12\mu} \frac{(p_{i+1}^n - p_{i-1}^n)}{\Delta x_1} + \frac{\bar{U}}{2} h_i^n \theta_i^n \right]. \quad (3.34)$$

while at $i = i_\beta^n - 1$ the discretization depends on the advance of β . The volume $h\theta$ at time t^n is set to the volume at time $n-1$, denoted M^{n-1} plus the volume flow $-\Delta t (Q_{\beta,\ell}^n + Q_{\beta,r}^n)$ and the volume variation due to the movement of β :

$$\left(\beta^n - X_{i_\beta^n - \frac{3}{2}} \right) h_i^n \theta_i^n = M^{n-1} - \Delta t (Q_{\beta,\ell}^n + Q_{\beta,r}^n - V_\beta^{n-1} h(\beta^n)) \quad (3.35)$$

where

$$Q_{\beta,\ell}^n = \left[-\frac{\left(h_{i-\frac{1}{2}}^n\right)^3}{12\mu} \frac{(p_i^n - p_{i-1}^n)}{\Delta x_1} + \frac{\bar{U}}{2} h_{i-1}^n \theta_{i-1}^n \right] (-1) \quad (3.36)$$

is the flux entering at the left side of the cell i and

$$Q_{\beta,r}^n = \left[-\frac{h(\beta^n)^3}{12\mu} \frac{(p_{cc} - p_{i_\beta^n-1}^n)}{\beta^n - X_{i_\beta^n-1}} + \frac{\bar{U}}{2} h(\beta^n) \right] (+1) \quad (3.37)$$

is the flux entering at its right side. In these two formulas (-1) and $(+1)$ corresponds to sign of the normal vector at the cell interface. The volume content at time $n-1$ of the cell $\omega_\ell(t^{n-1})$ reads

$$M^{n-1} = \begin{cases} \left(\beta^{n-1} - X_{i_\beta^{n-1} - \frac{3}{2}} \right) h_{i_\beta^{n-1}}^{n-1} \theta_{i_\beta^{n-1}}^{n-1} & \text{if } i_\beta^n = i_\beta^{n-1} \\ \left(\beta^{n-1} - X_{i_\beta^{n-1} - \frac{3}{2}} \right) h_{i_\beta^{n-1}}^{n-1} \theta_{i_\beta^{n-1}}^{n-1} + \Delta x_1 h_{i_\beta^{n-1}-1}^{n-1} \theta_{i_\beta^{n-1}-1}^{n-1} & \text{if } i_\beta^n = i_\beta^{n-1} - 1 \\ \left(\beta^{n-1} - X_{i_\beta^{n-1} - \frac{1}{2}} \right) h_{i_\beta^{n-1}}^{n-1} \theta_{i_\beta^{n-1}}^{n-1} & \text{if } i_\beta^n = i_\beta^{n-1} + 1 \end{cases} \quad (3.38)$$

The Courant number $\frac{\bar{U}}{2} \frac{\Delta t}{\Delta x_1}$ is restricted to be lower than 1/2. This way, since we are restricting V_β to be lower than $\bar{U}/2$, the point β advances a distance smaller than $\Delta x_1/2$.

2. Solve the transport equation for θ^n at the right side of β^n by means of an upwind Finite Volume scheme. This is done depending on whether the rupture point has passed through the point $X_{i_\beta^{n-1}-1}$ (moving to the left), it has passed through the point $X_{i_\beta^n}$ (moving to the right), or it has remained between these two points (moving to the left or right)

Case $i_\beta^n = i_\beta^{n-1} - 1$: For this case, schematized in Fig. 3.3.2, it is imposed

$$\theta_{i_\beta^n}^n = \hat{\theta}_0 \quad (3.39)$$

and mass balance at the left side of β reads

$$\begin{aligned} \left(X_{i_\beta^{n+\frac{1}{2}}} - \beta^n \right) h_{i_\beta^n}^n \hat{\theta}_0 + \Delta x_1 h_{i_\beta^n+1}^n \theta_{i_\beta^n+1}^n &= \left(X_{i_\beta^{n-1}+\frac{1}{2}} - \beta^{n-1} \right) h_{i_\beta^{n-1}}^{n-1} \theta_{i_\beta^{n-1}}^{n-1} \\ &\quad - \Delta t \left[-Q_{\beta,r}^n + V_\beta^{n-1} h(\beta^n) + \frac{\bar{U}}{2} h_{i_\beta^{n-1}}^{n-1} \theta_{i_\beta^{n-1}}^{n-1} \right]. \end{aligned} \quad (3.40)$$

Case $i_\beta^n = i_\beta^{n-1}$: Similarly to the previous case, mass balance gives

$$\begin{aligned} \left(X_{i_\beta^{n+\frac{1}{2}}} - \beta^n \right) h_{i_\beta^n}^n \theta_{i_\beta^n}^n &= \left(X_{i_\beta^{n-1}+\frac{1}{2}} - \beta^{n-1} \right) h_{i_\beta^{n-1}}^{n-1} \theta_{i_\beta^{n-1}}^{n-1} \\ &\quad - \Delta t \left[-Q_{\beta,r}^n + V_\beta^{n-1} h(\beta^n) + \frac{\bar{U}}{2} h_{i_\beta^{n-1}}^{n-1} \theta_{i_\beta^{n-1}}^{n-1} \right]. \end{aligned} \quad (3.41)$$

Case $i_\beta^n = i_\beta^{n-1} + 1$: In this case the cell $i_\beta^n - 1$ is fulfilled, i.e.,

$$\theta_{i_\beta^n-1}^n = 1,$$

and the mass in the next cell (to the right) is accommodated by

$$\begin{aligned} \left(X_{i_\beta^{n+\frac{1}{2}}} - \beta^n \right) h_{i_\beta^n}^n \theta_{i_\beta^n}^n &= (\beta^n - \beta^{n-1}) h_{i_\beta^{n-1}}^{n-1} \theta_{i_\beta^{n-1}}^{n-1} + \left(X_{i_\beta^{n-1}+\frac{3}{2}} - \beta^n \right) h_{i_\beta^{n-1}+1}^{n-1} \theta_{i_\beta^{n-1}+1}^{n-1} \\ &\quad - \Delta t \left[-Q_{\beta,r}^n + V_\beta^{n-1} h(\beta^n) + \frac{\bar{U}}{2} h_{i_\beta^{n-1}+1}^{n-1} \theta_{i_\beta^{n-1}+1}^{n-1} \right]. \end{aligned} \quad (3.42)$$

In these three cases the mass balance for the rest of the cells at the right side of β reads

$$\Delta x_1 h_i^n \theta_i^n = \Delta x_1 h_i^{n-1} \theta_i^{n-1} + \Delta t \left[\frac{\bar{U}}{2} h_{i-1}^{n-1} \theta_{i-1}^{n-1} - \frac{\bar{U}}{2} h_i^{n-1} \theta_i^{n-1} \right]. \quad (3.43)$$

3. Compute the new position β^{n+1} :

$$\beta^{n+1} = \beta^n + \Delta t V_\beta^n, \quad (3.44)$$

with V_β^n given by Eq. (3.33).

This numerical procedure is resumed in Algorithm 2. In that algorithm the discrete problem at the left side of β^n (the Elrod-Adams model) is written

$$a_i^{00} p_i^n + e_i^{00} \theta_i^n = C_i(\mathbf{p}^n, \boldsymbol{\theta}^n), \quad (3.45)$$

$$p_i^n \geq 0, \quad (3.46)$$

$$0 \leq \theta_{i,j}^n \leq 1, \quad (3.47)$$

$$p_i^n (1 - \theta_i^n) = 0, \quad (3.48)$$

with the arrays \mathbf{C} , \mathbf{e} and \mathbf{a} are defined as follows:

$$C_i(\mathbf{p}^n, \boldsymbol{\theta}^n) = -a_i^{-0} p_{i-1}^n - a_i^{+0} p_{i+1}^n - e_i^{-0} \theta_{i-1}^n + f_i^n \quad (3.49)$$

with, for $i < i_\beta^n - 1$

$$\begin{aligned} a_i^{00} &= s_{i+1}^n + s_{i-1}^n, & e_i^{00} &= (\bar{U} \Delta x_1 + 2\Delta x_1^2 / \Delta t) h_i^n, \\ a_i^{+0} &= -s_{i+1}^n, & a_i^{-0} &= -s_{i-1}^n, \\ e_i^{-0} &= -\bar{U} \Delta x_1 h_{i-1}^n, & s_{i\pm 1}^n &= \frac{1}{12\mu} ((h_i^n)^3 + (h_{i\pm 1}^n)^3), \\ f_i^n &= 2\Delta x_1^2 / \Delta t h_i^{n-1} \theta_i^{n-1}. \end{aligned}$$

and for $i = i_\beta^n - 1$

$$\begin{aligned} a_i^{00} &= s_{i-1}^n + \frac{\Delta x_1}{\beta^n - X_{i_\beta^n - 1}} s_\beta^n, & e_i^{00} &= \left(\bar{U} \Delta x_1 + 2 \frac{(\beta^n - X_{i_\beta^n - \frac{3}{2}})}{\Delta t} \Delta x_1 \right) h_i^n, \\ a_i^{+0} &= 0, & a_i^{-0} &= -s_{i-1}^n, \\ e_i^{-0} &= -\bar{U} \Delta x_1 h_{i-1}^n, & s_{i-1}^n &= \frac{1}{12\mu} ((h_i^n)^3 + (h_{i-1}^n)^3), \\ f_i^n &= 2 \frac{\Delta x_1}{\Delta t} M^{n-1} + \frac{\Delta x_1}{\beta^n - X_{i_\beta^n - 1}} s_\beta^n p_{cc}^n, & s_\beta^n &= \frac{1}{6\mu} h(\beta^n)^3. \end{aligned}$$

where M^n was defined in (3.38).

```

Input:  $h$ : gap function;  $\mathbf{p}^{n-1}$ ,  $\boldsymbol{\theta}^{n-1}$ : initial guess;  $\beta^0$ : initial rupture point
1 begin
2   | for  $n = 0$  to  $n = N_T$  do
3   |   | set  $\mathbf{p}^{n,0}$  and  $\boldsymbol{\theta}^{n,0}$ ;
4   |   | compute  $i_\beta^n$ ;
5   |   |  $k = 0$ ;
6   |   | set the arrays  $\mathbf{C}$ ,  $\mathbf{e}$  and  $\mathbf{a}$ ;
7   |   | while  $change > tol$  do
8   |   |   | for  $i = 1 \dots i_\beta^n - 1$  do
9   |   |   |   | if  $C_i - e_i \geq 0$  then
10  |   |   |   |   |  $p_i^{n,k} = (C_i - e_i)/a_i$ ;
11  |   |   |   |   |  $\theta_i^{n,k} = 1$ ;
12  |   |   |   | else
13  |   |   |   |   |  $\theta_i^{n,k} = C_i/e_i$ ;
14  |   |   |   |   |  $p_i^{n,k} = 0$ ;
15  |   |   |   | end
16  |   |   | end
17  |   | end
18  |   |  $change = \|\mathbf{p}^{n,k} - \mathbf{p}^{n,k-1}\| + \|\boldsymbol{\theta}^{n,k} - \boldsymbol{\theta}^{n,k-1}\|$ ;
19  |   |  $\mathbf{p}^{n,k+1} = \mathbf{p}^{n,k}$ ;  $\boldsymbol{\theta}^{n,k+1} = \boldsymbol{\theta}^{n,k}$ ;
20  |   |  $k = k + 1$ ;
21  | end
22  | if  $i_\beta^n < i_\beta^{n-1}$  then
23  |   | set  $\theta_{i_\beta^n}^n = \hat{\theta}_0$  and compute  $\theta_{i_\beta^n+1}^n$  with (3.40);
24  | end
25  | if  $i_\beta^n = i_\beta^{n-1}$  then
26  |   | compute  $\theta_{i_\beta^n}^n$  and  $\theta_{i_\beta^n+1}^n$  with (3.41) and (3.43) resp.>;
27  | end
28  | if  $i_\beta^n > i_\beta^{n-1}$  then
29  |   | compute  $\theta_{i_\beta^n}^n$  and  $\theta_{i_\beta^n+1}^n$  with (3.42) and (3.43) resp.>;
30  | end
31  | for  $i = i_\beta^n + 2 \dots N_{x_1}$  do
32  |   | compute  $\theta_i^n$  with (3.43);
33  | end
34  | if  $n < N_T$  then
35  |   | compute  $\beta^{n+1}$  with (3.44)-(3.33), and compute  $i_\beta^{n+1}$ ;
36  | end
37  | end
38 end

```

Algorithm 2: Solving the system (3.30) along a front-tracking algorithm for the rupture point β .

3.4 Numerical examples

In Section 3.4.1 stationary solutions of the Eq. (3.30) along Algorithm 1 and some modifications of it are presented. First, it is shown that the solution at which that algorithm may converge depends on the initial guess $(\mathbf{p}^0, \boldsymbol{\theta}^0)$. This issue is worked out by setting a value for θ_0 in condition (3.2), and different solutions for many values of θ_0 are presented. Finally, a 1D geometry where there exist at least two stationary solutions for the same value of θ_0 is exposed. In Section 3.4.2 transient solutions of the Eq. (3.30) are shown by means of Algorithm 1 and $T = T_{\epsilon=1}$. It is observed that such configuration imposes $\theta_0 = 1$ or, equivalently, a null-gradient condition for pressure at the rupture boundary. Finally, Section 3.4.3 shows stationary and transient cases where Algorithm 2 has been used. It is shown that such simulations correspond to the imposition of θ_0 different from the unit, which is done by solving Eq. (3.2) in time.

The physical parameters common to all these simulations are shown in Table 2

| Symbol | Value | Units | Description |
|-------------|--------------------|-------------------|------------------------------------|
| ρ_ℓ | 1000 | kg/m ³ | Liquid density |
| μ_ℓ | 4×10^{-3} | Pa·s | Liquid viscosity |
| p_{cc} | 0-100 | atm | Pressure condition at Γ_r |
| \bar{U} | 10 | m/s | Surfaces' relative speed |
| H | 1 | μm | x_3 -axis length scale |
| L | 1 | mm | x_1 and x_2 -axis length scale |

Table 2 – Physical parameters for the numerical examples of Section 3.4.

3.4.1 Stationary cases along Algorithm 1

3.4.1.1 1D cases with $\epsilon = 0, 1$

Let us fix the 1D domain $\Omega =]0, L[$ and the surfaces' gap

$$h(x_1) = 1[\mu\text{m}] + \frac{(x_1 - L/2)^2}{2R_c}. \quad (3.50)$$

The stationary numerical solutions obtained here correspond to time-converged results of Algorithm 1. Proposition 3.1 establishes the existence of multiple solutions for the stationary problem associated to the system (3.4)-(3.11). These multiple solutions are also found numerically by means of Algorithm 1 with $T = T_{\epsilon=0}$. To show this, a parameter $\beta^0 \in [0.5, 1]$ is fixed and the initial guess solution $(\mathbf{p}^0, \boldsymbol{\theta}^0)$ is defined as

$$p^0(x_1) = \begin{cases} 0 & \text{if } x_1/L < \beta^0 \\ p_{cc} & \text{if } x_1/L \geq \beta^0 \end{cases} \quad \text{and} \quad \theta^0(x_1) = \begin{cases} 1 & \text{if } x_1/L < \beta^0 \\ \frac{h(\beta^0)}{h(x_1)} & \text{if } x_1/L \geq \beta^0 \end{cases} \quad (3.51)$$

Notice that $p^0 = T(\theta^0)$. Taking $R_c = 64$ mm, $\beta^0 = 0.5, 0.7$ and 0.9 mm the resulting converged profiles for p and θ by means of Algorithm 1 are shown in Fig. 3.4.1 a), b) and c) respectively. The corresponding solutions for $T = T_{\epsilon=1}$ are also shown in Fig. 3.4.1 d), e) and f).

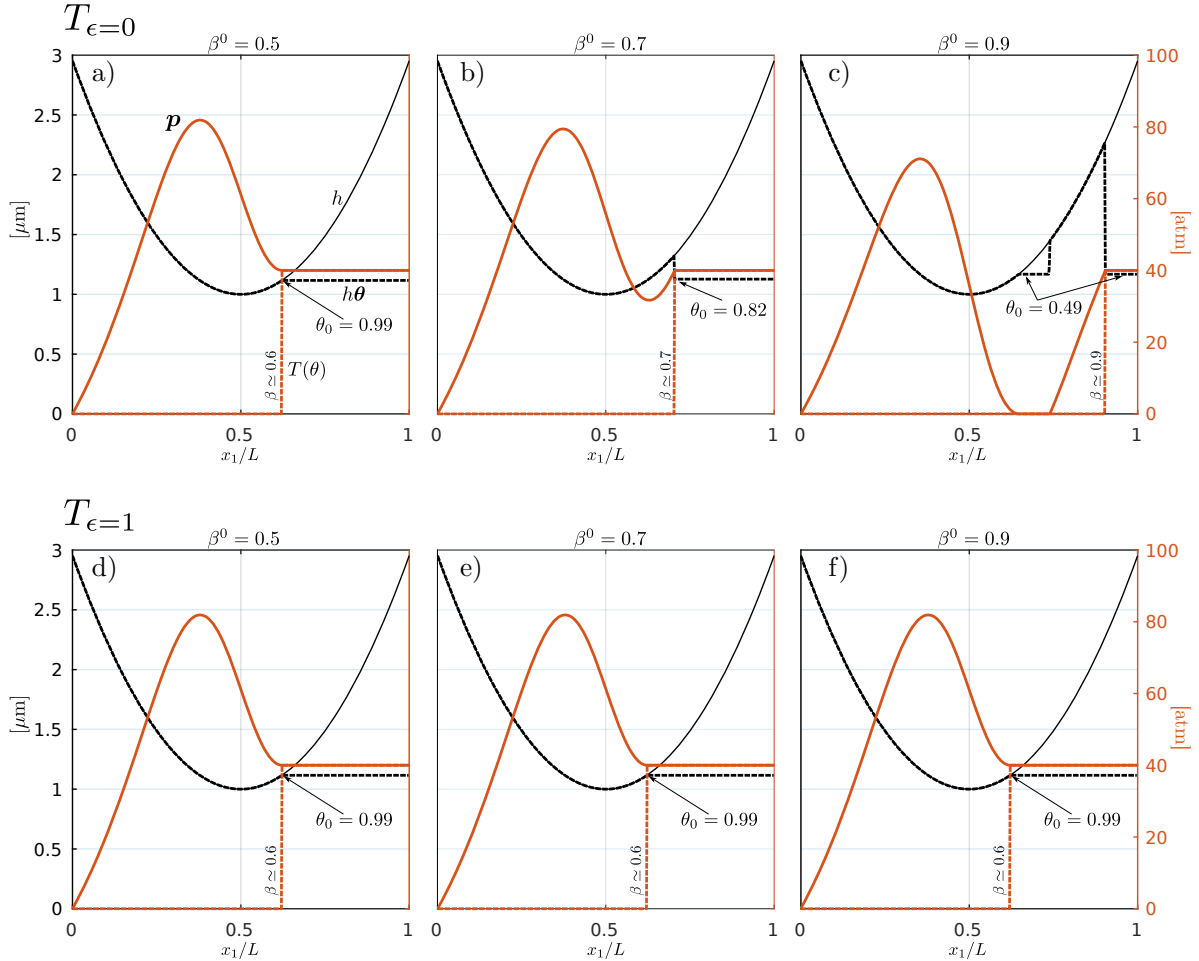


Figure 3.4.1 – Numerical results by means of Algorithm 1 and different initial solutions.

Regarding the results obtained setting $T = T_0$, for $\beta^0 = 0.5$ the resulting separation point is at $\beta \simeq 0.6$. The discrete derivative of p around $x_1 = \beta^-$ is approx. null and θ_0 is near to the unit. For $\beta^0 = 0.7$ the resulting separation point is at $\beta \simeq 0.7$. This time the pressure shows a clearly positive derivative and, compensating this positive gradient, one obtains $\theta_0 \simeq 0.82$. For $\beta^0 = 0.9$ a positive gradient is also observed at the separation point $\beta \simeq 0.9$, this time a cavitated region (where $p = 0$) is developed and $\theta_0 \simeq 0.49$. This existence of multiple discrete solutions is expected by the result obtained for the continuous problem in Proposition 3.1, where the existence of multiple solutions for the continuous problem is proved for this type of geometries. In that proposition, it is used the fact that the mass-conservation condition (3.2) does not restrict θ_0 to a unique value. Numerically, it is observed that setting $T = T_{\epsilon=1}$ instead of $T = T_{\epsilon=0}$ the discrete solutions $(\mathbf{p}^k, \boldsymbol{\theta}^k)$ converge to solutions where θ_0 converges to the unit (when refining the time and

space meshes) and the numerically computed gradient $\nabla p \cdot \mathbf{n}$ converges to zero at the rupture boundary. In that sense, we say that $T = T_{\epsilon=1}$ imposes a null-gradient condition.

3.4.1.2 A maximum value for p_{cc}

In Proposition 3.1 it was shown that for the particular case of a parabolic static 1D ring there exist a family of analytical solutions such that $\theta_0 = 1$. That function Λ has a unique maximum value Λ^* . It is worth noting that for h symmetric around $x_1 = L/2$ then $\Lambda^* = \Lambda(L/2)$. This is also observed numerically (see Fig. 3.4.2), Algorithm 1 along $T = T_{\epsilon=1}$ fails to converge to a solution for the initial time $t = 0$ when $p_{cc} > \Lambda^*$. The physical interpretation of this is that there exists a value $\Lambda^* > 0$ such that the mass flux on the domain Ω is reversed (going from the Combustion Chamber to the crankcase) when $p_{cc} > \Lambda^*$, which is a non desirable phenomenon. The prediction of this reversing flux is also made in Section 3.4.2.2 for more complex cases (transient cases with a 2D geometry).

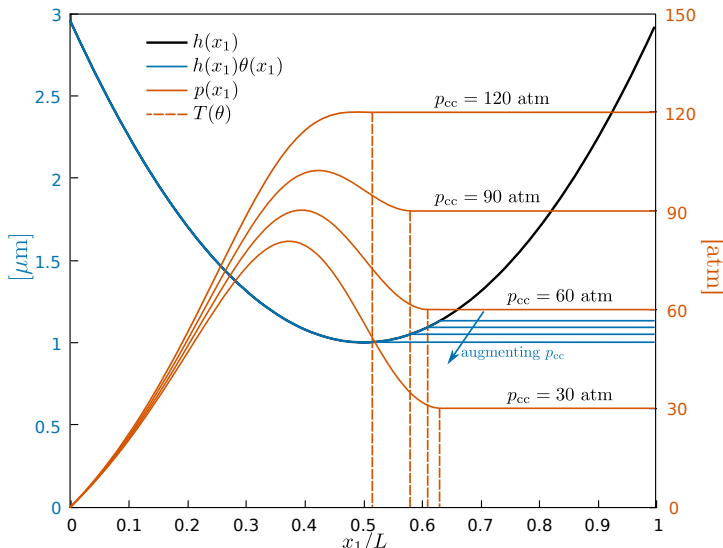


Figure 3.4.2 – Numerical results by means of Algorithm 1 with $\bar{U} > 0$, $R_c = 64$ mm, $T = T_{\epsilon=1}$, $\beta^0 = 0.9$ and different values of $p_{cc} < \Lambda^* \approx 120$ [atm].

In the previous case the lower surface motion is developed to the right, and so the separation point (which depends on p_{cc}) corresponds to a rupture point. Changing the relative speed \bar{U} from 10 m/s to -10 m/s one can repeat the same process to look for a maximum value of p_{cc} but this time β being a reformation point. This is shown in Fig. 3.4.3 for a film thickness equal to $1.25 \mu\text{m}$ at the inlet ($x_1/L = 1$). For these cases it can be noticed that for $p_{cc} = 30$ and 60 atm the fluid accumulates at the right side of β reaching then a full-film condition, thus $\beta/L = 1$ in the stationary regime. On the other hand for $p_{cc} \geq 90$ atm $\beta < 1$ mm in the stationary regimes and the pressure profiles coincide on the region $0 < x_1 < \beta$. The reformation point (for the stationary regime) moves to the left while augmenting p_{cc} and when $p(\beta)$ reaches a local maximum Algorithm 1 fails to converge.

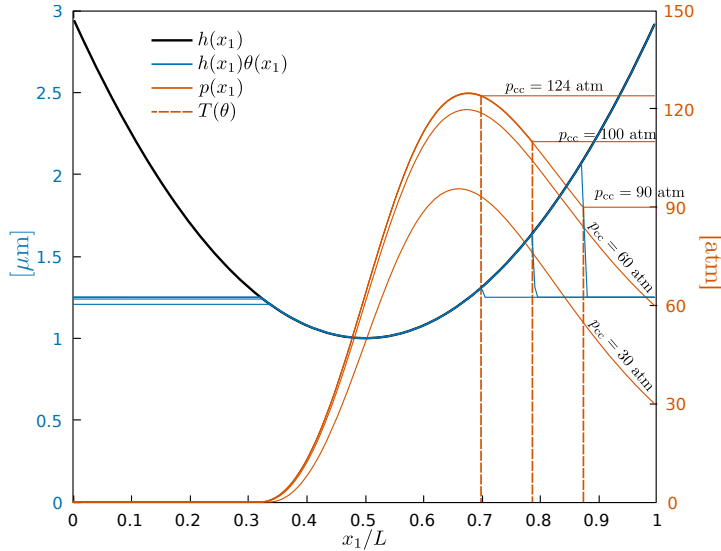


Figure 3.4.3 – Numerical results by means of Algorithm 1 with $\bar{U} < 0$, $R_c = 64$ mm, $T = T_{\epsilon=1}$, $\beta^0 = 0.9$ and different values of $p_{cc} < \Lambda^* \approx 125$ [atm].

Remark 3.3. From the observed in these last results, here the condition $\frac{\partial^2 p}{\partial x_1^2} \leq 0$ is proposed as a blow-by prediction condition for rupture points while the condition $\frac{\partial p}{\partial x_1} = 0$ is proposed for reformation points. These conditions are tested in the examples shown in Section 3.4.2.2: “Rings with a non-uniform wear”.

3.4.2 Transient cases along Algorithm 1

3.4.2.1 One-dimensional cases

A single ring

There results of a simulation for a single compression ring moving towards the combustion chamber at constant speed are presented (see Section 2.4.2). A fast variation of the combustion chamber pressure p_{cc} is modeled as the Gaussian pulse

$$p_{cc}(t) = A_{cc} \cdot \exp\left(-\frac{1}{2} \frac{(t - t_e)^2}{a^2}\right). \quad (3.52)$$

When modeling the Piston-Ring-Liner, few works have considered the effects that the time dependence of p_{cc} can have on the dynamics of that system. In the last years, the group of Morris et al. published two works where this variable is taken into account and the effects of disregarding it are discussed (MORRIS *et al.*, 2014; MORRIS *et al.*, 2015). However, in their works a non-conservative model was considered. Here it is presented an analysis similar to those performed by Morris' group but by means of the mass-conserving Algorithm 1 with $T = T_{\epsilon=1}$.

The parameters setting is given in Table 3. The Newton's equation for the ring reads

| Symbol | Value | Units | Description |
|----------------------|---------------------|---------------|--------------------------------|
| μ_ℓ | 4×10^{-3} | Pa·s | Lubricant viscosity |
| \bar{U} | 10 | m/s | Lower surface speed (liner) |
| L | 1 | mm | Domain length along x_1 |
| h_{left} | 3 | μm | Oil feeding condition |
| R_c | 64 | mm | Ring's curvature |
| M_R | 48×10^{-3} | kg/m | Ring's mass per length unit |
| W^{ps} | -40 | N/m | Ring's constant load |
| A_{cc} | 0-100 | Pa | Explosion amplitude |
| t_e | 0.015 | s | Explosion time |
| a | 0.0025 | s | Explosion time width parameter |
| γ_{cc} | 0.9 | - | Back-pressure factor |

Table 3 – Default parameters.

$$M_R \frac{d^2 Z}{dt^2} = W^h + W^{\text{ps}} + W^{\text{cc}}, \quad (3.53)$$

where

$$W^h = \int_0^L p(x_1, t) dx_1, \quad W^{\text{cc}} = -\gamma_{\text{cc}} p_{\text{cc}} L.$$

W^{ps} is the elastic response of the ring due to the deformation needed to fit it into its place. The term W^{cc} models the load on the ring due to the gas pressure on its back. This pressure is transmitted to the ring' back through the gap between the ring and the piston as depicted in Fig. 3.4.4. Equation (3.53) is solved by means of a Newmark' scheme.

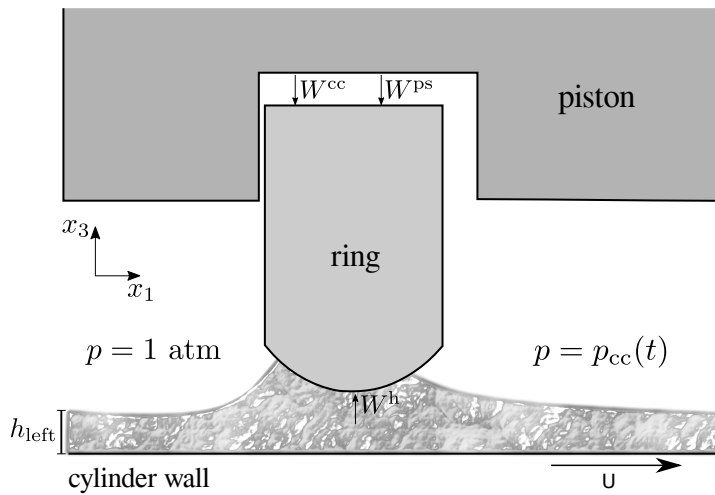


Figure 3.4.4 – Physical setting for the free single ring simulation.

The time averaged friction force per unit width, oppose to the movement of the ring along the x_1 -axis, is computed according to (CHECO *et al.*, 2016)

$$f = \frac{1}{T} \int_0^T \frac{1}{B} \int_0^L \left(-p \frac{\partial h_U}{\partial x_1} - \frac{h}{2} \frac{\partial p}{\partial x_1} - \frac{\bar{U}}{h} \right) dx_1 dt, \quad (3.54)$$

where h_U denotes the upper surface function. The ring's position in time, $Z(t)$, is shown in Fig. 3.4.5 for several explosion amplitudes A_{cc} . The results taking $T = 0$ in Algorithm 1 are also shown (corresponding to the Elrod-Adams model). Notice that for all the cases the ring reaches rapidly a stationary position around $Z \approx 2.8 \mu\text{m}$ returning to it after the explosion. It is observed that $p_{cc} = 0$ a minimum clearance $\approx 44\%$ smaller than the predicted by its extended model, which leads to a difference of $\approx 50\%$ in the time averaged friction force relative to the one computed with the extended model ($T = T_{\epsilon=1}$). This happens due to a higher hydrodynamic force (W^h) and due to a proper accommodation of the combustion chamber pressure at the rupture boundary when setting $T = T_{\epsilon=1}$.

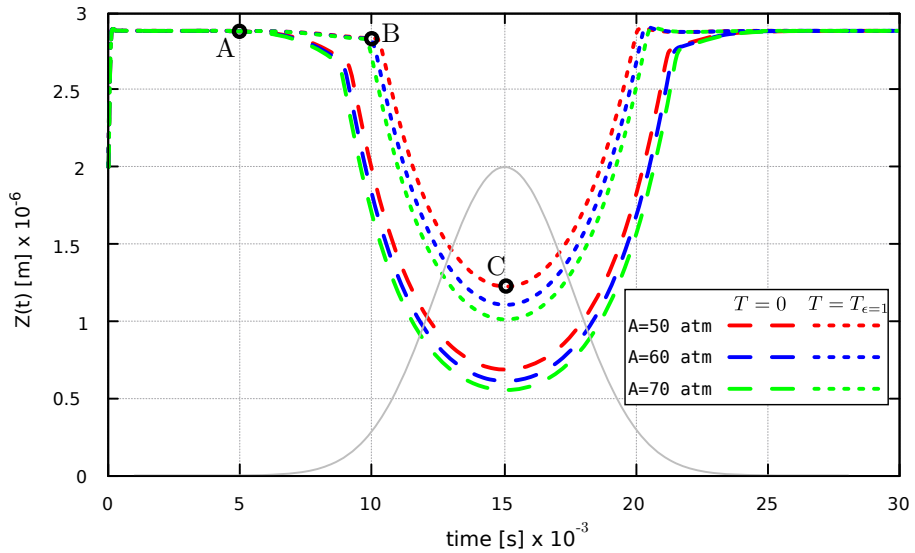


Figure 3.4.5 – Ring position for different cavitation models. $T = 0$ represents the results of the Elrod-Adams model. $T = T_{\epsilon=1}$ are the results when accomodating $p = p_{cc}(t)$ at the rupture boundary. The gray continuous line shows the normalized shape of $p_{cc}(t)$. The three times denoted by A, B and C (for $A_{cc} = 50$ atm) are detailed in Fig. 3.4.6.

Focusing on the results for $T = T_{\epsilon=1}$, one can notice from Fig. 3.4.5 that between $t = 5 \times 10^{-3}$ s and $t = 10 \times 10^{-3}$ s there is a slight change on the ring's position $Z(t)$ for the three values of A_{cc} considered. After that, a fast decrease in $Z(t)$ is observed. This change in the vertical speed of the ring has an interesting explanation. Let us recall that, since W^{cc} is directly proportional to p_{cc} and W^{ps} is constant, the load applied on the ring $W^a = W^{ps} + W^{cc}$ increases monotonically with p_{cc} . For $t < 10$ ms, this increase on the applied load is mainly compensated with an accumulation of fluid at the left side of the ring (without much change in $Z(t)$), i.e., the reformation point moves to the left. At $t \simeq 10$ ms the left side of the domain is fulfilled and the augmentation of the applied load is now compensated by a falling of the ring, an example of this is shown in Fig. 3.4.6 for the case $A_{cc} = 50$ atm of Fig. 3.4.5. As it can be observed, the oil-feeding condition is set to $h_{left} = 3 \mu\text{m}$.

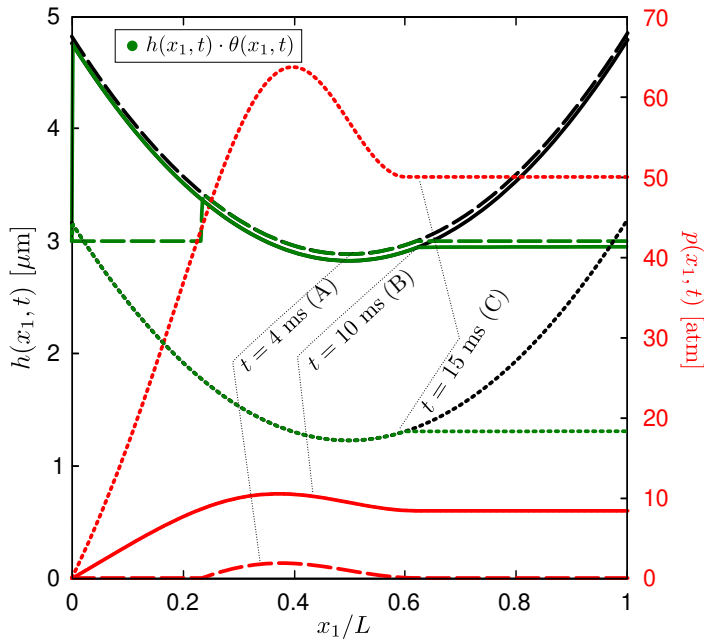


Figure 3.4.6 – Pressure field, saturation field and ring profile in time for the one-dimensional example of a short explosion model for $p_{cc}(t)$. These details correspond to three times (A, B and C) of the ring’s evolution showed in Fig. 3.4.5.

3.4.2.2 Two-dimensional cases

A single ring with textures

Here the 1D case presented in the previous section is modified to a 2D setting such that the boundary $\partial\Omega_0^r = \overline{\{T(\theta) = p_{cc}\}} \cap \overline{\{T(\theta) = 0\}}$ is non trivial. Moreover, that boundary evolves in response to the time variation of $p_{cc}(t)$ and $Z(t)$. The domain’s width is set to $B = 0.1$ mm. A 2D analytical texture is included on the ring’s profile, reading

$$h(x_1, x_2, t) = Z(t) + \frac{(x_1 - L/2)^2}{2R_c} + h_T(x_1, x_2) .$$

The function h_T corresponds to a set of ellipsoidal pockets with a depth of 1 μm , the details of it are shown in Fig. 3.4.7.

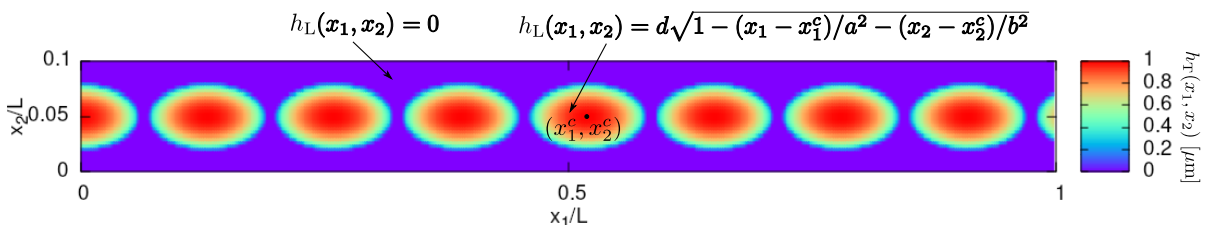


Figure 3.4.7 – Texture function h_T composed by ellipsoidal dimples, its depth (d) is equal to 1 μm .

Time is discretized by setting the Courant number $\eta = \frac{\bar{U}}{2} \frac{\Delta t}{\Delta x_1}$ equal to the unit. Space is discretized by setting $\Delta x_1 = L/512$ and $\Delta x_2 = B/32$.

The piston ring responded in a similar way to the 1D cases: the augment of W^{cc} is first mainly compensated by accumulating fluid at the left side of the ring and then, once the left side of the domain is fully-flooded, the compensation is obtained by a reduction of the distance between the surfaces.

Figure 3.4.8 shows the saturation field at several times along the corresponding value of $p_{cc}(t)$ and $Z(t)$ for $A_{cc} = 100$ atm. The contour lines $\theta = 1$ are also depicted. It is worth noting that these contour lines change in time. Additionally, there appears a full-film region ($\theta = 1$) for which the pressure is equal to $p_{cc}(t)$ at its boundary. This small region (denoted Ω_*^+) shrinks around $t \simeq 0.15$ s and expands again after the explosion, recovering the size and shape it had around $t \simeq 0.03$ s (compare the saturation field for $t = 0.03$ s and $t = 0.27$ s). In the lower part of Fig. 3.4.8 $\partial\Omega_0^r$ and $\partial\Omega_*^+$ are shown for different values of the explosion amplitude A_{cc} . Notice that when A_{cc} is augmented $\partial\Omega_*^+$ moves towards the ring's center ($x_1 = 0.5$ mm). The corresponding pressure fields are shown in Fig. 3.4.9 for the $t = 15 \times 10^{-3}$ s (the time for which $p_{cc}(t) = A_{cc}$).

These are the first simulations where the combustion chamber pressure is taken into account along a mass-conserving modeling of the oil flow for the Piston-Ring-Liner system. Among other type of numerical analyses possibles to be performed (e.g., energy loses dependence on geometrical parameters), in the next examples it is shown that these type of simulations can be used to predict a *reverse flow*, i.e., the flux of oil/gas from the combustion chamber to the space between the ring or to the crankshaft.

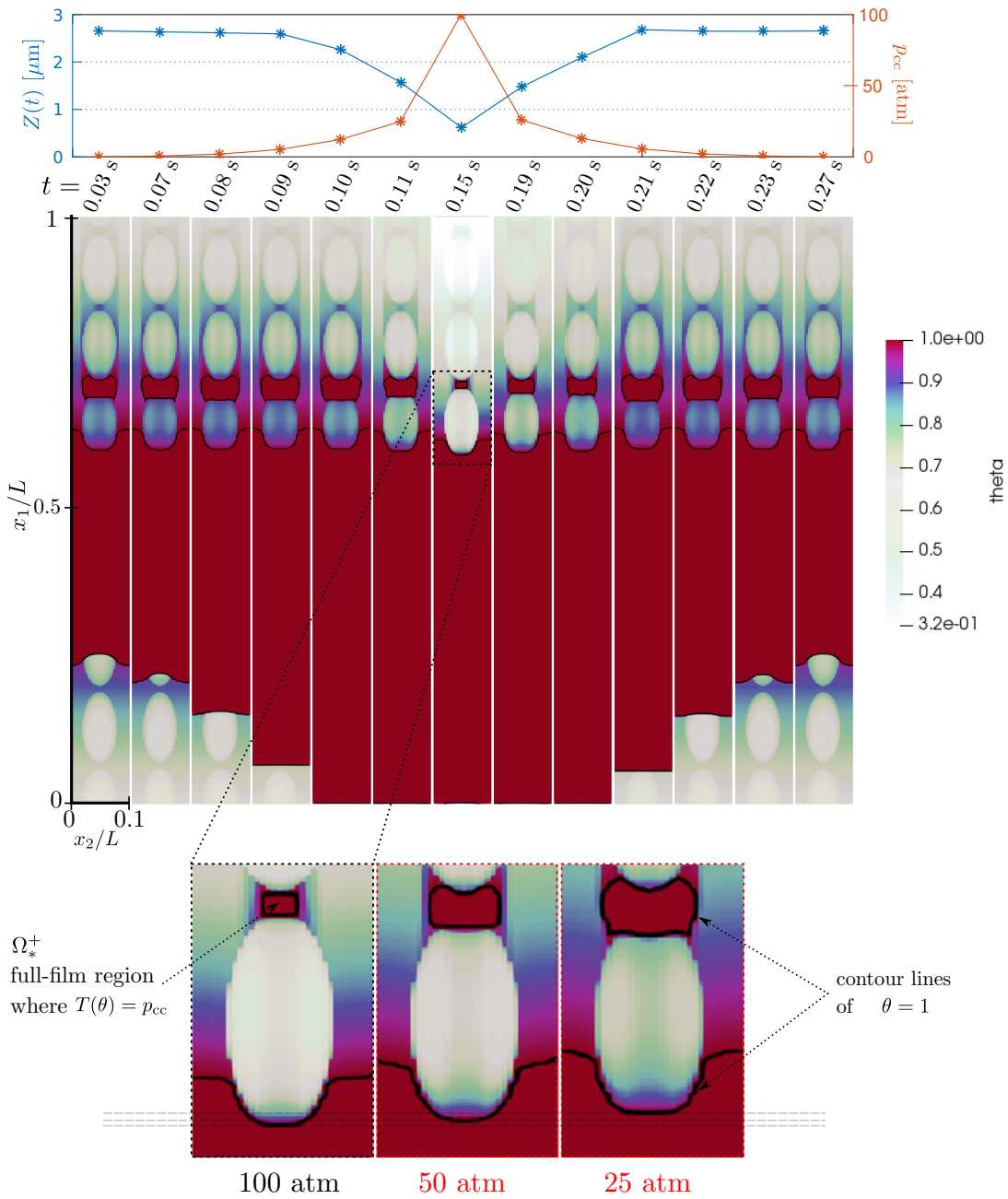


Figure 3.4.8 – From top to bottom: Gaussian pulse modeling $p_{cc}(t)$; saturation field for a 2D free textured ring; details around Ω_*^+ for different amplitudes A_{cc} .

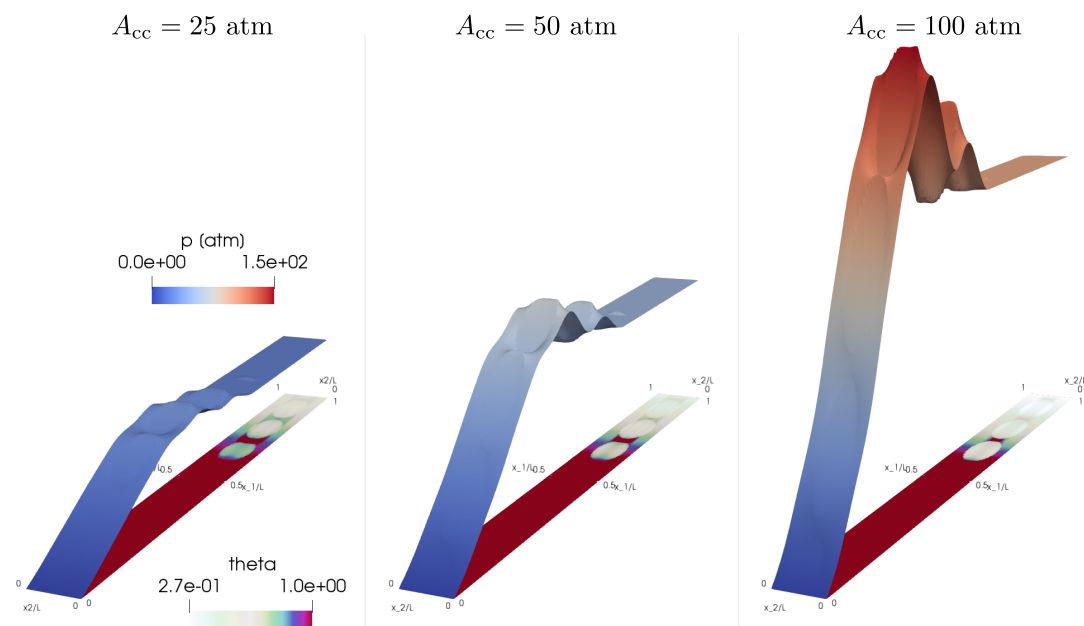


Figure 3.4.9 – Pressure fields (surfaces) and saturation fields (on the $x_1 - x_2$ plane) at for different explosion amplitudes at $t = t_e$.

Reversing flow

For the simple one-dimensional case regarded in Proposition 3.1 one has that there exists a maximum value Λ^* of p_{cc} for which an analytical stationary solution can be found. This was also observed numerically in Section 3.4.1.2, as for $p_{cc} > \Lambda^*$ the Algorithm 1 fails to converge. This loss of existence is here interpreted as a reverse flow that is out of the physical configurations that our modeling is able to reproduce.

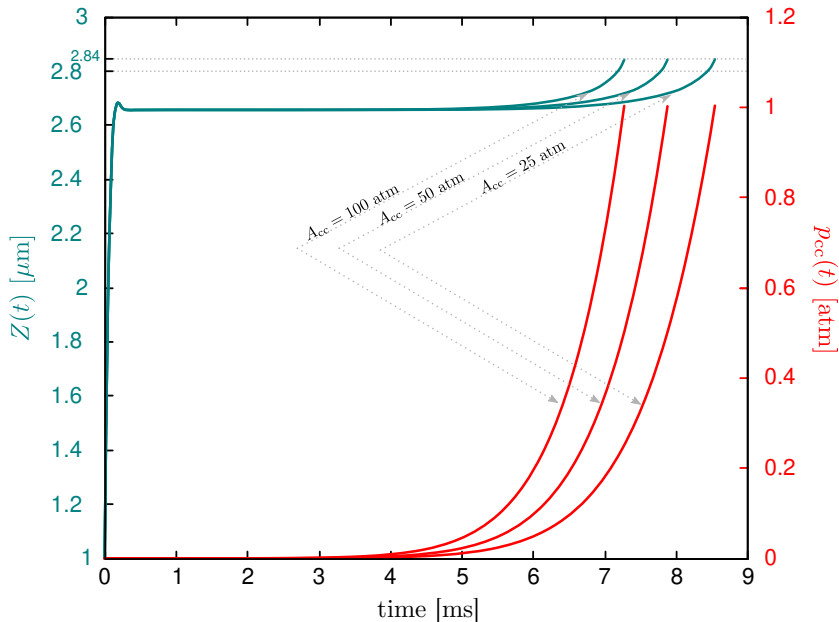


Figure 3.4.10 – Evolution of $Z(t)$ for $A_{cc} = 25, 50$ and 100 atm. In this case $\gamma_{cc} = 0.1$.

Focusing on the transient regime, in the previous example the force W^{cc} was relevant in order to prevent that reverse flux. To show this, here those simulations are repeated but this time changing the back-pressure factor γ_{cc} from 0.9 to 0.1. The same three values for A_{cc} where tested: 25, 50 and 100 atm. For each one of the simulations it is observed that when p_{cc} begins to rise the ring augments its distance to the liner, instead of diminishing it as in the previous examples. The numerical simulation is stopped when Algorithm 1 fails to converge to a solution for the discrete fields \mathbf{p} and $\boldsymbol{\theta}$ at a certain discrete time t^M , which happened for the whole range of A_{cc} explored.

The evolution of $Z(t)$ in response to $p_{cc}(t)$ is shown in Fig. 3.4.10. Notice that all the simulations ended when $p_{cc}(t) \approx 1$ atm and $Z(t) \approx 2.84 \mu\text{m}$. More details into this are given by showing the pressure and saturation fields for $A_{cc} = 100$ atm at $t = 2.0, 7.0$ and 7.3 ms (where the simulation stops) in Fig. 3.4.11. In the left side of that figure the surfaces are colored according to the local value of \mathbf{p} , while at the left side they are colored according to: red for the region $\{\theta < 1\}$, and blue for the region $\{\theta = 1\}$. It can be observed that just before the end of the simulation the pressure field at the very left side of $\partial\Omega_0^r$ tends to reach $p_{cc}(t)$. Notice that in the one-dimensional examples shown in

Fig. 3.4.2 the pressure profile for which $p_{cc} = 118$ atm ($\simeq \Lambda^*$, the maximum value for p_{cc}) exhibits a similar configuration. Thus, roughly speaking, it is observed that Algorithm 1 fails to converge to a solution since it does not reach a solution that accomplishes the null-gradient condition at the pressurized side of $\partial\Omega_0^r$, and this can be interpreted as a reverse flow when imposing that condition on the gradient (by means of the operator $T = T_\epsilon$). In the next example, it is shown that this issue is also found when including textures in the moving surface.

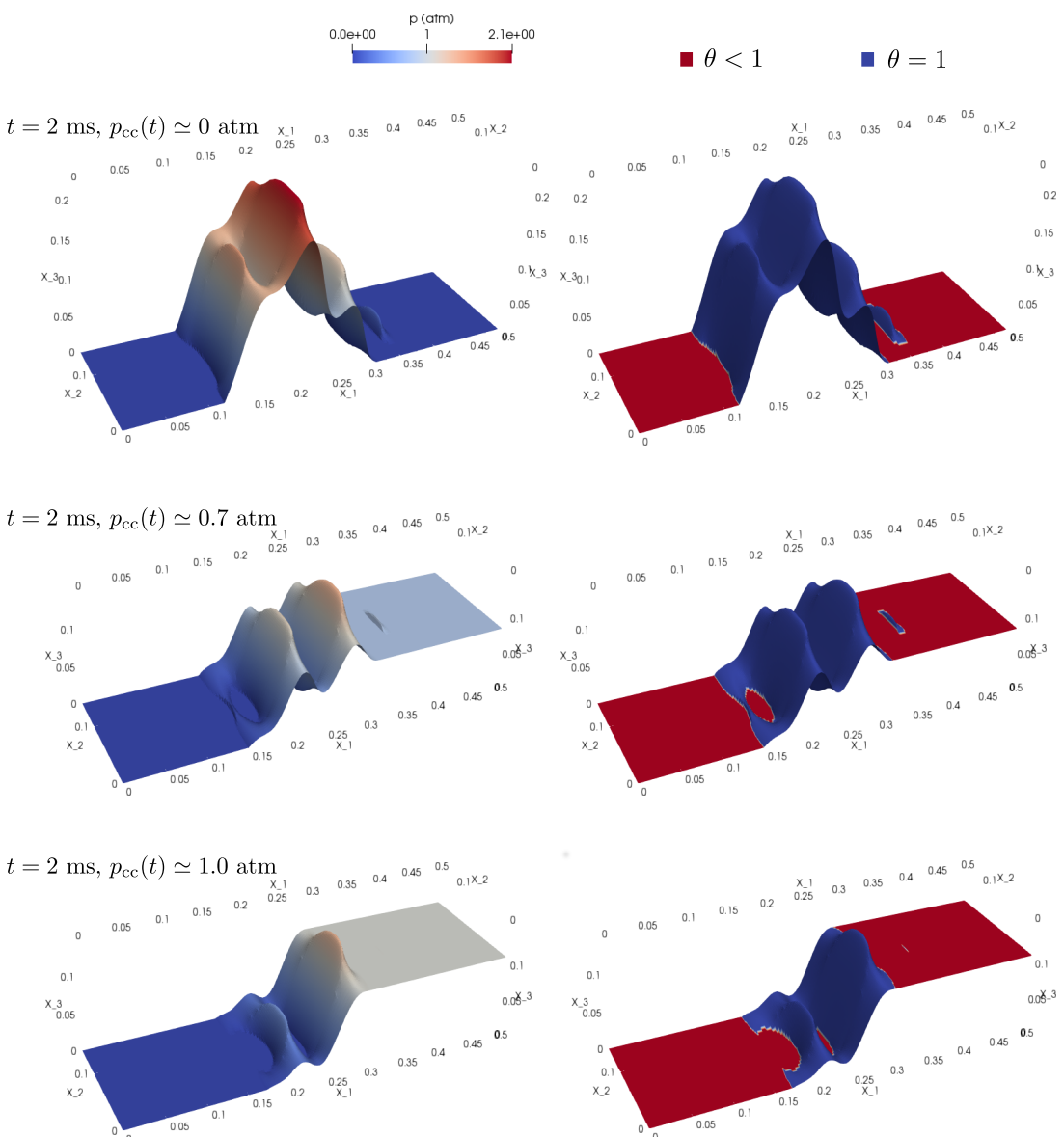


Figure 3.4.11 – Pressure fields (left column) and pressurized regions details (right column) for some time steps of a free textured ring with $\gamma_{cc} = 0.1$. Immediately after $t = 7.28$ ms Algorithm 1 fails to converge.

A moving texture

Here the upper surface corresponds to a smooth ring (without textures) that is fixed, i.e., $Z(t)$ is constant in time and equal to $1 \mu\text{m}$. At the initial time ($t = 0$) the system is in a stationary state. Just after that instant a single pocket tailored in the lower surface enters the domain, lowering the pressure build-up. In the two following cases Algorithm 1 gives a solution to \mathbf{p} and $\boldsymbol{\theta}$ for the first time steps, failing to converge at a certain time at which the pocket has not yet exited the domain.

In the first case the elliptical pocket has a depth of $12 \mu\text{m}$ ($d = 12 \mu\text{m}$ in Fig. 3.4.7). The pressure surface, traveling pocket and *cavitated* areas (where $\mathbf{p} = T(\boldsymbol{\theta})$) are shown for three time-steps in Fig. 3.4.12. In this case the pocket generates a moving cavitated region where $p = 0$, this region advances accompanying the movement of the pocket. At $t \simeq 2.58 \times 10^{-5} \text{ s}$ the pressure field around the boundary $\partial\Omega_0^r$ has a configuration analog to the one observed previously when Algorithm 1 failed to converge (e.g., 3.4.11). This is, the pressure at the left side of $\partial\Omega_0^r$ *tends* to be lower or equal to the pressure at the right side (where $\mathbf{p} = T(\boldsymbol{\theta}) = p_{cc}(t)$). At the next time step no numerical solution is reached by means of Algorithm 1.

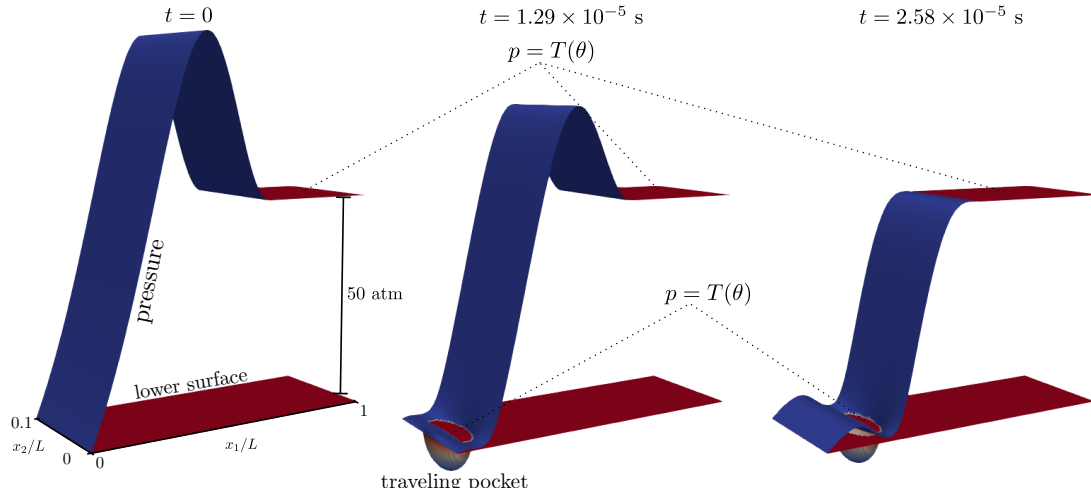


Figure 3.4.12 – Time steps along Algorithm 1 for a traveling pocket with depth equal to $12 \mu\text{m}$. A cavitated area travels accompanying the pocket. No solution for $(\mathbf{p}, \boldsymbol{\theta})$ is obtained after $t = 2.58 \times 10^{-5} \text{ s}$.

The second case corresponds to a pocket with a depth lower than in the first case and equal to $8 \mu\text{m}$. Three time steps of that simulation are shown in Fig. 3.4.13. Notice that for this case the pocket does not generate cavitation, the pressure field is instead positive in the region where the pocket passes. However, as the pocket moves, a region $\{p < p_{cc}\}$ appears near to $\partial\Omega_0^r$ (see the upper detailed frames of Fig. 3.4.13). Around $t = 6.02 \times 10^{-5} \text{ s}$ the distance between both regions becomes of the order of the mesh size and the pressure field *tends* to have a positive gradient at the left side of $\partial\Omega_0^r$, after that time step Algorithm 1 fails to provide a solution. It is noteworthy that this issue is

observed even for pockets with a depth as small as $0.5 \mu\text{m}$. A partial solution for this issue is explored in the next Section, where Algorithm 2 is used to allow a non-null gradient condition for pressure at the rupture point by means of the mass-conserving condition (3.2).

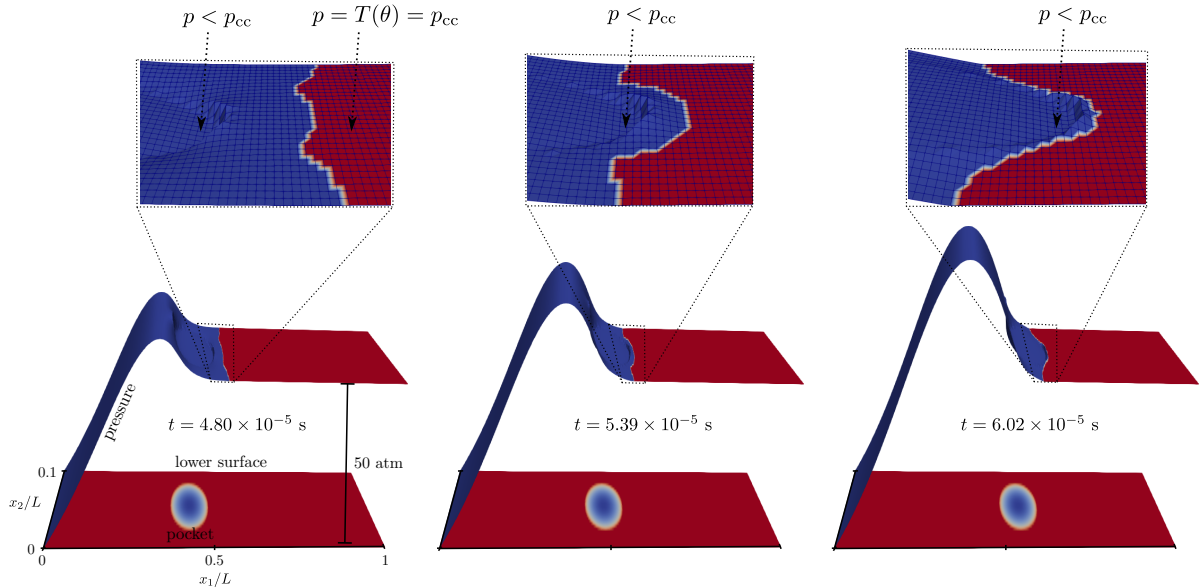


Figure 3.4.13 – Time steps along Algorithm 1 for a traveling pocket with a depth equal to $8 \mu\text{m}$. A cavitated area travels accompanying the pocket. No solution for $(\mathbf{p}, \boldsymbol{\theta})$ is obtained after $t = 6.02 \times 10^{-5} \text{ s}$.

Rings with a non-uniform wear

The compression ring can suffer from wear in the order of $10 \mu\text{m}$ just after some hundred hours of running (PRIEST; DOWSON; M., 1999). In this example it is shown that for a typical non-uniform wear profile (taken from (CHENG *et al.*, 2016)) blow-by can be predicted based in the condition proposed in Section 3.4.1.2.

In these examples both the surfaces of the ring and the liner are considered to be smooth (no surface roughness). The gap between the surfaces is modeled by the function

$$h(x_1, x_2, t) = Z(t) + \frac{(x_1 - L/2)^2}{2R_c} + h_{\text{wear}}^\delta(x_2), \quad (3.55)$$

where Z is the dynamic variable counting for the expansion/compression of the ring, and h_{wear}^δ is a function modeling a non-homogeneous wear of the ring surface along the transverse direction (see Fig. 3.4.14) that satisfies $\min_{x_2 \in [0, 2\pi B_r]} h_{\text{wear}}^\delta(x_2) = 0$, and is written as a Gaussian function that reads

$$h_{\text{wear}}^\delta(x_2) = \delta \exp\left(-(x_2 - \pi B_r)^2/c^2\right) \quad x_2 \in [0, 2\pi B_r], \quad (3.56)$$

where $B_r = 4.2 \times 10^{-2} \text{ m}$ corresponds to the bore radius (see Fig. 2.4.2) so the domain width is equal to $B = 2\pi B_r$ and $c = 2.44 \times 10^{-4} \text{ m}$ is set such that the wear width is

$\approx \frac{70}{360} \times 2\pi B_r$ (or 70 degrees). For these cases the ring dynamics is also given by Eq. (3.53) and the parameters values set in Table 3 (excepting R_c which will be specified). Based on a convergence analysis the cells size is set such that $\Delta x_1 = 1/200$ and $\Delta x_2 = 2\pi B_r/40$, and the Courant number is set to $\eta = 1$ during almost all the simulation. The film thickness at the fluid entrance is set to $1.5 \mu\text{m}$. The ring' speed and the normalized variation of $p_{cc}(t)$ are shown in Fig. 3.4.15. Some convergence issues related to the high value $p_{cc}(t)$ and the lower speed of the ring at the half of the cycle were overcome by setting the Courant number to 0.05 for $286 < t < 314$ ms.

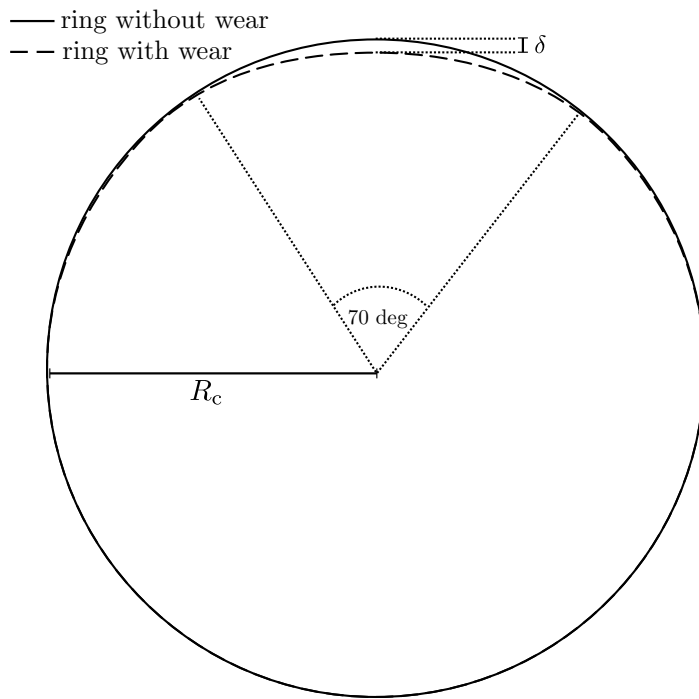


Figure 3.4.14 – Scheme of a ring with a non-uniform wear along the circumferential direction.

Set first the ring curvature to $R_c = 64$ mm and the wear amplitude to $\delta = 0.04 \mu\text{m}$. Five time instants are fixed as indicated in Fig. 3.4.15 and the corresponding pressure and saturation fields are shown in Fig. 3.4.16. Firstly, notice that for all the times selected the region $\{\theta = 1\}$ divide the domain into two subdomains and that around the point $(x_1, x_2) = (0.5, \pi B_r)$ the fluid is tinier due to the wear set on the ring.

Setting now $\delta = 0.05 \mu\text{m}$ for the same ring curvature ($R_c = 64$ mm), one observes that as t tends to $t = 185$ ms a small channel with $\theta < 1$ begins to form. After $t = 185$ ms the simulations does not end as Algorithm 1 fails to converge. At that simulation time, the CCP is equal to 0.06 atm and the proposed model loses validity since there is an encounter of the region where $p = 0$ and $p = p_{cc}$. When the ring curvature is augmented to $R_c = 32$ mm the same type of channel takes place even for $\delta = 0.01 \mu\text{m}$. While for $R_c = 128$ mm that phenomenon takes place for $\delta = 0.04 \mu\text{m}$. It is worth mentioning that

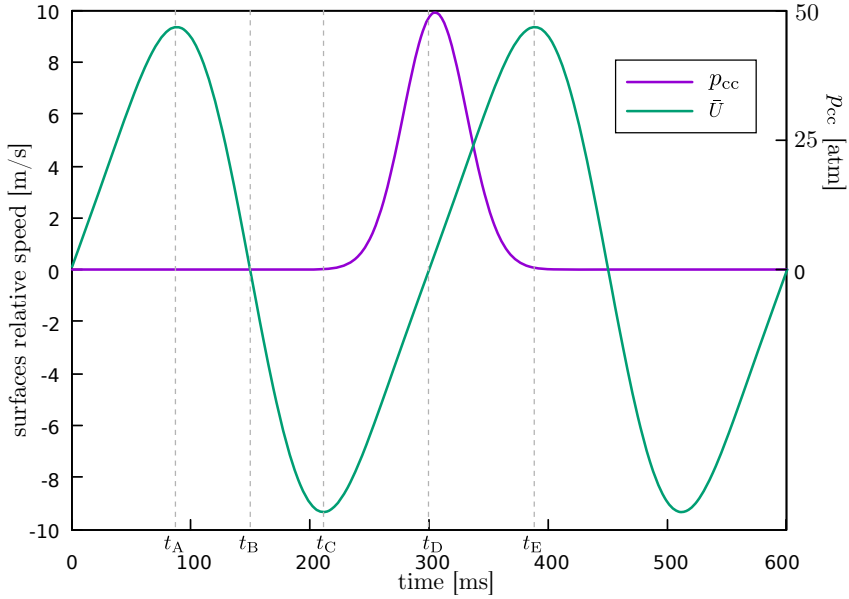


Figure 3.4.15 – Surfaces relative speed along the x_1 axis and combustion chamber pressure $p_{cc}(t)$.

for $\delta = 0$ the simulations are completed and no blow-by is observed for the three values of R_c here considered. Next, let us explore a way of predicting blow-by during a simulation.

Numerically the blow-by conditions proposed in Section 3.4.1.2 can be hard to implement due to mesh-related issues. However, to overcome these problems, one may use the *equivalent* discrete condition

$$d(\Omega_0^r, \{p < p_{cc}\}) \leq \max\{\epsilon_b L, N_b \Delta x_1\} \quad \text{and} \quad p_{cc} > 0, \quad (3.57)$$

where $d(\Omega_0^r, \{p < p_{cc}\})$ denotes the distance between the set Ω_0^r (where $p = p_{cc}$) and the set $\{p < p_{cc}\}$. Here $\epsilon_b = 1/50 = 0.02$ and $N_b = 4$ (for the cases tested here $\epsilon_b L > N_b \Delta x_1$). A convergence analysis where the CFL number was fixed to the unit showed that for the mesh sizes and time step considered here $d(\Omega_0^r, \{p < p_{cc}\})$ becomes mesh-independent as a function of time.

To test the condition (3.57) as being useful to predict blow-by, a series of simulations are performed for several values of R_c and δ . Doing so, it is observed that for each R_c there exists a value of δ , here denoted by δ^{\max} , for which the simulation fails at a certain time step before the whole cycle is completed, and the same is observed for every $\delta \geq \delta^{\max}$, while for $\delta < \delta^{\max}$ the simulation is completed. These results on δ_{\max} are summarized in Table 4. It is worth noticing that δ_{\max} is maximum (as a function of R_c) for R_c around 50 mm, which corresponds to typical values for the compression rings' curvatures (GADESCHI; BACKHAUS; KNOLL, 2012). The time-step at which the simulations fail varies with R_c and δ . In general, for $R_c \geq 32$ mm all the failures take place at $t \approx 300$ ms, where p_{cc} is maximum, while for $R_c < 32$ mm the time at which the simulations fail diminishes and the value of p_{cc} at that instant is much lower. In addition, Figure 3.4.18 shows $d(\Omega_0^r, \{p < p_{cc}\})$ for different configurations. For the ones where the simulation failed, it is observed that the

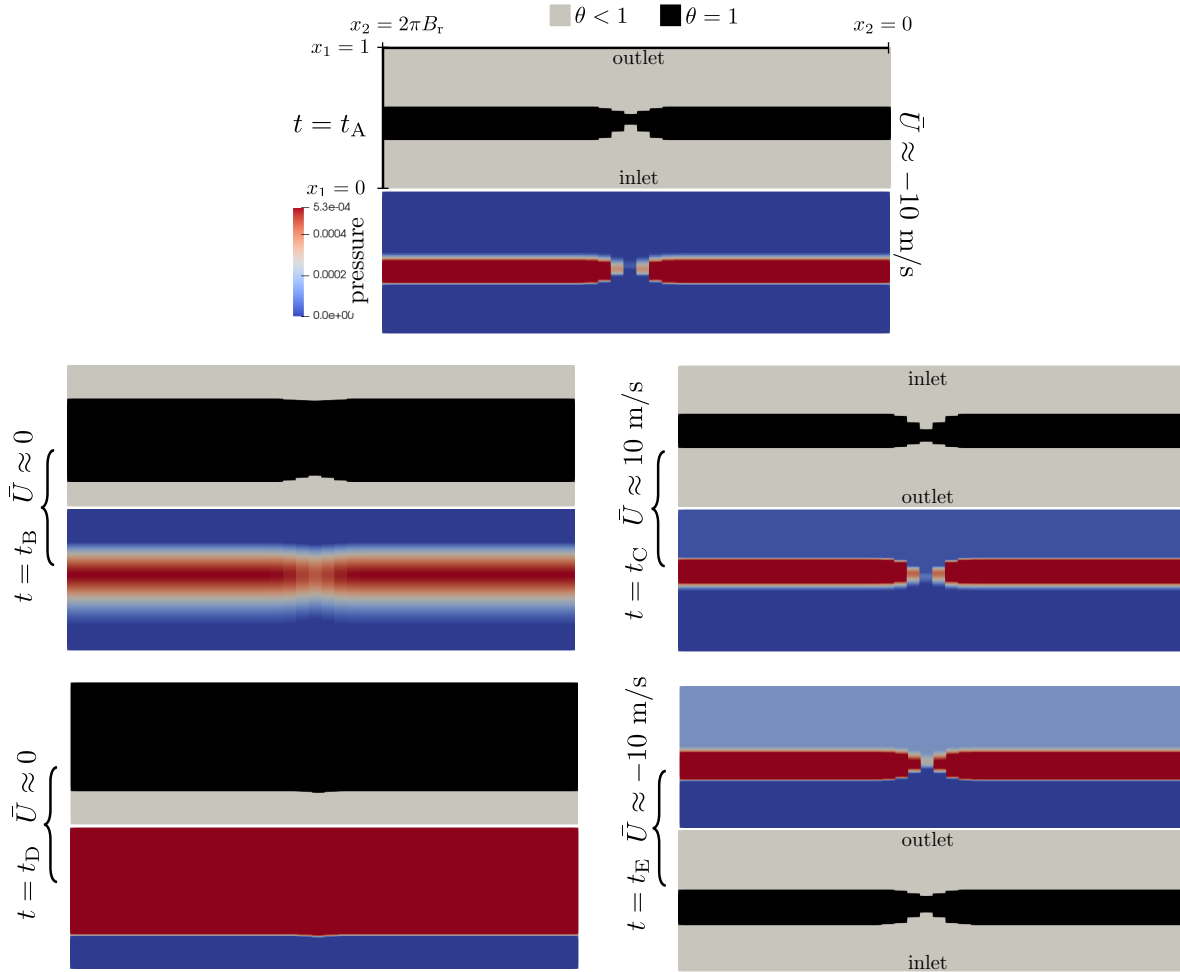


Figure 3.4.16 – Fields p and θ in time for a smooth ring with $R = 64 \text{ mm}$ and $\delta = 0.04 \mu\text{m}$.

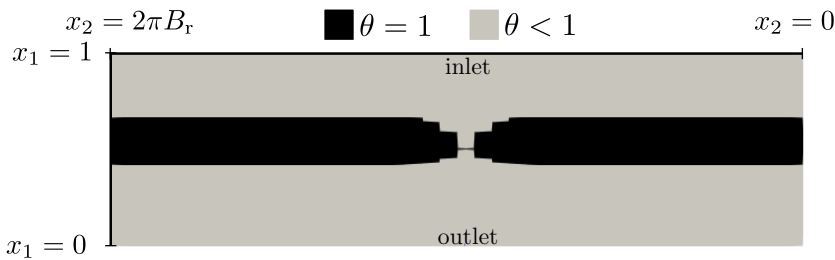


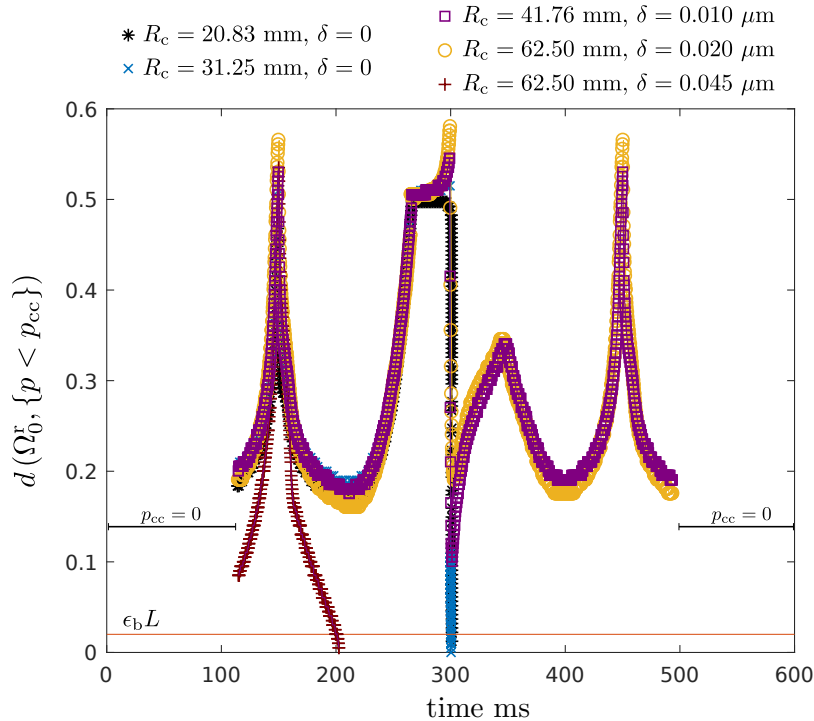
Figure 3.4.17 – Field θ in at $t = 185 \text{ ms}$ for $R = 64 \text{ mm}$ and $\delta = 0.05 \mu\text{m}$.

condition (3.57) is accomplished some time steps before the end of the simulation, while for the case where the whole cycle is completed the condition (3.57) is not accomplished during the while simulation.

3.4.3 Transient cases along Algorithm 2

Let us recall that Algorithm 2 is based in a Finite Volume Method where the Rankine-Hugoniot condition (3.2) is used to update the common interface of the cells

| | R_c [mm] | | | | | | | | |
|-----------------------------------|------------|-------|-------|-------|-------|-------|-------|-------|------------|
| | 250 | 125 | 83.3 | 62.5 | 50 | 41.7 | 35.7 | 32.0 | 31.25-15.6 |
| δ_{\max} [μm] | 0.025 | 0.035 | 0.040 | 0.045 | 0.050 | 0.055 | 0.025 | 0.005 | 0 |

Table 4 – Minimum value of δ for which the simulations fail for every $\delta \geq \delta_{\max}$.Figure 3.4.18 – Distance between the sets Ω_0^r and $\{p < p_{cc}\}$ for different configurations where. Blow-by is observed when $d(\Omega_0^r, \{p < p_{cc}\}) < \epsilon_b L$.

placed at the left and right sides of the rupture point β (see Section 3.3.1). The value $\theta_0 = 2/3$ is fixed based in a reverse flow condition and the experimental findings by [Coyne and Elrod \(1971\)](#). In this section some numerical results along this approach are shown, and some of its limitations are also discussed.

3.4.3.1 Semi-analytical solutions

In this section Algorithm 2 is tested by comparing its results to an analytic solution. For this, the lower surface is set to be smooth and flat and the upper surface to be a smooth fixed ring. An initial condition for $\boldsymbol{\theta}$ is defined depending on the initial position (β_0) of the rupture point (β). Recall that Δx_1 denotes the length of the Finite Volumes cells, and set β_0 as some point in the interval $[L/2, L]$ that accomplishes $i_0 \Delta x_1 < \beta_0 < (i_0 + 1) \Delta x_1$ for some index i_0 . Then, the initial saturation field $\boldsymbol{\theta}(t = 0)$ is defined as

$$\boldsymbol{\theta}_i(t = 0) = \begin{cases} 1 & \text{if } i \leq i_0 \\ h(\beta)/h(x_i) & \text{if } i > i_0 \end{cases} .$$

Let us denote by β_∞ the rupture point at the stationary state. If for some value of p_{cc} (high enough) the stationary solution does not cavitate at the left side of β_∞ , one can expect the existence of $\delta > 0$ such that for every $\beta_0 \in [\beta_\infty - \delta, \beta_\infty + \delta]$ the fields $(\mathbf{p}(t), \boldsymbol{\theta}(t))$ tends in time to the stationary solution and $\mathbf{p}(t) > 0$ for all t . This last condition is useful since it allows to obtain an analytic solution for $\beta(t)$. In fact, integrating the Reynolds equation on the interval $[0, \beta(t)]$ and denoting $h_\beta(t) = h(\beta(t))$ one obtains

$$\frac{dp}{dx_1} \Big|_{x_1=\beta(t)_-} = \frac{6\mu \bar{U}}{h_\beta(t)^2} + \left[\frac{p_{cc} - 6\mu \bar{U} \int_0^{\beta(t)} \frac{1}{h(s)^2} ds}{\int_0^{\beta(t)} \left(\frac{h_\beta(s)}{h(s)} \right)^3 ds} \right]. \quad (3.58)$$

The last equation can be substituted in Eq. (3.2) to obtain the next ODE for $\beta(t)$

$$\frac{d\beta}{dt} = \frac{\bar{U}}{2} - \frac{1}{1 - \theta_0} \left[\frac{\bar{U}}{2} + \frac{1}{12\mu h_\beta(t)} \left(\frac{p_{cc} - 6\mu \bar{U} \int_0^{\beta(t)} \frac{1}{h(s)^2} ds}{\int_0^{\beta(t)} \left(\frac{h_\beta(s)}{h(s)} \right)^3 ds} \right) \right], \quad (3.59)$$

which is just Eq. (3.2), to find $\beta(t)$ in time.

Here $R_c = 64$ mm (the ring's curvature), $Z(t) = 1.0 \mu\text{m}$ and $p_{cc}(t) = 100 \text{ atm}$ are set for all $t \geq 0$. For that configuration one has that $\beta_\infty \simeq 0.78321 \times 10^{-3} \text{ m}$. Taking $\beta_0 = 0.65 \times 10^{-3} \text{ m}$ and $\beta_0 = 0.9 \times 10^{-3} \text{ m}$ and fixing the Courant number to 0.4 the results for $\beta(t)$ are shown in Fig. 3.4.19 for different values of Δx_1 and for the exact solutions. It is observed a convergence of the time curves for β (when Δx_1 goes to zero) towards the exact solutions, and these exact solutions converge in time to the exact value of β_∞ .

3.4.3.2 Traveling pockets

Differently from Algorithm 1, which aims to impose $\theta_0 = 1$ at the right side of rupture point by means of the operator $T = T_{\epsilon=1}$, Algorithm 2 imposes some value $0 < \theta_0 < 1$ (here is taken as $2/3$). This characteristic allows $\frac{dp}{dx_1} \Big|_{x_1=\beta(t)_-}$ to be positive. In the next numerical examples it is shown that positive gradient allows transient solutions were cavitated areas traveling towards Ω_0^r are fulfilled by means of the Poiseuille flow associated to this positive pressure gradient.

Let us consider the lower surface to be smooth during the first interval of time in order for the fluid to reach a stationary state. After that interval, a series of elliptical pockets pass through the domain and a dynamic response of $\beta(t)$ is expected. Subsequently, the surface becomes smooth again and the system is expected to return to some stationary state. For these examples, the ring's curvature is taken as $R_c = 128$ mm, the distance between the surfaces is fixed and equal to $Z(t) = 1.5 \mu\text{m}$, the length of the pockets is set to $100 \mu\text{m}$ and the distance between their centers (texture period in the movement direction) is equal to $200 \mu\text{m}$. The boundary condition p_{cc} is constant in time and three values for it are explored, 10, 20 and 30 atm. The first pocket enters the domain at time $t \approx 0.2 \text{ ms}$, and the last one exits the domain at time $t \approx 0.8 \text{ ms}$. The resulting time curves

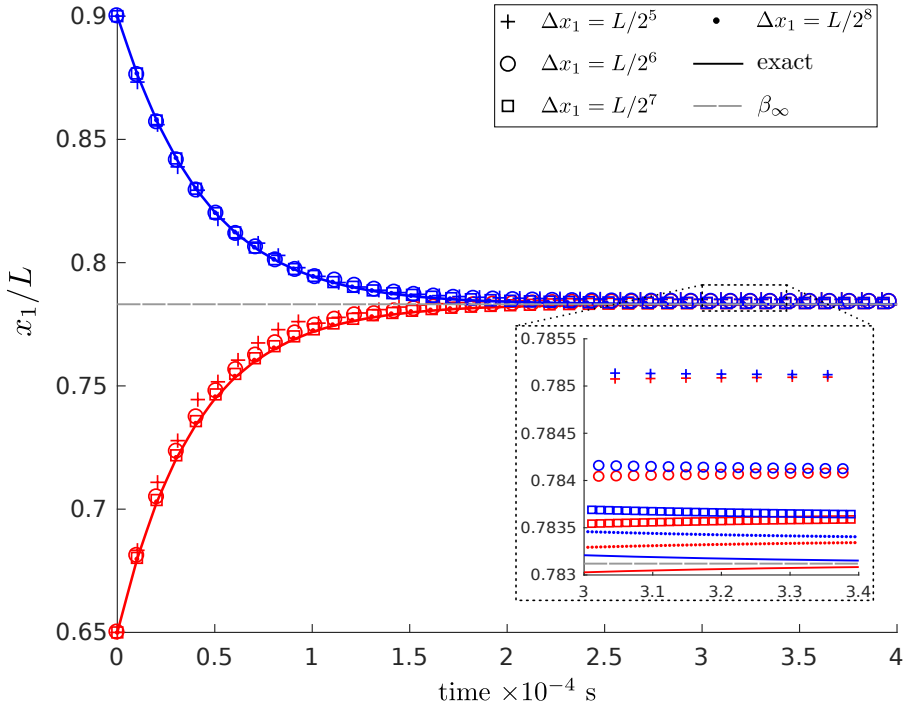


Figure 3.4.19 – Convergence of $\beta(t)$ when Δx_1 tends to zero by means of Algorithm 2. The red curves correspond to $\beta_0 = 0.65 \times 10^{-3}$ m and the blue ones to $\beta_0 = 0.9 \times 10^{-3}$ m. The continuous lines are the exact solutions obtained integrating Eq. (3.59). The dashed gray line corresponds to the exact value of β_∞ .

$\beta(t)$ are shown in Fig. 3.4.20. Notice that $\beta(t)$ develops a periodic behavior after $t \simeq 0.4$ ms in all the cases and, as expected, the higher the value of p_{cc} the closer $\beta(t)$ is to the center of the domain ($x_1/L = 0.5$) the major part of the time. It is also worth noting that during the periodic regime reached by the system while the textures are passing through the domain (between $t \approx 0.4$ ms and $t \approx 0.8$ ms) the time average of $|\beta(t) - L/2|$, i.e., the distance between the rupture point and the center of the domain, is $\approx 3\%$ lower than $|\beta_\infty - L/2|$ for each case.

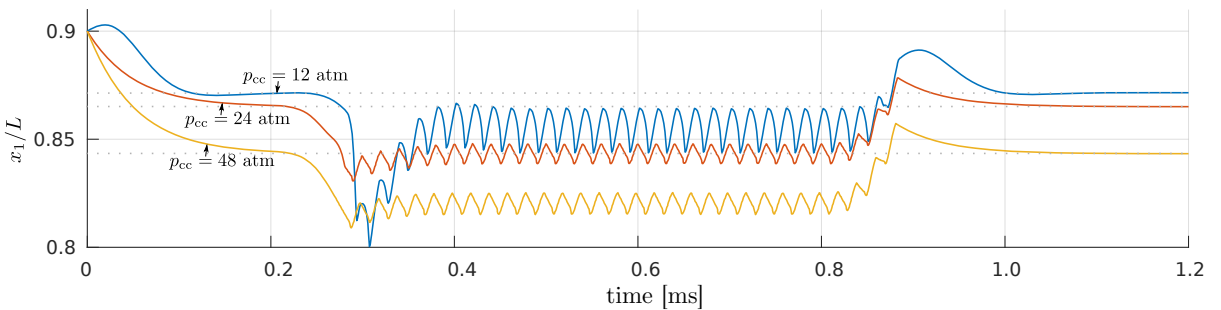


Figure 3.4.20 – Rupture point position (β) by means of Algorithm 2 for different values of p_{cc} (fixed in time) when a series of pockets pass through the domain.

The pressure field, the saturation field and the geometry of this example are shown in detail for some time steps in Fig. 3.4.21. These time steps belong to the periodic transient

regime shown in Fig. 3.4.20 (between $t \approx 0.4$ ms and $t \approx 0.8$ ms). Notice that the traveling pockets generate a cavitated region near the middle of the domain (see time $t = 0.405$ ms). This cavitated region advances to the right accompanying the pocket, collapsing after a time interval of length ≈ 0.035 ms (when β is near 0.8 mm). Let us remark that the pressure profile at which this collapse is developed is not possible to be produced along Algorithm 1 and $T = T_{\epsilon=1}$. In fact, this last model imposes a non-positive pressure gradient, not allowing the flux to be *reversed* in $x_1 = \beta$, which is necessary to fulfill the cavitated region at its left side as in the present example.

As mentioned before, we have restricted this numerical strategy to the case where $\beta(t)$ is a rupture point, i.e., $\dot{\beta}(t) < \bar{U}/2$. The development of $\dot{\beta}(t) \geq \bar{U}/2$ can be observed by simply changing the pocket's depth of the example presented here from 0.5 to 1 μm . Let us identify a second limitation of this strategy. Denote by $\alpha(t)$ the first reformation point in the domain at the left side of $\beta(t)$. For certain configurations it is observed that, instead of the collapse of the cavitated region placed at the right side of $\alpha(t)$, the distance $|\beta(t) - \alpha(t)|$ goes to zero. This situation is observed for the geometry shown in the last example when p_{cc} is changed to a value small enough. Taking $p_{cc} = 6$ atm the last time before hypothesis $|\beta(t) - \alpha(t)| \geq 2\Delta x_1$ is violated is shown in Fig. 3.4.22. Physically, the cavitated region present at the left side of $\alpha(t)$ and the separated region placed at the right side of $\beta(t)$ become closer in time, which represents a modeling problem that will be left open for future research.

3.5 Chapter Summary

In Section 3.4.1 some stationary numerical solutions of the system (3.4)-(3.11) obtained by means of Algorithm 1 are exposed. First, along one-dimensional configurations, it is found that when using $T = T_{\epsilon=0}$ the numerical problem is ill-posed, as the stationary solutions depend upon an initial guess $(\mathbf{p}^0, \boldsymbol{\theta}^0)$. Let us remark that those solutions exhibit different pressure gradients at the left side of the reformation point β , and this numerical observation is in accordance with the analytic solutions found in Proposition 3.1. Uniqueness is recovered making use of the operator $T = T_{\epsilon=1}$, which is observed to impose a null gradient condition at β .

In Section 3.4.2 transient numerical solutions of the system (3.4)-(3.11) obtained by means of Algorithm 1 and $T = T_{\epsilon=1}$ are shown. First, an explosion in the combustion chamber is simulated by taking $p_{cc}(t)$ as a Gaussian pulse in time. It is shown that the correct accommodation of p_{cc} as a boundary condition gives important differences in the friction and minimum clearance predicted numerically. This fact has been already stressed in the literature (MORRIS *et al.*, 2014; MORRIS *et al.*, 2015) along with a non-conservative model. The numerical results presented in this work (in both sections 3.4.2 and 3.4.3) aim

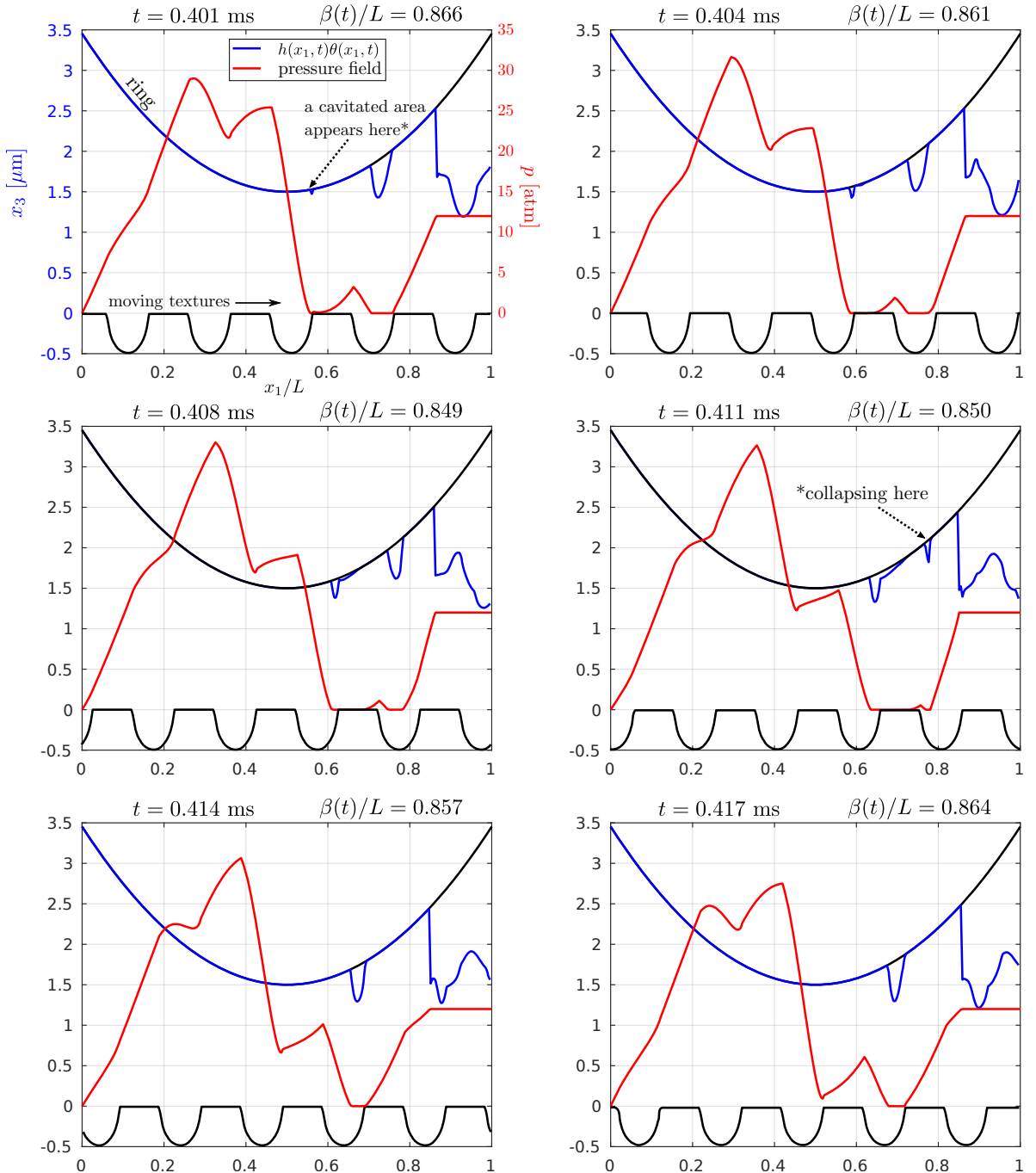


Figure 3.4.21 – Pressure and saturation fields along Algorithm 2 and a moving textured surface for $p_{cc} = 12 \text{ atm}$. Each time corresponds to the transient periodic regime of Fig. 3.4.20.

to predict the rupture boundary's position by means of mass-conservation, and represent the first simulations with this characteristic for $p_{cc} > 0$. However, due to the imposition of a non-positive pressure gradient at the rupture boundary $\partial\Omega_0^r$, this numerical scheme is limited to cases where the moving surface (along the $x_1 - x_2$ plane) is flat. To work on this issue, a different approach is explored in Section 3.4.3. There, the one-dimensional numerical scheme given by Algorithm 2 allows to perform simulations with the presence

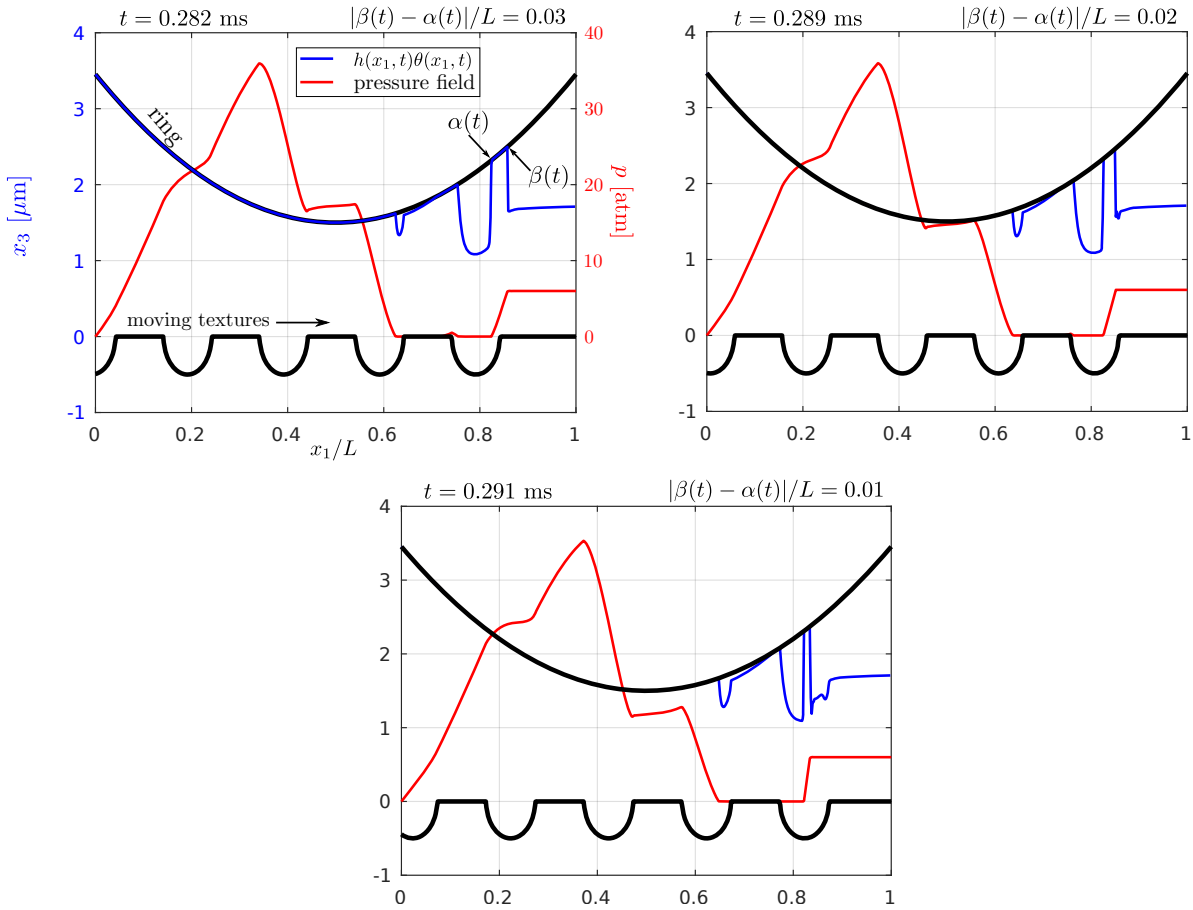


Figure 3.4.22 – Pressure and saturation fields along Algorithm 2 and a moving textured surface for $p_{cc} = 6$ atm. Here the pressurized interval $[\alpha(t), \beta(t)]$ tends to vanish.

of moving textures. This is done by means of a Finite Volume scheme, based on a work by Ausas *et al.* (2013) for a different related model, where $\beta(t)$ corresponds to one of the cells interfaces. The Rankine-Hugoniot flux continuity condition (3.2) is integrated with $\theta_0 = 2/3$ to find for $\beta(t)$ in time. The main limitation of this modeling is somewhat similar to the one found along Algorithm 1, and corresponds to the encounter of a region where $p = 0$ with a region where $p = p_{cc}$. This issue requires further research.

Both the numerical strategies that are shown in Section 3.3 aim to impose a non-homogeneous boundary condition for pressure in a mass-conserving framework. This is done by identifying a rupture boundary $\partial\Omega_0^r$ where the saturation variable becomes lower than the unit, and thus the PDE passes from elliptic (for p) to hyperbolic (for θ). In that boundary, mass-conservation is imposed by means of a pressure gradient condition or by fixing the value of θ_0 . The latter was chosen to be constant and equal to $2/3$ based in an analytic flow-reverse condition. However, as it has been shown in Section 3.2, there exist other possibilities for the setting of θ_0 . Thus, other models for that unknown, not necessarily constants, would be explored in future works.



THE REYNOLDS-RAYLEIGH-PLESSET COUPLING

An important source of cavitation inception in a liquid is the presence of immersed tiny bubbles of non-condensable gas/vapor (DOWSON; TAYLOR, 1979; BRENNEN, 1995). As long as these bubbles remain small, the effective fluid (liquid and gas/vapor mixture) density ρ and viscosity μ correspond to those of the liquid phase ($\rho \simeq \rho_\ell$ and $\mu \simeq \mu_\ell$), and thus the mixture hydrodynamics can be modeled disregarding the bubbles presence. However, under suitable conditions, like local pressure falls, the bubbles can grow big enough to affect both the effective ρ and μ . The Reynolds-Rayleigh-Plesset (RRP) coupling aims to model this kind of cavitation development. It is a three-equations model that assumes an initial distribution of spherical bubbles as a datum, and computes the fluid dynamics by means of a transport equation for the bubbles number per unit volume, $n_b(\mathbf{x}, t)$; the Rayleigh-Plesset equation for the bubbles local radii, $R(\mathbf{x}, t)$; and the Reynolds equation for the hydrodynamical pressure, $p(\mathbf{x}, t)$.

In the next Section the Rayleigh-Plesset equation and some of its basic properties are presented. In Section 4.2 the RRP coupling is presented along with some simplifications that are generally assumed in the literature.

4.1 The Rayleigh-Plesset equation

Let us consider a single spherical bubble of radius $R(t)$ immersed in an infinite domain of liquid. The bubbles content is composed by a mixture of non-condensable gas and vapor. The pressure $p_\infty(t)$ (time dependent) far away from the bubble is assumed to be known. The pressure at the interior of the bubble is assumed to be uniform in space and it is denoted by $p_{\text{bub}}(t)$. Then, from the momentum equations for the mixture, one can derive the Rayleigh-Plesset equation for the bubble dynamics (BRENNEN, 1995;

GEHANNIN, 2009)

$$\rho_\ell \left(\frac{3}{2} \dot{R}^2 + R \ddot{R} \right) + 4 \left(\frac{\mu_\ell + \kappa^s / R}{R} \right) \dot{R} = p_{\text{bub}}(t) - p_\infty(t) - \frac{2\sigma}{R}, \quad (4.1)$$

where \dot{R} is the total time derivative (following the bubbles), ρ_ℓ and μ_ℓ correspond to the liquid density and viscosity respectively, σ is the liquid surface tension coefficient, and κ^s is the surface dilatational viscosity (SNYDER; BRAUN; PIERSON, 2016). Two models for $p_{\text{bub}}(t)$ such that no energy equation (to solve for the bubbles temperature) is needed are distinguished next. First, denoting $V = \frac{4}{3}\pi R^3$ let us assume that the bubble is in equilibrium at some external pressure $p_\infty = p_{\text{eq}}$, temperature T_{eq} , and radius R_{eq} . Then, as the bubble inner pressure reads

$$p_{\text{bub}} = p_0(T_{\text{eq}}, V_{\text{eq}}) + p_{\text{vap}}(T_{\text{eq}}), \quad (4.2)$$

where

$$p_0(T_{\text{eq}}, V_{\text{eq}}) = \frac{m_0 \mathcal{R}_0 T_{\text{eq}}}{V_{\text{eq}}}, \quad (4.3)$$

m_0 is the mass of gas, \mathcal{R}_0 is the constant of the gas. Then, by the Young-Laplace equation one has

$$p_{\text{bub}} - p_{\text{eq}} = \frac{2\sigma(T_{\text{eq}})}{R_{\text{eq}}}, \quad (4.4)$$

where $\sigma(T_{\text{eq}})$ is the surface tension. Thus, substituting p_{bub} from (4.2) and (4.3) into Eq. (4.4), the equilibrium radius R_{eq} accomplishes:

$$p_{\text{bub}} = p_{\text{vap}}(T_{\text{eq}}) + \frac{3m_0 \mathcal{R}_0 T_{\text{eq}}}{4\pi R_{\text{eq}}^3} = p_{\text{eq}} + \frac{2\sigma}{R_{\text{eq}}}. \quad (4.5)$$

Adiabatic case with no mass transfer

Assume that there is no transfer of mass nor transfer of heat (adiabatic behavior) between the bubbles and the liquid. Also, the pressure $p_{\text{bub}}(t)$ is assumed to behave isoentropically, then:

$$p_{\text{bub}}(t) = (p_{\text{vap}}(T_{\text{eq}}) + p_{\text{gas}}(T_{\text{eq}}, V_{\text{eq}})) \left(\frac{V_{\text{eq}}}{V(t)} \right)^{3k} = \left(p_{\text{eq}} + \frac{2\sigma}{R_{\text{eq}}} \right) \left(\frac{R_{\text{eq}}}{R(t)} \right)^{3k}, \quad (4.6)$$

where k is restricted to 1.4 (air specific heat).

Isothermal case with mass transfer

Assume now that the temperature is T_{eq} everywhere, and that the vapor pressure inside the bubble is equal to $p_{\text{vap}}(T_{\text{eq}})$ for all time t . Then,

$$p_{\text{bub}}(t) = p_{\text{vap}}(T_{\text{eq}}) + p_0(T_{\text{eq}}, V_{\text{eq}}) \frac{V_{\text{eq}}}{V(t)} = p_{\text{vap}}(T_{\text{eq}}) + \left(p_{\text{eq}} + \frac{2\sigma}{R_{\text{eq}}} - p_{\text{vap}}(T_{\text{eq}}) \right) \left(\frac{R_{\text{eq}}}{R(t)} \right)^3. \quad (4.7)$$

Remark 4.1. Observe that in the isothermal case for the vapor pressure inside the bubble to be equal to $p_{\text{vap}}(T_{\text{eq}})$ for every time t there must be a transference of mass of vapor (condensation or evaporation). Thus, if m denotes the total mass content of the bubbles, for these cases $\frac{dm}{dt}$ could be different from zero.

4.1.1 Cavitation pressure for a gas/vapor bubble

Let us suppose a single bubble is initially in equilibrium at radius R_{eq} and internal pressure $p_{\text{bub}}(R_{\text{eq}})$. Then, the external pressure satisfies p_∞

$$p_\infty = p_{\text{bub}}(R_{\text{eq}}) - \frac{2\sigma}{R_{\text{eq}}}. \quad (4.8)$$

If one changes p_∞ to some lower value p_∞^* and the temperature $T = T_{\text{eq}}$ of the bubble remains constant, then one has that for the bubble to reach a new equilibrium radius R_{eq}^* the pair $(p_\infty^*, R_{\text{eq}}^*)$ also satisfies Eq. (4.8) (substituting R_{eq} by R_{eq}^* and p_∞ by p_∞^*). Therefore, if p_∞^* is lower than

$$p_{\text{cav}} := \min_{R>0} \left\{ p_{\text{bub}}(R) - \frac{2\sigma}{R} \right\}, \quad (4.9)$$

no equilibrium radius exists. In fact, as initially one has $\dot{R}(t=0) = \ddot{R}(t=0) = 0$, if the external pressure is diminished to a certain value $p_\infty^* < p_{\text{cav}}$, then

$$p_{\text{bub}}(t) - \frac{2\sigma}{R} - p_\infty^* < 0,$$

and Eq. (4.1) implies that the bubble will grow indefinitely. For this reason, p_{cav} is called the *cavitation pressure* in the context of the RRP cavitation model.

For instance, taking the derivative with respect to R_{eq} in (4.8), with p_{bub} computed by replacing $R(t) = R_{\text{eq}}^*$ in (4.6), and taking $p_{\text{vap}} = 0$, one has

$$p_{\text{cav}} = \left(p_{\text{eq}} + \frac{2\sigma}{R_{\text{eq}}} \right) \left(\frac{R_{\text{eq}}}{R^*} \right)^{3k} - \frac{2\sigma}{R^*} \quad \text{with} \quad R^* = \left[\left(p_{\text{eq}} + \frac{2\sigma}{R_{\text{eq}}} \right) \frac{3kR_{\text{eq}}^{3k}}{2\sigma} \right]^{\frac{1}{3k-1}}, \quad (4.10)$$

or, equivalently:

$$p_{\text{cav}} = p_{\text{bub}} \left(\frac{R_{\text{eq}}}{R^*} \right)^{3k} - \frac{2\sigma}{R^*} \quad \text{with} \quad R^* = \left[p_{\text{bub}} \frac{3kR_{\text{eq}}^{3k}}{2\sigma} \right]^{\frac{1}{3k-1}}. \quad (4.11)$$

Fig. 4.1.1 shows the curve $(p_{\text{eq}}^*, R_{\text{eq}}^*)$ for several values of R_{eq} around 1 micron. A minimum value for p_{eq}^* is observed.

4.1.2 The linearized equation

Let us introduce the dimensionless variables shown in Table 5. Then, the Rayleigh-Plesset equation can be written

$$\frac{3}{2}\dot{\chi}^2 + \chi\ddot{\chi} = \frac{\hat{P}_0}{\chi^{3k}} - \hat{P}_\infty - \Sigma \frac{1}{\chi} - M \frac{\dot{\chi}}{\chi} - K \frac{\dot{\chi}}{\chi^2}. \quad (4.12)$$

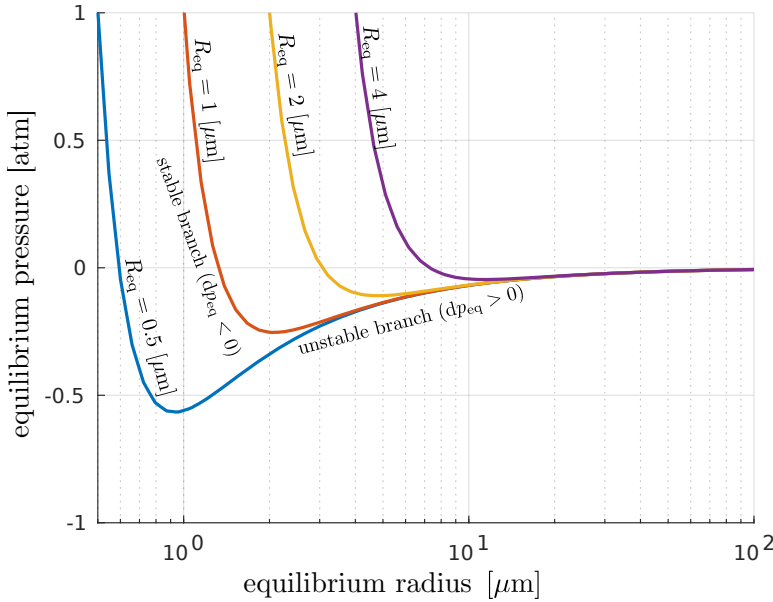


Figure 4.1.1 – Equilibrium states $(p_{\text{eq}}^*, R_{\text{eq}}^*)$ for several values of R_{eq} and $p_{\text{eq}} = 1 \text{ [atm]}$.

| Symbol | Description |
|--|---|
| $\hat{p} = p/A$ | dimensionless pressure |
| $\chi = R/R_{\text{eq}}$ | non-dimensional bubble radius |
| $\tau = \frac{t}{R_{\text{eq}} \sqrt{\frac{\rho_\ell}{A}}}$ | non-dimensional time |
| $\hat{\omega}_0 = R_{\text{eq}} \sqrt{\frac{\rho_\ell}{A}} \omega_0$ | non-dimensional natural frequency |
| $\hat{\omega} = R_{\text{eq}} \sqrt{\frac{\rho_\ell}{A}} \omega$ | non-dimensional forcing term frequency |
| $\Sigma = \frac{2\sigma}{R_{\text{eq}} A}$ | non-dimensional surface tension |
| $K = \frac{4\kappa^s}{R_{\text{eq}}^2 \sqrt{A \rho_\ell}}$ | non-dimensional surface viscosity |
| $M = \frac{4\mu_\ell}{R_{\text{eq}} \sqrt{A \rho_\ell}}$ | non-dimensional viscosity of the liquid |

Table 5 – Physical parameters and non-dimensional variables for the 0-dimensional study.

Looking for the behavior of the bubbles near their equilibrium state, let us suppose that for $p_\infty = A$ the bubble has an equilibrium radius R_{eq} and its inner pressure is equal to p_{bub} , thus

$$p_{\text{bub}} = A + \frac{2\sigma}{R_{\text{eq}}}, \quad \text{or} \quad \hat{p}_{\text{bub}} = 1 + \Sigma, \quad (4.13)$$

and impose the next type of time perturbation on the pressure

$$\hat{p}_\infty(\tau) = 1 - \delta \cos \hat{\omega}\tau. \quad (4.14)$$

Along this two last relations, the Rayleigh-plesset equation can be written

$$\begin{aligned} \frac{d}{d\tau} \begin{bmatrix} \chi \\ \dot{\chi} \end{bmatrix} &= \begin{bmatrix} \dot{\chi} \\ (1 + \Sigma)\chi^{-3k-1} - \chi^{-1} - \Sigma\chi^{-2} - M\dot{\chi}\chi^{-2} - K\dot{\chi}\chi^{-3} - \frac{3}{2}\dot{\chi}^2\chi^{-1} \end{bmatrix} + \begin{bmatrix} 0 \\ \delta \cos \hat{\omega}\tau \end{bmatrix} \\ &= F(\chi, \dot{\chi}) + \begin{bmatrix} 0 \\ \delta \cos \hat{\omega}\tau \end{bmatrix}. \end{aligned}$$

To linearize this equation we compute the derivative of F , reading

$$DF(\chi, \dot{\chi}) = \begin{bmatrix} 0 & 1 \\ D_1 F_2 & D_2 F_2 \end{bmatrix}, \quad (4.15)$$

where

$$D_1 F_2(\chi, \dot{\chi}) = -(3k+1)(1+\Sigma)\chi^{-3k-2} + \chi^{-2} + 2\Sigma\chi^{-3} + 2M\dot{\chi}\chi^{-3} + 3K\dot{\chi}\chi^{-4} + \frac{3}{2}\dot{\chi}^2\chi^{-2},$$

and

$$D_2 F_2(\chi, \dot{\chi}) = -M\chi^{-2} - K\chi^{-3} - 3\dot{\chi}\chi^{-1}.$$

A linearization of Eq. (4.12) reads

$$\frac{d}{d\tau} \begin{bmatrix} \chi \\ \dot{\chi} \end{bmatrix} = DF(1, 0) \cdot \begin{bmatrix} \chi - 1 \\ \dot{\chi} - 0 \end{bmatrix} + \begin{bmatrix} 0 \\ \delta \cos \hat{\omega}\tau \end{bmatrix}$$

obtaining

$$\ddot{\chi} + 2\gamma \dot{\chi} + \hat{\omega}_0^2(\chi - 1) = \delta \cos \hat{\omega}\tau \quad (4.16)$$

where $2\gamma = K + M$, $\hat{\omega}_0^2 = 3k(1 + \Sigma) - \Sigma$. Notice that $\hat{\omega}_0$ is real since $1 \leq k < 2$. The last equation corresponds to the harmonic damped forced oscillator with equilibrium state $(1, 0)$ for $\delta = 0$. The natural frequency of that system is given by

$$\hat{\omega}_0^2 = 3k(1 + \Sigma) - \Sigma, \quad \text{or} \quad \omega_0 = \frac{1}{R_{\text{eq}}} \sqrt{\frac{1}{\rho_\ell} \left(3k p_{\text{bub}} - \frac{2\sigma}{R_{\text{eq}}} \right)}. \quad (4.17)$$

As an example, varying R_{eq} and determining p_{bub} from Eq. (4.13). Figure 4.1.2 shows different natural frequencies ω_0 depending on R_{eq} . The energy of the linearized system is defined as

$$E = \frac{\hat{\omega}_0^2}{2}(\chi - 1)^2 + \frac{1}{2}\dot{\chi}^2,$$

so one can write

$$\frac{dE}{dt} = \dot{\chi} (\hat{\omega}_0^2(\chi - 1) + \ddot{\chi}) = -2\gamma \dot{\chi}^2 + \dot{\chi} \delta \cos \hat{\omega}t. \quad (4.18)$$

Observe that $\delta = 0$ implies a decay of energy such that the system converges in time to its equilibrium state.

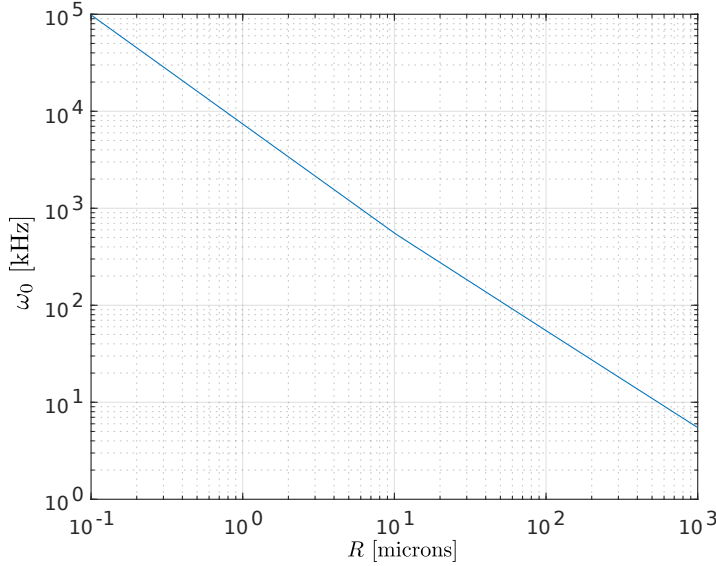


Figure 4.1.2 – Natural frequencies, by means of Eq. (4.17), for a bubble near the equilibrium state for $k = 1.4$, $\rho_\ell = 850 \text{ kg/m}^3$, $\sigma = 3.5 \times 10^{-2} \text{ N/m}$ and $p_{\text{bub}} = 1 \text{ atm} + 2\sigma/R_{\text{eq}}$.

4.1.3 Bubbles resonance and inertial terms

Let us assume the perturbation amplitude δ is small enough such that the solution of Eq. (4.16) is a good approximation of the full Rayleigh-Plesset Eq. (4.12). The general solution of Eq. (4.16) reads

$$\chi(\tau) = \chi_h(\tau) + \chi_p(\tau), \quad (4.19)$$

where χ_h is the solution of homogeneous equation ($\delta = 0$), and χ_p is a particular solution of the full system. Depending on the sign of $\gamma - \hat{\omega}_0$, one has (C_1 and C_2 are integration constants)

$$\chi_h(\tau) = \begin{cases} e^{-\gamma\tau} C_1 \cos(\sqrt{\hat{\omega}_0^2 - \gamma^2}\tau + C_2) & \text{if } \gamma < \hat{\omega}_0, \\ e^{-\gamma\tau} (C_1 + \tau C_2) & \text{if } \gamma = \hat{\omega}_0, \\ e^{-\gamma\tau} (C_1 e^{\lambda_+ \tau} + C_2 e^{\lambda_- \tau}) & \text{if } \gamma > \hat{\omega}_0, \end{cases} \quad (4.20)$$

where $\lambda_{\pm} = \pm\sqrt{\gamma^2 - \hat{\omega}_0^2}$. Observe that, independently of sign $(\gamma - \hat{\omega}_0)$, $\chi_h(\tau)$ decays to zero with characteristic time $\gamma = (K + M)/2$, which grows with both μ_ℓ and κ^s . Because of this, the next analysis is focused in the transient part of χ (χ_p), which can be written

$$\chi_p(\tau) = \frac{\delta}{\hat{\omega}_0^2} \frac{\sin(\hat{\omega}\tau - (\phi - \pi/2))}{\sqrt{4\alpha^2\epsilon^2 + (1 - \epsilon^2)^2}}, \quad \tan \phi = 2\alpha \frac{\epsilon}{1 - \epsilon^2}, \quad (4.21)$$

where $\alpha = \gamma/\hat{\omega}_0$ and $\epsilon = \omega/\hat{\omega}_0$. Denote now by χ_p^- the solution of Eq. (4.16) obtained when the inertial term ($\ddot{\chi}$) is disregarded. Then, χ_p^- reads

$$\chi_p^-(\tau) = \frac{\delta}{\hat{\omega}_0^2} \frac{2\alpha\epsilon \sin \hat{\omega}\tau + \cos \hat{\omega}\tau}{4\alpha^2\epsilon^2 + 1}. \quad (4.22)$$

One can notice that the difference

$$d(\alpha, \epsilon) = \frac{\max_{\tau \in [0, 2\pi]} |\chi_p(\tau) - \chi_p^-(\tau)|}{\max_{\tau \in [0, 2\pi]} |\chi_p(\tau)|} \quad (4.23)$$

depends only on α and ϵ . The function $d(\alpha, \epsilon)$ quantifies the error (in the max-norm) for $t \rightarrow \infty$ when approximating χ_p by χ_p^- . A sample of this function is shown in Fig. 4.1.3. Please notice that $d(\alpha, \epsilon)$ increases when ϵ is near to the unit. As it can be observed from the definition of χ_p this is due to resonance of the system when the driven term frequency ($\hat{\omega}$) is near to the bubble natural frequency ($\hat{\omega}_0$). It is worth observing that this error does not depend on δ . Thus inertial terms can be relevant even for small perturbation amplitudes. For instance, the surface roughness (with a scale of microns along direction of motion) of a Journal Bearing of 25 mm of radius rotating at 5000 rpm would imply would produce small oscillations in pressure (due to the roughness acting as small dimples) at a frequency of $\approx 1.3 \times 10^4$ kHz. Considering the configuration shown in Fig. 4.1.2, this would produce resonance of bubbles of radius around 1 μm .

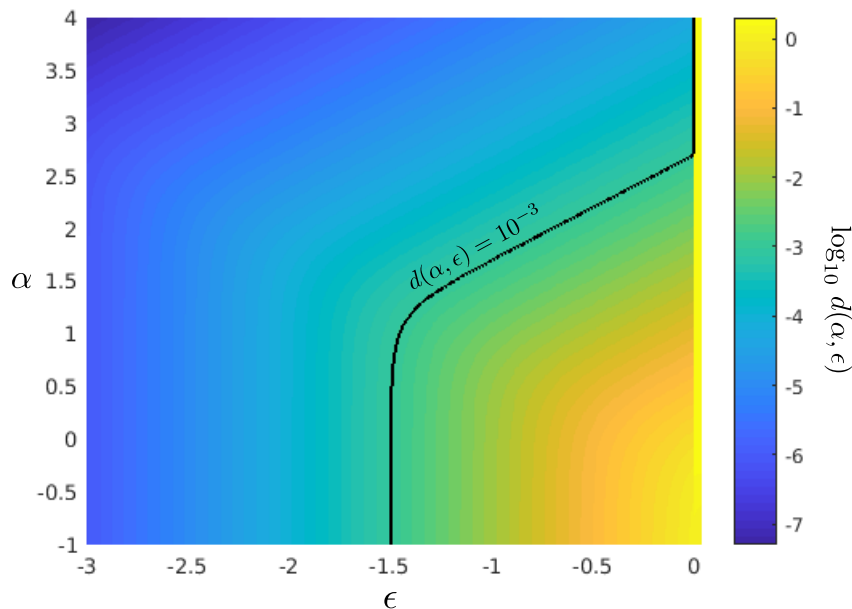


Figure 4.1.3 – $d(\alpha, \epsilon)$: error quantification for the disregard of the inertial term on the linearized Rayleigh-Plesset Eq. (4.16).

4.2 Coupling the Reynolds and the Rayleigh-Plesset equations

The coupling of the Reynolds and the Rayleigh-Plesset equations has been used in several numerical works regarding lubricated devices. To the author's knowledge, this kind of models was first used by Tønder (TØNDER, 1977) applied to Michell Bearings. After that article, and progressively increasing the complexity of the gas-nuclei dynamics, several works have been published concerning tilting-pad thrust bearings (SMITH, 1980), journal bearings (NATSUMEDA; SOMEYA, 1987; SOMEYA, 2003; SNYDER; BRAUN; PIERSON, 2016;

BRAUN; PIERSON; SNYDER, 2017a), squeeze film dampers (GEHANNIN; ARGHIR; BONNEAU, 2009; GEHANNIN; ARGHIR; BONNEAU, 2016) and parallel plates (GEIKE; POPOV, 2009a; GEIKE; POPOV, 2009b).

In the works cited above the fluid is supposed to be a mixture of two phases: an incompressible liquid phase (with density ρ_ℓ and viscosity μ_ℓ) and a gas phase (with density ρ_g and viscosity μ_g). Next, heuristic arguments are presented to justify the RRP coupling. This presentation is based in the Theory of Multicomponent Fluids (DREW; PASSMAN, 1999), which has been already used by Carrica et al. in several works modeling the dynamics of a mixture “water / immersed gas bubbles” around a surface ship (Guido-Lavalle *et al.*, 1994; CARRICA *et al.*, 1998; CARRICA *et al.*, 1999; CASTRO; CARRICA, 2013; CASTRO; LI; CARRICA, 2016)

4.2.1 The mass and momentum conservation equations

The mixture density and velocity vector are denoted by ρ and \mathbf{u} and the pressure field is denoted by p . The characteristic functions of the phases are denoted by $X_k(\mathbf{x}, t)$, $k = \ell, g$ for the liquid and gas phase respectively. This is, $X_k(\mathbf{x}, t) = 1$ if the phase k is present in \mathbf{x} at time t , and $X_k(\mathbf{x}, t) = 0$ otherwise.

An ensemble of physical realizations is assumed to exist. Each of these realizations corresponds to an evolution of the physical system (fluid mixture - limiting surfaces - boundary conditions) for which the initial conditions are *near enough* to a set of ideal smooth initial conditions (DREW; PASSMAN, 1999). A probability of occurrence for each realization is assumed. Here $\langle \cdot \rangle$ denotes the statistical averaging with respect to this distribution function at the point $\mathbf{x} \in \Omega^V$ and time t . The fields

$$\alpha_g(\mathbf{x}, t) = \langle X_g \rangle, \quad \alpha_\ell(\mathbf{x}, t) = \langle X_\ell \rangle, \quad (4.24)$$

are called the *gas fraction*, and the *liquid fraction*. In the statistical model, the phases occupy the whole domain, thus $\alpha_g + \alpha_\ell = 1$. With this, the averaged density, velocity vector and stress tensor for each phase $k = \ell, g$ are defined as

$$\bar{\rho}_k(\mathbf{x}, t) = \frac{\langle \rho X_k \rangle}{\alpha_k}, \quad \bar{\mathbf{u}}_k(\mathbf{x}, t) = \frac{\langle \rho \mathbf{u} X_k \rangle}{\alpha_k \bar{\rho}_k}, \quad \bar{\mathbf{T}}_k = \frac{\langle \mathbf{T} X_k \rangle}{\alpha_k}. \quad (4.25)$$

Observe that as the liquid phase is incompressible one has $\bar{\rho}_\ell = \rho_\ell$. Applying the averaging process to the conservation equations of mass and momentum, one obtains (DREW; PASSMAN, 1999)

$$\frac{\partial(\alpha_k \bar{\rho}_k)}{\partial t} + \nabla \cdot (\alpha_k \bar{\rho}_k \bar{\mathbf{u}}_k) = \Gamma_k \quad \text{in } \Omega^V \quad (4.26)$$

and (disregarding turbulence effects)

$$\frac{\partial(\alpha_k \bar{\rho}_k \mathbf{u}_k)}{\partial t} + \nabla \cdot (\alpha_k \bar{\rho}_k \bar{\mathbf{u}}_k \otimes \bar{\mathbf{u}}_k) = \nabla \cdot (\alpha_k \bar{\mathbf{T}}_k) + \mathbf{M}_k + v_{ki} \Gamma_k \quad \text{in } \Omega^V, \quad (4.27)$$

where \mathbf{M}_k is the interfacial momentum source and, v_{ki} is the interfaces speed and Γ_k is the interfacial mass generation source. Now, a series of hypotheses are made to simplify these equations:

- Averaged quantities are smooth;
- Interfacial mass sources are negligible ($\Gamma_k \simeq 0$);
- Interfacial momentum sources are negligible ($\mathbf{M}_k \simeq 0$);
- The gas phase average velocity is equal to the liquid phase average velocity, $\bar{\mathbf{u}}_g = \bar{\mathbf{u}}_\ell$;
- The gas phase density is equal to the gas reference density ρ_g , $\bar{\rho}_g = \rho_g$.

With these hypotheses, adding up Eq. (4.26) for both phases, simplifying the notation by setting $\alpha \stackrel{\text{def}}{=} \alpha_g$, and introducing the variable

$$\bar{\rho}(\alpha) = \alpha(\mathbf{x}, t) \rho_g + (1 - \alpha(\mathbf{x}, t)) \rho_\ell, \quad (4.28)$$

it is obtained the conservation law:

$$\frac{\partial \bar{\rho}}{\partial t} + \nabla \cdot (\bar{\rho} \bar{\mathbf{u}}_\ell) = 0 \quad \text{in } \Omega^V. \quad (4.29)$$

Similarly, adding up Eq. (4.27) for both phases we have

$$\frac{\partial(\bar{\rho} \bar{\mathbf{u}}_\ell)}{\partial t} + \nabla \cdot (\bar{\rho} \bar{\mathbf{u}}_\ell \otimes \bar{\mathbf{u}}_\ell) = -\nabla \bar{p} + \mu_{\text{eff}} \nabla^2 \bar{\mathbf{u}}_\ell \quad \text{in } \Omega^V, \quad (4.30)$$

where it has been assumed the existence of an effective fluid viscosity μ_{eff} (that depends smoothly on α , the liquid viscosity and the gas viscosity) such that

$$\nabla \cdot (\alpha \bar{\mathbf{T}}_g + (1 - \alpha) \bar{\mathbf{T}}_\ell) \simeq -\nabla \bar{p} + \mu_{\text{eff}} \nabla^2 \bar{\mathbf{u}}_\ell \quad \text{in } \Omega^V, \quad (4.31)$$

where \bar{p} is the averaged pressure. An example off μ_{eff} is given by

$$\mu_{\text{eff}}(\alpha) = \alpha(\mathbf{x}, t) \mu_g + (1 - \alpha(\mathbf{x}, t)) \mu_\ell. \quad (4.32)$$

To our knowledge, there is a lack of works justifying (4.31) or some similar relation, and further research on the topic is needed.

As shown in Chapter 2, the thin-film hypothesis allows to approximate the Navier-Stokes Eqs. (4.30) along Eq. (4.29) by the incompressible Reynolds equation:

$$\nabla \cdot \left(\frac{\bar{\rho} h^3}{12 \mu_{\text{eff}}} \nabla \bar{p} \right) = \nabla \cdot \left(\frac{\mathbf{U}}{2} \bar{\rho} h \right) + \frac{\partial \bar{\rho} h}{\partial t} \quad \text{in } \Omega. \quad (4.33)$$

4.2.2 The multigroup approach

In the works where the RRP coupling is used to model cavitation in lubricated devices (TØNDER, 1977; SMITH, 1980; NATSUMEDA; SOMEYA, 1987; SOMEYA, 2003; GEHANNIN; ARGHIR; BONNEAU, 2009; GEIKE; POPOV, 2009a; GEIKE; POPOV, 2009b; SNYDER; BRAUN; PIERSON, 2016; GEHANNIN; ARGHIR; BONNEAU, 2016; BRAUN; PIERSON; SNYDER, 2017a) it is generally assumed that the gas phase corresponds to a high number of spherical bubbles dispersed in the liquid. In these works, the next phenomena are disregarded:

Coalescence and break-up: bubbles of different sizes that are near enough can collapse into a single one. Also, a single bubble can suddenly *broke* into two bubbles.

Mass transference: this can occur at the bubbles' interface due to evaporation or condensation of the bubbles content.

Here we write a formulation where the dynamics of the bubbles' distribution can be modeled along these phenomena. For this, let us denote by m the mass of the bubbles (which is an *internal variable*). Suppose that there exists a distribution function $f(m, \mathbf{x}, t)$ such that for each \mathbf{x} and t the number of bubbles of mass between m and $m + dm$ is given by $f(m, \mathbf{x}, t) dm$. Thus, the quantity $n_b(\mathbf{x}, t)$ defined by

$$n_b(\mathbf{x}, t) = \int_0^\infty f(m, \mathbf{x}, t) dm \quad (4.34)$$

corresponds to the *bubble number density*, i.e., the number of bubbles per unit volume. Denoting by $\mathbf{u}_b(m, \mathbf{x}, t)$ the bubbles velocity, it is assumed that f satisfies the Boltzmann's transport equation (CARRICA *et al.*, 1999):

$$\begin{aligned} \frac{\partial f(m, \mathbf{x}, t)}{\partial t} + \nabla_x \cdot (\mathbf{u}_b(m, \mathbf{x}, t) f(m, \mathbf{x}, t)) + \frac{\partial m}{\partial t} \frac{\partial (f(m, \mathbf{x}, t))}{\partial m} \\ = \mathcal{C}(m, \mathbf{x}, t) + \mathcal{B}(m, \mathbf{x}, t), \end{aligned} \quad (4.35)$$

where \mathcal{C} is the coalescence source and \mathcal{B} is the breakup source. Assuming the mass change rate depends only on t one can rewrite the third term in this equation as:

$$\frac{\partial m}{\partial t} \frac{\partial (f(m, \mathbf{x}, t))}{\partial m} = \frac{\partial}{\partial m} \left(\frac{dm}{dt} f(m, \mathbf{x}, t) \right). \quad (4.36)$$

Considering only binary interactions (a single bubble splits only into two other ones) and mass-conservation of the bubbles content, the breakup source can be written as:

$$\mathcal{B}(m, \mathbf{x}, t) = \int_m^\infty b(m, m' - m|m') f(m', \mathbf{x}, t) dm' - \int_0^m b(m', m - m'|m) f(m, \mathbf{x}, t) dm', \quad (4.37)$$

where $b(m, m' - m|m')$ is the breakup kernel. This function represents the probability per unit time and mass that a bubble of mass m' splits into a bubble of mass $m' - m$

and another bubble of mass m . Under similar assumptions, the coalescence kernel can be written:

$$\mathcal{C}(m, \mathbf{x}, t) = \frac{1}{2} \int_0^m c(m - m', m') T(m - m', m', \mathbf{x}, t) dm' - \int_0^\infty c(m', m) T(m, m', \mathbf{x}, t) dm' , \quad (4.38)$$

where $c(m, m')$ is the probability of coalescence if a collision between two bubbles of sizes m and m' occurs, and the kernel $T(m - m', m', \mathbf{x}, t)$ represents the collision probability per unit time between bubbles of mass m' and m .

The multigroup approach gives a numerical framework to solve Eq. (4.35). It assumes that the bubbles of mass between $m_{g-\frac{1}{2}}$ and $m_{g+\frac{1}{2}}$ can be represented in a group by a single bubble mass, m_g . Integrating Eq. (4.35) between $m_{g-\frac{1}{2}}$ and $m_{g+\frac{1}{2}}$, and considering Eq. (4.36), one obtains

$$\frac{\partial N_g}{\partial t} + \sum_{i=1}^3 \frac{\partial J_{g,i}^N}{\partial x_i} + \left[\frac{dm}{dt} f(m, \mathbf{x}, t) \right]_{m_{g-\frac{1}{2}}}^{m_{g+\frac{1}{2}}} = \int_{m_{g-\frac{1}{2}}}^{m_{g+\frac{1}{2}}} (\mathcal{C}(m, \mathbf{x}, t) + \mathcal{B}(m, \mathbf{x}, t)) dm \quad (4.39)$$

where

$$J_{g,i}^N(\mathbf{x}, t) = \int_{m_{g-\frac{1}{2}}}^{m_{g+\frac{1}{2}}} u_{g,i}(m, \mathbf{x}, t) f(m, \mathbf{x}, t) dm , \quad (4.40)$$

is the bubble flux in the group g and

$$N_g(\mathbf{x}, t) = \int_{m_{g-\frac{1}{2}}}^{m_{g+\frac{1}{2}}} f(m, \mathbf{x}, t) dm , \quad (4.41)$$

is the group number density. Assuming that the distribution function, the bubbles velocities, the bubbles mass exchange rate and the breakup and coalescence probability can be taken to be constants in each group, and using an upwind scheme for the groups fluxes, Eq. (4.39) can be simplified to:

$$\begin{aligned} \frac{\partial N_g}{\partial t} + \sum_{i=1}^3 \frac{\partial (u_{g,i} N_g)}{\partial x_i} &= b_g + c_g \\ &- \left[\min \left(\frac{dm}{dt}, 0 \right) \left(\frac{N_g(\mathbf{x}, t)}{m_{g+1} - m_g} \right) \right]_{g+1} + \left[\min \left(\frac{dm}{dt}, 0 \right) \left(\frac{N_g(\mathbf{x}, t)}{m_g - m_{g-1}} \right) \right]_g \\ &- \left[\max \left(\frac{dm}{dt}, 0 \right) \left(\frac{N_g(\mathbf{x}, t)}{m_{g+1} - m_g} \right) \right]_g + \left[\max \left(\frac{dm}{dt}, 0 \right) \left(\frac{N_g(\mathbf{x}, t)}{m_{g+1} - m_g} \right) \right]_{g-1} \end{aligned} \quad (4.42)$$

where the terms

$$b_g = \int_{m_{g-\frac{1}{2}}}^{m_{g+\frac{1}{2}}} \mathcal{B}(m, \mathbf{x}, t) dm \quad \text{and} \quad c_g = \int_{m_{g-\frac{1}{2}}}^{m_{g+\frac{1}{2}}} \mathcal{C}(m, \mathbf{x}, t) dm ,$$

model the *integroup* transfer due to breakup and coalescence respectively. An example of its discretization can be found in (CASTRO; CARRICA, 2013) for a bubbly fluid around a ship.

4.2.3 The Reynolds-Rayleigh-Plesset coupling

4.2.3.1 Modeling the bubble number density

In this Section the RRP coupling is presented by writing first simplified equation for the bubble number density $n_b(\mathbf{x}, t)$. For this, the next hypotheses are made

- The bubbles mass distribution is *monodispersed*. This means that locally there exist bubbles of one and only one mass $M(\mathbf{x}, t)$, which is written as:

$$f(m, \mathbf{x}, t) = n_b(\mathbf{x}, t) \delta(m - M(\mathbf{x}, t)), \quad (4.43)$$

where δ is the Dirac delta distribution.

- The bubbles transport velocity \mathbf{U}_b depends only on \mathbf{x} and t .
- Coalescence and breakup effects are disregarded. Thus b_g and c_g are set to zero in Eq. (4.42).
- The mass change rate is negligible, thus one takes $\frac{dm}{dt} = 0$ in Eq. (4.42). Observe that this is not necessarily true when considering the *Isothermal case with mass transfer* described at the beginning of Section 4.1.

With all this, Eq. (4.42) is reduced to

$$\frac{\partial n_b(\mathbf{x}, t)}{\partial t} + \nabla \cdot (\mathbf{U}_b(\mathbf{x}, t) n_b(\mathbf{x}, t)) = 0. \quad (4.44)$$

In general, in the literature it is also assumed that:

- \mathbf{U}_b is a known constant (in space and time).

Thus, Eq. (4.44) can be solved independently and n_b can be assumed to be a constant and datum of the model.

Remark 4.2. Altough there are some recent works where \mathbf{U}_b depends on time and space (SNYDER; BRAUN; PIERSON, 2016; BRAUN; PIERSON; SNYDER, 2017a) (particularly, on the pressure gradient), the authors have not considered Eq. (4.44) in their modeling.

4.2.3.2 The bubbles radii field $R(\mathbf{x}, t)$

In this modeling it is generally assumed that initially the bubbles are in equilibrium. Let us assume that at $t = 0$ the temperature is equal to T_{eq} and the pressure is equal to $p_{eq} > p_{cav}$ for every \mathbf{x} . Then, from Eq. (4.5) one observes that to suppose the bubbles have some initial monodisperse mass distribution

$$f(m, \mathbf{x}, t = 0) = n_b(\mathbf{x}, t) \delta(m - M_0(\mathbf{x})),$$

is equivalent to suppose the bubbles have some initial monodisperse radii distribution

$$g(r, \mathbf{x}, t = 0) = n_b(\mathbf{x}, t) \delta(r - R_0(\mathbf{x})).$$

This initial radii distribution is assumed to evolve according to a field $R(\mathbf{x}, t)$ that satisfies the Rayleigh-Plesset equation (4.1) but substituting the derivative \dot{R} by a material derivative

$$\frac{D}{Dt} = \frac{\partial}{\partial t} + (\mathbf{U}_b \cdot \nabla), \quad (4.45)$$

in order to account for the bubbles transport, and considering p_{bub} and p_∞ to depend on \mathbf{x} . Obtaining the equation

$$\rho_\ell \left[\frac{3}{2} \left(\frac{DR}{Dt} \right)^2 + R \frac{D^2 R}{Dt^2} \right] + 4 \left(\frac{\mu_\ell + \kappa^s/R}{R} \right) \frac{DR}{Dt} = p_{\text{bub}}(\mathbf{x}, t) - p_\infty(\mathbf{x}, t) - \frac{2\sigma}{R}. \quad (4.46)$$

4.2.3.3 The full RRP model

Equations (4.33) and (4.46) are coupled by adding the next hypotheses:

- The pressure field $p_\infty(\mathbf{x}, t)$ can be taken as the average pressure field $\bar{p}(\mathbf{x}, t)$ obtained by means of Eq. (4.33), computing $p_{\text{bub}}(t)$ along (4.6) or (4.7);
- The gas fraction $\alpha(\mathbf{x}, t)$, the bubble number density $n_b(\mathbf{x}, t)$, and the radii field $R(\mathbf{x}, t)$ accomplish the next geometrical relation (e.g., (DREW; PASSMAN, 1999) Section 10.1.2)

$$\alpha(\mathbf{x}, t) = n_b(\mathbf{x}, t) \frac{4}{3} \pi R(\mathbf{x}, t)^3. \quad (4.47)$$

In the literature one can find two ways to model $n_b(\mathbf{x}, t)$:

1. The model exposed in Section 4.2.3.1, where $n_b(\mathbf{x}, t)$ is assumed to accomplish Eq. (4.44);
2. The model where it is assumed that the number of bubbles per unit volume of liquid, denoted n_b^ℓ , is constant (ZWART; GERBER; BELAMR, 2004). Thus, using Eq. (4.47), the next relation is accomplished

$$n_b(\mathbf{x}, t) = n_b^\ell \alpha(\mathbf{x}, t) = n_b^\ell (1 - \alpha(\mathbf{x}, t)), \quad (4.48)$$

and then one obtains

$$\alpha(\mathbf{x}, t) = \frac{n_b^\ell \frac{4}{3} \pi R(\mathbf{x}, t)^3}{1 + n_b^\ell \frac{4}{3} \pi R(\mathbf{x}, t)^3}. \quad (4.49)$$

Remark 4.3. A notable difference between formulae (4.47) and (4.49) is that the former one is not necessarily bounded by the unit when R grows. This issue is regarded in the numerical implementation of this model in Chapter 6. On the other hand, for the theoretical results exposed in Chapter 5, it is assumed that the gas fraction α is a bounded function of R .

To simplify the exposition, hereafter we fix the modeling of $p_{\text{bub}}(t)$ by means of Eq. (4.6) (with $k = 1.4$). Thus, no mass transfer at the bubbles interface is considered.

With this consideration, the RRP cavitation model consists in solving the problem of:

“Find the fields $p(\mathbf{x}, t)$ and $R(\mathbf{x}, t) > 0$, with $\mathbf{x} \in \Omega$ and $t \geq 0$, accomplishing the system of equations

$$\begin{aligned} \nabla \cdot \left(\frac{\rho h^3}{12\mu} \nabla p \right) &= \nabla \cdot \left(\frac{\mathbf{U}}{2} \rho h \right) + \frac{\partial \rho h}{\partial t}, \\ p &= 0 \quad \text{on } \partial\Omega. \end{aligned} \quad (4.50)$$

$$\rho_\ell \left[\frac{3}{2} \left(\frac{D R}{D t} \right)^2 + R \frac{D^2 R}{D t^2} \right] + 4 \left(\frac{\mu_\ell + \kappa^s/R}{R} \right) \frac{D R}{D t} = \left(p_{\text{eq}} + \frac{2\sigma}{R_{\text{eq}}} \right) \left(\frac{R_{\text{eq}}}{R(t)} \right)^{3k} - (p + p_\partial) - \frac{2\sigma}{R(t)}, \quad (4.51)$$

where p_∂ is the boundary condition for p at $\partial\Omega$ and

$$\frac{D}{D t} = \frac{\partial}{\partial t} + (\mathbf{U}_b \cdot \nabla). \quad (4.52)$$

$\mathbf{U} \in \mathbb{R}^2$ is the surfaces relative velocity, and the bubbles transport velocity $\mathbf{U}_b \in \mathbb{R}^2$ depends on the application. Along the initial conditions for every $\mathbf{x} \in \bar{\Omega}$:

$$\begin{aligned} R(\mathbf{x}, 0) &= R_0(\mathbf{x}), \\ \frac{\partial R}{\partial t}(\mathbf{x}, 0) &= R_0^*(\mathbf{x}) \end{aligned} \quad (4.53)$$

with R_0 and R_0^* known regular functions and

$$\mu(R) = \alpha(R) \mu_g + (1 - \alpha(R)) \mu_\ell, \quad (4.54)$$

$$\rho(R) = \alpha(R) \rho_g + (1 - \alpha(R)) \rho_\ell. \quad (4.55)$$

And the gas fraction variable is given either by

$$\alpha(\mathbf{x}, t) = n_b(\mathbf{x}, t) \frac{4}{3} \pi R(\mathbf{x}, t)^3 \quad (4.56)$$

where $n_b(\mathbf{x}, t)$ accomplishes

$$\begin{aligned} \frac{\partial n_b(\mathbf{x}, t)}{\partial t} + \nabla \cdot (\mathbf{U}_b(\mathbf{x}, t) n_b(\mathbf{x}, t)) &= 0, \\ n_b(\mathbf{x}, 0) &= n_b^0(\mathbf{x}), \end{aligned} \quad (4.57)$$

and n_b^0 is a known regular function; or it is given by

$$\alpha(\mathbf{x}, t) = \frac{n_b^0 \frac{4}{3} \pi R(\mathbf{x}, t)^3}{1 + n_b^0 \frac{4}{3} \pi R(\mathbf{x}, t)^3}, \quad (4.58)$$

and proper conditions in time for the transport equations are specified at the inlet boundaries.”

In the next Chapter some mathematical properties of this cavitation model are studied, while its numerical implementation is presented in Chapter 6.



MATHEMATICAL ANALYSIS OF THE RRP COUPLING

This Chapter is devoted to the well-posedness of the Reynold-Rayleigh-Plesset cavitation model presented in Chapter 4 for the particular case where the transport velocity of the bubbles is null ($\mathbf{U}_b = 0$). Firstly, in Section 5.1, an abstract form of the RRP model written in Section 4.2.3.3 is presented. General hypotheses for that abstract form are identified and some auxiliary results on it are given. Afterward, the mathematical analysis is divided into two cases: 1) including inertial terms in the Rayleigh-Plesset equation and 2) disregarding these terms. For both cases the analysis is performed by transforming the 2-equations coupled system into a single evolution equation problem. Some mathematical tools (like the Implicit Mapping and the Cauchy-Lipschitz theorems) are given in Appendix B. In that Appendix the definitions of stability and instability and the associated results used here are also given.

The first case is studied in Section 5.2. A local existence in time is obtained and the existence of *non-trivial* stationary solutions is obtained by means of continuity arguments. The study without inertial terms continue by showing a stability result of these stationary solutions for the surfaces relative speed $\|\mathbf{U}\|$ small enough; finishing with a result of instability for flat surfaces for $\|\mathbf{U}\|$ big enough.

The analysis of the second case is exposed in Section 5.3. As in the first case, a local existence in time is proved and the existence of non-trivial stationary solutions is established. Remarkably, this time the stability result of these stationary solutions is obtained not only for the cases where $\|\mathbf{U}\|$ is small enough but also for surfaces near to flat.

The results presented here have been submitted in an article which preprint is available online ([JARAMILLO *et al.*, 2018](#)).

5.1 Mathematical framework

Let $\Omega \subset \mathbb{R}^N$, $N = 1, 2$, be a regular domain and consider the abstract problem of finding $p(\mathbf{x}, t)$, $R(\mathbf{x}, t) > 0$, with $\mathbf{x} \in \Omega$ and $t \geq 0$, such that

$$\frac{3}{2} \frac{1}{R} \left(\frac{\partial R}{\partial t} \right)^2 + \frac{\partial^2 R}{\partial t^2} = \frac{f_1(R) - p}{R} - \frac{\partial R}{\partial t} f_2(R) \quad (5.1)$$

and

$$\begin{aligned} \nabla \cdot (f_3(R) h^3 \nabla p) &= \nabla \cdot (f_4(R) \mathbf{U} h) + h f_5(R) \frac{\partial R}{\partial t}, \\ p &= 0 \quad \text{on } \partial\Omega, \end{aligned} \quad (5.2)$$

where $\mathbf{U} \in \mathbb{R}^N$. Along the initial conditions for every $\mathbf{x} \in \bar{\Omega}$:

$$\begin{aligned} R(\mathbf{x}, 0) &= R_0(\mathbf{x}), \\ \frac{\partial R}{\partial t}(\mathbf{x}, 0) &= R_0^*(\mathbf{x}), \end{aligned} \quad (5.3)$$

and R_0 , R_0^* are regular known functions. The terms in the left hand side of Eq. (5.1) are named *inertial terms*. In the next sections the well-posedness of problem (5.1)-(5.3) when including or disregarding the inertial terms is studied. For this, given $\alpha, \beta \in \mathbb{R}$ with $\alpha < \beta$ let us define:

$$B_{\alpha, \beta} = \{w \in L^\infty(\Omega) : \alpha \leq w \leq \beta \text{ a.e. on } \Omega\},$$

and assume also the following hypotheses on the auxiliary functions:

H1: $f_1 \in C^2(\mathbb{R}_*^+; \mathbb{R})$, $\exists \bar{R}, \delta_1 \in \mathbb{R}_*^+$ such that $f_1(\bar{R}) = 0$ and $f'_1(R) < 0 \forall R \in [\bar{R} - \delta_1, \bar{R} + \delta_1]$. And denote $m_1 = \min_{R \in [\bar{R} - \delta_1, \bar{R} + \delta_1]} |f'_1(R)|$ and $M_1 = \max_{R \in [\bar{R} - \delta_1, \bar{R} + \delta_1]} |f'_1(R)|$;

H2: $f_2 \in C^2(\mathbb{R}_*^+; \mathbb{R}_*^+)$;

H3: $f_3 \in C^2(\mathbb{R}_*^+; \mathbb{R})$ and $\exists m_3, M_3 > 0$ such that $m_3 \leq f_3(r) \leq M_3 \forall r \in \mathbb{R}^+$;

H4: $f_4 \in C^2(\mathbb{R}_*^+; \mathbb{R}^+)$, $f'_4(r) < 0 \forall r > 0$;

H5: $f_5 \in C^2(\mathbb{R}_*^+; \mathbb{R}_*^-)$;

H6: $h \in B_{m_0, M_0}$ for $0 < m_0 < M_0$ constants. And denote $h_0 = \text{ess-inf}_{\Omega} h$.

Remark 5.1. The physical model given by the system of Eqs. (4.50)-(4.55) and (4.58) (bounded $\alpha(R)$) is a particular case of the abstract problem given by Eqs. (5.1)-(5.3) for $\mathbf{u}_b = 0$ and

$$f_1(R) = \left(p_{\text{eq}} + \frac{2\sigma}{R_{\text{eq}}} \right) \left(\frac{R_{\text{eq}}}{R} \right)^{3k} - (p + p_\partial) - \frac{2\sigma}{R}, \quad (5.4)$$

$$\begin{aligned} f_2(R) &= 4 \left(\frac{\mu_\ell + \kappa^s/R}{R^2} \right), & f_3(R) &= \frac{1}{12} \frac{(1 - \alpha(R))\rho_\ell + \alpha(R)\rho_g}{(1 - \alpha(R))\mu_\ell + \alpha(R)\mu_g}, \\ f_4(R) &= \frac{1}{2} [\rho_\ell + \alpha(R)(\rho_g - \rho_\ell)], & f_5(R) &= f'_4(\alpha(R)) \alpha'(R). \end{aligned}$$

accomplishing all the hypotheses from H1 to H6.

The next result is a particular case of Theorem 4.2 in (BENSOUSSAN; LIONS; PAPANI-COLAOU, 1978). It will be useful in order to fix a Sobolev Space (ADAMS, 1975) $W^{1,q}(\Omega)$ (with $q > 2$) to be used along this Chapter.

Lemma 5.1. Let Ω be a smooth domain on \mathbb{R}^N , $f \in H^{-1}(\Omega)$ and $u \in H_0^1(\Omega)$ be the unique solution of the elliptic problem

$$\begin{aligned} \nabla \cdot (a \nabla u) &= f && \text{in } \Omega, \\ u &= 0 && \text{on } \partial\Omega, \end{aligned}$$

for $a \in B_{\alpha,\beta}$, $0 < \alpha < \beta$. Then there exists $q > 2$ (which depends on α, β, Ω and on the dimension N) such that, if $f \in W^{-1,q}(\Omega)$, then u belongs to $W_0^{1,q}(\Omega)$ and satisfies

$$\|u\|_{W_0^{1,q}(\Omega)} \leq C \|f\|_{-1,q},$$

where $C = C(\alpha, \beta, \Omega, N)$.

Now, the following open subset $Q \subset C(\bar{\Omega})$ is defined

$$Q = \left\{ R \in C(\bar{\Omega}) : R(\mathbf{x}) > 0 \quad \forall \mathbf{x} \in \bar{\Omega} \right\}, \quad (5.5)$$

and set $q > 2$ given by Lemma 5.1 with $\alpha = m_0^3 m_3 \min\{m_1, 1\}$ and $\beta = M_0^3 M_3 \max\{M_1, 1\}$.

In order to write Problem (5.1)-(5.3) as a Cauchy problem, it is useful to introduce the following decomposition of the solution Eq. (5.2):

$$\begin{aligned} A : Q \times C(\bar{\Omega}) &\longrightarrow C(\bar{\Omega}) \\ (R_1, R_2) &\longrightarrow A_1(R_1) + A_2(R_1, R_2), \end{aligned} \quad (5.6)$$

where $A_1 : Q \mapsto C(\bar{\Omega})$ is such that $A_1(R_1)$ is the unique solution of the elliptic problem

$$\begin{aligned} \nabla \cdot (h^3 f_3(R_1) \nabla A_1(R_1)) &= \nabla \cdot (\mathbf{U} h f_4(R_1)) && \text{in } \Omega, \\ A_1(R_1) &= 0 && \text{on } \partial\Omega, \end{aligned} \quad (5.7)$$

and $A_2 : Q \times C(\bar{\Omega}) \mapsto C(\bar{\Omega})$ is such that $A_2(R_1, R_2)$ is the unique solution of the elliptic problem

$$\begin{aligned} \nabla \cdot (h^3 f_3(R_1) \nabla A_2(R_1, R_2)) &= h f_5(R_1) R_2 && \text{in } \Omega, \\ A_2(R_1, R_2) &= 0 && \text{on } \partial\Omega. \end{aligned} \quad (5.8)$$

Next, some of the properties of this decomposition are given.

Remark 5.2. Both the solutions of (5.7) and (5.8) are in $C(\bar{\Omega})$ since $W^{1,p}(\Omega) \subset C(\bar{\Omega})$ continuously for any $p > N$.

Remark 5.3. For any $R_1 \in Q$, $A_2(R_1, \cdot)$ is a bounded linear operator.

Lemma 5.2. The application A is of class C^2 from $Q \times C(\bar{\Omega})$ into $C(\bar{\Omega})$.

Proof. Define $\phi : Q \times C(\bar{\Omega}) \times W_0^{1,q}(\Omega) \mapsto W^{-1,q}(\Omega)$ by

$$\phi(R_1, R_2, p) = \nabla \cdot (h^3 f_3(R_1) \nabla p) - \nabla \cdot (\mathbf{U} h f_4(R_1)) - h f_5(R_1) R_2. \quad (5.9)$$

It is shown first that ϕ is of class C^2 . Since f_3 , f_4 and f_5 are of class C^2 , it is enough to prove that the application $\phi^1 : C(\bar{\Omega})^4 \times W_0^{1,q}(\Omega) \mapsto W^{-1,q}(\Omega)$ defined by

$$\phi^1(\xi_1, \xi_2, \xi_3, \xi_4, w) = \nabla \cdot (h^3 \xi_1 \nabla w) - \nabla \cdot (\mathbf{U} h \xi_2) - h \xi_3 \xi_4$$

is of class C^2 , which follows from observing that its first and third terms are quadratic and the second one is linear.

By the Lax-Milgram Theorem and Lemma 5.1 the partial derivative

$$\begin{aligned} \frac{\partial \phi}{\partial p}(R_1, R_2, p)(z) : W_0^{1,q}(\Omega) &\longrightarrow W^{-1,q}(\Omega) \\ z &\longrightarrow \nabla \cdot (h^3 f_3(R_1) \nabla z) \end{aligned}$$

is an isomorphism. Therefore, the result follows from noticing that

$$\phi(R_1, R_2, A(R_1, R_2)) = 0 \quad \forall (R_1, R_2) \in Q \times C(\bar{\Omega}),$$

and applying the Implicit Mapping Theorem B.2 to the application ϕ . \square

For a linear operator \mathcal{L} , $\text{Vp}(\mathcal{L})$ denotes its set of eigenvalues and $\text{Sp}(\mathcal{L})$ denotes its spectrum. The following result will be useful to extend the stability of trivial stationary solutions for non-trivial stationary solutions.

Lemma 5.3. Let X be a Banach space, let A be a bounded linear operator on X and $\epsilon > 0$. Then there exists $\delta > 0$ such that, if B is a bounded linear operator on X and $\|A - B\| < \delta$, then for every $\lambda \in \text{Sp}(B)$ there exists $\xi \in \text{Sp}(A)$ such that $|\lambda - \xi| < \epsilon$.

For a detailed proof of the previous Lemma the reader is referred to Lemma 3 in (DUNFORD; SCHWARTZ, 1957).

5.2 Well-posedness with inertial terms

This section begins by giving a local solution in time for problem (5.1)-(5.3) that follows directly from the Cauchy-Lipschitz Theorem B.3. After that, in Section 5.2.3 stability results are established for trivial solutions, i.e., obtained for flat surfaces or $\mathbf{U} = 0$. This stability is extended for non-trivial stationary solutions by means of the Implicit Mapping Theorem B.2.

5.2.1 Existence of a local solution

Let us denote $R_1 = R$, $R_2 = \frac{\partial R}{\partial t}$ and $\tilde{R} = \begin{pmatrix} R_1 \\ R_2 \end{pmatrix}$. Then, the problem (5.1)-(5.3) can be rewritten as

$$\begin{aligned} \frac{d\tilde{R}}{dt} &= F(\tilde{R}), \\ \tilde{R}(0) &= \tilde{R}_0, \end{aligned} \tag{5.10}$$

where $\tilde{R}_0 = \begin{pmatrix} R_0 \\ R_0^* \end{pmatrix} \in Q \times C(\bar{\Omega})$ and $F : Q \times C(\bar{\Omega}) \mapsto (C(\bar{\Omega}))^2$ with

$$F(R_1, R_2) = \begin{pmatrix} R_2 \\ -\frac{3}{2}\frac{R_2^2}{R_1} - R_2 f_2(R_1) + \frac{f_1(R_1) - A(R_1, R_2)}{R_1} \end{pmatrix}. \tag{5.11}$$

By means of Lemma 5.2 one has that F is of class C^2 . Thus, from the Cauchy-Lipschitz Theorem the next local existence and uniqueness result is obtained:

Theorem 5.1. There exists $T > 0$ such that the problem (5.10) has a unique solution in $C^3([0, T]; Q \times C(\bar{\Omega}))$.

5.2.2 Existence of stationary solutions

Observe that a stationary solution (R_s, p_s) of problem (5.1)-(5.2) satisfies $p_s = f_1(R_s)$. For the next result, let us denote $h^+ = h - h_0$ (notice that $h^+ = 0$ if and only if h is constant). Thus (R_s, p_s) is solution of the system

$$\begin{aligned} \nabla \cdot ((h^+ + h_0)^3 f_3(R_s) \nabla p_s) &= \nabla \cdot (\mathbf{U}(h^+ + h_0) f_4(R_s)) && \text{in } \Omega, \\ p_s &= f_1(R_s) && \text{in } \Omega, \\ p_s &= 0 && \text{on } \partial\Omega. \end{aligned} \tag{5.12}$$

Notice that in the particular case $h^+ = 0$ or $\mathbf{U} = 0$, $(R_s, p_s) = (\bar{R}, 0)$ is solution of (5.12), with \bar{R} given in (H1).

Theorem 5.2. Fix $\mathbf{U} \in \mathbb{R}^2$ and $h_0 > 0$. Then the problem (5.12) has a unique solution (R_s, p_s) with $R_s > 0$ whenever $\|h^+\|_\infty$ is small enough. Moreover, the solution (R_s, p_s) depends continuously on h^+ .

Proof. Use first the relation $p_s = f_1(R_s)$ to rewrite the stationary problem. Since $\nabla p_s = f'_1(R_s) \nabla R_s$, making the change of variable $R_s = \bar{R} + \xi$ problem (5.12) can be written in function of ξ as

$$\begin{aligned} -\nabla \cdot ((h^+ + h_0)^3 a_0(\xi) \nabla \xi) &= \nabla \cdot (\mathbf{U} h^+ b_0(\xi)) + \nabla \cdot (\mathbf{U} h_0 b_0(\xi)) && \text{in } \Omega, \\ \xi &> -\bar{R} && \text{in } \Omega, \\ \xi &= 0 && \text{on } \partial\Omega, \end{aligned} \tag{5.13}$$

where $a_0(\xi) = -f_3(\bar{R} + \xi)f'_1(\bar{R} + \xi)$, and $b_0(\xi) = f_4(\bar{R} + \xi)$. We introduce the set

$$W = \left\{ \xi \in W_0^{1,q}(\Omega) : \text{ess-inf}_{\Omega} \xi > -\bar{R} \right\},$$

which is open since the continuous embedding $W_0^{1,q} \subset C(\bar{\Omega})$, and the application

$$\begin{aligned} \phi_2 : W \times L^\infty(\Omega) &\longmapsto W^{-1,q}(\Omega) \\ (\xi, \delta) &\longmapsto \nabla \cdot ((\delta + h_0)^3 a_0(\xi) \nabla \xi) + \nabla \cdot (\mathbf{U} \delta b_0(\xi)) + \nabla \cdot (\mathbf{U} h_0 b_0(\xi)). \end{aligned} \quad (5.14)$$

Using an argument analogous to the one used in Lemma 5.2 to prove that ϕ^1 is of class C^2 , it is possible to prove that ϕ_2 is of class C^2 . Now noticing that $\phi_2(0, 0) = 0$, let us assume that $\frac{\partial \phi_2}{\partial \xi}(0, 0)$ is invertible. Then, by means of the Implicit Mapping Theorem, one has that

- $\exists V_1 \subset W$ neighborhood of 0 on $W_0^{1,q}(\Omega)$; V_2 neighborhood of 0 on $L^\infty(\Omega)$;
- $\exists \psi : V_2 \longmapsto V_1$ function of class C^1 such that $\forall \delta \in V_2$, $\psi(\delta)$ is solution of problem (5.13). Equivalently, $(R_s, p_s) = (\bar{R} + \psi(\delta), f_1(\bar{R} + \psi(\delta)))$ is solution of problem (5.12).

which is the result desired as the existence of V_2 can also be described as $\|h^+\|_\infty$ small enough.

It only remains to show that $\frac{\partial \phi_2}{\partial \xi}(0, 0)$ is invertible. Indeed, $\forall z \in W_0^{1,q}(\Omega)$ it holds that

$$\begin{aligned} \frac{\partial \phi_2}{\partial \xi}(0, 0)(z) &= \nabla \cdot \left((h_0 + \delta)^3 (a_0(\xi) \nabla z + a'_0(\xi) z \nabla \xi) + (h_0 + \delta) b'_0(\xi) \mathbf{U} z \right) \Big|_{(\xi, \delta)=(0,0)} \\ &= \nabla \cdot (h_0^3 a_0(0) \nabla z + h_0 b'_0(0) \mathbf{U} z). \end{aligned}$$

Fixing an arbitrary $g \in W^{-1,q}(\Omega)$ and denoting $\ell = h_0 b'_0(0) \mathbf{U} \in \mathbb{R}^2$, there exists a unique $z \in W_0^{1,q}(\Omega)$ such that

$$\nabla \cdot (h_0^3 a_0(0) \nabla z + \ell z) = g \quad \text{in } \Omega.$$

In fact, since $g \in H^{-1}(\Omega)$, $a_0(0) > 0$ and $h_0 > 0$ (see (H1) and (H3)), by means of the Lax-Milgram Theorem the variational problem

$$-\int_{\Omega} (h_0^3 a_0(0) \nabla z + \ell z) \cdot \nabla \phi d\Omega = \int_{\Omega} g \phi d\Omega \quad \forall \phi \in H_0^1(\Omega),$$

has a unique solution $z \in H_0^1(\Omega)$. Moreover, from the continuous inclusion $H^1(\Omega) \subset L^q(\Omega)$, we have $\nabla \cdot (\ell z) \in W^{-1,q}(\Omega)$ and thus $z \in W_0^{1,q}(\Omega)$ by Lemma 5.1. \square

A proof analogous to the one of Theorem 5.2 may be written for the next result:

Theorem 5.3. Fix $h \in B_{m_0, M_0}$, $0 < m_0 < M_0$. Then there exists $\epsilon(h) > 0$ such that the problem (5.12) has a unique solution (R_s, p_s) with $R_s > 0$ whenever $\|\mathbf{U}\| < \epsilon(h)$. Moreover, the solution (R_s, p_s) depends continuously on \mathbf{U} .

5.2.3 Stability Analysis

Recalling the application F given by (5.11) and the stationary solution (R_s, p_s) introduced in the previous section, \mathcal{L}_F denotes the Fréchet derivative of F at $(R_s, 0)$, i.e.,

$$\begin{aligned} \mathcal{L}_F : \quad & \left(C(\bar{\Omega}) \right)^2 \mapsto \left(C(\bar{\Omega}) \right)^2 \\ (S_1, S_2) \quad & \mapsto D F(R_s, 0)(S_1, S_2). \end{aligned} \quad (5.15)$$

Here it will show the stability of the stationary solution in some particular cases. For this, it is shown that the spectrum of \mathcal{L}_F is such that $\operatorname{Re}(\lambda) < 0 \ \forall \lambda \in \operatorname{Sp}(\mathcal{L}_F) \setminus \{0\}$. Previously, some computations are performed.

Recalling that $f_1(R_s) = p_s = A(R_s, 0)$, one obtains:

$$(\mathcal{L}_F(S_1, S_2))_1 = S_2, \quad (5.16)$$

$$\begin{aligned} (\mathcal{L}_F(S_1, S_2))_2 = & \frac{f'_1(R_s) S_1}{R_s} - \frac{1}{R_s} (D_1 A(R_s, 0)(S_1) + D_2 A(R_s, 0)(S_2)) + \\ & + \frac{1}{R_s^2} A(R_s, 0) S_1 - f_2(R_s) S_2. \end{aligned} \quad (5.17)$$

Since $A_2(R, 0) = 0$ for any R in Q , we have that $D_1 A(R_s, 0) = D A_1(R_s)$. With this, deriving (5.7) with respect to R_1 and denoting $\pi_1(S_1) = D_1 A(R_s, 0)(S_1)$ one obtains that $\pi_1(S_1)$ is the solution of

$$\begin{aligned} -\nabla \cdot (h^3 f_3(R_s) \nabla \pi_1(S_1)) &= \nabla \cdot (h^3 f'_3(R_s) S_1 \nabla A_1(R_s) - \mathbf{U} h f'_4(R_s) S_1), \\ \pi_1(S_1) &= 0 \quad \text{on } \partial\Omega. \end{aligned} \quad (5.18)$$

Similarly, there holds that $D_2 A(R_s, 0)(S_2) = D_2 A_2(R_s, 0)(S_2) = A_2(R_s, S_2)$. Thus, denoting $\pi_2(S_2) = D_2 A(R_s, 0)(S_2)$ one obtains that $\pi_2(S_2)$ is the solution of

$$\begin{aligned} -\nabla \cdot (h^3 f_3(R_s) \nabla \pi_2(S_2)) &= -h f_5(R_s) S_2 \quad \text{in } \Omega, \\ \pi_2(S_2) &= 0 \quad \text{on } \partial\Omega. \end{aligned} \quad (5.19)$$

Remark 5.4. Since $q > 2$, one of the Sobolev Embeddings (Rellich-Kondrachov Theorem, (ADAMS, 1975), Chapter VI) implies that both π_1 and π_2 are compact operators from $C(\bar{\Omega})$ into itself.

For the next results, let us introduce the notations: $b_1 = -f'_1(\bar{R})\bar{R}^{-1} > 0$, $b_2 = f_2(\bar{R}) > 0$, $b_r = 1/\bar{R}$, $b_3 = f_3(\bar{R})$, $b_4 = -f'_4(\bar{R})$ and $b_5 = -f_5(\bar{R})$. All positive constants as follows from (H1)-(H5).

Remark 5.5. If $h^+ = 0$ or $\mathbf{U} = 0$. Then $A_1(R_s) = 0$. Therefore $A(R_s, 0) = p_s = 0$, $R_s = \bar{R}$, and $\mathcal{L}_F(S_1, S_2)$ can be written

$$\mathcal{L}_F(S_1, S_2) = B \begin{pmatrix} S_1 \\ S_2 \end{pmatrix} - b_r \begin{pmatrix} 0 \\ \pi_1(S_1) + \pi_2(S_2) \end{pmatrix}, \quad (5.20)$$

where $B = \begin{pmatrix} 0 & 1 \\ -b_1 & -b_2 \end{pmatrix}$. Moreover, Eq. (5.18) reads

$$\begin{aligned} -b_3 \nabla \cdot (h^3 \nabla \pi_1(S_1)) &= b_4 \nabla \cdot (\mathbf{U} h S_1) && \text{in } \Omega, \\ \pi_1(S_1) &= 0 && \text{on } \partial\Omega. \end{aligned} \quad (5.21)$$

The set of eigenvalues of B are denoted by $\{\lambda_1^B, \lambda_2^B\}$. Notice that $\operatorname{Re}(\lambda_1^B) < 0$ and $\operatorname{Re}(\lambda_2^B) < 0$.

Lemma 5.4. Let $h^+ = 0$ or $\mathbf{U} = 0$. Then

$$\operatorname{Sp}(\mathcal{L}_F) \subset \operatorname{Vp}(\mathcal{L}_F) \cup \{\lambda_1^B, \lambda_2^B\}.$$

Moreover if $\lambda \in \operatorname{Vp}(\mathcal{L}_F) \setminus \{\lambda_1^B, \lambda_2^B\}$ with associated eigenfunction $(S_1, S_2) \in C(\bar{\Omega})^2$ then $(S_1, S_2) \in H_0^1(\Omega)^2$, $S_2 = \lambda S_1$ and S_1 is solution of the problem

$$\frac{b_3}{b_r} \xi(\lambda) \nabla \cdot (h^3 \nabla S_1) = b_4 \mathbf{U} \cdot \nabla (h S_1) + \lambda b_5 h S_1 \quad \text{in } \Omega, \quad (5.22)$$

$$S_1 = 0 \quad \text{on } \partial\Omega, \quad (5.23)$$

where $\xi(\lambda) = \lambda^2 + b_2 \lambda + b_1$ with roots $\{\lambda_1^B, \lambda_2^B\}$.

Proof. Remind that $p_s = A(R_s, 0) = 0$ and $R_s = \bar{R}$. From Eq. (5.20), the next equation is accomplished for any $\lambda \in \mathbb{C} \setminus \{\lambda_1^B, \lambda_2^B\}$

$$(\mathcal{L}_F - \lambda I) \begin{pmatrix} S_1 \\ S_2 \end{pmatrix} = (B - \lambda I) \left[\begin{pmatrix} S_1 \\ S_2 \end{pmatrix} - b_r (B - \lambda I)^{-1} \begin{pmatrix} 0 \\ \pi_1(S_1) + \pi_2(S_2) \end{pmatrix} \right].$$

Since the map $(S_1, S_2) \mapsto \pi_1(S_1) + \pi_2(S_2)$ is compact, by means of the Fredholm alternative Theorem the mapping at the right hand side of this equation (from $C(\bar{\Omega})^2$ into itself) is injective if and only if it is surjective, therefore $\operatorname{Sp}(\mathcal{L}_F) \subset \operatorname{Vp}(\mathcal{L}_F) \cup \{\lambda_1^B, \lambda_2^B\}$.

Fix now $\lambda \in \operatorname{Vp}(\mathcal{L}_F) \setminus \{\lambda_1^B, \lambda_2^B\}$ with associated eigenvector $(S_1, S_2) \neq (0, 0)$, then

$$\begin{aligned} S_2 &= \lambda S_1, \\ -b_1 S_1 - b_2 S_2 - b_r [\pi_1(S_1) + \pi_2(S_2)] &= \lambda S_2. \end{aligned}$$

From which it holds that

$$\pi_2(\lambda S_1) + \pi_1(S_1) = -\frac{\xi(\lambda)}{b_r} S_1.$$

Since $\xi(\lambda) \neq 0$ and from the definitions of π_1 and π_2 it is deduced that $(S_1, S_2) \in H_0^1(\Omega)^2$. Then, Eqs. (5.22)-(5.23) are obtained using this last relation along with Eq. (5.19) and Eq. (5.21). \square

Theorem 5.4. Let h be as in Theorem 5.3. Then there exists $\epsilon = \epsilon(h) > 0$ such that if $\|\mathbf{U}\|_\infty < \epsilon$ the solution (R_s, p_s) of problem (5.12) is asymptotically stable for the evolution problem (5.10).

Proof. Assume first $\mathbf{U} = 0$ and denote $\mathcal{L}_F^0 = \mathcal{L}_F|_{\mathbf{U}=0}$. Then for that particular case and due to Lemma 5.4 it is enough to study the eigenvalues of \mathcal{L}_F^0 . Thus, take $\lambda \in \text{Vp}(\mathcal{L}_F) \setminus \{\lambda_1^B, \lambda_2^B\}$ with associated eigenfunction (S_1, S_2) , from Lemma 5.4 we have $S_2 = \lambda S_1$ and $S_1 \in H_0^1(\Omega)$ accomplishing Eqs. (5.22) and (5.23), which read

$$\begin{aligned} \frac{b_3}{b_r} \xi(\lambda) \nabla (h^3 \nabla S_1) &= \lambda b_5 h S_1 \quad \text{in } \Omega, \\ S_1 &= 0 \quad \text{on } \partial\Omega. \end{aligned}$$

Since $\xi(\lambda)$ is not null we deduce that $\lambda \neq 0$, otherwise (S_1, S_2) would be null. Then, it is obtained that S_1 accomplishes the next variational formulation

$$-\frac{b_3}{b_r} \frac{\xi(\lambda)}{\lambda} \int_{\Omega} h^3 \nabla S_1 \nabla \phi \, d\Omega = b_5 \int_{\Omega} h S_1 \phi \, d\Omega \quad \forall \phi \in H_0^1(\Omega). \quad (5.24)$$

Taking $\phi = S_1$ one obtains $\gamma = -\xi(\lambda)/\lambda \in \mathbb{R}^+$ and since λ accomplishes the equation $\lambda^2 + (\gamma + b_2)\lambda + b_1 = 0$ it is obtained that $\text{Re}(\lambda) < 0$. The result has been proved for the case $\mathbf{U} = 0$.

For the general case, observe from Theorem 5.3 that the mapping $\mathbf{U} \mapsto R_s(\mathbf{U})$ is continuous in a neighborhood $V_1 \ni 0$ in \mathbb{R}^2 , thus if $\mathbf{U} \rightarrow 0$ in \mathbb{R}^2 then

$$\|DF(R_s(\mathbf{U}), 0) - DF(\bar{R}, 0)\| \rightarrow 0$$

in the space of linear continuous operators from $C(\bar{\Omega})^2$ into itself. Then the result follows from Lemma 5.3 and Theorem B.4. \square

Now, a result of instability for $\|\mathbf{U}\|$ big enough is proved.

Theorem 5.5. Set $h^+ = 0$ and consider the one-dimensional case ($N = 1$). Then there exists $M > 0$ such that if $\|\mathbf{U}\|_\infty > M$ the solution (R_s, p_s) of problem (5.12) is unstable for the evolution problem (5.10).

Proof. Denote $U = \mathbf{U} \in \mathbb{R}$. Let us assume $\Omega = [0, 1]$. Due to Lemma 5.4 it is enough to study the eigenvalues of \mathcal{L}_F . Fix now $\lambda \in \text{Vp}(\mathcal{L}_F) \setminus \{\lambda_1^B, \lambda_2^B\}$ with associated eigenvector $(S_1, S_2) \neq (0, 0)$. Now defining $\gamma_1, \gamma_2 \in \mathbb{C}$ by

$$\gamma_1 = -\frac{b_4 b_r}{h_0^2 b_3 \xi(\lambda)}, \quad \gamma_2 = -\frac{b_5 b_r \lambda}{h_0^2 b_3 \xi(\lambda)},$$

from Eqs. (5.22) and (5.23) S_1 satisfies

$$S_1'' + \gamma_1 U S_1' + \gamma_2 S_1 = 0, \quad S_1(0) = S_1(1) = 0.$$

Therefore, $\lambda \neq 0$. In fact, if $\lambda = 0$ then $\gamma_2 = 0$ and thus $S_1 = 0, S_2 = \lambda S_1 = 0$, which is not possible. Now, the roots of the characteristic polynomial, $P(r) = r^2 + \gamma_1 Ur + \gamma_2$, of the last equation are denoted by r_1, r_2 . Notice first that $r_1 \neq r_2$, otherwise S_1 would be null. Thus, S_1 can be written

$$S_1(x) = C_1 \exp(r_1 x) + C_2 \exp(r_2 x),$$

and the boundary conditions imply

$$\begin{aligned} C_1 + C_2 &= 0, \\ C_1 \exp r_1 + C_2 \exp r_2 &= 0. \end{aligned}$$

Since $(C_1, C_2) \neq (0, 0)$ one obtains that

$$\det \begin{pmatrix} 1 & 1 \\ \exp r_1 & \exp r_2 \end{pmatrix} = 0,$$

hence r_1 and r_2 satisfy the equation $r_2 - r_1 = 2k\pi i \forall k \in \mathbb{N}^*$, from which it is possible to compute the next relation

$$(r_1 + r_2)^2 - 4r_1 r_2 = -4k^2\pi^2, \quad \forall k \in \mathbb{N}^*.$$

Using the fact that the $r_1 + r_2 = -\gamma_1 U$ and $r_1 r_2 = \gamma_2$ one obtains that λ is root of the fourth degree polynomial given by

$$\begin{aligned} P_k(\lambda) &= 4k^2\pi^2\lambda^4 + (4\sigma_2 + 8\pi^2k^2b_2)\lambda^3 + (4\sigma_2b_2 + 4\pi^2k^2(b_2^2 + 2b_1))\lambda^2 + \\ &\quad + (4\sigma_2b_1 + 8\pi^2k^2b_1b_2)\lambda + 4\pi^2k^2b_1^2 + \sigma_1U^2, \end{aligned}$$

where $\sigma_1 = \frac{b_2^2 b_r^2}{b_3^2 h_0^4}$ and $\sigma_2 = \frac{b_5 b_r}{b_3 h_0^2}$ are both positive constants. Rewriting this polynomial as $P_k(\lambda) = \alpha_0\lambda^4 + \beta_0\lambda^3 + \alpha_1\lambda^2 + \beta_1\lambda + \alpha_2$, let us now denote the Hurwitz determinants associated to P_k :

$$\Delta_1 = \det(\beta_0), \quad \Delta_2 = \det \begin{pmatrix} \beta_0 & \beta_1 \\ \alpha_0 & \alpha_1 \end{pmatrix}, \quad \Delta_3 = \det \begin{pmatrix} \beta_0 & \beta_1 & 0 \\ \alpha_0 & \alpha_1 & \alpha_2 \\ 0 & \beta_0 & \beta_1 \end{pmatrix}, \quad \Delta_4 = \det \begin{pmatrix} \beta_0 & \beta_1 & 0 & 0 \\ \alpha_0 & \alpha_1 & \alpha_2 & 0 \\ 0 & \beta_0 & \beta_1 & 0 \\ 0 & \alpha_0 & \alpha_1 & \alpha_2 \end{pmatrix}.$$

Then one obtains $\Delta_1 = 4\sigma_2 + 8\pi^2k^2b_2$, $\Delta_2 = (4\sigma_2 + 8\pi^2k^2b_2)(4\sigma_2b_2 + 4\pi^2k^2(b_2^2 + b_1))$,

$$\begin{aligned} \Delta_3 &= (320b_1b_2^2\pi^2k^2 - 16\sigma_1U^2)\sigma_2^2 + (512b_1b_2^3\pi^4k^4 - 64b_2\pi^2\sigma_1U^2k^2)\sigma_2 - 64b_2^2\pi^4k^4\sigma_1U^2 + \\ &\quad + 256b_1b_2^4\pi^6k^6 + 64b_1b_2\sigma_2^3, \end{aligned}$$

and $\Delta_4 = \alpha_2\Delta_3$. According to the Routh-Hurwitz Theorem ([GANTMACHER, 1959](#)) the number of roots of the polynomial P_k with positive real part is equal to the total number of changes of sign in the sequence $\{\alpha_0, \Delta_1, \frac{\Delta_2}{\Delta_1}, \frac{\Delta_3}{\Delta_2}, \frac{\Delta_4}{\Delta_3}\}$. One may compute $\alpha_0 > 0$, $\Delta_1 > 0$, $\frac{\Delta_2}{\Delta_1} > 0$, $\frac{\Delta_4}{\Delta_3} > 0$ and $\frac{\Delta_3}{\Delta_2} < 0$ for $|U|$ big enough, which ends the proof recalling that $\text{Vp}(\mathcal{L}_F) \subset \text{Sp}(\mathcal{L}_F)$ and Theorem B.5. \square

5.3 Well-posedness without inertial terms

Disregarding the inertial terms in Eq. (5.1) (e.g., (NATSUMEDA; SOMEYA, 1987; SNYDER; BRAUN; PIERSON, 2016; BRAUN; PIERSON; SNYDER, 2017b)), the following simplified version of the Rayleigh-Plesset equation is obtained

$$\frac{\partial R}{\partial t} = \frac{f_1(R) - p}{R f_2(R)}, \quad (5.25)$$

along the initial condition

$$R(\mathbf{x}, 0) = R_0(\mathbf{x}) \quad \forall \mathbf{x} \in \Omega, \quad (5.26)$$

where $R_0 \in C(\bar{\Omega})$ known and $p \in W_0^{1,q}(\Omega)$ is the solution of (5.2).

When disregarding the inertial terms the proof of existence of a local solution in time, presented in Section 5.3.1, is more involved. Indeed, compared to Theorem 5.1, which followed directly from the Cauchy-Lipschitz Theorem, this time the Fredholm alternative Theorem is needed to express problem (5.25)-(5.26) as a Cauchy problem.

Observe that the existence of non-trivial stationary solutions for problem (5.25)-(5.26) was already established in theorems 5.2 and 5.3. In Section 5.3.2 a similar analysis to the one performed in Section 5.2.1 is made, a worth-notice difference is that this time there is no explicit expression for the derivative of the right hand side of the Cauchy problem. Instead, a differential equation for it is obtained (see Eq. (5.32)) and again the Fredholm alternative Theorem is used to study the spectrum of that derivative.

5.3.1 Existence of a local solution

Firstly, let us prove that from (5.25) the derivative $\partial R / \partial t$ can be expressed in terms of R . In fact, denoting $R_1 = R$, $R_2 = \frac{\partial R}{\partial t}$, recall the decomposition

$$p = A(R_1, R_2) = A_1(R_1) + A_2(R_1, R_2),$$

with A_1 and A_2 as in (5.7) and (5.8) respectively. Then, defining $\Pi : Q \times C(\bar{\Omega}) \mapsto C(\bar{\Omega})$ by

$$\Pi(R_1, R_2) = \frac{f_1(R_1) - A_1(R_1) - A_2(R_1, R_2)}{R_1 f_2(R_1)}, \quad (5.27)$$

the following result is obtained:

Lemma 5.5. Given $R \in Q$, there exists a unique $G(R) \in C(\bar{\Omega})$ such that

$$G(R) = \Pi(R, G(R)),$$

and the mapping $R \mapsto G(R)$ is of class C^2 .

Proof. Fix $R \in Q$, it will be shown that there exists a unique $S \in C(\bar{\Omega})$ such that $S = \Pi(R, S)$. Using (5.27), notice first that the equation $S = \Pi(R, S)$ is equivalent to

$$S + \frac{A_2(R, S)}{Rf_2(R)} = \frac{f_1(R) - A_1(R)}{Rf_2(R)},$$

and denote by $J : C(\bar{\Omega}) \mapsto C(\bar{\Omega})$ the linear mapping $S \mapsto S + A_2(R, S) / (Rf_2(R))$. To prove the existence of a unique solution for the last equation J is proved to be bijective, which gives the existence of G by taking $G(R) = S$. Now, since the mapping $S \mapsto A_2(R, S)$ is compact, by means of the Fredholm alternative Theorem it is enough to prove that J is injective. Indeed, let us take $w \in C(\bar{\Omega})$ such that $J(w) = 0$, then

$$Rf_2(R)w + A_2(R, w) = 0.$$

Multiplying this equation by $-f_5(R)hw$ and integrating by parts one has

$$\int_{\Omega} Rf_2(R)(-f_5(R))hw^2 d\Omega + \int_{\Omega} (-f_5(R))hA_2(R, w)w d\Omega = 0. \quad (5.28)$$

Now, multiplying (5.8) by $A_2(R_1, R_2)$, integrating and using (H5), the next relation is accomplished by any $(R_1, R_2) \in Q \times C(\bar{\Omega})$:

$$\int_{\Omega} (-f_5(R_1))hA_2(R_1, R_2)R_2 d\Omega \geq 0. \quad (5.29)$$

Taking $R_1 = R$ and $R_2 = w$ in the last equation and carrying that into Eq. (5.28) we obtain $w = 0$. Therefore J is injective.

Next, it is proved that G is of class C^2 . For this, define the mapping $\Phi : Q \times C(\bar{\Omega}) \mapsto C(\bar{\Omega})$ such that

$$\Phi(R, S) = S - \Pi(R, S),$$

which is of class C^2 since all the involved functions are regular enough. Now, fixing some arbitrary $(R_*, S_*) \in Q \times C(\bar{\Omega})$ such that $\Phi(R_*, S_*) = 0$ we have for any $w \in C(\bar{\Omega})$

$$\frac{\partial \Phi}{\partial S}(R_*, S_*)(w) = w + \frac{A_2(R_*, w)}{R_*f_2(R_*)} = J(w).$$

From where we obtain that $\frac{\partial \Phi}{\partial S}(R_*, S_*)$ is an automorphism on $C(\bar{\Omega})$. Thus, it is obtained that G is of class C^2 by means of the Implicit Mapping theorem. \square

Theorem 5.6. There exists $T > 0$ such that problem (5.2)-(5.25)-(5.26) has a unique solution in $C^3([0, T]; Q)$.

Proof. The result follows directly from applying the Cauchy-Lipschitz Theorem to the equivalent Cauchy problem

$$\frac{\partial R}{\partial t} = G(R), \quad (5.30)$$

along the initial condition (5.26). \square

5.3.2 Stability analysis

Let us notice the stationary solution of (5.25) is also the couple (R_s, p_s) obtained in Section 5.2.2. Here the stability of that solution for the evolution problem (5.30) is studied.

Here \mathcal{L}_G denotes the derivative

$$\begin{aligned} \mathcal{L}_G : C(\bar{\Omega}) &\longmapsto C(\bar{\Omega}) \\ w &\longmapsto D G(R_s)(w). \end{aligned} \quad (5.31)$$

Using the definition of $\Pi(R, S)$, the derivative with respect to R in the equation $S = \Pi(R, S)$ is computed and evaluated at $R = R_s, S = 0$, then it is obtained that $\mathcal{L}_G(w)$ satisfies:

$$R_s f_2(R_s) \mathcal{L}_G(w) - f'_1(R_s) w + \pi_1(w) + \pi_2(\mathcal{L}_G(w)) = 0, \quad (5.32)$$

with π_1 and π_2 as in Eqs. (5.18) and (5.19) respectively.

For the next results we denote $d_1 = -f'_1(\bar{R}) / (\bar{R} f_2(\bar{R}))$, $d_2 = (\bar{R} f_2(\bar{R}))^{-1}$, $d_3 = \bar{R} f_3(\bar{R}) f_2(\bar{R})$, $d_4 = -f'_4(\bar{R})$ and $d_5 = -f_5(\bar{R})$. All these constants are positive as follows from (H1)-(H5).

Lemma 5.6. Asumme $h^+ = 0$ or $\mathbf{U} = 0$. Then

$$\text{Sp}(\mathcal{L}_G) \subset \text{Vp}(\mathcal{L}_G) \cup \{-d_1\}.$$

Moreover, if $w \in C(\bar{\Omega})$ is an eigenvector of \mathcal{L}_G with associated eigenvalue λ , then $w \in H_0^1(\Omega)$ and it satisfies

$$\begin{aligned} d_3(d_1 + \lambda) \nabla \cdot (h^3 \nabla w) &= d_4 \mathbf{U} \cdot \nabla(hw) + \lambda d_5 hw && \text{in } \partial\Omega, \\ w &= 0 && \text{on } \partial\Omega. \end{aligned} \quad (5.33)$$

Proof. Notice from Remark 5.5 that $(R_s, p_s) = (\bar{R}, 0)$. Putting this into Eq. (5.32), the next equation is satisfied for any $\lambda \in \mathbb{C}$:

$$\mathcal{L}_G(w) - \lambda w = (\lambda + d_1) \left[-w - \frac{d_2}{\lambda + d_1} [\pi_1(w) + \pi_2(\mathcal{L}_G(w))] \right], \quad (5.34)$$

with $\pi_1(w)$ given by (5.21). Since the map $w \mapsto \pi_1(w) + \pi_2(\mathcal{L}_G(w))$ is compact, the Fredholm alternative Theorem implies $\text{Sp}(\mathcal{L}_G) \subset \text{Vp}(\mathcal{L}_G) \cup \{-d_1\}$.

Take now $w \in C(\bar{\Omega})$ eigenvector of \mathcal{L}_G with associated eigenvalue λ , carrying this into equation (5.34) we obtain

$$\frac{\lambda + d_1}{-d_2} w = \pi_1(w) + \lambda \pi_2(w).$$

then $w \in H_0^1(\Omega)$ and Equation (5.33) follows from this last relation and Eqs. (5.21) and (5.19). \square

Theorem 5.7. For every $\mathbf{U} \in \mathbb{R}^2$ there exists $\epsilon = \epsilon(\mathbf{U}) > 0$ such that if $\|h^+\|_\infty < \epsilon$, then the solution (R_s, p_s) of problem (5.12) is asymptotically stable for the evolution problem (5.2)-(5.25)-(5.26).

Proof. Let us assume first that $h^+ = 0$. By Lemma 5.6 it is enough to study the eigenvalues of \mathcal{L}_G . Hence, take $\lambda \in \mathbb{C} \setminus \{-d_1\}$ such that $\mathcal{L}_G(w) = \lambda w$ for some $w \neq 0$. Then (5.33) reads

$$\begin{aligned} h_0^2 d_3 (d_1 + \lambda) \Delta w &= d_4 \mathbf{U} \cdot \nabla w + \lambda d_5 w \quad \text{in } \Omega, \\ w &= 0 \quad \text{on } \partial\Omega. \end{aligned} \quad (5.35)$$

Assume that $\lambda = 0$, then multiplying the Eq. (5.35) by w and integrating by parts we obtain $w = 0$, which is not possible, thus $\lambda \neq 0$. Decomposing $\lambda = \lambda_1 + i\lambda_2$ and $w = w_1 + iw_2$, the next differential equation for w_1 and w_2 can be obtained

$$\begin{aligned} -h_0^2 d_3 (d_1 + \lambda_1) \Delta w_1 + h_0^2 d_3 \lambda_2 \Delta w_2 + d_4 \mathbf{U} \cdot \nabla w_1 + d_5 (\lambda_1 w_1 - \lambda_2 w_2) &= 0, \\ -h_0^2 d_3 (d_1 + \lambda_1) \Delta w_2 - h_0^2 d_3 \lambda_2 \Delta w_1 + d_4 \mathbf{U} \cdot \nabla w_2 + d_5 (\lambda_1 w_2 + \lambda_2 w_1) &= 0. \end{aligned}$$

Multiplying the first equation by w_1 , the second equation by w_2 and integrating by parts we may obtain

$$\begin{aligned} h_0^2 d_3 (d_1 + \lambda_1) \int_{\Omega} |\nabla w_1|^2 d\Omega - h_0^2 d_3 \lambda_2 \int_{\Omega} \nabla w_2 \nabla w_1 d\Omega + d_5 \lambda_1 \int_{\Omega} w_1^2 d\Omega - d_5 \lambda_2 \int_{\Omega} w_1 w_2 d\Omega &= 0, \\ h_0^2 d_3 (d_1 + \lambda_1) \int_{\Omega} |\nabla w_2|^2 d\Omega + h_0^2 d_3 \lambda_2 \int_{\Omega} \nabla w_2 \nabla w_1 d\Omega + d_5 \lambda_1 \int_{\Omega} w_2^2 d\Omega + d_5 \lambda_2 \int_{\Omega} w_1 w_2 d\Omega &= 0. \end{aligned}$$

Adding up both equations we have

$$h_0^2 d_3 (d_1 + \lambda_1) \int_{\Omega} (|\nabla w_1|^2 + |\nabla w_2|^2) d\Omega + d_5 \lambda_1 \int_{\Omega} (|w_1|^2 + |w_2|^2) d\Omega = 0.$$

Observe that $\lambda_1 \geq 0$ implies $w = 0$, which is not possible, thus $\operatorname{Re}(\lambda) = \lambda_1 < 0$.

The stability for $h^+ = 0$ has been shown. Now, from Theorem 5.2 the mapping $h^+ \mapsto R_s(h^+)$ is continuous in a neighborhood $V_1 \ni 0$ in $L^\infty(\Omega)$. Thus, if $h^+ \rightarrow 0$ in $L^\infty(\Omega)$ then

$$\|DG(R_s(h^+), 0) - DG(\bar{R}, 0)\| \rightarrow 0,$$

in the space of linear continuous operators from $C(\bar{\Omega})$ into itself. Then the result follows from Lemma 5.3 and Theorem B.4. \square

Theorem 5.8. Fix $h \in B_{m_0, M_0}$, $0 < m_0 < M_0$. Then there exists $\epsilon > 0$ such that if $\|\mathbf{U}\| < \epsilon$ then the solution (R_s, p_s) of problem (5.12) is asymptotically stable for the evolution problem (5.2)-(5.25)-(5.26).

Proof. Let us assume first that $\mathbf{U} = 0$. By Lemma 5.6 it is enough to study the eigenvalues of \mathcal{L}_G . Hence, take $\lambda \in \mathbb{C} \setminus \{-d_1\}$ such that $\mathcal{L}_G(w) = \lambda w$ for some $w \neq 0$. Recall that

w satisfies Eq. (5.33), if $\lambda = 0$ the only solution for that equation is $w = 0$, which is a contradiction. Thus, we have $\lambda \neq 0$ and this time Eq. (5.33) in its variational version reads

$$-d_3 \frac{(\lambda + d_1)}{\lambda} \int_{\Omega} h^3 \nabla w \nabla \phi \, d\Omega = d_5 \int_{\Omega} h w \phi \, d\Omega \quad \forall \phi \in H_0^1(\Omega).$$

By means of the same arguments used in Theorem 5.4, the last implies $\lambda \in \mathbb{R}^-$. The result follows analogously to the end of Theorem 5.7 proof, this time using the continuity of the mapping $\mathbf{U} \mapsto R_s(\mathbf{U})$ asserted in Theorem 5.3. \square



NUMERICAL METHODS FOR THE RRP COUPLING

This chapter is devoted to the numerical methods developed in this work for solving the RRP coupling. As done for the theoretical results shown in Chapter 5, here the development is divided into two cases: 1) Disregarding inertial terms and 2) Including inertial terms.

The first case is exposed in Section 6.1. A numerical strategy, the *single-step* scheme, is developed and compared with one found in the literature, named the *staggered* scheme. The former scheme is shown to solve stability issues exhibited by the latter one. Particularly, that scheme increases significantly the range of geometrical parameters able to be simulated. By means of the proposed numerical method, simulations of the Journal Bearing mechanism (Section 2.4.1) are performed and a comparison of these results with the ones for the state-of-the-art Elrod-Adams cavitation model (Section 2.3.2) is made. These findings are part of an article published in a peer-reviewed journal ([JARAMILLO; BUSCAGLIA, 2019](#)) during this work.

The case where inertial terms are included in the RRP cavitation model is covered in Section 6.2. There a numerical method is proposed and some interesting mechanical examples where the inertial terms are relevant are shown. Particularly, it is shown a dependence of this relevance on the bubbles equilibrium radius R_{eq} .

6.1 Disregarding the inertial terms

Assuming the inertial terms in Eq. (4.51) are negligible one obtains the following equation

$$\frac{\partial R}{\partial t} + \mathbf{U}_b \cdot \nabla R = G(R) (F(R) - p), \quad (6.1)$$

where

$$G(R) = \frac{R}{4\mu_\ell + 4\kappa^s/R} \quad (6.2)$$

and

$$F(R) = \left(p_{\text{eq}} + \frac{2\sigma}{R_{\text{eq}}} \right) \left(\frac{R_{\text{eq}}}{R} \right)^{3k} - p_\partial - \frac{2\sigma}{R}. \quad (6.3)$$

The Reynolds equation (4.50) can be written as:

$$\nabla \cdot \left(\frac{\rho h^3}{12\mu} \nabla p \right) = \nabla \cdot \left(\frac{\mathbf{U}}{2} \rho h \right) + \rho \frac{\partial h}{\partial t} + h \frac{\partial \rho}{\partial t}. \quad (6.4)$$

The right hand side of this equation contains the different terms that generate a *pressure build-up*. The first term corresponds to the pressure build-up due to the relative movement of the surfaces (or *Couette* flux); the second term represents the effect due to the *squeeze* between the surfaces; the third one represents a change in the average density of the mixture due to the bubbles compression or decompression.

Although there exist several numerical works where the RRP coupling is used to simulate lubricated devices (NATSUMEDA; SOMEYA, 1987; SOMEYA, 2003; GEHANNIN; ARGHIR; BONNEAU, 2009; GEHANNIN; ARGHIR; BONNEAU, 2016; SNYDER; BRAUN; PIERSON, 2016; BRAUN; PIERSON; SNYDER, 2017a), a lack of a detailed numerical procedure has been identified during this work. Among these works, in the article of 2016 the group of Snyder et al. provided an algorithm that hereafter will be named *staggered scheme* (some of its details were obtained by private communication). Although the authors were able to perform simulations regarding the Journal Bearing, an instability issue in their method is identified next.

6.1.1 The Staggered scheme

Assuming Ω to be a rectangular domain, Eq. (6.4) is discretized by means of a Finite Volume scheme using rectangular cells of length Δx_1 (Δx_2) along the x_1 -axis (x_2 -axis). The coordinates (x_i, y_j) correspond to the cells' centers. Using a constant time step Δt , we denote $t^n = n \Delta t$ for $n \geq 1$. Hereupon the total number of unknowns at each time step is denoted by M .

Consider that the scalars R_{ij}^n and R_{ij}^{n-1} have already been calculated for all cells. The Staggered scheme of discretization for the inertialess RRP coupling is defined by the following equations:

Stage 1: Computation of \mathbf{p}^n

$$\begin{aligned} \frac{c_{i-\frac{1}{2},j} p_{i-1,j}^n - (c_{i-\frac{1}{2},j} + c_{i+\frac{1}{2},j}) p_{i,j}^n + c_{i+\frac{1}{2},j} p_{i+1,j}^n}{\Delta x_1^2} \\ + \frac{c_{i,j-\frac{1}{2}} p_{i,j-1}^n - (c_{i,j-\frac{1}{2}} + c_{i,j+\frac{1}{2}}) p_{i,j}^n + c_{i,j+\frac{1}{2}} p_{i,j+1}^n}{\Delta x_2^2} \\ = \frac{U}{2} \left(\frac{\rho_{i,j}^n h_{i,j}^n - \rho_{i-1,j}^n h_{i-1,j}^n}{\Delta x_1} \right) + \rho_{i,j}^n (\mathbf{D}_t \mathbf{h})_{i,j}^n + h_{i,j}^n \frac{\rho_{i,j}^n - \rho_{i,j}^{n-1}}{\Delta t} \quad (6.5) \end{aligned}$$

with

$$c_{i\pm\frac{1}{2},j} = \frac{\rho_{i,j}^n (h_{i,j}^n)^3 / (12\mu) + \rho_{i\pm 1,j}^n (h_{i\pm 1,j}^n)^3 / (12\mu)}{2},$$

$$c_{i,j\pm\frac{1}{2}} = \frac{\rho_{i,j}^n (h_{i,j}^n)^3 / (12\mu) + \rho_{i,j\pm 1}^n (h_{i,j\pm 1}^n)^3 / (12\mu)}{2}.$$

Where $\mathbf{D}_t \mathbf{h}$ is a first order approximation of $\frac{\partial \mathbf{h}}{\partial t}$. Eq. (6.5) is used at each cell that belongs to the domain, while for the cells belonging to the boundary of Ω we have either

$$p_{i,j}^n = p_\partial|_{x_i,y_j} \quad (6.6)$$

or

$$(\mathbf{D}_{\hat{n}} p)_{i,j}^n = 0, \quad (6.7)$$

where $(\mathbf{D}_{\hat{n}} p)_{i,j}^n$ is a first order approximation of the normal derivative at the boundary $\partial\Omega_N$.

Stage 2: Computation of R^{n+1}

In the lubrication approximation w (the vertical speed) is neglected in Eq. (6.1), turning it into a two-dimensional transport equation. Among many possibilities, our implementation adopts the following implicit scheme:

$$R_{i,j}^{n+1} = R_{i,j}^n + \Delta t \left\{ G(R_{i,j}^{n+1}) (F(R_{i,j}^{n+1}) - p_{i,j}^n) - (u \mathbf{D}_1 R)_{i,j}^{n+1} - (v \mathbf{D}_2 R)_{i,j}^{n+1} \right\}, \quad (6.8)$$

where $\mathbf{D}_1 = \frac{\partial}{\partial x_1}$, $\mathbf{D}_2 = \frac{\partial}{\partial x_2}$, and the convective terms $u \mathbf{D}_1 R$ and $v \mathbf{D}_2 R$ are discretized by means of an upwind scheme. Notice that (6.8) is a discretization of Eq. (6.1), which is a transport equation but *not* a conservation law because $\nabla \cdot \mathbf{U}_b \neq 0$ in general.

After the two stages above all variables have been updated and the computations may proceed to the next time step. The scheme is called staggered because the *Reynolds solver* (Stage 1) computes p^n assuming that $R = R^n$ and $(\partial \rho / \partial t)^n = (\rho^n - \rho^{n-1}) / \Delta t$, both already calculated, and then the *Rayleigh-Plesset solver* (Stage 2) computes R^{n+1} with the pressure fixed at $p = p^n$. The implementation of the staggered scheme of RRP coupling is straightforward since no modification is required in the Reynolds solver. It should be

noticed, however, that $\partial\rho/\partial t$ is approximated with information from the previous time step. Both R^{n-1} and R^n are required to compute R^{n+1} . This gives rise to initialization issues and also, as shown along the next sections, to stability issues. A method that only requires information of the current time step is described next.

6.1.2 The Single-step scheme

This is the method proposed in this work, which can be seen as an adaptation of that in (GEIKE; POPOV, 2009a). The basic idea is to compute $(\partial\rho/\partial t)^n$ using only information about R^n (and thus α^n and ρ^n). From the chain rule, assuming ρ_ℓ constant, we have

$$\frac{\partial\rho}{\partial t} = -(\rho_\ell - \rho_g) \frac{\partial\alpha}{\partial t} + \alpha \frac{\partial\rho_g}{\partial t} = -4\pi(\rho_\ell - \rho_g)n_b R^2 \frac{\partial R}{\partial t} + \frac{4\pi(\rho_\ell - \rho_g)R^3}{3} \frac{\partial n_b}{\partial t} + \alpha \frac{\partial\rho_g}{\partial t}. \quad (6.9)$$

To simplify the exposition, as done by other authors (NATSUMEDA; SOMEYA, 1987; GEHANNIN; ARGHIR; BONNEAU, 2009; GEIKE; POPOV, 2009a; GEIKE; POPOV, 2009b), one may assume that $\partial\rho_g/\partial t = 0$ and that $\partial n_b/\partial t = 0$ (NATSUMEDA; SOMEYA, 1987; SNYDER; BRAUN; PIERSON, 2016; GEHANNIN; ARGHIR; BONNEAU, 2009; GEIKE; POPOV, 2009a; GEIKE; POPOV, 2009b). Denoting $K(R) = 4\pi(\rho_\ell - \rho_g)n_b R^2$, one arrives at

$$\frac{\partial\rho}{\partial t} = -K(R) \frac{\partial R}{\partial t}. \quad (6.10)$$

It is worth mentioning that $\partial\rho_g/\partial t$ is in fact equal to $-(3\rho_{\text{eq}}R_{\text{eq}}^3/R^4)\partial R/\partial t$, where ρ_{eq} is the density when $R = R_{\text{eq}}$. Incorporating this effect in the model amounts to adding the term $3\alpha\rho_{\text{eq}}R_{\text{eq}}^3/R^4$ to the definition of $K(R)$. Similarly, if one adopts the model (4.49) the factor $K(R)$ changes to $\tilde{K}(R) = (1 + \alpha)K(R)$. These changes in $K(R)$ have no numerical consequences, so that the algorithm presented below can be applied in any case.

Combining Eqs. (6.10) and (6.1) justifies the following discretization of $\partial\rho/\partial t$,

$$\left(\frac{\partial\rho}{\partial t} \right)_{i,j}^n = -K_{i,j}^n \left[G(R_{i,j}^n) \left(F(R_{i,j}^n) - p_{i,j}^n \right) - (u D_1 R)_{i,j}^n - (v D_2 R)_{i,j}^n \right],$$

Inserting this approximation into Eq. (6.5) instead of $(\rho_{i,j}^n - \rho_{i,j}^{n-1})/\Delta t$ leads to the *Single-step* scheme. The equations are as follows:

Stage 1: Computation of p^n

$$\begin{aligned}
 & \frac{c_{i-\frac{1}{2},j} p_{i-1,j}^n - (c_{i-\frac{1}{2},j} + c_{i+\frac{1}{2},j}) p_{i,j}^n + c_{i+\frac{1}{2},j} p_{i+1,j}^n}{\Delta x_1^2} \\
 & + \frac{c_{i,j-\frac{1}{2}} p_{i,j-1}^n - (c_{i,j-\frac{1}{2}} + c_{i,j+\frac{1}{2}}) p_{i,j}^n + c_{i,j+\frac{1}{2}} p_{i,j+1}^n}{\Delta x_2^2} - h_{i,j}^n K_{i,j}^n G(R_{i,j}^n) p_{i,j}^n = \\
 & = \frac{U}{2} \left(\frac{\rho_{i,j}^n h_{i,j}^n - \rho_{i-1,j}^n h_{i-1,j}^n}{\Delta x_1} \right) + \rho_{i,j}^n (\mathrm{D}_t h)_{i,j}^n \\
 & - h_{i,j}^n K_{i,j}^n (G(R_{i,j}^n) F(R_{i,j}^n) - (u \mathrm{D}_1 R)_{i,j}^n - (v \mathrm{D}_2 R)_{i,j}^n). \quad (6.11)
 \end{aligned}$$

Where $\mathrm{D}_t h$ is a first order approximation of $\frac{\partial h}{\partial t}$. Notice that the matrix to be solved for p^n is not the standard one in Reynolds-equation solvers such as Eq. (6.5). There is the additional term $-h_{i,j}^n K_{i,j}^n G(R_{i,j}^n)$ in the diagonal elements which is key to the enhanced stability of the scheme.

Stage 2: Computation of R^{n+1}

This stage of the Single-step scheme coincides with that of the Staggered scheme: Equation (6.8) is solved to obtain $R_{i,j}^{n+1}$.

6.1.3 Numerical results and stability analysis

6.1.3.1 The Planar Fracture

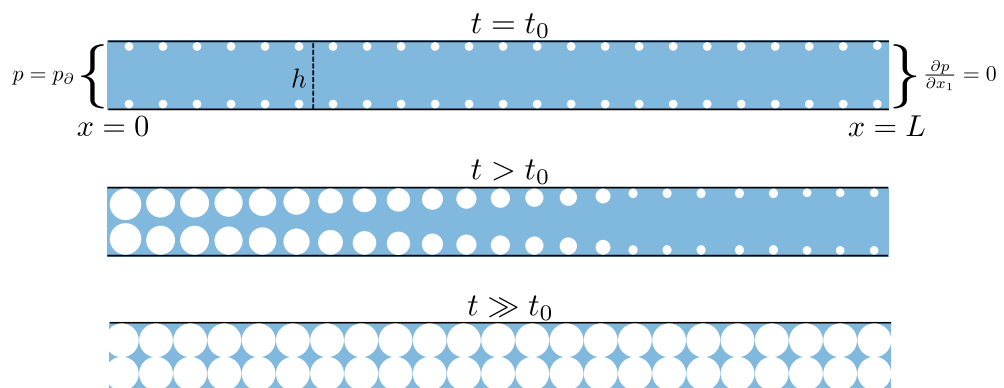


Figure 6.1.1 – Scheme of the 1D fracture setup. The liquid is trapped between two parallel plates, at the left boundary a Dirichlet condition on pressure is imposed, at the right boundary a no-flux condition is imposed. The white regions represent the presence of gas-bubbles in the liquid.

Consider a fluid trapped between two smooth planar plates set parallel to the x_1 - x_2 plane and in close proximity at distance h (see Fig. 6.1.1). The plates are infinite along the x_2 -axis, so that the liquid pressure can be modeled by the 1D compressible Reynolds

equation, which reads

$$h^2 \frac{\partial}{\partial x_1} \left(\frac{\rho}{12\mu} \frac{\partial p}{\partial x_1} \right) = \frac{\partial \rho}{\partial t}. \quad (6.12)$$

with the boundary conditions

$$p(0, t) = p_\partial(t), \quad \frac{\partial p}{\partial x_1}(x_1 = L, t) = 0$$

For this application it is assumed that the bubbles are attached to the surfaces ($\mathbf{U}_b = 0$), and that they are uniformly distributed. Denoting by n_b^s the number of bubbles per unit area, the number of bubbles per unit volume is computed as $n_b = n_b^s/h$. Thus, from Eq. (4.56) one obtains

$$\alpha = \left(\frac{n_b^s}{h} \right) \frac{4}{3} \pi R^3. \quad (6.13)$$

If there is no presence of bubbles in the liquid ($n_b^s = 0$), then $\alpha \equiv 0$ in (4.54) and (4.55), the fluid density ρ is constant in time and so Eq. (6.12) implies that the pressure along the domain is constant and equal to the boundary condition at $x_1 = 0$ (i.e., $p(x_1, t) = p_\partial(t)$). That is, the pressure in the domain adjusts instantaneously to the boundary value.

On the other hand, if $n_b^s > 0$, the response of the system to changes in the boundary pressure is much more involved. Consider the system with n_b^s independent of x_1 , and with bubbles of initial radius $R(x_1, t = 0) = R_{eq}$ and external equilibrium pressure p_{eq} . This system is in equilibrium with a boundary pressure $p_\partial = p_{eq}$ in the sense that $\partial R / \partial t = 0$ for all x_1 . The specific problem considered here is the response of the system, initially in equilibrium, after the boundary pressure p_∂ is suddenly changed from $p_{eq} > p_{cav}$ to some different value $p_\partial^* < p_{cav}$ at $t = 0$ ($p_\partial(t) = p_\partial^*$, $t > 0$).

Since $p(x_1, t)$ is continuous in x_1 , there will exist a region where $p < p_{cav}$ and thus, recalling that p_{cav} is the minimum of F , where the right hand side of Eq. (6.1) (with $\mathbf{U}_b = 0$) will be strictly positive. In that region the bubbles are expected to grow until touching one another or until filling the volume between the surfaces, which makes the model to loose physical meaning. This numerical example aims at showing how this fully-gaseous region progresses through the domain as predicted by the RRP model. To extend the model in order to handle fully-gaseous regions, we introduce an upper limitation to the definition of $\alpha(R)$ given in Eq. (6.13), reading

$$\alpha(R) = \min \left\{ \left(\frac{n_b^s}{h} \right) \frac{4}{3} \pi R^3, 1 \right\}, \quad (6.14)$$

and also turn off the right-hand side of the Rayleigh-Plesset equation when $\alpha \geq 1$, i.e.,

$$\frac{dR}{dt} = \begin{cases} G(R)(F(R) - p) & \text{if } \alpha(R) < 1, \\ 0 & \text{if } \alpha(R) \geq 1. \end{cases} \quad (6.15)$$

Notice that this is *not* a good model in general situations. In particular it cannot model problems in which a fully-gaseous region ($\alpha = 1$) transitions back into a liquid-gas region ($\alpha < 1$).

6.1.3.2 Parameters setup

| Symbol | Value | Units | Description |
|------------------|----------------------------|-------------------|--|
| ρ_ℓ | 1000 | kg/m ³ | Liquid density |
| μ_ℓ | 8.9×10^{-4} | Pa·s | Liquid viscosity |
| ρ_g | 1 | kg/m ³ | Gas density |
| μ_g^r | 1.81×10^{-5} | Pa·s | Gas viscosity |
| κ^s | 7.85×10^{-5} | Pa·s·m | Surface dilatational viscosity |
| σ | 7.2×10^{-2} | N/m | Liquid surface tension |
| H | 10 | μm | Gap thickness |
| R_{eq} | 0.5 | μm | Bubbles' radii at 1 atm |
| p_{vap} | 0 | - | Bubbles' vapor pressure |
| n_b^s | 1.91×10^{11} | m ⁻² | Number of bubbles per unit area |
| δp | $1.5 \cdot p_{\text{cav}}$ | Pa | Reference value for $p_\partial^* - p_{\text{cav}}$ (notice that $\delta p < 0$) |

Table 6 – Default parameters.

For the simulations presented in this Section, a set of parameters are fixed and their values are shown in Table 6. Recalling that in the equilibrium the bubbles' internal pressure accomplishes:

$$p_{\text{bub}} = p_{\text{eq}} + \frac{2\sigma}{R_{\text{eq}}},$$

we set the reference value $p_{\text{bub}}^r = 1 \text{ atm} + \frac{2\sigma}{R_{\text{eq}}}$. We set also $\delta p = 1.5 \cdot p_{\text{cav}} < 0$ (where p_{cav} depends on p_{bub} according to Eq. (4.11)) is also defined. The remaining free parameters, such as the length of the domain (L), the boundary condition for $t > 0$ (p_∂^*) and the fluid viscosity (μ_ℓ), are varied over wide ranges to explore the ability of the numerical methods to yield convergent solutions. The results shown below correspond to $\Delta x = L/1024$ and $\Delta t = 1 \times 10^{-6}$ s. The choice of these values is based on a mesh and time step convergence analysis such that further refinement would not be noticeable in the graphs.

6.1.3.3 Results for the Staggered scheme

The first striking result of the experiments is that if $L > 8.59 \times 10^{-4}$ m the Staggered scheme produces numerical outcomes that explode exponentially after a few time steps. This instability cannot be avoided by refining the mesh or reducing the time step. Furthermore, no relevant dependency of the instability on the boundary condition $p_\partial^* - p_{\text{cav}}$ was observed.

The next section explains this issue by linearizing the RRP coupling and performing a stability analysis of the Staggered scheme. Before that, let us provide a sample of the results that *could* be obtained to illustrate the behavior of the system for L being small. Selecting $L = 2.15 \times 10^{-4}$ m, Fig. 6.1.2 depicts the profiles of α over the domain at several times, with two boundary conditions, $p_{\partial}^* = p_{\text{cav}} + \delta p$ and $p_{\partial}^* = p_{\text{cav}} + 2\delta p$ (remember that $\delta p < 0$). It can be observed that for such a small value of L the pressure field is almost independent of x_1 . One can also notice that the bigger the magnitude of $p_{\partial}^* - p_{\text{cav}}$, the faster the growth of α in time.

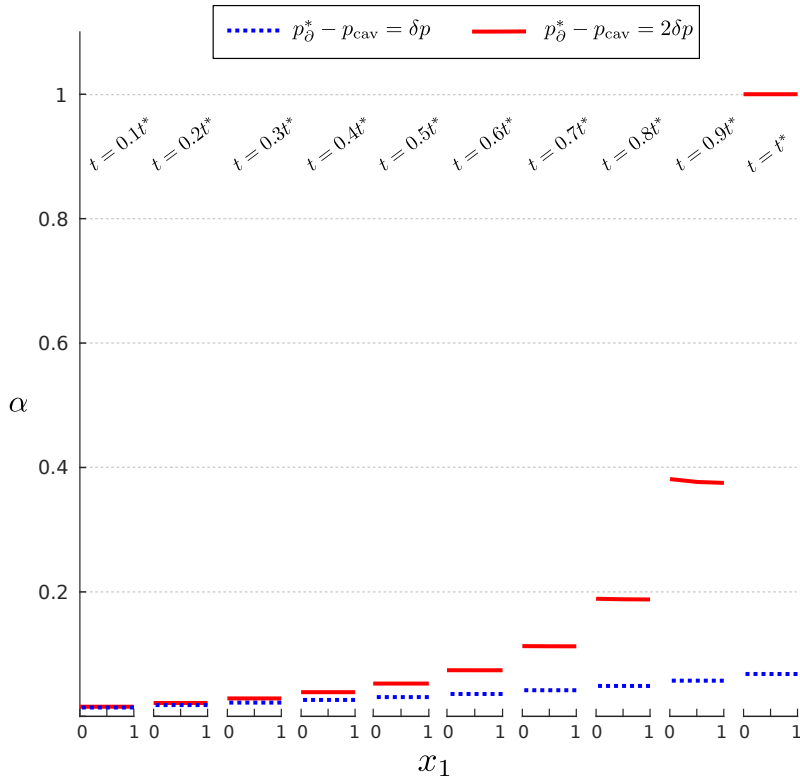


Figure 6.1.2 – Results of the Staggered scheme for $L = 2.15 \times 10^{-4}$ m. Shown are some snapshots of the gas fraction profiles $\alpha(x_1, t)$, for $p_{\partial}^* - p_{\text{cav}} = \delta p$, $2\delta p$. The rest of the parameters were set to their default values.

6.1.3.4 Stability analysis

Linearizing Eq. (6.1) (with $\mathbf{U}_b = 0$) around an equilibrium state $(R_{\text{eq}}, p_{\text{eq}})$ one gets

$$\frac{dR}{dt} = \beta_0 (\beta_1 R - p), \quad (6.16)$$

where

$$\beta_0 = \frac{R_{\text{eq}}}{4\mu_\ell + 4\kappa^s/R_{\text{eq}}}, \quad \beta_1 = \left. \frac{dF}{dR} \right|_{R=R_{\text{eq}}}.$$

Notice that $\beta_1 < 0$ since it is assumed that $(R_{\text{eq}}, p_{\text{eq}})$ is an equilibrium state (stable branch in Fig. 4.1.1). Recalling now that ρ/μ is a function of R and assuming that

$R(x_1, t) \simeq R_{\text{eq}}$ (as a C^1 function of x_1), one can choose the perturbation small enough so that

$$\left| \frac{\partial(\rho/\mu)}{\partial R} \left(|R - R_{\text{eq}}| + \frac{\partial(R - R_{\text{eq}})}{\partial x_1} \frac{\partial p}{\partial x_1} \right) \right| \ll \left| \frac{\partial^2 p}{\partial x_1^2} \right|,$$

which justifies the approximation

$$\frac{\partial}{\partial x_1} \left(\frac{\rho}{\mu} \frac{\partial p}{\partial x_1} \right) \approx \frac{\rho(R_{\text{eq}})}{\mu(R_{\text{eq}})} \frac{\partial^2 p}{\partial x_1^2}.$$

Using this approximation, one can linearize Eq. (6.12) and use Eq. (6.16) to get

$$\beta_2 \frac{\partial^2 p}{\partial x_1^2} = \frac{\partial R}{\partial t} \quad (6.17)$$

$$\text{where } \beta_2 = -\frac{h^2}{(\rho_e - \rho_g) \frac{\partial \alpha}{\partial R} \Big|_{R=R_{\text{eq}}}} \frac{\rho(R_{\text{eq}})}{\mu(R_{\text{eq}})}.$$

Let us now discretize Eqs. (6.16) and (6.17) in space to get, respectively,

$$\frac{1}{\beta_0} \frac{d\mathbf{R}}{dt} = \beta_1 \mathbf{R} - \mathbf{p} \quad \text{and} \quad (6.18)$$

$$\beta_2 \mathcal{L}_\Delta \mathbf{p} = \frac{d\mathbf{R}}{dt}, \quad (6.19)$$

where $\mathbf{R}(t)$ and $\mathbf{p}(t)$ are radii and pressure vectors in \mathbb{R}^M and \mathcal{L}_Δ is the discrete Laplacian operator corresponding to the grid size $\Delta = \Delta x_1$. Let $\{\mathbf{g}_i\}_{i=1}^M$ be an orthonormal basis of \mathbb{R}^M formed by the eigenvectors of \mathcal{L}_Δ s.t. $\mathcal{L}_\Delta \mathbf{g}_i = \lambda_i \mathbf{g}_i$, $i = 1 \dots M$. Then, \mathbf{p} can be expressed as $\mathbf{p} = \sum_{i=1}^M \gamma_i(t) \mathbf{g}_i$ and so Eq. (6.18) implies

$$\frac{1}{\beta_0} \frac{d}{dt} \langle \mathbf{R}, \mathbf{g}_i \rangle = \beta_1 \langle \mathbf{R}, \mathbf{g}_i \rangle - \gamma_i(t), \quad i = 1 \dots M, \quad (6.20)$$

where the fact that each \mathbf{g}_i is time-independent has been used. In the same way, Eq. (6.19) implies

$$\beta_2 \lambda_i \gamma_i(t) = \frac{d}{dt} \langle \mathbf{R}, \mathbf{g}_i \rangle, \quad i = 1 \dots M. \quad (6.21)$$

These last two equations imply that stability analyses can be made independently for each mode $\langle \mathbf{R}, \mathbf{g}_i \rangle$, $i = 1 \dots M$. To simplify notation we denote $\tilde{R} = \langle \mathbf{R}, \mathbf{g}_i \rangle$, $\tilde{\lambda} = \lambda_i$ and $\tilde{\gamma}(t) = \gamma_i(t)$ for some arbitrary index i . In Section 6.1.3.1, the Eqs. (6.20) and (6.21) are discretized in time with a constant time step Δt , such that $t^0 = 0$ and $t^n = n \Delta t$.

Stability of the Staggered scheme

The time discretization of Eqs. (6.20) and (6.21) by the Staggered scheme is

$$\begin{aligned} \frac{1}{\beta_0} \frac{\tilde{R}^{n+1} - \tilde{R}^n}{\Delta t} &= \beta_1 \tilde{R}^{n+1} - \tilde{\gamma}^n, \\ \tilde{\gamma}^n &= \frac{1}{\beta_2 \tilde{\lambda}} \frac{\tilde{R}^n - \tilde{R}^{n-1}}{\Delta t}. \end{aligned}$$

Substituting $\tilde{\gamma}^n$ from the latter equation into the former leads to

$$\tilde{\lambda}(1 - \Delta t \beta_1 \beta_0) \beta_2 \tilde{R}^{n+1} + (\beta_0 - \beta_2 \tilde{\lambda}) \tilde{R}^n - \beta_0 \tilde{R}^{n-1} = 0.$$

This methodology thus corresponds to a multistep method (e.g., (LEVEQUE, 2007) Section 5.9). Its characteristic polynomial is given by

$$Q(\chi) = \tilde{\lambda}(1 - \Delta t \beta_1 \beta_0) \beta_2 \chi^2 + (\beta_0 - \beta_2 \tilde{\lambda}) \chi - \beta_0.$$

A necessary condition for this type of multistep method to be stable in time is that the roots of $Q(\chi)$ must lie within the unit circle of the complex plane (Leveque (2007) Theorem 6.3, pag. 147). Denoting these roots by χ_1 and χ_2 ,

$$\chi_1 = 1 + \frac{\beta_1 \Delta t}{\frac{1}{\beta_0} + \frac{1}{\beta_2 \tilde{\lambda}}} + \mathcal{O}(|\Delta t|^2)$$

and

$$\chi_2 = -\frac{\beta_0}{\beta_2 \tilde{\lambda}} - \frac{\beta_0^3 \beta_1 \Delta t}{\beta_2^2 \tilde{\lambda}^2} + \mathcal{O}(|\Delta t|^2).$$

Recalling that $\beta_0 > 0$, $\beta_1 < 0$, $\beta_2 < 0$ and $\tilde{\lambda} < 0$, one observes that $|\chi_1| < 1$ for Δt small enough. On the other hand, if $\tilde{\lambda} < \beta_0/\beta_2$, then $|\chi_2|$ is always bigger than one. Therefore, as the minimum eigenvalue (in magnitude) of the Laplacian operator \mathcal{L}_Δ is $\tilde{\lambda} \simeq -\pi^2/(4L^2)$, instability is predicted for $L > \sqrt{\pi^2 \beta_2 / (4\beta_0)}$. The Staggered scheme is thus not stable for L large enough.

For the default values of the parameters (see Table 6) it turns out that $\beta_0 = 8.0 \times 10^{10}$ and $\beta_2 = -1.9 \times 10^{-13}$ (in SI units), then one should have numerical instability for $L > 0.024$ m. This behavior is indeed observed when a *small* perturbation is imposed on $p_\partial(t)$. In Section 6.1.3.3 a *large* perturbation was imposed and in fact instability was observed for much smaller values of L ($L > 8.59 \times 10^{-4}$ m). The reason for this is that the nonlinear behavior that corresponds to cavitation amplifies the instability of the Staggered scheme, which can be explained from the change in sign of $F'(R)$ from negative to positive when cavitation occurs.

Stability of the Single-step scheme

The time discretization of Eqs. (6.20) and (6.21) by the Single-step scheme consists in substituting $\gamma_i(t)$ from Eq. (6.21) into Eq. (6.20). The resulting equation reads

$$\frac{\tilde{R}^{n+1} - \tilde{R}^n}{\Delta t} = \left(\frac{1}{\beta_0} + \frac{1}{\beta_2 \tilde{\lambda}} \right)^{-1} \beta_1 \tilde{R}^{n+1}.$$

Thus,

$$\tilde{R}^{n+1} = \frac{1}{1 - \Delta t \beta_1 \frac{\tilde{\lambda} \beta_2 + \beta_0}{\tilde{\lambda} \beta_2 \beta_0}} \tilde{R}^n.$$

For this scheme to be stable the factor multiplying \tilde{R}^n must be lower than the unit in magnitude. But this is *always* true, since we have $\beta_0 > 0$, $\beta_1 < 0$, $\beta_2 < 0$ and $\tilde{\lambda} < 0$. This does not guarantee numerical stability, since nonlinear effects could deteriorate its behavior. This motivates the numerical experiments below, which show that the method is stable beyond the linear regime.

6.1.3.5 Results for the Single-step scheme

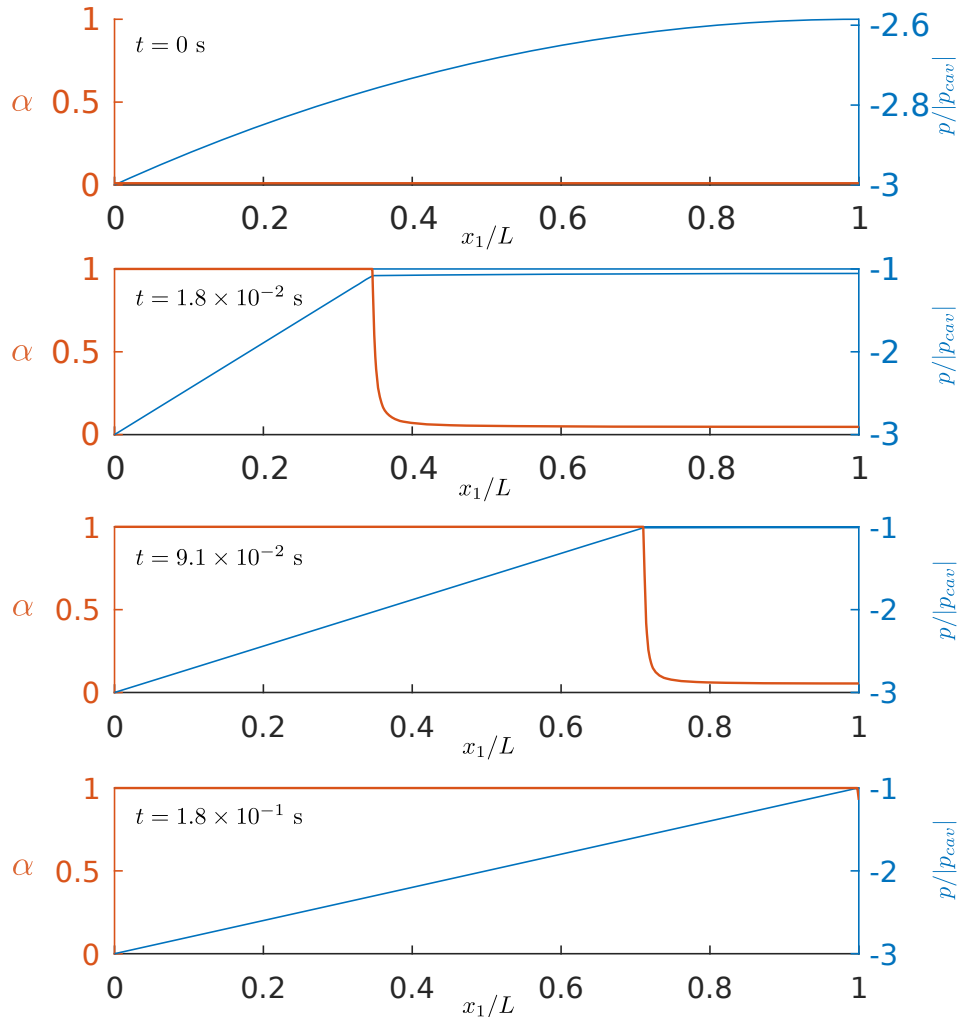


Figure 6.1.3 – Gas fraction and pressure in time along the fracture setup for $L = 6.9 \times 10^{-3}$ m, $p_{\partial}^* - p_{cav} = 4\delta p$, and the rest of the parameters set to their default values.

The Single-step scheme allows to perform simulations for arbitrary values of the domain length L . A wave-like solution, with the cavitated region advancing towards the right side, develops whenever $L > L^* \approx 1.7 \times 10^{-3}$ m. An example is shown in Fig. 6.1.3 for $L = 6.9 \times 10^{-3}$ m. To depict the front advance, the position $\xi(t)$ such that $\alpha(x_1 < \xi(t), t) = 1$ and $\alpha(x_1 > \xi(t), t) < 1$ is tracked in time and the resulting curves are shown in Fig. 6.1.4 for several values of L . Notice that the time variable has been

non-dimensionalized by dividing it by T^f , the *filling time*, defined as the first time for which $\alpha = 1$ on the whole domain.

Interestingly, with the proposed non-dimensionalization the curves of $\xi(t)$ converge to a unique curve when L is large enough (in this case, for $L > L^{**} = 0.0275$ m). The relative difference between the curves corresponding to $L = 0.0275$ m and $L = 0.055$ m, for example, is less than 2%. Next, a numerical study of the dependence of the filling time T^f on the liquid parameters and the boundary condition p_∂^* is presented. For these analyses, the domain's length is also varied from values lower than L^* up to values higher than L^{**} .

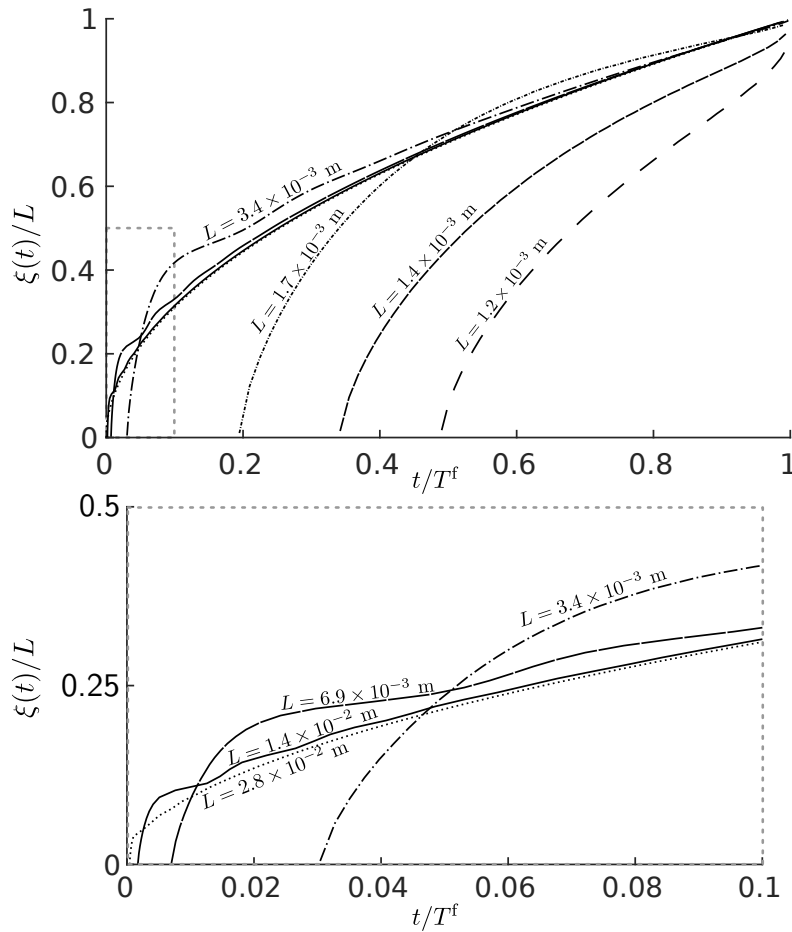


Figure 6.1.4 – Non-dimensional advance of the wave for the 1D Fracture Problem for several values of L and the default parameters.

Varying $p_\partial^* - p_{\text{cav}}$ and fixing both $p_{\text{bub}} = p_{\text{bub}}^r$ and $\mu_g = \mu_g^r$ the resulting filling times are shown in Fig. 6.1.5 for several values of L . For the shorter domains, T^f does not depend on the domain's length, while for the larger domains it grows quadratically with it. Notice also that T^f is roughly inversely proportional to $p_\partial^* - p_{\text{cav}}$.

Regarding the bubbles' initial internal pressure, simulations where p_{bub} is varied and p_∂^* is fixed to -3.83 atm are reported in Fig. 6.1.6. This value of p_∂^* corresponds to the boundary pressure condition for the default case $p_{\text{bub}} = p_{\text{bub}}^r$. It is found that

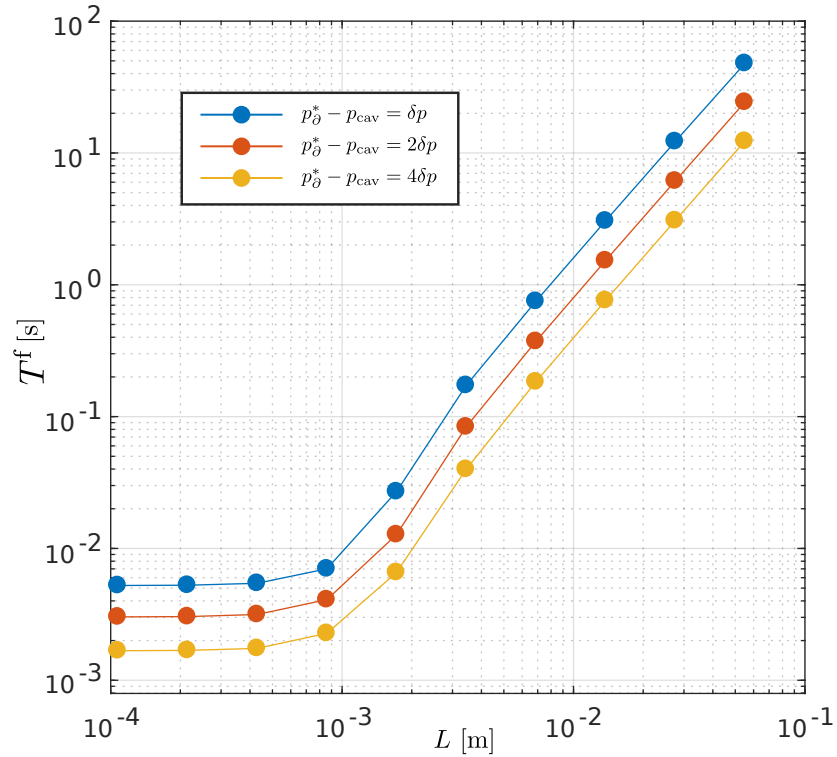


Figure 6.1.5 – Filling time for several values of L and $p_∂^* - p_{cav}$, and the rest of the parameters set to their default values.

the filling time diminishes when augmenting p_{bub} , which is expected since p_{cav} increases monotonically with p_{bub} .

In the cavitated region (where $\alpha = 1$) the Poiseuille flux is inversely proportional to the gas kinematic viscosity (μ_g/ρ_g). This affects T_f when L is large enough, as shown in Fig. 6.1.7. Finally, the value of κ^s is varied and the results for T^f are shown in Fig. 6.1.8. Notably, T^f is proportional to κ^s for small values of L , and independent of κ^s for the larger domains considered.

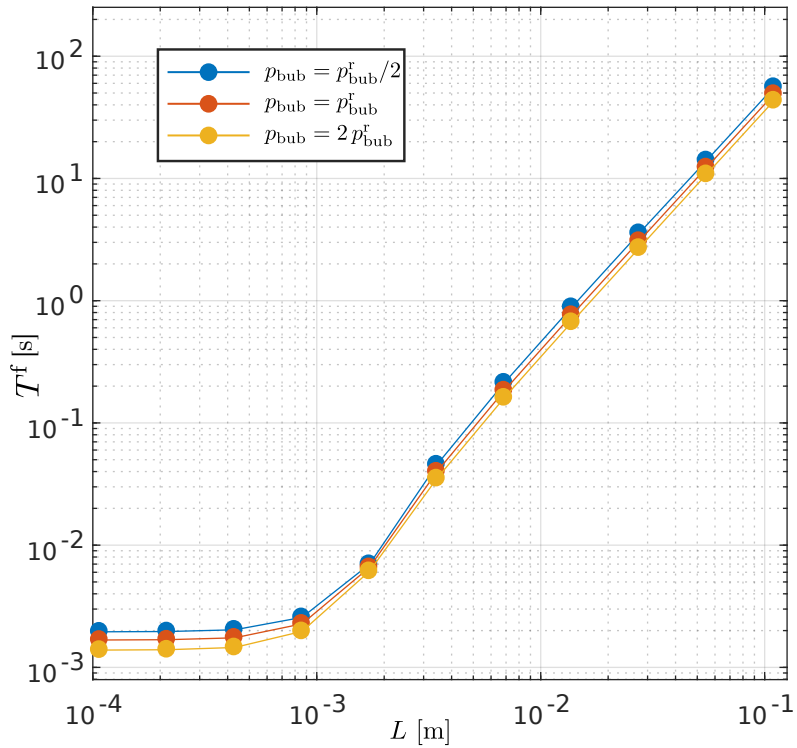


Figure 6.1.6 – Filling time for several values of L and p_{bub} ; fixing $p_{\partial}^* = -3.83$ atm and the rest of the parameters set to their default values.

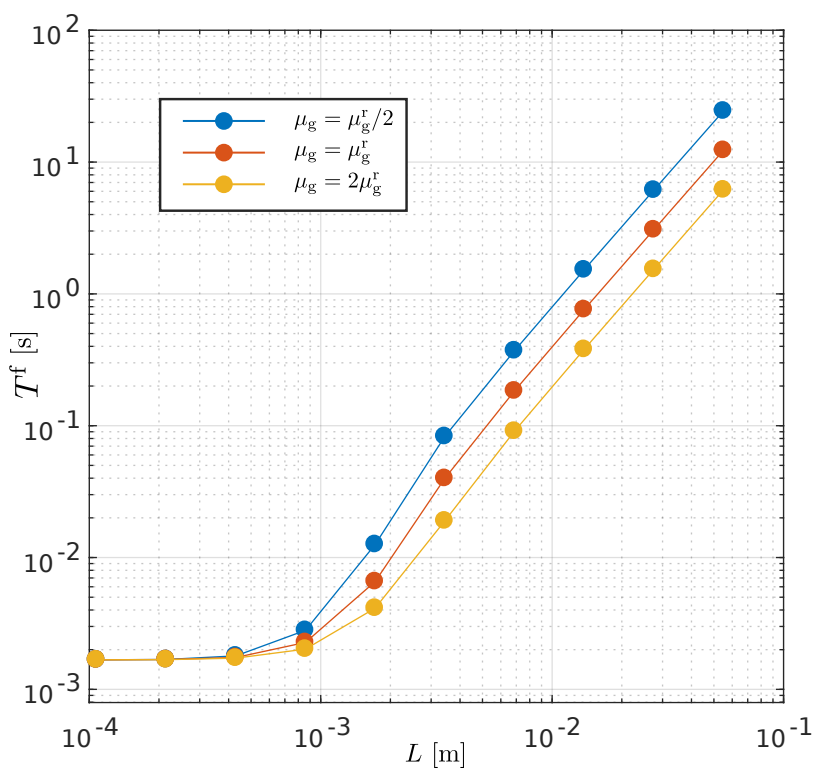


Figure 6.1.7 – Filling time for several values of L and μ_g ; fixing $p_{\partial}^* - p_{\text{cav}} = 4\delta p$ and the rest of the parameters set to their default values.

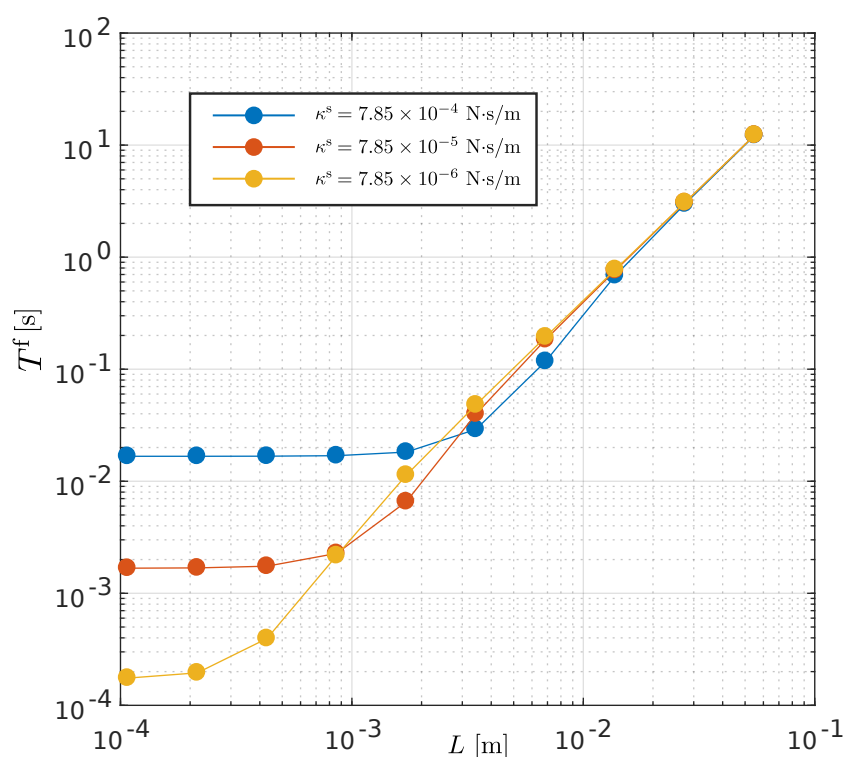


Figure 6.1.8 – Filling time for several values of L and κ^s ; fixing $p_\partial^* - p_{\text{cav}} = 4\delta p$ and the rest of the parameters set to their default values.

6.1.3.6 A 2D example of the Fracture Problem

To assess the robustness of the Single-step scheme, 2D simulations of the Fracture Problem are here reported. The domain corresponds to the rectangle $[0, L] \times [0, W]$ with $L = 1.25 \times 10^{-2}$ m and $W = 1 \times 10^{-2}$ m. The grid length along x_1 was set to $\Delta x_1 = L/348$ and along x_2 to $\Delta x_2 = W/256$, while the time step was fixed to $\Delta t = 1 \times 10^{-5}$ s. The Dirichlet condition $p_\partial^* = -2$ atm is set at $x_2 = 0$, and the null-flux condition is set at $x_2 = W$, $x_1 = 0$ and $x_1 = L$.

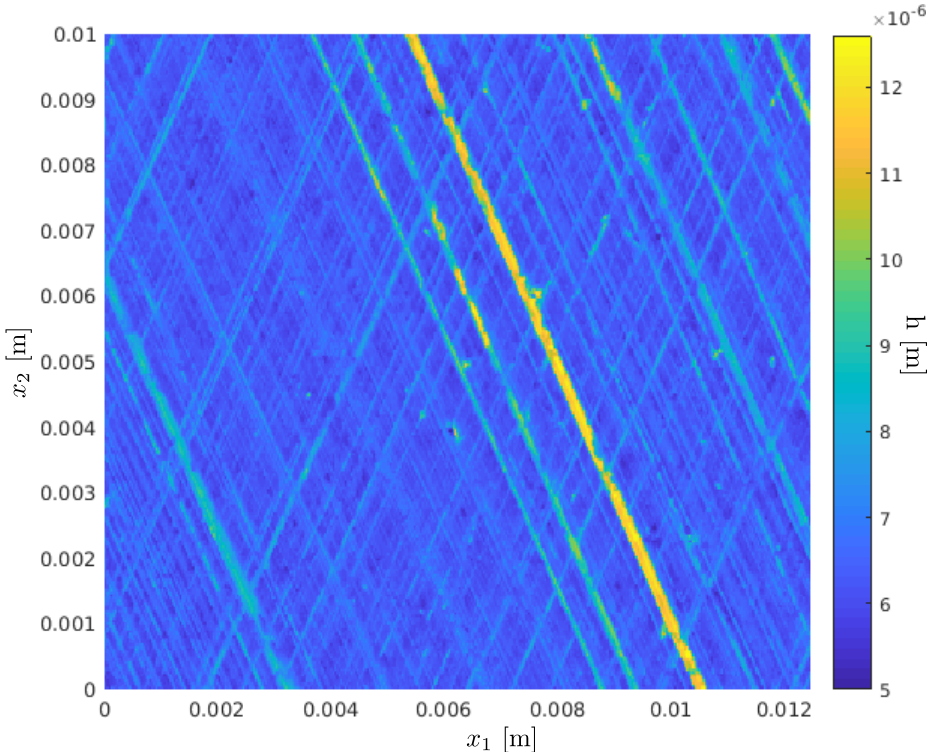


Figure 6.1.9 – Height function $h(x_1, x_2)$ for the 2D Fracture Problem example. This gap represents the realistic distance between a flat surface and a rough surface with the presence of honed *channels*.

For the 2D cases the gap h depends on \mathbf{x} as shown in Fig. 6.1.9. To fix an initial gas fraction $\alpha_0 = 0.01$, the initial bubbles' radii are taken as $R_{\text{eq}} = [\alpha_0 3h(\mathbf{x})/(4\pi n_b^s)]^{1/3}$. This way, R_{eq} assumes values between $0.40 \mu\text{m}$ and $0.54 \mu\text{m}$ (for the parameters here considered). Since it is assumed that the bubbles are in equilibrium at 1 atm, the initial internal pressure is set according to Eq. (4.5) or, equivalently, $p_{\text{bub}}(R_{\text{eq}}) = 1 \text{ atm} + 2\sigma/R_{\text{eq}}$. Thus, the cavitation pressure depends on \mathbf{x} since it varies with p_{bub} (see Eq. (4.11)).

The results here exposed are obtained with the Single-step scheme since simulations with the Staggered scheme invariably crashed. In Fig. 6.1.10 the advance of cavitation in time along the 2D domain is shown. The complexity of the field α can be also observed in Fig. 6.1.11. Notice the presence of cavitation in the crevices (regions with a higher value of h) even in places where the wave (traveling in the positive x_2 -direction) has not arrived.

This can be explained due to a higher cavitation pressure in these regions.

Remark 6.1. Another possibility to perform these simulations is to set a constant R_{eq} and an initial gas fraction that depends on the position. For instance, $\alpha(\mathbf{x}, t = 0) = 4/3\pi R_{\text{eq}} n_b^s / h(\mathbf{x})$. The corresponding simulation yields solutions that are much smoother than the case presented and are not shown here since the objective is to test the Single-step method in a demanding situation.

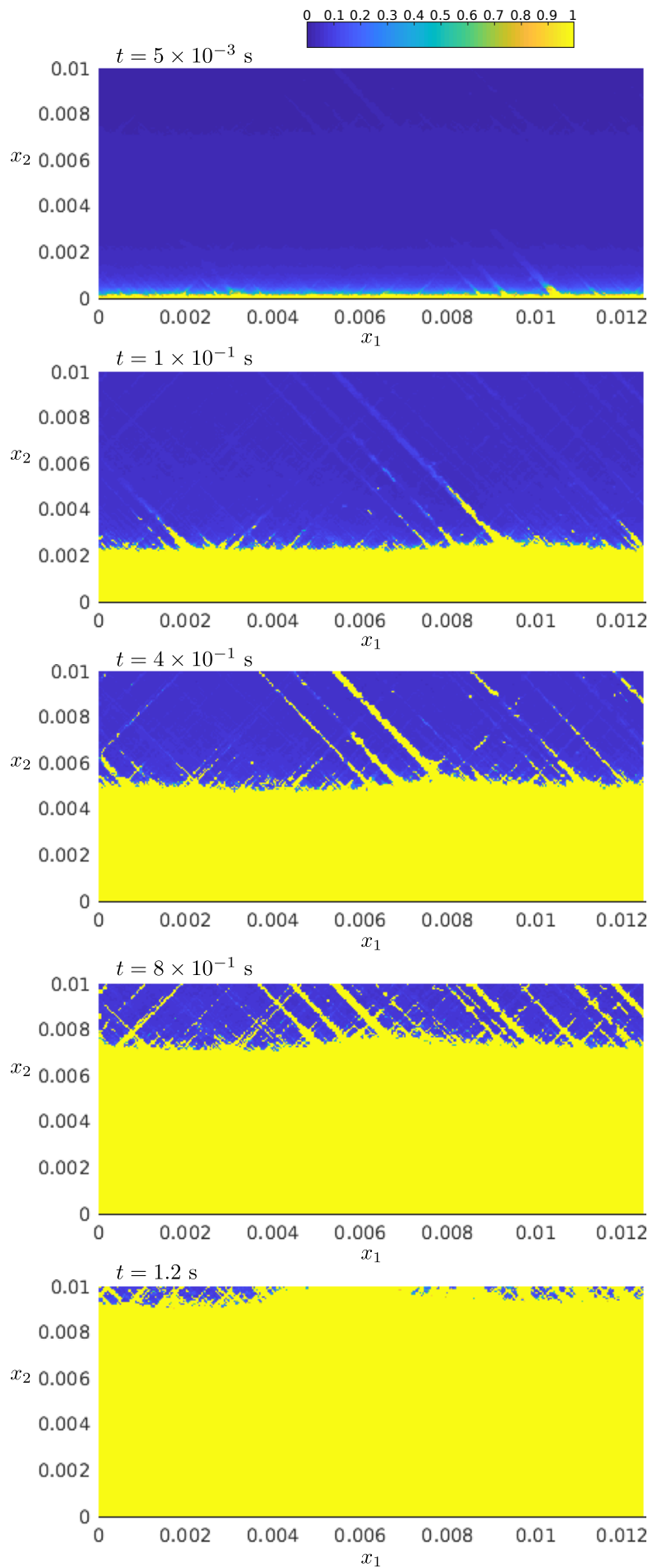


Figure 6.1.10 – Evolution of the field α in a 2D fracture problem with a uniform initial gas fraction α_0 .

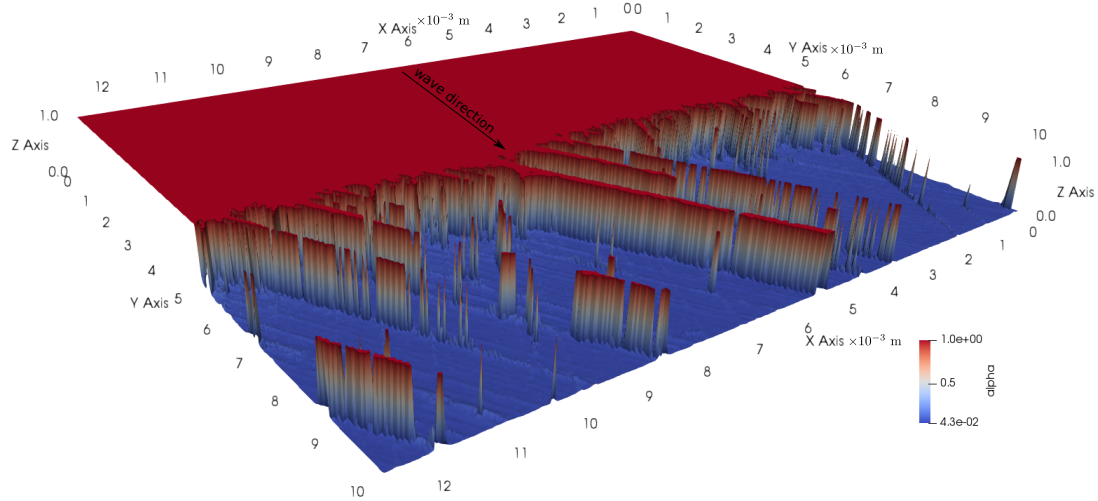


Figure 6.1.11 – Three dimensional view of the gas-fraction field α at time $t = 4 \times 10^{-1}$ s for the 2D fracture problem with uniform initial gas fraction $\alpha_0 = 0.01$.

6.1.4 The Journal Bearing

In this section results of simulations of the Journal Bearing mechanism are presented (2.4.1). This problem is a typical benchmark and has already been used by other authors (NATSUMEDA; SOMEYA, 1987; SOMEYA, 2003; SNYDER; BRAUN; PIERSON, 2016; BRAUN; PIERSON; SNYDER, 2017a). For this application, the transport of bubbles is incorporated by setting $\mathbf{U}_b = \eta(\mathbf{U}, 0)$ with $\eta \in [0, 1]$, and the bubbles are assumed to be uniformly distributed in the fluid at the initial time $t = 0$. The geometrical and fluid/gas parameters are shown in Table 7. As in (SNYDER; BRAUN; PIERSON, 2016), the initial bubbles' radii is set to $R(\mathbf{x}, t = 0) = R_{\text{eq}} = 0.385 \mu\text{m}$. The number of bubbles per unit volume n_b is assumed to be constant in space and time. Let us observe that in this setting, and by means of Eq. (4.47), to fix n_b is equivalent to fixing $\alpha_0 = \alpha(R_{\text{eq}})$.

While traveling through the domain, the bubbles evolution is strongly dependent on the surface dilatational viscosity κ^s (SNYDER; BRAUN; PIERSON, 2016), and so are the pressure and gas fraction fields. Considering the same problem, Natsumeda and Someya set κ^s to $7.85 \times 10^{-4} \text{ N}\cdot\text{s}/\text{m}$ (NATSUMEDA; SOMEYA, 1987). Here we explore the range 7.85×10^{-6} to $7.85 \times 10^{-3} \text{ N}\cdot\text{s}/\text{m}$, with the results shown in Figs. 6.1.12 and 6.1.13. It is observed that for $\kappa^s = 7.85 \times 10^{-3} \text{ N}\cdot\text{s}/\text{m}$ the liquid fraction $1 - \alpha$ is almost constant throughout the domain and thus the pressure profile is similar to the full-Sommerfeld curve (which is the solution of the Reynolds equation when cavitation is disregarded). For lower values of κ^s the liquid fraction shows significant inhomogeneities which very much suggest the appearance of a *cavitated region* (low liquid fraction, quasi-uniform pressure). This is further discussed in section 6.1.4.2.

Remark 6.2. The results above are qualitatively similar to those reported by Snyder et al. (SNYDER; BRAUN; PIERSON, 2016) for the same journal geometry, rotational speeds, and fluid/gas physical properties. However, our results for $\kappa^s = 7.85 \times 10^{-6} \text{ N}\cdot\text{s}/\text{m}$ best agree with theirs for $\kappa^s = 7.85 \times 10^{-4} \text{ N}\cdot\text{s}/\text{m}$. Similar differences on κ^s were observed when trying to reproduce other results in their article. This difference may possibly arise from differences in the definition of α in terms of R .

Remark 6.3. If the bubbles' transport velocity is taken as $\mathbf{U}_b = \frac{1}{2}\mathbf{U} - \frac{h^2}{12\mu}\nabla p$, as done in (SNYDER; BRAUN; PIERSON, 2016), then the number concentration of bubbles n_b can no longer be considered a datum of the problem and it must be computed by means of a transport equation (e.g., Eq. (4.44)).

6.1.4.1 Stability and convergence

To test the stability of both methods a series of simulations were performed for $\kappa^s = 7.85 \times 10^{-4}$, 7.85×10^{-5} and $7.85 \times 10^{-6} \text{ N}\cdot\text{s}/\text{m}$, rotational speeds of 1000, 2000 and 4000 rpm, $\eta = 0, 0.5, 1$, and $\alpha_0 = 0.1$ which gives a total of 27 configurations. The mesh

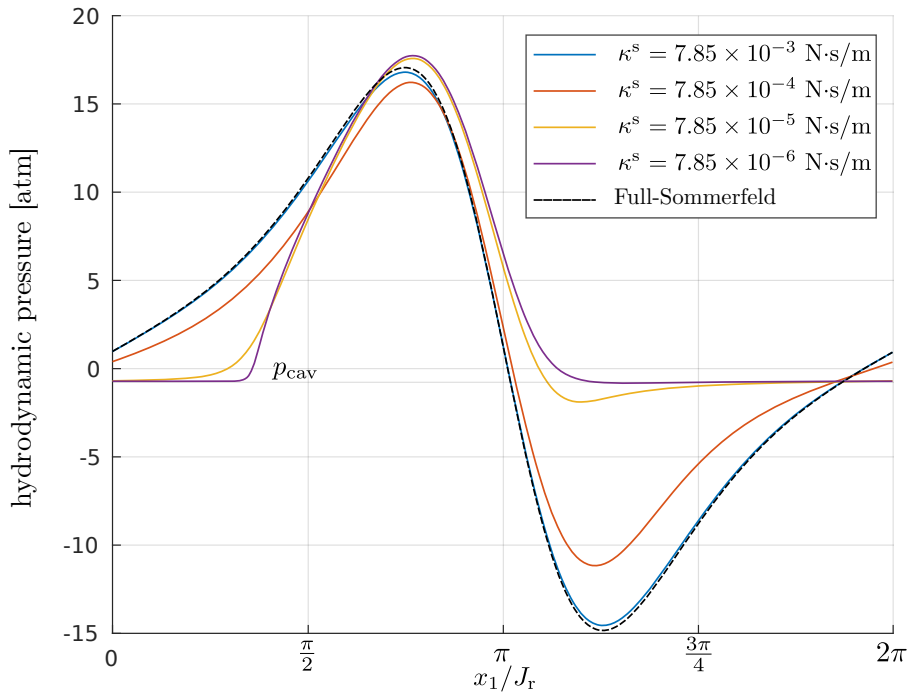


Figure 6.1.12 – Pressure profiles solution of the RRP model when varying the surface dilatational viscosity κ^s for the journal bearing rotating at 5000 rpm. Here $\alpha_0 = 0.05$ and $\eta = 0.5$.

adopted was 512×64 , but the same conclusions were obtained on other meshes. The time step was adjusted so that $\text{CFL} \approx 1$.

The Single-step scheme exhibits stable behavior for all of the tested configurations, reaching a stationary solution in finite time. On the other hand, the Staggered scheme fails to provide stable solutions in most of the cases. The instabilities persist even if the time step is reduced a thousand times with respect to the unit-CFL value. Only for $\kappa^s = 7.85 \times 10^{-4}$ N·s/m and $\eta \in \{0.5, 1\}$ the Staggered scheme behaves stably.

A convergence analysis is now presented for the Single-step scheme. This analysis is done for the journal rotating at 2000 rpm, with an initial gas fraction $\alpha_0 = 0.1$ and $\kappa^s = 7.85 \times 10^{-4}$ N·s/m. To test the dependence of the solutions on the time step, the grid size is set to $\Delta x_1 = 2\pi J_R / 512$ and $\Delta x_2 = J_w / 64$. A reference solution, denoted by $(p_{\text{ref}}, R_{\text{ref}})$, is computed by setting Δt to 640 time steps per cycle and running the simulation until $t = 0.06$ s. The measure of the temporal discretization error for a variable f (which can be p or R) is defined as

$$E^{\Delta t}(f) = \frac{\|f^{\Delta t}(t = 0.06\text{s}) - R_{\text{ref}}\|_2}{\|R_{\text{ref}}\|_2},$$

where $f^{\Delta t}$ is the numerical solution computed with time step Δt . The results are shown on the left side of Fig. 6.1.14, with strong evidence of a convergence rate of order ≈ 1 .

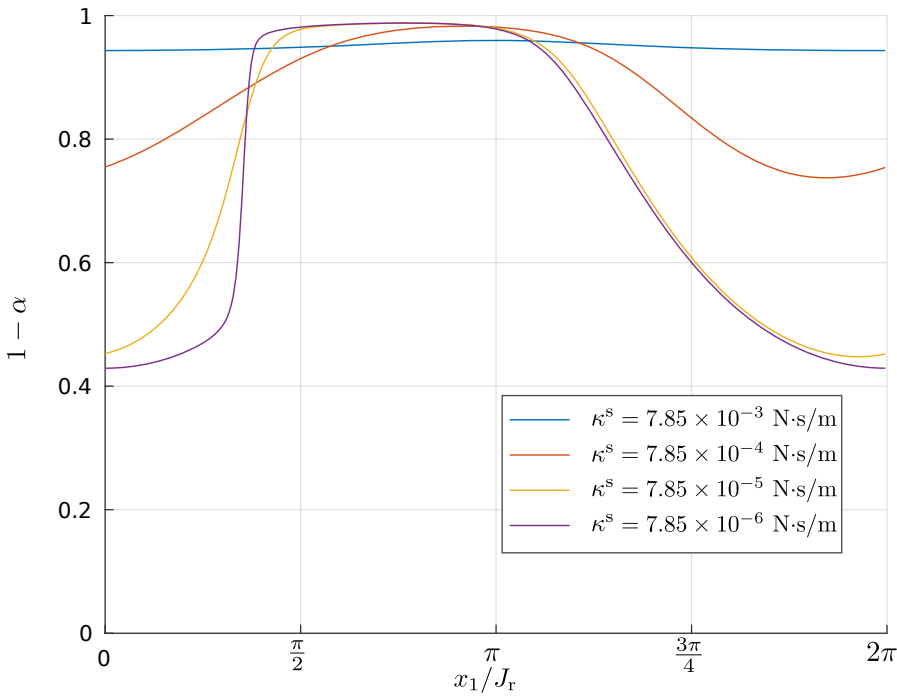


Figure 6.1.13 – Liquid fraction solution of the RRP model when varying the surface dilatational viscosity κ^s for the journal bearing rotating at 5000 rpm. Here $\alpha_0 = 0.05$ and $\eta = 0.5$.

The convergence of the discretization in space is studied for the stationary solution ($t = +\infty$) to avoid interference with time discretization errors. A sequence of nested meshes is built by setting $\Delta x_1 = 2\pi J_R/N_x$ and $\Delta x_2 = 8J_w/N_x$, with $N_x = 64, 128, 256$, etc. The reference solutions p_{ref} and R_{ref} are computed by setting $N_x = 2048$. The measure of the spatial discretization error is

$$E^{\Delta x}(f) = \frac{\|f^{N_x}(t = +\infty) - R_{\text{ref}}\|_2}{\|R_{\text{ref}}\|_2},$$

where f^{N_x} is the numerical solution computed with the grid corresponding to N_x . The empirical convergence order as the spatial mesh is refined is of order ≈ 1 , as shown in the right side of Fig. 6.1.14. Notice that the discrete convective term for ρh in Eq. (6.11) is a first order approximation of $\frac{U}{2}(\rho h)'$ and that the convergence analysis on space was made computing stationary solutions. For the stable stationary solutions R can be written in terms of p as $R = F^{-1}(p)$. This way, the local density is given by $\rho = \rho(R) = \rho(F^{-1}(p))$. Therefore, for the stable stationary cases ρ is a smooth function of p , which explains the observed order of convergence.

To the extent of our knowledge, this is the first numerical convergence study of algorithms for RRP coupling. It shows that the Single-step method is indeed stable and convergent in problems with strong nonlinear effects. The accuracy is however limited to first order in both space and time.

| Parameter | Value | Units | Description |
|-----------------|---|-------------------|--------------------------------|
| ρ_ℓ | 854 | kg/m ³ | Liquid density |
| μ_ℓ | 7.1×10^{-3} | Pa·s | Liquid viscosity |
| ρ_g | 1 | kg/m ³ | Gas density |
| μ_g | 1.81×10^{-5} | Pa·s | Gas viscosity |
| κ^s | $\approx 10^{-4} - 10^{-6}$ | Pa·s·m | Surface dilatational viscosity |
| σ | 3.5×10^{-2} | N/m | Liquid surface tension |
| p_∂^* | 1 | atm | $p_\partial(t)$ for $t > 0$ |
| p_{eq} | 1 | atm | Bubbles' equilibrium pressure |
| R_{eq} | 0.385 | μm | Bubbles' radii at 1 atm |
| α_0 | 0.05 - 0.1 | | Initial gas fraction |
| J_w | 25.4×10^{-3} | m | Journal width |
| J_r | 25.4×10^{-3} | m | Journal radius |
| J_c | $0.001 \cdot J_r$ | m | Journal clearance |
| J_ϵ | $0.4 \cdot J_c$ | m | Journal eccentricity |
| ω | $2\pi \frac{1000}{60} - 2\pi \frac{5000}{60}$ | | Journal angular speed |

Table 7 – Parameter values for the Journal Bearing.

6.1.4.2 Comparison with Elrod-Adams and Reynolds models

When the value of κ^s is small enough (e.g., $\kappa^s = 7.85 \times 10^{-6}$ N·s/m) the pressure profiles that develop in the journal bearing are observed to satisfy the condition $p \geq p_{\text{cav}}$, with p_{cav} computed from Eq. (4.11). In fact, a large region where $p \simeq p_{\text{cav}}$ is observed, which resembles the cavitation regions predicted by more traditional models. This motivates to incorporate $p_{\text{cav}} = -0.77$ atm into the Elrod-Adams and Reynolds cavitation models in order to perform comparisons with the RRP model. Doing so, the resulting pressure profiles are shown in Fig. 6.1.15 for rotating speeds of 1000 and 5000 rpm and $\kappa^s = 7.85 \times 10^{-5}$ and 7.85×10^{-6} N·s/m. Notice that the rupture point for both the Elrod-Adams and Reynolds models are the same (which is a well-known fact), while for the RRP coupling the rupture is placed further along the fluid's movement direction. On the other hand, it is also known that the Reynolds model fails to accurately predict the reformation point when compared to a mass-conserving model (AUSAS *et al.*, 2007). Remarkably, when κ^s is small enough the RRP model predicts a reformation point similar to that of the Elrod-Adams model. Furthermore, Fig. 6.1.16 shows the comparison of the fluid fraction produced by the RRP model, $1 - \alpha$, with the fluid fraction produced by the Elrod-Adams model, θ . Qualitatively both fluid fraction fields are similar, the one corresponding to the RRP model being a regularized version of the other, in some sense. Notice that increasing κ^s to 7.85×10^{-5} N·s/m significantly reduces the similarities between the two models.

Let us remark that the results shown in these last comparisons were obtained with a mesh having $\Delta x_1 = 2\pi J_r / 512$ and $\Delta x_2 = J_w / 64$ (i.e., $N_x = 512$) and with the time step fixed to 400 steps per cycle (CFL=1.3).

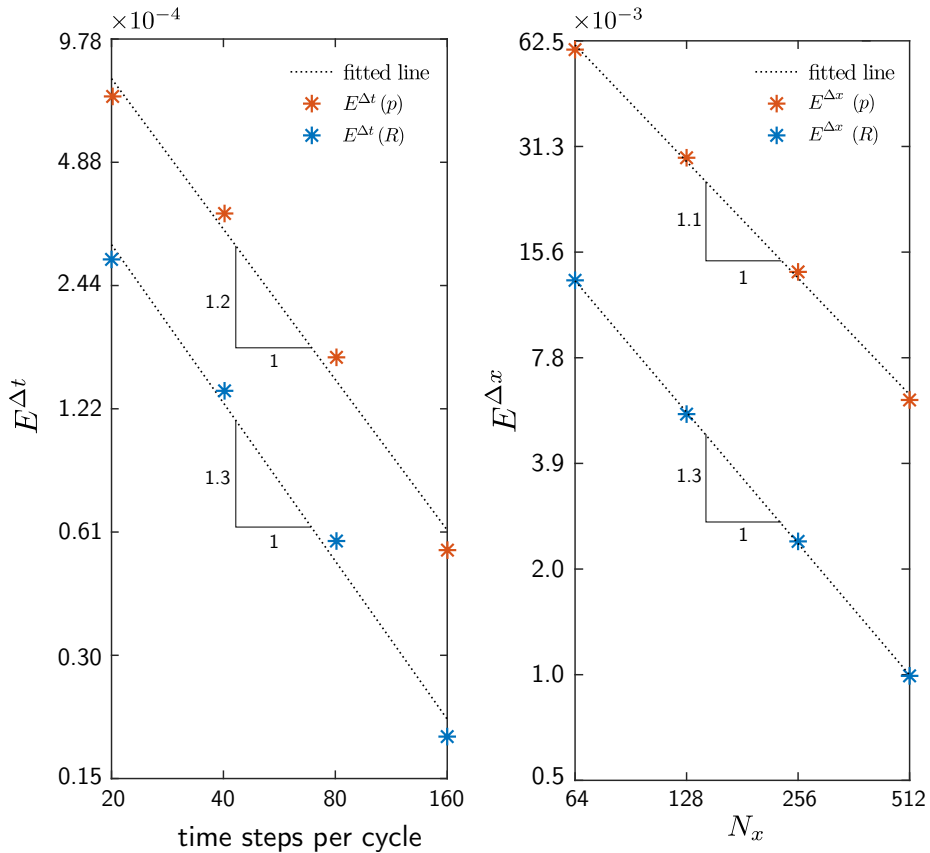


Figure 6.1.14 – Convergence analysis for the journal bearing at 2000 rpm, with $\kappa^s = 7.85 \times 10^{-4}$ N·s/m, $\alpha_0 = 0.1$ and $\eta = 0.5$. Left: Time discretization error measure. Right: Space discretization error measure (N_x is the number of grid cells along the circumferential direction). The triangles indicate the slope of the fitted lines.

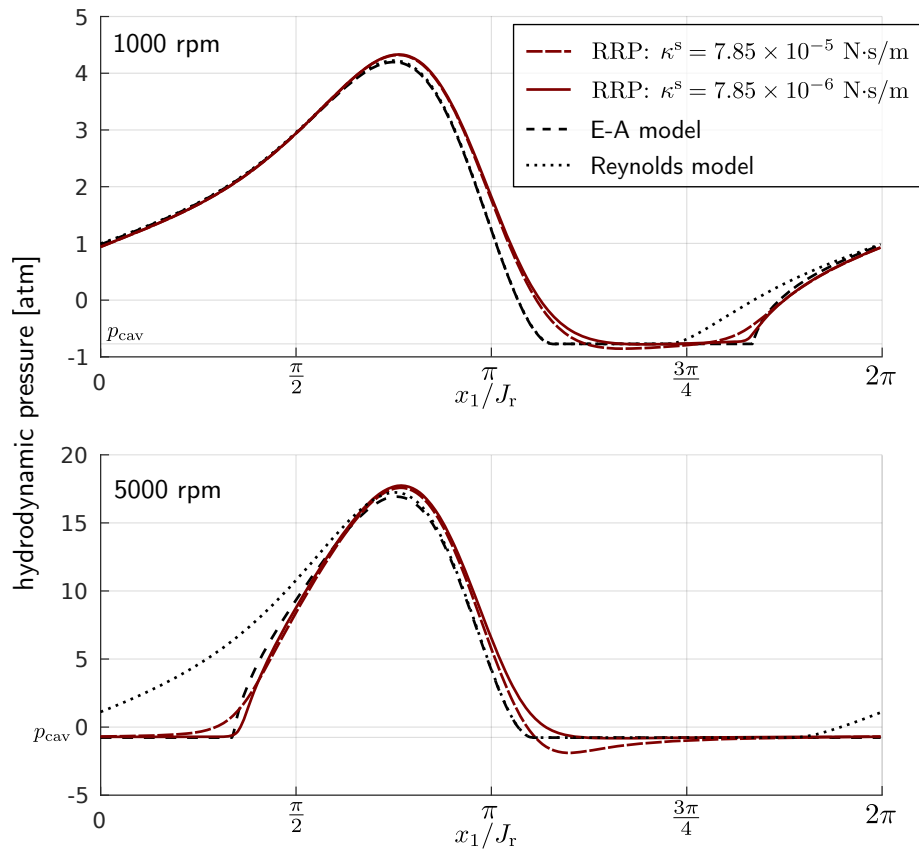


Figure 6.1.15 – Pressure profiles obtained with the RRP, Elrod-Adams and Reynolds models for a journal bearing rotating at 1000 and 5000 rpm. Here $\alpha_0 = 0.05$, $\kappa^s = 7.85 \times 10^{-5}, 7.85 \times 10^{-6} \text{ N}\cdot\text{s}/\text{m}$ and $\eta = 0.5$.

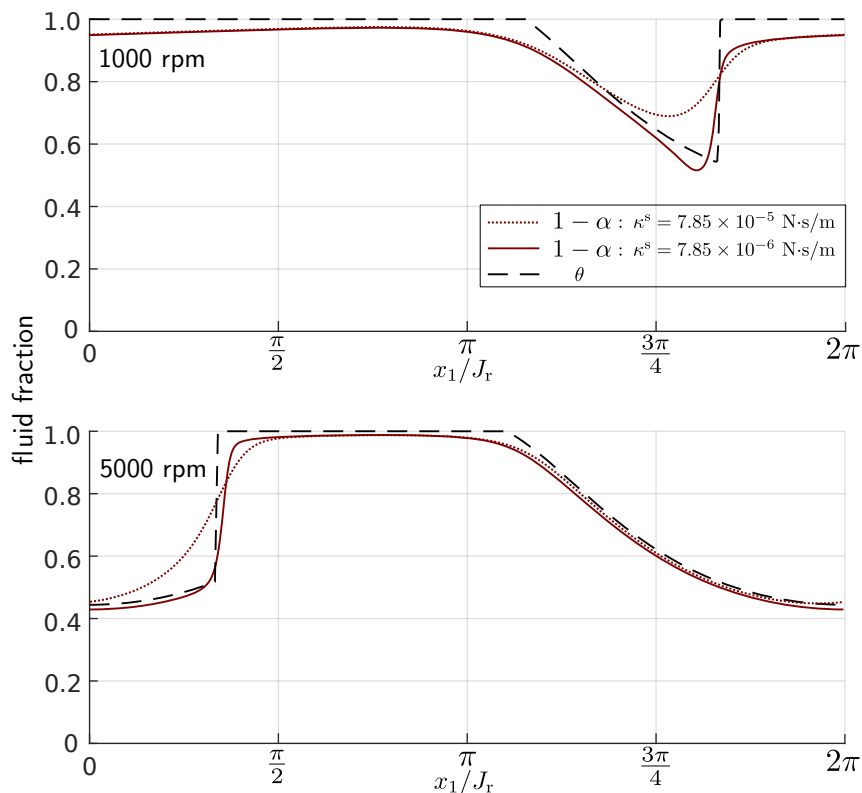


Figure 6.1.16 – Fluid fractions obtained along the RRP coupling, Elrod-Adams and Reynolds models for a journal bearing rotating at 1000 and 5000 rpm. Here $\alpha_0 = 0.05$, $\kappa^s = 7.85 \times 10^{-5}, 7.85 \times 10^{-6}$ N·s/m and $\eta = 0.5$.

6.2 Including the inertial terms

In this section a numerical method to solve the full Eq. (4.51) is proposed. To our knowledge, currently there are no works exploring inertial effects by means of numerical analysis. Instead, these terms are generally disregarded by means of a non-dimensional analysis.

Let us denote R by R_1 and $\frac{\partial R}{\partial t}$ by R_2 . Then, rewriting the Eq. (4.51) as a first-order system and coupling it to the Reynolds equation we obtain

$$\frac{\partial R_1}{\partial t} = R_2 - \mathbf{U}_b \cdot \nabla R_1, \quad (6.22)$$

$$\rho_\ell \frac{\partial R_2}{\partial t} = -\rho_\ell \mathbf{U}_b \cdot \nabla R_2 - \rho_\ell \frac{3}{2} \frac{R_2^2}{R_1} - 4(\mu_\ell R_1 + \kappa^s) \frac{R_2}{R_1^3} + \frac{F(R_1) - p}{R_1}, \quad (6.23)$$

$$\nabla \cdot \left(\frac{\rho h^3}{12\mu} \nabla p \right) = \frac{U}{2} \frac{\partial \rho h}{\partial x_1} + \rho \frac{\partial h}{\partial t} + h \rho'(R_1) (R_2 - \mathbf{U}_b \cdot \nabla R_1), \quad (6.24)$$

where F is defined in (6.3) and $\mu = \mu(R_1)$, $\rho = \rho(R_1)$ are given by Eqs. (4.54) and (4.55) respectively and ρ' is the derivative of ρ .

Focusing in the physical setting of the Journal Bearing (with parameters shown in Table 7) the next reference value for p , R_1 and R_2 are chosen

$$p^r = p_{\text{eq}}, \quad R_1^r = R_{\text{eq}}, \quad R_2^r = \frac{(R_1^r)^2 p^r}{\mu_\ell R_1^r + \kappa^s}, \quad x_1^r = J_r, \quad x_2^r = J_r, \quad h^r = J_c, \quad t^r = R_1^r / R_2^r.$$

Notice that in this case $\mathbf{U} = (\omega J_r, 0)$, thus the quantity ωJ_r is taken as reference speed. Notice that R_2^r corresponds to $G(R_1^r) p^r$, the value of $\frac{\partial R_1}{\partial t}$ according to Eq. (6.1) for $\mathbf{U}_b = 0$ and $F(R) - p = p^r$. Leading to the non-dimensional equations

$$\frac{\partial \hat{R}_1}{\partial \hat{t}} = -\gamma_2^{-1} \hat{\mathbf{U}}_b \cdot \hat{\nabla} \hat{R}_1 + \hat{R}_2, \quad (6.25)$$

$$\epsilon_p \frac{\partial \hat{R}_2}{\partial \hat{t}} = -\epsilon_\omega \hat{\mathbf{U}}_b \cdot \hat{\nabla} \hat{R}_2 - \epsilon_p \frac{3}{2} \frac{\hat{R}_2^2}{\hat{R}_1} - 4(\beta_1 \hat{R}_1 + \beta_2) \frac{\hat{R}_2}{\hat{R}_1^3} + \frac{\hat{F}(\hat{R}_1) - \hat{p}}{\hat{R}_1}, \quad (6.26)$$

$$\gamma_1 \hat{\nabla} \cdot \left(\frac{\hat{\rho} h^3}{12\hat{\mu}} \hat{\nabla} \hat{p} \right) = \frac{1}{2} \frac{\partial \hat{\rho} \hat{h}}{\partial \hat{x}_1} + \gamma_3 \hat{\rho} \frac{\partial \hat{h}}{\partial \hat{t}} + \hat{h} \rho'(\hat{R}_1) (\gamma_2 \hat{R}_2 - \hat{\mathbf{U}}_b \cdot \hat{\nabla} \hat{R}_1), \quad (6.27)$$

with

$$\begin{aligned} \epsilon_p &= p_{\text{eq}} \frac{\rho_\ell R_{\text{eq}}^2}{(\mu_\ell + \kappa^s / R_{\text{eq}})^2}, \quad \beta_1 = \frac{\mu_\ell}{\mu_\ell + \kappa^s / R_{\text{eq}}}, \quad \beta_2 = \frac{\kappa^s / R_{\text{eq}}}{\mu_\ell + \kappa^s / R_{\text{eq}}}, \quad \epsilon_\omega = \omega \frac{\rho_\ell R_{\text{eq}}^2}{\mu_\ell + \kappa^s / R_{\text{eq}}} \\ \gamma_1 &= \frac{p_{\text{eq}}}{\mu_\ell \omega (J_r / J_c)^2}, \quad \gamma_2 = \frac{p_{\text{eq}}}{\omega} \frac{1}{(\mu_\ell + \kappa^s / R_{\text{eq}})}, \quad \gamma_3 = \frac{p_{\text{eq}}}{\omega} \frac{R_{\text{eq}}}{(\mu_\ell + \kappa^s / R_{\text{eq}})}. \end{aligned}$$

For typical reference values (like the ones exhibited in Table 7) both ϵ_p and ϵ_ω are several order smaller than the coefficients associated to viscous effects (β_1 and β_2). For instance, taking $\kappa^s = 10^{-5}$ N·s/m one has $\epsilon_p / \beta_1 \simeq 10^{-5}$ and $\epsilon_p / \beta_2 \simeq 10^{-9}$ and $\epsilon_p / \epsilon_\omega \simeq 1$. This small parameter (ϵ_p) multiplying the time derivative in Eq. (6.26) is typical of stiff equations (HAIRER; WANNER, 1996). These facts lead us to choose an implicit method in time to solve the system (6.25)-(6.27).

6.2.1 Discretization

After space discretization by Finite Volumes, the system of equations (6.25)-(6.27) is discretized in time (with a uniform time step length Δt) by means of a backward Euler scheme, obtaining a system of equations that can be written as (for each time step)

$$Q(\mathbf{R}_1^{n+1}, \mathbf{R}_2^{n+1}, \mathbf{p}^{n+1}) = 0, \quad (6.28)$$

with $Q : \mathbb{R}^M \times \mathbb{R}^M \times \mathbb{R}^M \mapsto \mathbb{R}^{3M}$ defined by

$$Q(\mathbf{R}_1^{n+1}, \mathbf{R}_2^{n+1}, \mathbf{p}^{n+1}) = \begin{pmatrix} \mathbf{R}_1^{n+1} - \mathbf{R}_1^n - \Delta t (\mathbf{R}_2^{n+1} - \gamma_2^{-1} \mathbb{A}_c \mathbf{R}_1^n) \\ \epsilon (\mathbf{R}_2^{n+1} - \mathbf{R}_2^n) - \Delta t g_2(\mathbf{R}_1^{n+1}, \mathbf{R}_2^{n+1}, \mathbf{p}^{n+1}) \\ \gamma_1 \mathbb{A}_d(\mathbf{R}_1^n) \mathbf{p}^{n+1} - g_3(\mathbf{R}_1^{n+1}, \mathbf{R}_2^{n+1}) \end{pmatrix}, \quad (6.29)$$

where $\mathbb{A}_d(\mathbf{R}_1^n)$ is a diffusion matrix, \mathbb{A}_c is a convection matrix that depends on \mathbf{U}_b and is computed by means of an upwind scheme, and $g_2 : \mathbb{R}^M \times \mathbb{R}^M \times \mathbb{R}^M \rightarrow \mathbb{R}^M$ and $g_3 : \mathbb{R}^M \times \mathbb{R}^M \rightarrow \mathbb{R}^M$ are defined respectively as

$$g_2(\mathbf{y}_1, \mathbf{y}_2, \mathbf{y}_3) = -\beta_3 \mathbb{A}_c \mathbf{R}_2^n - \epsilon \frac{3}{2} \frac{(\mathbf{y}_2)^2}{\mathbf{y}_1} - 4(\beta_1 \mathbf{y}_1 + \beta_2) \frac{\mathbf{y}_2}{(\mathbf{y}_1)^3} + \frac{F(\mathbf{y}_1) - \mathbf{y}_3}{\mathbf{y}_1} \quad (6.30)$$

where division and power operations on vectors are component-wise and

$$g_3(\mathbf{y}_1, \mathbf{y}_2) = \frac{1}{2} \mathbb{D}_{x_1} (\underline{\rho(\mathbf{y}_1)} h)^{n+1} + \gamma_3 \underline{\rho(\mathbf{y}_1)} (\underline{\partial_t h})^{n+1} + \underline{h}^{n+1} \underline{\rho'(\mathbf{y}_1)} (\gamma_2 \mathbf{y}_2 - \mathbb{A}_c \mathbf{R}_1^n), \quad (6.31)$$

where \mathbb{D}_{x_1} is a Finite Difference matrix that discretizes the operator ∂_{x_1} , and for an arbitrary function f defined in Ω , \underline{f} denotes the vector formed by taking the values of f at the cells' centers. Observe that the right hand side of (6.31) depends on h^{n+1} . The Jacobian matrix of Q will be further used to solve Eq. (6.28), and it reads

$$\mathbf{D}Q = \begin{pmatrix} \mathbb{I} & -\Delta t \mathbb{I} & \mathbb{O} \\ -\Delta t D_1 g_2 & \epsilon \mathbb{I} - \Delta t D_2 g_2 & -\Delta t D_3 g_2 \\ -D_1 g_3 & -D_2 g_3 & \gamma_1 \mathbb{A}_d(\mathbf{R}_1^n) \end{pmatrix}, \quad (6.32)$$

where $\mathbb{I} \in \mathbb{R}^{M \times M}$ and $\mathbb{O} \in \mathbb{R}^{M \times M}$ are the identity and null matrices respectively, and the components of the block matrices at the right hand side of Eq. (6.32) read ($\delta_{i,j}$ denotes de Kronecker delta)

$$\begin{aligned} [D_1 g_2(\mathbf{y}_1, \mathbf{y}_2, \mathbf{y}_3)]_{i,j} &= \left(\epsilon \frac{3}{2} \frac{(\mathbf{y}_2)_i^2}{(\mathbf{y}_1)_i^2} - 4\beta_1 \frac{(\mathbf{y}_2)_i}{(\mathbf{y}_1)_i^3} + 12(\beta_1 \mathbf{y}_1 + \beta_2) \frac{(\mathbf{y}_2)_i}{(\mathbf{y}_1)_i^4} \right) \delta_{i,j} + \\ &\quad + \frac{F'(\mathbf{y}_1)_i (\mathbf{y}_1)_i - F(\mathbf{y}_1)_i + \mathbf{y}_3}{(\mathbf{y}_1)_i^2} \delta_{i,j}, \\ [D_2 g_2(\mathbf{y}_1, \mathbf{y}_2, \mathbf{y}_3)]_{i,j} &= -3\epsilon \frac{(\mathbf{y}_2)_i}{(\mathbf{y}_1)_i} \delta_{i,j} - 4 \frac{(\beta_1 (\mathbf{y}_1)_i + \beta_2)}{(\mathbf{y}_1)_i^3} \delta_{i,j} \\ [D_3 g_2(\mathbf{y}_1, \mathbf{y}_2, \mathbf{y}_3)]_{i,j} &= -\frac{1}{(\mathbf{y}_1)_i} \delta_{i,j}, \end{aligned}$$

$$\begin{aligned} [\mathbf{D}_1 g_3(\mathbf{y}_1, \mathbf{y}_2)]_{i,j} &= \frac{1}{2} \mathbb{D}_{x_1} \underline{\rho'(\mathbf{y}_1)} h \delta_{i,j} + \gamma_3 \underline{\rho'(\mathbf{y}_1)} \left(\underline{\partial_t h} \right)^{n+1} \delta_{i,j} + \\ &\quad + h^{n+1} \underline{\rho''(\mathbf{y}_1)} (\gamma_2 \mathbf{y}_2 - \mathbb{A}_c \mathbf{R}_1^n) \delta_{i,j}, \\ [\mathbf{D}_2 g_3(\mathbf{y}_1, \mathbf{y}_2)]_{i,j} &= \gamma_2 (h)_i^{n+1} \left(\underline{\rho'(\mathbf{y}_1)} \right)_i \delta_{i,j}. \end{aligned}$$

6.2.1.1 A one-dimensional dynamically loaded Journal

In this Section a numerical method to couple Equation (6.28) along the Newton's equation for the Journal dynamics is presented. A one-dimensional problem is obtained by setting null-flux boundary conditions at $x_2 = 0$ and $x_2 = J_w$, and by using surface textures independent of x_2 .

Assume first that all the unknowns have been already computed at time \hat{t}^n , and that the geometry for the next time step (\hat{h}^{n+1}) is also known. Denote by $\hat{\mathbf{X}} = (\hat{X}, \hat{Y})^T = \mathbf{X}/(J_c) \in \mathbb{R}^2$ the non-dimensional journal position at time \hat{t} (which uniquely determines \hat{h} at time \hat{t} , and vice versa) and by $\mathcal{P} : \mathbb{R}^2 \mapsto \mathbb{R}^M$ the function such that $\mathcal{P}(\hat{\mathbf{X}})$ corresponds to the pressure vector at time \hat{t} , observe that this function is known as this can be obtained by means of Eq. (6.28). Before time discretization, Newton's equation for the journal reads

$$\hat{M}_J \frac{d^2 \hat{\mathbf{X}}}{d\hat{t}^2} = \hat{\mathbf{W}}(\mathcal{P}(\hat{\mathbf{X}})) + \hat{\mathbf{W}}^a, \quad (6.33)$$

where $\hat{M}_J = \frac{J_c}{(J_r t_r^r)^2 p^r} M_J$ is the non-dimensional journal mass, and $\hat{\mathbf{W}}(\mathcal{P}(\hat{\mathbf{X}}))$, $\hat{\mathbf{W}}^a$ correspond to the hydrodynamical force (some discretization of formula (2.28)) and to the applied load respectively (which is a datum). The reference force corresponds to $p^r J_r^2$. This last equation is discretized by means of a Newmark' scheme, the resulting equation for $\hat{\mathbf{X}}^{n+1}$ reads

$$\mathcal{L}(\hat{\mathbf{X}}^{n+1}) = \hat{\mathbf{X}}^{n+1} - \hat{\mathbf{X}}^n - \Delta \hat{t} \hat{V}_J^n - \frac{\Delta \hat{t}^2}{2 \hat{M}_J} \left(\hat{\mathbf{W}}(\mathcal{P}(\hat{\mathbf{X}}^{n+1})) + \hat{\mathbf{W}}^a \right) = 0, \quad (6.34)$$

where \hat{V}_J^n is the non-dimensional journal velocity vector, already computed for time \hat{t}^n . That vector is updated at each time step according to

$$\hat{V}_J^{n+1} = \hat{V}_J^n + \frac{\Delta \hat{t}}{\hat{M}_J} \left(\hat{\mathbf{W}}(\mathcal{P}(\hat{\mathbf{X}}^{n+1})) + \hat{\mathbf{W}}^a \right). \quad (6.35)$$

Equation (6.34) depends only on $\hat{\mathbf{X}}^{n+1}$ and can be solved by traditional iterative algorithms. For the results shown in the next section, that task has been performed by means of the Octave's function `fsolve`. Notice that this strategy to compute $\hat{\mathbf{X}}^{n+1}$ implies the computation of \mathbf{p}^{n+1} , \mathbf{R}_1^{n+1} and \mathbf{R}_2^{n+1} .

6.2.2 Numerical results

Here results obtained by means of the scheme (6.28)-(6.31) and (6.34) are shown. An Octave¹ code was written to solve Eq. (6.34) by means of a Newton-like method for non-linear equations (implemented inside the function `fsolve` of Octave). That function may use Eq. (6.28) several times looking for the optimal $\hat{\mathbf{X}}^{n+1}$.

6.2.2.1 Comparison with inertial terms / without inertial terms

For the next results the number of cells along the circumferential direction was set to $N_x = 512$. The journal rotational speed was fixed to 2000 rpm. While the time step was set to 40000 time steps per cycle ($\Delta t = 7.5 \times 10^{-7}$ s) for $0 \leq t \leq 5 \times 10^{-4}$ s and 4000 time steps per cycle ($\Delta t = 7.5 \times 10^{-6}$ s) for $t \geq 5 \times 10^{-4}$ s. This adaption of the time step allows to handle a fast transient behavior observed at the beginning of the simulations. The journal mass was set to $M_J = 3$ kg, the surface dilatational viscosity was fixed to $\kappa^s = 7.85 \times 10^{-6}$ N·s/m, and the bubbles equilibrium radius R_{eq} was taken between 0.25 and 2 microns. The other parameters were set as in Table 7. It only remains to specify \mathbf{W}^a , the force applied to the journal, which reads:

$$\mathbf{W}^a(t) = \mathbf{W}^{a,c} + \mathbf{W}^{a,p}(t), \quad (6.36)$$

where the first term is a constant load equal to $\mathbf{W}^{a,c} = [8000, -5000]^T$ N, and the second term $\mathbf{W}^{a,p}(t) = [W_X^{a,p}(t), W_Y^{a,p}(t)]^T$ corresponds to a series of short pulses with a time duration of a quarter of a cycle, or $\approx 8 \times 10^{-3}$ s, reading

$$\mathbf{W}^{a,p}(t) = \begin{pmatrix} F_X^A \\ F_Y^A \end{pmatrix} \left[\exp(-400(\text{mod}(t/\tau, 2) - 0.2)^2) \right] [0.5 + 0.5 \tanh(50(t/\tau - 15))], \quad (6.37)$$

where F_X^A and F_Y^A are the amplitudes of the perturbation and $\tau = 0.03$ s is the time period of the journal. Observe that the perturbation is placed each 2 journal cycles in time (the term $\text{mod}(t/\tau, 2)$). An example of $W_Y^{a,p}(t)$ is shown in Fig. 6.2.1 for $F_Y^A = 1000$ N and $0 < t < 0.9$ s.

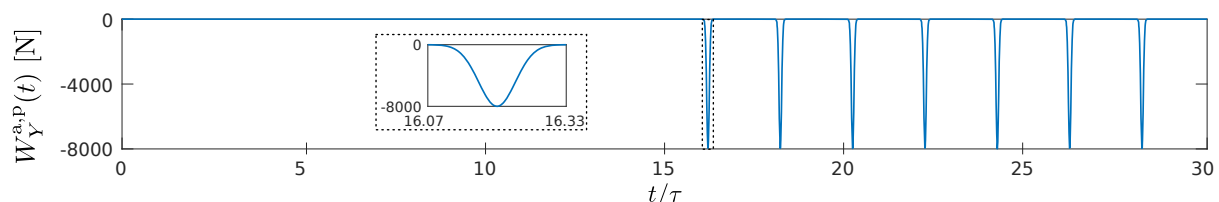


Figure 6.2.1 – $W_Y^{a,p}$: pulses in time used to perturb the position of the Journal once it has arrived near its equilibrium, in this case $F_Y^A = 8000$ N.

Based in a convergence analysis, the number of cells along the x_1 axis was set to 512 and the number of time steps was fixed to 4000 per journal cycle $\Delta t = 7.5 \times 10^{-6}$ s.

¹ www.gnu.org/software/octave/

Small perturbation varying R_{eq}

Here F_X^A and F_Y^A are set to 0 and 1000 N respectively, and the surfaces considered are smooth ($h_T = 0$ in (2.26)). The journal eccentricity is defined as

$$\varepsilon(t) = \sqrt{\hat{X}(t)^2 + \hat{Y}(t)^2}, \quad (6.38)$$

which is a measure of the displacement of the journal's center with respect to the bush's center, when both the centers coincide $\varepsilon = 0$, and when the journal and the bush touch $\varepsilon = 1$. The results for ε in time are shown in Fig. 6.2.2 when setting $R_{\text{eq}} = 0.25, 1.0$ and $2.0 \mu\text{m}$. For $t/\tau \approx 15$ the journal has arrived to its equilibrium point. Overall, the

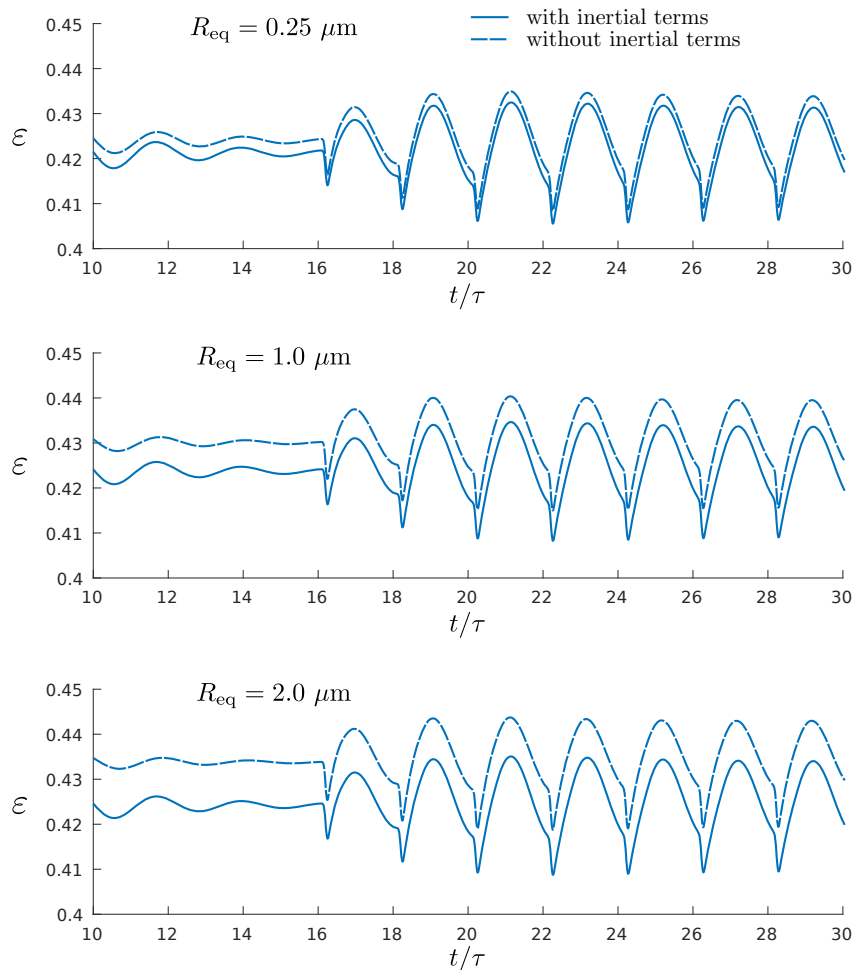


Figure 6.2.2 – Eccentricity in time when varying the equilibrium radii R_{eq} with $F_Y^A = 1000 \text{ N}$ and $F_X^A = 0$ (small load perturbation).

higher the value of R_{eq} the bigger the difference for ε when including inertial terms or disregarding them. In fact, time averaging ε between $t/\tau \approx 24$ and $t/\tau \approx 30$ (the last six journal cycles), and denoting that average by $\bar{\varepsilon}_{+i}$ ($\bar{\varepsilon}_{-i}$) when including (disregarding) the inertial terms the relative differences between these averages are shown in Table 8.

These results indicate a dependence of the journal dynamics on the inertial terms and on the bubbles equilibrium radii. This motivates further research on polydisperse

| | $R_{\text{eq}} = 0.25 \mu\text{m}$ | $R_{\text{eq}} = 1.0 \mu\text{m}$ | $R_{\text{eq}} = 2.0 \mu\text{m}$ |
|---|------------------------------------|-----------------------------------|-----------------------------------|
| $\left \frac{\bar{\varepsilon}_{+i} - \bar{\varepsilon}_{-i}}{\bar{\varepsilon}_{+i}} \right $ | 0.007 | 0.015 | 0.023 |

Table 8 – Relative differences for the time averaged journal eccentricities for different bubbles equilibrium radii.

radius distributions as described in Section 4.2.2.

Strong perturbation and friction torque

In this section the bubbles equilibrium radii is set to $R_{\text{eq}} = 1 \mu\text{m}$, and F_X^A and F_Y^A are set to -8000 and 5000 N respectively, which means that $[F_X^A, F_Y^A]^T = -\mathbf{W}^{\text{a,c}}$. This load perturbation is called *strong* as it generates a high variation of the journal's eccentricity compared with the variation generated along the small perturbation used in the previous section as shown in Fig. 6.2.3.

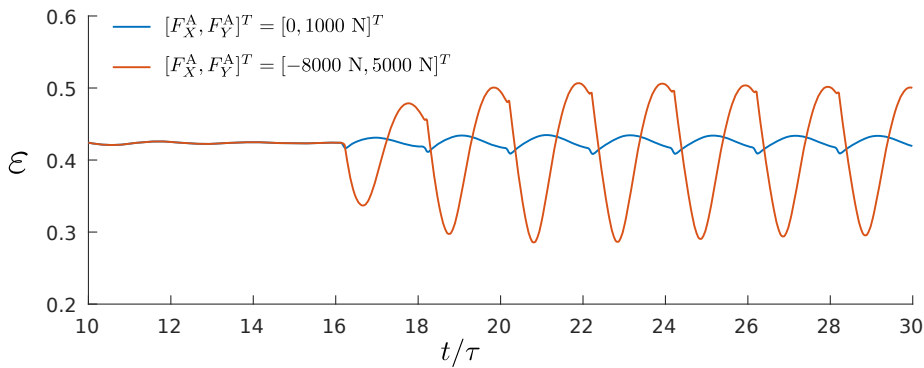


Figure 6.2.3 – Eccentricity in time for smooth journals with a small and strong load perturbations, and $R_{\text{eq}} = 1.0 \mu\text{m}$.

A quantity of interest in Tribology is the friction torque opposite to the journal angular momentum, which can be computed as

$$\tau_{\text{friction}}(t) = J_r \int_{\Omega} \left(\frac{h(x_1, t)}{2} \frac{\partial p}{\partial x_1} + \frac{\mu(\rho(x_1, t)) \bar{U}}{h(x_1, t)} \right) d\Omega, \quad (6.39)$$

where $\bar{U} = \omega J_r$ is the relative speed between the journal surfaces. Let us denote by $\bar{\tau}_{+i}^{\text{smooth}}$ ($\bar{\tau}_{-i}^{\text{smooth}}$) the time averaged torque between $t/\tau = 24$ and $t/\tau = 30$ when disregarding (including) the inertial terms without textures on the surfaces. For the small perturbation it was observed $\frac{|\bar{\tau}_{+i}^{\text{smooth}} - \bar{\tau}_{-i}^{\text{smooth}}|}{|\bar{\tau}_{+i}^{\text{smooth}}|} = 0.002$, a very slight difference. While for the strong perturbation $\frac{|\bar{\tau}_{+i}^{\text{smooth}} - \bar{\tau}_{-i}^{\text{smooth}}|}{|\bar{\tau}_{+i}^{\text{smooth}}|} = 0.012$, a difference that would not justify the computational cost differences (the computing time along the inertial terms is ≈ 10 times the computational terms without the inertial terms, at least for the current code). Next, let us set a stationary texture on the bush.

The texture along the x_1 -axis consists of 10 identical elliptically-shaped pockets that are equally distributed, with a depth equal to $9.4 \mu\text{m}$ (depicted in Fig. 6.2.4). The first notable consequence of including the texture is the change on the equilibrium point of the journal and the higher variation of ε when the load perturbation is applied, as shown in 6.2.5. This time it was observed $\frac{|\bar{\tau}_{+i}^{\text{text}} - \bar{\tau}_{-i}^{\text{text}}|}{|\bar{\tau}_{+i}^{\text{text}}|} = 0.032$, a relative difference that suggests that there exist cases where the inertial terms are not negligible.

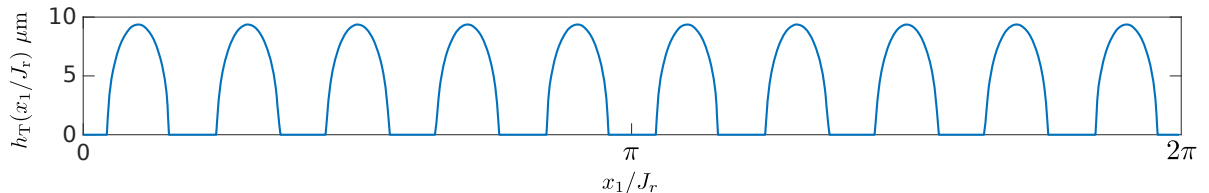


Figure 6.2.4 – Time independent texture placed on the bush.

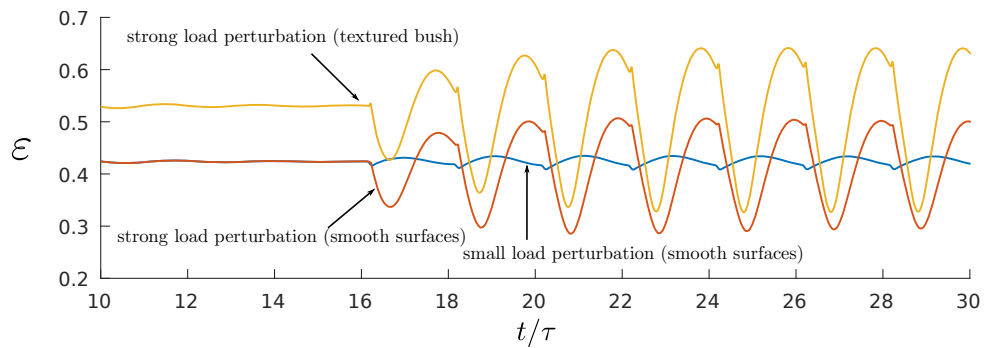


Figure 6.2.5 – Eccentricity in time for smooth journals with a small and strong load perturbations, and for a textured bush.



CONCLUSIONS

7.1 Conclusions

In this thesis the modeling of cavitation on Hydrodynamic Lubrication has been addressed along with the robust numerical treatment of the related models. Also, a mathematical analysis of a trending cavitation model was developed by means of some classical Functional Analysis tools.

The first problem where a contribution was made is in the incorporation of the mechanical pressure variation of the Combustion Chamber of an engine as a boundary condition for the flow equation. The Elrod-Adams cavitation model was taken as a starting point as it imposes continuity of the flux function. Two approaches were explored: one imposing a null pressure gradient, which was observed as being suitable for transient regimes where the liner is flat. When including textures on the liner an incompatibility between the pressure profiles developed in time and the continuity of the flux was numerically observed. The second approach tackles that issue when considering one-dimensional configurations. Instead of imposing a null pressure gradient, mass-conservation is obtained by a dynamical restriction for the rupture point β . This dynamical restriction is simply the Rankine-Hugoniot condition, which one-dimensional version corresponds to a first-order differential equation for β . The extension of that approach for two-dimensional cases is not obvious. By means of the first approach, a numerical analysis along the Piston-Ring-Liner simulations showed relevant differences when computing the minimum clearance and friction whether the Combustion Chamber pressure is set as boundary condition or not. This proves the importance of this type of studies to obtain accurate results. Focusing on the stationary state, the parameter θ_0 was fixed to 2/3 based on a reversing flux condition presented in (DOWSON; TAYLOR, 1979). However, a whole range of values for θ_0 is admissible respecting the Rankine-Hugoniot mass-conserving condition. A dynamical modeling of θ_0 remains as being an open problem for which the physics behind the rupture phenomenon

should be incorporated.

The Reynolds-Rayleigh-Plesset coupling is a current trend on cavitation modeling for hydrodynamics. While other models assume some compressibility law, the RRP model tries to capture the physics of cavitation by solving the dynamics of a distribution of bubbles immersed in a liquid. Studying that model, the first struggle was the lack of detailed numerical methods in the literature. With all, a numerical strategy used in the literature was identified and implemented. Unfortunately, that method was found to have an unstable behavior, first by numerical means and later by performing a linear perturbation analysis. Thus, tackling the lack of robust numerical codes for the RRP coupling represents the second contribution of this work. Firstly, for the case where the inertial terms are disregarded in the Rayleigh-Plesset equation, a numerical method based on a suitable handling of the time derivative $\frac{\partial \rho}{\partial t}$ was proposed. This time the linear perturbation analysis showed unconditional stability and numerical robustness was observed, allowing to perform simulations along with a wide range of parameters on a test problem (the Fracture Problem, in which the pressure build-up takes place solely by an expansion of the bubbles) as well as for the well-known Journal Bearing problem. A convergence analysis resulted in first-order convergence ratio both in space and time. The simulations of the Journal Bearing also included a comparison to the Elrod-Adams model. Good agreement between both models was found when the surface dilatational viscosity is small enough. In particular, the liquid fraction $1 - \alpha$ from the RRP model is quite close to the fluid fraction θ from the Elrod-Adams model. To our knowledge, this is the first time such a comparison is made and further work is underway to obtain a better insight into the relationship between both models. Further, a numerical method for the RRP coupling when the inertial terms are not disregarded was also developed. As that system has the characteristics of a stiff evolution problem, a backward Euler scheme in time was used. In general, inertial terms are disregarded by means of a non-dimensional analysis, or, when numerical comparisons are made, some other terms (like the surface energy) are taken off of the Rayleigh-Plesset equation. The numerical code developed for the *full* RRP model allowed us to perform these comparisons without further simplifications.

In collaboration with a research group from the *Institut National des Sciences Appliquées* (INSA-Lyon, France), a lack of theoretical works around the RRP coupling was identified. Thus, another set of problems tackled during this research project was related to the analysis of the well-posedness of the RRP model. This study was made separately for two cases: 1) including the inertial terms of the Rayleigh-Plesset equation or 2) not including them. In both these cases the transport of the bubbles was disregarded ($\mathbf{U}_b = 0$). Identifying suitable functional spaces, local existence in time was proved by means of the Cauchy-Lipschitz Theorem. Existence of stationary solutions and stability of these (by means of continuity arguments) were proved conditioned to the hypotheses of the surfaces being near to flat or small relative speed $\|\mathbf{U}\|$. Although in general these

hypotheses assured stability, it is remarkable that when the inertial terms are included and the surfaces are flat (both h_U and h_L considered as constants) there exists a surfaces relative speed high enough such that the stationary solution is asymptotically unstable.

7.2 Future Work

Here some tasks that would be interesting to perform in future research are listed:

On the non-homogeneous boundary conditions for pressure

1. To propose dynamical models for the rupture boundary along the Rankine-Hugoniot condition allowing both the surfaces to be textured in the two-dimensional case. For this, a better understanding of rupture boundary's physics is needed.

On the Reynolds-Rayleigh-Plesset coupling

1. To consider the dynamics of polydisperse distributions of bubbles, instead of the monodisperse hypothesis made in the literature. The numerous works of Carrica's group ([CARRICA et al., 1998](#); [CARRICA et al., 1999](#); [CASTRO](#); [CARRICA, 2013](#); [CASTRO; LI](#); [CARRICA, 2016](#)) for the dynamics of a two-phase flow around a ship indicate the multigroup approach as a promising framework for this task. This would allow for more realistic modeling and the incorporation of bubbles interaction, like bubbles break-up or coalescence.
2. To perform a mathematical analysis of the RRP coupling for the case where the transport of the bubbles is considered ($\mathbf{U}_b \neq 0$). Since in that case the operator at the right-hand-side of the evolution problem is unbounded, a more general theory is needed, like the Hille-Yosida Theorem ([PAZY, 1983](#); [BREZIS, 2010](#)).

BIBLIOGRAPHY

- ADAMS, R. A. **Sobolev Spaces**. 1. ed. [S.l.]: Academic Press, 1975. Citations on pages [93](#) and [97](#).
- ALT, H. W. Numerical solution of steady-state porous flow free boundary problems. **Numer. Math.**, v. 36, n. 1, p. 73–98, 1980. ISSN 0029-599X. Available: <<http://link.springer.com/10.1007/BF01395990>>. Citations on pages [46](#), [47](#), and [48](#).
- ANDERBERG, C.; DIMKOVSKI, Z.; ROSÉN, B.-G.; THOMAS, T. Low friction and emission cylinder liner surfaces and the influence of surface topography and scale. **Tribology International**, Elsevier Ltd, 2018. Citation on page [22](#).
- ARCOUMANIS, C.; DUSZYNSKI, M.; FLORA, H.; OSTOVAR, P. Development of a Piston-Ring Lubrication Test-Rig and Investigation of Boundary Conditions for Modelling Lubricant Film Properties. In: . [s.n.], 1995. Available: <<http://papers.sae.org/952468/>>. Citation on page [36](#).
- AUSAS, R.; JAI, M.; CIUPERCA, I. S.; BUSCAGLIA, G. C. Conservative one-dimensional finite volume discretization of a new cavitation model for piston-ring lubrication. **Tribol. Int.**, v. 57, p. 54–66, 2013. Citations on pages [24](#), [32](#), [48](#), [49](#), and [76](#).
- AUSAS, R.; RAGOT, P.; LEIVA, J.; JAI, M.; BAYADA, G.; BUSCAGLIA, G. The impact of the Cavitation model in the Analysis of Micro-Textured Lubricated Journal bearings. **ASME J. Tribol.**, v. 129, n. 4, p. 868–875, 2007. Citations on pages [21](#), [29](#), [30](#), and [129](#).
- BAI, L.; MENG, Y.; ZHANG, V. Experimental Study on Transient Behavior of Cavitation Phenomenon in Textured Thrust Bearings. **Tribology Letters**, v. 63, n. 2, p. 1–15, 2016. Citation on page [28](#).
- BAYADA, G.; CHAMBAT, M. Analysis of a free boundary problem in partial lubrication. **Quart. Appl. Math.**, v. 40, n. 4, p. 369–375, 1983. Citation on page [23](#).
- _____. The transition between the Stokes equations and the Reynolds equation: A mathematical proof. **Applied Mathematics & Optimization**, v. 14, n. 1, p. 73–93, 1986. Citation on page [21](#).
- BENSOUSSAN, A.; LIONS, J. L.; PAPANICOLAOU, G. Asymptotic analysis for periodic structures. In: _____. [S.l.]: North-Holland, 1978. chap. 1, p. 38. Citation on page [93](#).
- BENZONI-GAVAGE, S. **Calcul différentiel et équations différentielles: cours et exercices corrigés**. [S.l.]: SIAM, 2010. Citation on page [158](#).
- BERMÚDEZ, A.; DURANY, J. Numerical solution of cavitation problems in lubrication. **Computer Methods in Applied Mechanics and Engineering**, v. 75, n. 1, p. 457–466, 1989. Citation on page [23](#).
- BOU-SAÏD, B. Finite bearing model. In: _____. **Encyclopedia of Tribology**. [S.l.]: Springer US, 2013. p. 1131–1136. Citation on page [32](#).

BRAUN, M.; HANNON, W. Cavitation formation and modelling for fluid film bearings: A review. **J. Engineering Tribol.**, v. 224, p. 839–863, 2010. Citation on page [22](#).

BRAUN, M.; PIERSON, K.; SNYDER, T. Two-way coupled Reynolds, Rayleigh-Plesset-Scriven and energy equations for fully transient cavitation and heat transfer modeling. **IOP Conference Series: Materials Science and Engineering**, v. 174, n. 1, p. 012030, 2017. Citations on pages [83](#), [84](#), [86](#), [88](#), [108](#), and [126](#).

_____. Two-way coupled Reynolds, Rayleigh-Plesset-Scriven and energy equations for fully transient cavitation and heat transfer modeling. **IOP Conference Series: Materials Science and Engineering**, v. 174, p. 012030, 2017. Citation on page [101](#).

BRENNEN, C. E. **Cavitation and Bubble Dynamics**. [S.l.]: Oxford University Press, 1995. Citations on pages [77](#) and [78](#).

BREZIS, H. **Functional Analysis, Sobolev Spaces and Partial Differential Equations**. [S.l.]: Springer, 2010. Citations on pages [143](#) and [157](#).

BRIZMER, V.; KLIGERMAN, Y.; ETSION, I. A laser surface textured parallel thrust bearing. **Tribol. T.**, v. 46, p. 397–403, 2003. Citation on page [22](#).

BUSCAGLIA, G.; CIUPERCA, I.; JAI, M. Topological asymptotic expansions for the generalized Poisson problem with small inclusions and applications in lubrication. **Inverse Problems**, p. 695–711, 2007. Citation on page [23](#).

BUSCAGLIA, G. C.; CIUPERCA, I.; DALISSLIER, E.; JAI, M. A new cavitation model in lubrication: the case of two-zone cavitation. **Journal of Engineering Mathematics**, v. 83, p. 57–79, 2013. Citation on page [41](#).

BUSCAGLIA, G. C.; CIUPERCA, I.; JAI, M. Existence and uniqueness for several nonlinear elliptic problems arising in lubrication theory. **Journal of Differential Equations**, v. 218, p. 187–215, 2005. Citation on page [23](#).

BUSCAGLIA, G. C.; El Alaoui Talibi, M.; JAI, M. Mass-conserving cavitation model for dynamical lubrication problems. Part I: Mathematical analysis. **Mathematics and Computers in Simulation**, v. 118, p. 130–145, 2015. Citation on page [23](#).

CAMERON, A. **Basic lubrication theory**. [S.l.]: Longman Publishing Group Ltd., 1971. Citation on page [21](#).

CARRICA, P.; DREW, D.; BONETTO, F.; LAHEY, R. A polydisperse model for bubbly two-phase flow around a surface ship. **Int. J. Multiphase Flow**, v. 25, p. 257–305, 1999. Citations on pages [84](#), [86](#), and [143](#).

CARRICA, P. M.; BONETTO, F. J.; DREW, D. A.; LAHEY, R. T. The interaction of background ocean air bubbles with a surface ship. **International Journal for Numerical Methods in Fluids**, v. 28, n. 4, p. 571–600, 1998. Citations on pages [84](#) and [143](#).

CASTRO, A.; CARRICA, P. Bubble size distribution prediction for large-scale ship flows: Model evaluation and numerical issues. **Int. J. Multiphase Flow**, v. 57, p. 131–150, 2013. Citations on pages [84](#), [87](#), and [143](#).

CASTRO, A.; LI, J.; CARRICA, P. A mechanistic model of bubble entrainment in turbulent free surface flows. **Int. J. Multiphase Flow**, v. 86, p. 35–55, 2016. Citations on pages 84 and 143.

CHECO, H. M. **Models and methods for the direct simulation of rough and micropatterned surfaces**. Phd Thesis (PhD Thesis) — Instituto de Ciências Matemáticas e de Computação, USP, 2015. Citation on page 24.

CHECO, H. M.; AUSAS, R.; JAI, M.; CADALEN, J.; CHOUKROUN, F.; BUSCAGLIA, G. C. Moving textures: Simulation of a ring sliding on a textured liner. **Tribol. Int.**, v. 72, p. 131–142, 2014. Citation on page 22.

CHECO, H. M.; JARAMILLO, A.; AUSAS, R.; BUSCAGLIA, G. The lubrication approximation of the friction force for the simulation of measured surfaces. **Tribol. Int.**, v. 97, p. 390–399, 2016. Citation on page 58.

CHENG, J.; MENG, X.; XIE, Y.; KONG, X. Blow-by and tribological performance of piston ring pack during cold start and warm idle operations. **Science China Technological Sciences**, v. 59, n. 7, p. 1085–1099, 2016. Citation on page 67.

CIMATTI, G. On a problem of the theory of lubrication governed by a variational inequality. **Applied Mathematics and Optimization**, v. 3, n. 2, p. 227–242, 1976. Citation on page 23.

_____. A free boundary problem in the theory of lubrication. **International Journal of Engineering Science**, v. 18, n. 5, p. 703–711, 1980. Citation on page 23.

COYNE, J. C.; ELROD, H. G. Conditions for the Rupture of a Lubricating Film. Part I: Theoretical Model. **J. Lubr. Technol.**, v. 92, n. 3, p. 451, 1970. ISSN 00222305. Available: <<http://tribology.asmedigitalcollection.asme.org/article.aspx?articleid=1461903>>. Citation on page 36.

_____. Conditions for the Rupture of a Lubricating Film—Part II: New Boundary Conditions for Reynolds Equation. **J. Tribol.**, v. 93, n. 1, p. 156–167, 1971. ISSN 0742-4787. Available: <<http://dx.doi.org/10.1115/1.3451506>>. Citations on pages 36, 48, and 71.

DHANDE, D. Y.; PANDE, D. W. Multiphase flow analysis of hydrodynamic journal bearing using cfd coupled fluid structure interaction considering cavitation. **Journal of King Saud University - Engineering Sciences**, 2016. ISSN 1018-3639. Citation on page 23.

DOBRICA, M. B.; FILION, M.; PASCOVICI, M. D.; CICONE, T. Optimizing surface texture for hydrodynamic lubricated contacts using a mass-conserving numerical approach. **Proc. IMechE**, v. 224, n. 8, p. 737–750, 2010. Citation on page 22.

DONEA, J.; HUERTA, A. **Finite Element Methods for Flow Problems**. [S.l.]: Wiley, 2003. Citation on page 155.

DOWSON, D. Piston Assemblies; Background and Lubrication Analysis. In: **Tribol. Ser.** [s.n.], 1993. v. 26, n. C, p. 213–240. ISBN 9780444897558. Available: <<http://linkinghub.elsevier.com/retrieve/pii/S0167892208700130>>. Citation on page 36.

DOWSON, D.; TAYLOR, C. Cavitation in bearings. **Annu. Rev. Fluid Mech.**, v. 11, p. 35–66, 1979. Citations on pages 21, 26, 28, 41, 77, and 141.

DREW, D.; PASSMAN, S. **Theory of Multicomponent Fluids.** [S.l.]: Springer-Verlag New York, 1999. Citations on pages 84 and 89.

DUNFORD, N.; SCHWARTZ, J. T. Linear operators, part i: General theory. In: _____. [S.l.]: Interscience Publishers, 1957. chap. VII, p. 585. Citation on page 94.

ELROD, H. G.; ADAMS, M. A computer program for cavitation. Technical report 190. 1st LEEDS LYON Symposium on Cavitation and Related Phenomena in Lubrication, I.M.E., v. 103, p. 354, 1974. Citations on pages 30 and 42.

ETSION, I. State of the art in laser surface texturing. **J. Tribol.: Trans. ASME**, v. 127, p. 248–253, 2005. Citation on page 22.

_____. Modeling of surface texturing in hydrodynamic lubrication. **Friction**, v. 1, n. 3, p. 195–209, Jul. 2013. ISSN 2223-7690. Available: <<http://link.springer.com/10.1007/s40544-013-0018-y>>. Citation on page 22.

FLOBERG, L. On hydrodynamic lubrication with special reference to sub-cavity pressures and number of streamers in cavitation regions. In: **Acta Polytech. Scand. Mech. Eng. Ser.**, **19**. [S.l.: s.n.], 1965. p. 3–35. Citation on page 36.

GADESCHI, G. B.; BACKHAUS, K.; KNOLL, G. Numerical Analysis of Laser-Textured Piston-Rings in the Hydrodynamic Lubrication Regime. **ASME J. Tribol.**, v. 134, n. 4, p. 1–8, October 2012. Citations on pages 22 and 69.

GANTMACHER, F. R. Applications of the theory of matrices. In: _____. [S.l.]: Interscience Publishers, 1959. chap. V, p. 230. Citation on page 100.

GEHANNIN, J. **Analyse théorique des amortisseurs à film fluide fonctionnant à des nombres de Reynolds élevés.** Phd Thesis (PhD Thesis) — Université de Poitiers, 2009. Citations on pages 77 and 78.

GEHANNIN, J.; ARGHIR, M.; BONNEAU, O. Evaluation of Rayleigh-Plesset Equation Based Cavitation Models for Squeeze Film Dampers. **Journal of Tribology**, v. 131, n. 2, p. 024501, 2009. Citations on pages 84, 86, 108, and 110.

_____. A volume of fluid method for air ingestion in squeeze film dampers. **Tribology Transactions**, Taylor & Francis, v. 59, n. 2, p. 208–218, 2016. Citations on pages 84, 86, and 108.

GEIKE, T.; POPOV, V. A Bubble Dynamics Based Approach to the Simulation of Cavitation in Lubricated Contacts. **Journal of Tribology**, v. 131, n. 1, p. 011704, 2009. Citations on pages 84, 86, and 110.

_____. Cavitation within the framework of reduced description of mixed lubrication. **Tribology International**, v. 42, n. 1, p. 93–98, 2009. Citations on pages 84, 86, and 110.

Guido-Lavalle, G.; CARRICA, P.; CLAUSSE, A.; QAZI, M. A bubble number density constitutive equation. **Nuclear Engineering and Design**, v. 152, p. 213–224, 1994. Citation on page 84.

HAIRER, E.; WANNER, G. **Solving Ordinary Differential Equations II: Stiff and Differential-Algebraic Problems.** Second. [S.l.]: Springer, 1996. Citation on page 133.

HAKL, R.; TORRES, P. J.; ZAMORA, M. Periodic solutions to singular second order differential equations: the repulsive case. **Topol. Methods Nonlinear Anal.**, Nicolaus Copernicus University, Juliusz P. Schauder Centre for Nonlinear Studies, v. 39, n. 2, p. 199–220, 2012. Citation on page [23](#).

HOLMBERG, K.; ANDERSSON, P.; ERDEMIR, A. Global energy consumption due to friction in passenger cars. **Tribol. Int.**, v. 47, p. 221–234, 2012. Citation on page [22](#).

JAKOBSON, B.; FLOBERG, L. The Finite Journal Bearing Considering Vaporization. **Tran. Chalmers University of Technology**, v. 190, p. 1–119, 1957. Citation on page [31](#).

JARAMILLO, A. **Mathematical modeling of micro-textured lubricated contacts**. Master's Thesis (Master's Thesis) — Instituto de Ciências Matemáticas e de Computação, Junho 2015. Citation on page [30](#).

JARAMILLO, A.; BAYADA, G.; CIUPERCA, I.; JAI, M. **On the well-posedness of Reynolds-Rayleigh-Plesset coupling**. 2018. <<https://arxiv.org/abs/1805.07219>>. Citations on pages [91](#) and [161](#).

JARAMILLO, A.; BUSCAGLIA, G. A stable numerical strategy for Reynolds-Rayleigh-Plesset coupling. **Tribol. Int.**, v. 130, p. 191–205, 2019. Citations on pages [35](#), [107](#), and [161](#).

JARAMILLO, A.; BUSCAGLIA, G. C.; M., J. **Tribological effects of the combustion chamber pressure along an extended Elrod-Adams model**. 2017. Oral presentation in the 44th Leeds-Lyon Symposium on Tribology, Lyon, France. Citation on page [39](#).

JARAMILLO, A.; CHECO, H.; BUSCAGLIA, G. Incorporation of back-pressure effects in the modeling of the cylinder/piston-rings system. **Proceedings of the XXXVII Iberian Latin American Congress on Computational Methods in Engineering - CILAMCE2016**, 2016. Citation on page [39](#).

JARAMILLO, A.; CHECO, H. M.; BUSCAGLIA, G. Non-homogeneous boundary conditions and cavitation modeling for Reynolds equation. **Mecánica Computacional**, XXXIX, n. 4, p. 2087–2100, 2016. Citation on page [39](#).

KINDERLEHRER, D.; STAMPACCHIA, G. An Introduction to Variational Inequalities and Their Applications. In: _____. [S.l.]: SIAM, 1980. chap. VII, p. 223–227. Citations on pages [23](#) and [29](#).

KLIGERMAN, Y.; SHINKARENKO, A. Analysis of friction in surface textured components of reciprocating mechanism. **Proc. Inst. Mech. Eng. Part J J. Eng. Tribol.**, v. 229, n. 4, p. 336–349, apr 2015. ISSN 1350-6501. Available: <<http://pij.sagepub.com/lookup/doi/10.1177/1350650114545635>>. Citation on page [36](#).

KOVALCHENKO, A.; AJAYI, O.; ERDEMIR, A.; FENSKE, G.; ETSION, I. The Effect of Laser Texturing of Steel Surfaces and Speed-Load Parameters on the Transition of Lubrication Regime from Boundary to Hydrodynamic. **Tribol. T.**, v. 47, n. 2, p. 299–307, 2004. Available: <<http://www.tandfonline.com/doi/abs/10.1080/05698190490440902>>. Citation on page [22](#).

KU, C.-P.; TICHY, J. An Experimental and Theoretical Study of Cavitation in a Finite Submerged Squeeze Film Damper. **Journal of Tribology**, v. 112, n. 4, p. 725, 1990. Citation on page [28](#).

KUBOTA, A.; KATO, H.; YAMAGUCHI, H. A new modelling of cavitating flows: a numerical study of unsteady cavitation on a hydrofoil section. **Journal of Fluid Mechanics**, v. 240, p. 59–96, 1992. Citation on page [23](#).

KUNDU, P. K.; COHEN, I. M. **Fluid Mechanics**. Third. [S.l.]: Elsevier Academic Press, 2004. Citation on page [26](#).

LANG, S. Fundamentals of differential geometry. In: _____. [S.l.]: Springer-Verlag New York, 1999. chap. I, p. 19–20. Citation on page [157](#).

LEVEQUE, R. **Finite Volume Methods for Hyperbolic Problems**. 1. ed. [S.l.]: Cambridge University Press, 2002. Citation on page [31](#).

_____. Finite difference methods for ordinary and partial differential equations. In: _____. [S.l.]: SIAM, 2007. Citation on page [116](#).

LIU, Y.; WANG, L.; ZHU, Z. Numerical study on flow characteristics of rotor pumps including cavitation. **Proceedings of the Institution of Mechanical Engineers, Part C: Journal of Mechanical Engineering Science**, v. 229, n. 14, p. 2626–2638, 2015. Citation on page [23](#).

LIUZZI, D. **Two-Phase Cavitation Modelling**. Phd Thesis (PhD Thesis) — University of Rome, 2012. Citation on page [23](#).

LYUBARSKYY, P.; BARTEL, D. 2D CFD-model of the piston assembly in a diesel engine for the analysis of piston ring dynamics, mass transport and friction. **Tribology International**, v. 104, n. September, p. 352–368, 2016. Citation on page [35](#).

MARINI, L. D.; PIETRA, P. Fixed-point algorithms for stationary flow in porous media. **Comput. Methods Appl. Mech. Eng.**, Elsevier Sequoia S. A., Lausanne, Switzerland, Switzerland, v. 56, n. 1, p. 17–45, May 1986. Citation on page [46](#).

MORRIS, N.; LEIGHTON, M.; De la Cruz, M.; RAHMANI, R.; RAHNEJAT, H.; HOWELL-SMITH, S. Combined numerical and experimental investigation of the micro-hydrodynamics of chevron-based textured patterns influencing conjunctinal friction of sliding contacts. **Proc. Inst. Mech. Eng. Part J J. Eng. Tribol.**, n. 4, nov 2014. Citations on pages [22](#), [36](#), [37](#), [39](#), [57](#), and [74](#).

MORRIS, N.; RAHMANI, R.; RAHNEJAT, H.; KING, P. D.; HOWELL-SMITH, S. A Numerical Model to Study the Role of Surface Textures at Top Dead Center Reversal in the Piston Ring to Cylinder Liner Contact. **J. Tribol.**, v. 138, n. 2, p. 021703, nov 2015. Available: <<http://tribology.asmedigitalcollection.asme.org/article.aspx?doi=10.1115/1.4031780>>. Citations on pages [22](#), [36](#), [37](#), [39](#), [57](#), and [74](#).

NATSUMEDA, S.; SOMEYA, T. T. Paper iii(ii) negative pressures in statically and dynamically loaded journal bearings. In: DOWSON, D.; TAYLOR, C.; GODET, M.; BERTHE, D. (Ed.). **Fluid Film Lubrication - Osborne Reynolds Centenary**. [S.l.]: Elsevier, 1987, (Tribology Series, v. 11). p. 65 – 72. Citations on pages [83](#), [84](#), [86](#), [101](#), [108](#), [110](#), and [126](#).

- OHNAWA, M.; SUZUKI, Y. Mathematical and Numerical Analysis of the Rayleigh-Plesset and the Keller Equations. In: **Mathematical Fluid Dynamics, Present and Future.** [S.l.]: Springer Japan, 2016. p. 159–180. Citation on page 23.
- OLSSON, K. Cavitation in dynamically loaded bearings. **Tran. Chalmers University of Technology**, v. 308, 1965. Citation on page 31.
- PAZY, A. **Semigroups of Linear Operators and Applications to Partial Differential Equations.** [S.l.]: Springer, 1983. Citation on page 143.
- PENG, E.; HUANG, S. Wear performance of cylinder liner surface texturing on cylinder liner-piston ring assembly. **Proceedings of the Institution of Mechanical Engineers, Part J: Journal of Engineering Tribology**, v. 0, 2017. Citation on page 22.
- POLYCHRONIS, D. Cavitation in engine lubricants: visualisation experiments in both a single ring test rig and a single cylinder motored diesel engine to complement on the theoretical modeling of cavitation. In: **10th International Symposium on Cavitation - CAV2018.** [S.l.: s.n.], 2018. p. 206–210. Citation on page 22.
- PRIEST, M.; DOWSON, D.; C., T. Theoretical modelling of cavitation in piston ring lubrication. **Proc. Instn. Mech. Engrs**, v. 214, n. 1, p. 435–447, 2000. Citation on page 36.
- PRIEST, M.; DOWSON, D.; M., T. C. Predictive wear modelling of lubricated piston rings in a diesel engine. **Wear**, v. 231, n. 1, p. 89–101, 1999. Citation on page 67.
- PRIEST, M.; TAYLOR, R. I.; DOWSON, D.; TAYLOR, C. M. Boundary Conditions for Reynolds Equation with Particular Reference to Piston Ring Lubrication. In: **The Third Body Concept Interpretation of Tribological Phenomena.** [S.l.]: Elsevier, 1996, (Tribology Series, v. 31). p. 441 – 452. Citations on pages 36 and 41.
- QIU, Y.; KHONSARI, M. Experimental investigation of tribological performance of laser textured stainless steel rings. **Tribol. Int.**, v. 44, p. 635–644, 2011. Citation on page 28.
- QIU, Y.; KHONSARI, M. M. On the Prediction of Cavitation in Dimples Using a Mass-Conservative Algorithm. **ASME, J. of Trib.**, v. 131, n. 4, p. 041702–1, 2009. Citation on page 30.
- RODRIGUEZ, J.-F. **Obstacle Problems in Mathematical Physics.** [S.l.]: North Holland, 1987. Citation on page 30.
- SCHMIDT, M.; REINKE, P.; NOBIS, M.; RIEDEL, M. Three-dimensional simulation of cavitating flow in real journal bearing geometry. In: **4th Micro and Nano Flows Conference (MNF2014).** [S.l.: s.n.], 2014. p. 7–10. Citation on page 23.
- SCHNERR, G.; SAUER, J. Physical and Numerical Modeling of Unsteady Cavitation Dynamics. **Fourth International Conference on Multiphase Flow**, n. May 2001, p. 1–12, 2001. Citation on page 23.
- SHEN, C.; KHONSARI, M. M. On the Magnitude of Cavitation Pressure of Steady-State Lubrication. **Tribol. Lett.**, v. 51, n. 1, p. 153–160, may 2013. ISSN 1023-8883. Available: <<http://link.springer.com/10.1007/s11249-013-0158-2>>. Citation on page 21.

SINGHAL, A. K.; LI, H. Y.; ATHAVALE, M. M.; JIANG, Y. Mathematical Basis and Validation of the Full Cavitation Model. **J. Fluids Eng.**, v. 124, n. 3, p. 617–624, 2001. Citation on page [23](#).

SMITH, E. The Influence of Surface Tension on Bearings Lubricated With Bubbly Liquids. **ASME Journal Lubrication Technology**, v. 102, n. January 1980, p. 91–96, 1980. Citations on pages [83](#) and [86](#).

SNYDER, T. A.; BRAUN, M. J.; PIERSON, K. C. Two-way coupled Reynolds and Rayleigh-Plesset equations for a fully transient, multiphysics cavitation model with pseudo-cavitation. **Tribology International**, Elsevier, v. 93, p. 429–445, jan 2016. Citations on pages [78](#), [83](#), [84](#), [86](#), [88](#), [101](#), [108](#), [110](#), and [126](#).

SÖDERFJALL, M.; LARSSON, R.; MARKLUND, P.; ALMQVIST, A. Texture-induced effects causing reduction of friction in mixed lubrication for twin land oil control rings. **Proceedings of the Institution of Mechanical Engineers, Part J: Journal of Engineering Tribology**, v. 0, 2017. Citation on page [22](#).

SOMEYA, T. On the Development of Negative Pressure in Oil Film and the Characteristics of Journal Bearing. **Meccanica**, v. 38, n. 6, p. 643–658, 2003. Citations on pages [83](#), [84](#), [86](#), [108](#), and [126](#).

TOMANIK, E. Friction and wear bench test of different engine liner surface finishes. **Tribol. Int.**, v. 41, p. 1032–1038, 2008. Citation on page [22](#).

_____. Modelling the hydrodynamic support of cylinder bore and piston rings with laser textured surfaces. **Tribol. Int.**, v. 59, p. 90–96, 2013. Citation on page [22](#).

TØNDER, K. Effect of Gas Bubbles on Behavior of Isothermal Michell Bearings. **Journal of Lubrication Technology**, v. 99, n. 3, p. 354, 1977. Citations on pages [83](#) and [86](#).

USMAN, A.; PARK, C. W. Optimizing the tribological performance of textured piston ring-liner contact for reduced frictional losses in SI engine: Warm operating conditions. **Tribol. Int.**, Elsevier, v. 99, p. 224–236, 2016. ISSN 0301679X. Citations on pages [22](#), [36](#), and [37](#).

VIJAYARAGHAVAN, D.; KEITH, T. Development and evaluation of a cavitation algorithm. **Tribology Transactions**, v. 32, n. 2, p. 225–233, 1989. Citation on page [23](#).

WALTERS, M. J. **An Investigation into the Effects of Viscoelasticity on Cavitation Bubble Dynamics with Applications to Biomedicine**. Phd Thesis (PhD Thesis) — Cardiff University, 2015. Citation on page [23](#).

ZHANG, J.; MENG, Y. Direct observation of cavitation phenomenon and hydrodynamic lubrication analysis of textured surfaces. **Tribol. Lett.**, v. 46, p. 147–158, 2012. Citations on pages [21](#) and [28](#).

ZHAO, B.; DAI, X. D.; ZHANG, Z. N.; XIE, Y. B. A new numerical method for piston dynamics and lubrication analysis. **Tribol. Int.**, Elsevier, v. 94, p. 395–408, 2016. Citation on page [23](#).

ZWART, P.; GERBER, A.; BELAMR, T. A Two-Phase Flow Model for Predicting Cavitation Dynamics. In: **2005 Fall Technical Conference of the ASME Internal Combustion Engine Division**. [S.l.: s.n.], 2004. p. 2. Citations on pages [23](#) and [89](#).

APPENDIX

A

FINITE VOLUME METHODS NOTATION

Let Ω be a regular domain in \mathbb{R}^N , $N = 1, 2$, and assume the next conservation equation holds

$$\frac{\partial q}{\partial t} + \operatorname{div} \vec{Q} = 0 \quad \text{in } \Omega, \quad (\text{A.1})$$

where the scalar field q is the conserved quantity and the vector field \vec{Q} is the flux-function. The Finite Volume Method discretizes Eq. (A.1) in its integral form. For this, it is introduced a (possible time-dependent) finite partition \mathcal{T}^δ of Ω by subdomains. For each time t , the elements $K \in \mathcal{T}^\delta$, called *cells*, are disjoint open sets such that $\cup_{K \in \mathcal{T}^\delta} \bar{K} = \Omega$; they are assumed to be rectangular and the parameter δ is set to the maximum length size of the cells.

Setting some $K \in \mathcal{T}^\delta$, Eq. (A.1) holds in K , thus, integration gives

$$\int_K \left(\frac{\partial q}{\partial t} + \operatorname{div} \vec{Q} \right) dK = \int_K \frac{\partial q}{\partial t} dK + \int_{\partial K} \vec{Q} \cdot \hat{\mathbf{n}} dS = 0$$

by means of the Reynolds Transport Theorem (DONEA; HUERTA, 2003), if $\mathbf{v}(\vec{x}, t)$ is the velocity at which the boundary of K moves, one obtains

$$\frac{d}{dt} \int_K q dK = - \int_{\partial K} \vec{Q} \cdot \hat{\mathbf{n}} dS + \int_{\partial K} q \mathbf{v} \cdot \hat{\mathbf{n}} dS = - \left(\int_{\partial K} (\vec{Q} - q \mathbf{v}) \cdot \hat{\mathbf{n}} dS \right). \quad (\text{A.2})$$

Time is discretized by $t^n = n \Delta t$ and the next approximation is used for each time t^n

$$\frac{1}{|K|} \int_K q dK \approx q(x, t^n)|_{x=x_K} = q_K^n$$

where $x_K \in K$ is generally the center of the cell. Then the left hand side of Eq. (A.2) is discretized in time according to

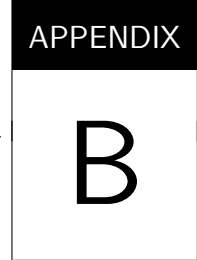
$$\frac{d}{dt} \int_K q dK \approx \frac{|K|^{n+1} q_K^{n+1} - |K|^n q_K^n}{\Delta t} \quad (\text{A.3})$$

The right hand side of Eq. (A.2) is discretized by setting a proper discretization for the function $\vec{Q} - q \mathbf{v}$ at the interfaces, this would depend on values of the involved variables

at time t^n and t^{n+1} . For instance, in Section 3.3.1 a one-dimensional model is described where the conserved quantity and flux-function correspond to

$$q = h\theta \quad \text{and} \quad \vec{Q} = -\frac{h^3}{12\mu} \frac{\partial p}{\partial x_1} + \frac{U}{2} h\theta, \quad (\text{A.4})$$

where θ is a saturation variable. In that example the common interface of two contiguous cells is allowed to move ($\mathbf{v} \neq 0$). Thus, the discretization of $\vec{Q} - q \mathbf{v}$ must be done carefully in order to accommodate mass conservation (the details are given in Section 3.3.1).



SOME MATHEMATICAL BACKGROUND

In this appendix some basic results and definitions needed in Chapter 5 are given.

Hereafter, E and F denote two Banach spaces.

Definition B.1 (Spectrum and eigenvalues). Let $T : E \mapsto E$ be a continuous and linear operator. The identity operator is denoted by I . The set

$$\text{Res}(T) = \{\lambda \in \mathbb{C} : T - \lambda I \text{ is bijective from } E \text{ onto } E\}$$

is called the *resolvent set* of T and

$$\text{Sp}(T) = \mathbb{C} \setminus \text{Res}(T)$$

is called the *spectrum* of T .

An element $\lambda \in \mathbb{C}$ is called *eigenvalue* of T if the operator $T - \lambda I$ is not injective. This means that there exists a vector v , called *eigenvector* of T , such that $Tv - \lambda v = 0$. The set of eigenvalues of T is denoted by $\text{Vp}(T)$. Clearly $\text{Vp}(T) \subset \text{Sp}(T)$.

Definition B.2. Let $T : E \mapsto F$ be a continuous and linear operator. Let B_E denote the unit ball in E . T is said to be *compact* if $T(B_E)$ has compact closure in F (in the strong topology).

For sake of brevity, a reduced version of the Fredholm alternative Theorem is given here, its proof can be found in ([BREZIS, 2010](#)):

Theorem B.1 (Fredholm alternative Theorem). Let $T : E \mapsto E$ be a compact operator. Then the operator $I - T$ is injective if and only if $I - T$ is surjective.

The proof of the following result can be found in ([LANG, 1999](#)).

Theorem B.2 (The Implicit Mapping Theorem). Let U, V be open sets in E, F respectively, and let

$$f : U \times V \mapsto G$$

be a mapping of class C^p . Let $(a, b) \in U \times V$, and assume that

$$D_2 f(a, b) : F \mapsto G$$

(the Fréchet derivative with respect to the second variable) is an isomorphism. Let $f(a, b) = 0$. Then there exists a continuous map $g : U_0 \mapsto V$ defined on an open neighborhood U_0 of a such that $g(a) = b$ and such that

$$f(x, g(x)) = 0 \quad \forall x \in U_0 .$$

If U_0 is taken to be a sufficiently small ball, then g is uniquely determined and it is also of class C^p .

The next results and definitions for Ordinary Differential Equations (ODE) on Banach Spaces are adapted from (BENZONI-GAVAGE, 2010). The corresponding proofs can also be found in that reference (Sections 5.4, 8.1 and 8.2).

Theorem B.3 (Cauchy-Lipschitz). Let $f \in C(U; E)$, where U is an open set of E and $u_0 \in U$, and assume that f is of class C^r , $r \in \mathbb{N}^*$. Then the next properties hold

Existence: There exists $T > 0$ and u in $C^1([t_0 - T, t_0 + T]; U)$ solution of the (autonomous) Cauchy problem:

$$\begin{cases} u' = f(u) , \\ u(t_0) = u_0 . \end{cases} \quad (\text{B.1})$$

Uniqueness: If v is another solution of (B.1). Then $v = u$ on a non-empty interval contained in $[t_0 - T, t_0 + T]$.

Regularity: u is of class C^{r+1} .

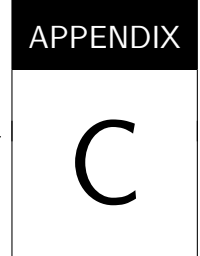
Definition B.3. A solution $u \in C^1([0, T]; E)$ of the Cauchy problem $u' = f(u)$, $u(0) = u_0$ is called *maximal* if u cannot be extended to a solution on an interval containing $[0, T]$.

Definition B.4. Let $f \in C(U; E)$ and $v \in U$. The point v such that $f(v) = 0$ is said to be an asymptotically stable solution of the ODE $u' = f(u)$ if there exist $\eta > 0$ such that for any u_0 such that $\|u_0 - v\| \leq \eta$, the maximal solution of $u' = f(u)$, $u(0) = u_0$ is well defined for every $t \geq 0$ and $\|u(t) - v\| \leq \epsilon$ for every $t \geq 0$ and $\lim_{t \rightarrow \infty} \|u(t) - v\| = 0$.

Theorem B.4. Let $f \in C^2(U; E)$ and $v \in U$ be such that $f(v) = 0$. Assume that $\text{Sp}(Df(v)) \subset \{\lambda \in \mathbb{C} : \text{Re } \lambda < 0\}$. Then v is an asymptotically stable solution of the ODE $u' = f(u)$.

Definition B.5. Let $f \in C(U; E)$ and $v \in U$. The point v such that $f(v) = 0$ is said to be an unstable solution of the ODE $u' = f(u)$ if there exists $\epsilon_0 > 0$ such that for every $\eta > 0$ there exists $T > 0$ and a solution $u \in C^1([0, T], E)$ of $u' = f(u)$ that accomplished $\|u(0) - v\| \leq \eta$ and $\|u(T) - v\| \geq \epsilon_0$.

Theorem B.5. Let $f \in C^2(U; E)$ and $v \in U$ be such that $f(v) = 0$. Suppose that $\max\{\operatorname{Re} \lambda : \lambda \in \operatorname{Sp}(Df(v))\}$ is reached at an eigenvalue of $Df(v)$ with real part strictly positive. Then v is an unstable solution of the ODE $u' = f(u)$.



PUBLISHED WORKS LIST

During this PhD project the next works were published/submitted:

Journal publications:

1. *A stable numerical strategy for Reynolds-Rayleigh-Plesset coupling.* Jaramillo A., Buscaglia G. Tribology International. 2019. ([JARAMILLO; BUSCAGLIA, 2019](#)).
2. *Analysis of a cavitation model including bubbles in thin film lubrication.* Jaramillo A., Bayada G., Ciuperca I., Jai M. Submitted. ([JARAMILLO et al., 2018](#)).

Conference publications:

1. *Tribological effects of the combustion chamber pressure along an extended Elrod-Adams model.* Jaramillo A., Buscaglia G. Oral presentation in the 44th Leeds-Lyon Symposium on Tribology, Lyon, France. 2017.
2. *Non-homogeneous boundary conditions and cavitation modeling for Reynolds equation.* Jaramillo A., Checo H., Buscaglia G. XXII Congreso sobre Métodos Numéricos y sus Aplicaciones, ENIEF, Córdoba, Argentina. 2016.
3. *Incorporation of back-pressure effects in the modeling of the cylinder/piston-rings system.* Jaramillo A., Checo H., Buscaglia G. Ibero-Latin American Congress on Computational Methods in Engineering, CILAMCE, Brasília, Brasil. 2016.

The first page of each of these publications is provided in the following pages in the same order as listed before.



A stable numerical strategy for Reynolds-Rayleigh-Plesset coupling

Alfredo Jaramillo*, Gustavo C. Buscaglia



Instituto de Ciências Matemáticas e de Computação, Universidade de São Paulo, 13560-970, São Carlos, Brazil

ARTICLE INFO

Keywords:
Reynolds equation
Rayleigh-Plesset equation
Cavitation
Numerical simulation

ABSTRACT

The coupling of Reynolds and Rayleigh-Plesset equations has been used in several works to simulate lubricated devices considering cavitation. The numerical strategies proposed so far are variants of a staggered strategy where Reynolds equation is solved considering the bubble dynamics frozen, and then the Rayleigh-Plesset equation is solved to update the bubble radius with the pressure frozen. We show that this strategy has severe stability issues and a stable methodology is proposed. The proposed methodology performance is assessed on two physical settings. The first one concerns the propagation of a decompression wave along a fracture considering the presence of cavitation nuclei. The second one is a typical journal bearing, in which the coupled model is compared with the Elrod-Adams model.

1. Introduction

Cavitation modeling is a challenging issue when studying the hydrodynamics of lubricated devices [1,2]. It is experimentally known that gases (small or large bubbles of air or vapor) appear in the liquid lubricant in regions where the pressure would otherwise be negative. The volume occupied by these gas bubbles affects the pressure field, to the point of preventing it from developing negative regions. It is customary to think of the whole fluid (lubricant + gas) as a mixture for which it is possible to define effective fields of pressure (p), density (ρ) and viscosity (μ). These three fields are linked by the well-known Reynolds equation, which expresses the conservation of mass and must thus hold for the cavitating mixture as well as for the pure lubricant.

Notice, however, that while in problems in which the lubricant is free of gases the density and viscosity are given material data, in problems with significant gas content ρ and μ are two additional unknown fields (totalling three with p). The overall behavior of the mixture exhibits low-density regions (i.e., regions where the fraction of gas is high), in such a way that the overall pressure field does not exhibit negative (or very negative) values.

These low-density regions are usually called *cavitated* regions, though the gas may have appeared there by different mechanisms: cavitation itself (the growth of bubbles of vapor), growth of bubbles of dissolved gases, ingestion of air from the atmosphere surrounding the lubricated device, etc.

Many mathematical models have been developed over the years to predict the behavior of lubricated devices that exhibit cavitation, and most of them have been implemented numerically (see, e.g. [2]). The

most widely used models assume that the data (geometry, fluid properties) and the resulting flow are smooth in time, with time scales governed by the macroscopic dynamics of the device. In particular, the fast transients inherent to the dynamics of microscopic bubbles, though being the physical origin of cavitation, are averaged out of the model. To accomplish this, these models propose phenomenological laws relating ρ , p and μ . These laws vary from very simple to highly sophisticated and nonlocal, and may involve one or more additional (e.g., auxiliary) variables.

A representative example of the aforementioned models is Vijayaraghavan and Keith's bulk compressibility modulus model [3,4]. Without going into the details, it essentially postulates that

$$p = \begin{cases} p_{\text{cav}} + \beta \ln(\frac{\rho}{\rho_e}) & \text{if } \rho \geq \rho_e \\ p_{\text{cav}} & \text{otherwise} \end{cases}, \quad (1)$$

where ρ_e is the liquid density and p_{cav} and β are constants. Another example is the Elrod-Adams model, which here is considered in the mathematical form made precise by Bayada and Chambat [5] and which can be viewed, to some extent, as a limit of (1) for $\beta \rightarrow +\infty$.

In recent years, detailed measurement and simulation of lubricated devices with wide ranges in their spatial and temporal scales has become affordable [6–8]. Micrometric features of the lubricated surfaces can now be incorporated into the simulated geometry, down to the roughness scale. These micrometric spatial features of the two lubricated surfaces, being in sliding relative motion, generate rapid transients in the flow. This reason, among others, has lately revived the interest on models that take the microscopic dynamics of the incipient

* Corresponding author.

E-mail address: ajaramillopalma@gmail.com (A. Jaramillo).

Analysis of a cavitation model including bubbles in thin film lubrication

Alfredo Jaramillo^a, Guy Bayada^b, Ionel Ciuperca^c, Mohammed Jai^b

(a) Instituto de Ciências Matemáticas e de Computação, Universidade de São Paulo, 13560-970 São Carlos, Brazil

(b) Université de Lyon, CNRS, INSA de Lyon, Institut Camille Jordan UMR 5208, F-69621 Villeurbanne, France

(c) Université de Lyon, CNRS, Institut Camille Jordan UMR 5208, F-69622 Villeurbanne, France

September 18, 2018

Abstract

In the lubrication area, which is concerned with thin film flow, cavitation has been considered as a fundamental element to correctly describe the characteristics of lubricated mechanisms. Here, the well-posedness of a cavitation model that can explain the interaction between viscous effects and micro-bubbles of gas is studied. This cavitation model consists in a coupled problem between the compressible Reynolds PDE (that describes the flow) and the Rayleigh-Plesset ODE (that describes micro-bubbles evolution). This coupled model seems never to be studied before from its mathematical aspects. Local times existence results are proved and stability theorems are obtained based on the continuity of the spectrum for bounded linear operators. Numerical results are presented to illustrate these theoretical results. Particularly, a loss of well-posedness depending upon a geometrical parameter is shown numerically.

Keywords: Cavitation modeling, Thin film lubrication, Reynolds equation, Rayleigh-Plesset equation.

1 Introduction

Cavitation is observed in various engineering devices, ranging from hydraulic systems to turbo pumps for space applications. It is a challenging issue linked with various phenomenon: acoustic, thermodynamic and fluid dynamic. In the lubrication area, which is concerned with thin film flow, cavitation has been considered as a fundamental element to correctly describe the characteristics of lubricated mechanisms [1, 2]. Cavitation has often been primary associated with a diminution of the pressure p in the liquid falling below the vapor pressure. Numerous models have been introduced to couple this unilateral condition with the Reynolds equation, which is usually used to model the pressure evolution in thin film flow. Mathematical studies of these models can be found in [3, 4, 5, 6, 7, 8] in which existence and uniqueness results are given for both the stationary and transient cases. Another approach has been proposed in [9] by considering cavitation as a multifluid problem with a free boundary between two immiscible fluids. However, it is physically recognized that the cavitation phenomenon is linked with the existence and evolution of micro-bubbles in a liquid. This aspect has not been taken into account in these models. It is however used in the well known software Fluent for fluid mechanics [10, 11, 12] in which micro bubbles evolution is coupled with the Navier Stokes system for a 3-dimensional flow. In the lubrication area, this phenomenon has been ignored until the works of Someya's group [13, 14] who proposed to couple the full Rayleigh-Plesset equation (which describes the evolution of a bubble) with the Reynolds equation (which describes the fluid). Numerous works follow in the lubrication literature using simplified forms of the Rayleigh-Plesset equation for various kind of applications [15, 16, 17, 18, 19]. The paper of Snyder et al. [20] can be considered as a review paper in this field.

Mass and momentum conservation equations

The fluid is contained in a domain $\Omega^V \subset \mathbb{R}^3$, limited by a domain $\Omega \subset \mathbb{R}^2$ in the x_1 - x_2 plane, an upper surface given by the gap function $h(x_1, x_2)$ defined on Ω and by a vertical lateral boundary as shown in Fig. 1. The surfaces are in relative movement along the x_1 - x_2 plane at velocity $\mathbf{U} \in \mathbb{R}^2$. It is also assumed that the relative speed of the surfaces along the x_3 -axis is null. In this work theoretical results

44th Leeds-Lyon Symposium on Tribology - September 4-6, 2017, Lyon, France

TRIBOLOGICAL EFFECTS OF THE COMBUSTION CHAMBER PRESSURE ALONG AN EXTENDED ELROD-ADAMS MODEL

A. Jaramillo ^{a*}, G. Buscaglia ^a, M. Jai ^b

*ajaramillopalma@gmail.com

^a Instituto de Ciências Matemáticas e de Computação,
Av. Trabalhador São-Carlense 400, São Carlos, Brazil

^b Institut National des Sciences Appliquées,
20 Avenue Albert Einstein, Lyon, France

KEYWORDS

Piston rings; combustion chamber pressure; Elrod-Adams model

ABSTRACT

The Piston Ring/Cylinder Liner (PRCL) is a tribological mechanism that have received great deal of attention during the last decades. The source of this attention becomes from the important amount of energy losses due to friction in the PRCL [1]. During the compression stroke, the combustion chamber pressure (CCP) achieves values as high as 100atm. The compression ring is in direct contact with the combustion chamber gas through the gap present between the piston and the cylinder. Thus, when simulating the PRCL including the CCP (which depends on time), the value of the CCP must be imposed as a Dirichlet condition for the pressure on the hydrodynamical model considered.

As mass-conservation is essential when considering the texturization of lubricated mechanisms [2], in this work we extend the Elrod-Adams cavitation model (which is already an extension of the Reynolds Equation) to accommodate non-homogeneous boundary conditions. This is, in the side of the ring in touch with the combustion gas, the boundary condition for pressure is the CCP value, while on the other side we impose 1 atm.

In this work, we compare the friction losses predicted by the proposed extension of the Elrod-Adams model, with those friction losses predicted by a non-mass conservative model, which represents the state-of-the-art when including the CCP as a boundary condition [3].

ACKNOWLEDGMENTS

The authors acknowledge the financial support of CAPES (grant PROEX-8434433/D) and CNPQ (grant 447904/2011-0).

REFERENCES

- [1] Holmberg, K., Andersson, P. and Erdemir, A., "Global energy consumption due to friction in passenger cars," *Tribology International*, 47, 2012, 221-234.
- [2] Ausas, R., "The impact of the Cavitation model in the Analysis of Micro-Textured Lubricated Journal bearings," *AMSE J. Tribology*, 129, 4, 2007, 868-875.
- [3] Kligerman, Y. and Shinkarenko, A., "Analysis of friction in surface textured components of reciprocating mechanism," *Proc. IMechE., Part J: J Engineering Tribology*, 229, 4, 2015, 336-349.

Asociación Argentina

de Mecánica Computacional



Mecánica Computacional Vol XXXIV, págs. 2087-2100 (artículo completo)
 Sebastián Giusti, Martín Pucheta y Mario Storti (Eds.)
 Córdoba, 8-11 Noviembre 2016

NON-HOMOGENEOUS BOUNDARY CONDITIONS AND CAVITATION MODELING FOR REYNOLDS EQUATION

Alfredo Jaramillo^a, Hugo M. Checo^a and Gustavo C. Buscaglia^a

^a*Inst. de Ciências Matemáticas e de Computação, Universidade de São Paulo, 13560-970 São Carlos,
 Brazil, <http://www.icmc.usp.br>*

Keywords: Surface-texturing, cavitation modeling, Elrod-Adams model, back-pressure effects.

Abstract. When simulating numerically the hydrodynamical lubrication of tribological devices, a common assumption is that the boundary pressure and the cavitation pressure are equal (and taken equal to zero). This allows to include cavitation effects through some of the available algorithms, like the mass-conserving Elrod-Adams cavitation model. However, tribological devices often work under non-homogeneous pressure conditions. An example of this is the cylinder/piston-rings system, where the pressure difference between both sides of the ring reach levels in the order of 50 atm during compression and ignition. In this work we propose an extension of the Elrod-Adams model in order to accommodate such non-homogeneous pressure conditions by assuming a dependence of the algorithmic cavitation pressure on the saturation variable. A first algorithm for solving the resulting model is proposed. Also, preliminary tests results on how the back-pressure may affect the dynamics of the rings during the compression/power stroke are reported.



INCORPORATION OF BACK-PRESSURE EFFECTS IN THE MODELING OF THE PISTON RING/CYLINDER LINER

Alfredo Jaramillo Palma^(a)

ajaramillopalma@icmc.usp.br

Hugo Checo Silva^(a)

hcoco@icmc.usp.br

Gustavo Carlos Buscaglia^(a)

gustavo.buscaglia@icmc.usp.br

(a) Universidade de São Paulo

13560-970, São Carlos, São Paulo, Brazil

Abstract. The piston ring/cylinder liner system is responsible for about 5% of the energy loss due to friction in a passenger car (Holmberg et al., 2012). Consequently, automotive industry and academy have made efforts seeking for designs that diminish both friction and wear. During the last year, several numerical and experimental studies have shown that texturization can have favorable or detrimental effects on the tribological characteristics of lubricated mechanisms. However, few studies have included the effects of the gas pressure in the combustion chamber, which varies rapidly in the compression stroke and can reach values as high as 60[atm]. Reynolds equation with zero-pressure Dirichlet conditions is mainly adopted in numerical works along with Elrod-Adams cavitation model. This cavitation model only admits a constant cavitation pressure, in spite it is known that cavitation pressure can vary according to the operational conditions (Shen et al., 2013). This work is devoted to the study of the effects that the combustion chamber pressure can have on both the mechanical dynamic of the rings and the cavitation pressure p_{cav} .

Keywords: Hydrodynamic lubrication; Friction force; Back-pressure effects; Elrod-Adams model

